Universität Hamburg
DER FORSCHUNG | DER LEHRE | DER BILDUNG

Modeling the Propagation of High-Energy Cosmic Messengers

Dissertation zur Erlangung des Doktorgrades
an der Fakultät für Mathematik, Informatik und Naturwissenschaften
der Universität Hamburg

vorgelegt von

Simone Rossoni

aus Pescara, Italien

Hamburg, 2025

Gutachter/innen der Dissertation:

Prof. Dr. Dieter Horns

Prof. Dr. Günter Sigl

Zusammensetzung der Prüfungskommission:

Prof. Dr. Carmelo Evoli

Prof. Dr. Caren Hagner

Prof. Dr. Gregor Kasieczka

Prof. Dr. Sven-Olaf Moch

Prof. Dr. Günter Sigl

Vorsitzende/r der Prüfungskommission:

Prof. Dr. Gregor Kasieczka

Datum der Disputation: 16.07.2025

Vorsitzender des Fach-Promotionsausschusses PHYSIK:

Prof. Dr. Wolfgang J. Parak

Leiter des Fachbereichs PHYSIK:

Prof. Dr. Markus Drescher

Dekan der Fakultät MIN:

Prof. Dr.-Ing. Norbert Ritter

© 2025 Simone Rossoni

Dieses Werk ist lizenziert unter einer

Creative Commons Namensnennung 4.0 International Lizenz:

http://creativecommons.org/licenses/by/4.0/

Declaration on oath

I hereby declare and affirm that this doctoral dissertation is my own work and that I have not used any aids and sources other than those indicated.

If electronic resources based on generative artificial intelligence (gAI) were used in the course of writing this dissertation, I confirm that my own work was the main and value-adding contribution and that complete documentation of all resources used is available in accordance with good scientific practice. I am responsible for any erroneous or distorted content, incorrect references, violations of data protection and copyright law or plagiarism that may have been generated by the gAI.

Hamburg, 22/05/2025

Ort, Datum | *Place, date*

Unterschrift | *Signature*

Zusammenfassung

Die extragalaktische Ausbreitung hochenergetischer Teilchen wird durch die Präsenz kosmischer Photonen und Magnetfelder gestört, welche alle physikalischen Beobachtungen beeinflussen. Darüber hinaus macht das begrenzte Wissen über die Magnetisierung des extragalaktischen Raums den Einsatz umfangreicher numerischer Simulationen zu einem grundlegenden Werkzeug zur Rekonstruktion ihrer Ausbreitung. In dieser Arbeit untersuchen wir die Ausbreitung der kosmischen Strahlung in gebundenen und magnetisierten Nachbildungen des lokalen Universums in einer Reihe von Szenarien. Anlass dafür ist die Beobachtung einer dipolaren Komponente in der Ankunftsrichtung der kosmischen Strahlung oberhalb von 8 EeV durch das Pierre Auger Observatorium. Wir berücksichtigen verschiedene Annahmen zur Verteilung und Dichte der kosmischen Strahlenquellen sowie zu den galaktischen und extragalaktischen Magnetfeldern. Wir stellen fest, dass das Anisotropiesignal oberhalb von 8 EeV hauptsächlich von den Eigenschaften der Quellenverteilung beeinflusst wird, während die Magnetisierung des extragalaktischen Raums lediglich zur Verringerung des Horizonts kosmischer Strahlung beiträgt. Darüber hinaus finden wir heraus, dass es möglich ist, das beobachtete Energiespektrum, die Massenzusammensetzung und die dipolare Komponente der kosmischen Strahlung zu reproduzieren. Die vorhergesagten höheren Multipolmomente, wie etwa die quadrupolare Komponente, sind jedoch im Vergleich zu den Beobachtungen im Allgmeinen zu groß.

Die gleiche numerische Konfiguration, die für die extragalaktische Ausbreitung verwendet wird, kann auch angepasst werden, um die Ausbreitung hochenergetischer Teilchen in ihren Quellenumgebungen zu untersuchen. Zusätzlich kann die Produktion neutraler und stabiler Sekundärteilchen wie Neutrinos und Photonen berücksichtigt werden. Da Neutrinos nicht mit Photonenfeldern wechselwirken und nicht durch Magnetfelder abgelenkt werden, stellen sie ideale kosmische Sonden zur Untersuchung astrophysikalischer Quellen dar. Aus diesen Gründen untersuchen wir die Produktion hochenergetischer Neutrinos in den Umgebungen, die durch Verschmelzungen binärer Neutronensterne entstehen. Wir kombinieren verschiedene Modelkonfigurationen um die Produktion, das Entweichen aus der Quelle sowie die extragalaktische Ausbreitung hochenergetischer kosmischer Strahlen und Neutrinos zu untersuchen. Wir erhalten den propagierten Neutrinofluss, der durch diese Verschmelzungen erzeugt wird, und vergleichen ihn mit dem beobachteten diffusen Neutrinofluss. Zudem charakterisieren wir die Quellenumgebungen, indem wir das Verhältnis zwischen der Leuchtkraft kosmischer Strahlung während der Beschleunigung und der Fallback-Leuchtkraft, sowie die Ereignisdichterate einschränken.

Schließlich betrachten wir auch die Ausbreitung von sehr hochenergetischen γ-Strahlen, da auch diese mit Hintergrund-Photonenfeldern interagieren und eine elektromagnetische Kaskade von Sekundärteilchen erzeugen. Obwohl die Entwicklung dieser

Kaskaden gut verstanden ist, bestehen weiterhin Diskrepanzen zwischen den theoretischen Vorhersagen und den experimentellen Beobachtungen des Photonflusses von fernen Blazaren. Insbesondere wird eine Unterdrückung im GeV-Photonenspektrum beobachtet. Als mögliche Erklärung betrachten wir die Auswirkung von Plasmainstabilitäten auf die Elektronen-Positronen-Paare der Kaskaden. Wir beziehen diesen Mechanismus in die Entwicklung der elektromagnetischen Kaskaden ein und rekonstruieren zum ersten Mal das propagierte Photonenspektrum, um die spektralen Parameter bei der Injektion für verschiedene Parametrisierungen der Plasmainstabilitäten zu erhalten. Wir stellen fest, dass das beobachtete Photonenspektrum reproduziert werden kann, wenn der Energieverlust aufgrund von Plasmainstabilitäten mit dem der inversen Compton-Streuung vergleichbar ist.

Abstract

The extragalactic propagation of high-energy particles is influenced by the presence of cosmic photons and magnetic fields, which affect all their physical observables. Moreover, the limited knowledge of the magnetization of the extragalactic space makes the use of extensive numerical simulations a fundamental tool to reconstruct their propagation. In this thesis, motivated by the observation of a dipolar component in the arrival direction distribution of cosmic rays above 8 EeV by the Pierre Auger Observatory, we study their propagation in constrained and magnetized replicas of the local Universe for a wide range of scenarios. We consider several assumptions for the cosmic ray source distribution and density, as well as for the extragalactic and galactic magnetic fields. We find that the anisotropy signal above 8 EeV is mainly affected by the properties of the source distribution, while the magnetization of the extragalactic space only contributes to the reduction of the cosmic ray horizon. Furthermore, we find that, while it is possible to reproduce the observed cosmic ray energy spectrum, mass composition and dipolar component, the predicted higher multipoles, such as the quadrupole component, are generally too large with respect to the observations.

The same numerical framework used for extragalactic propagation, can also be adapted to study the propagation of high-energy particles within their source environments. In addition, the production of neutral and stable secondary particles, such as neutrinos and photons, can be taken into account. Since neutrinos do not interact with photon fields and are not deflected by magnetic fields, they are ideal cosmic probes to study astrophysical sources. For these reasons, we study the production of high-energy neutrinos in the environment created by binary-neutron-star merges. We combine different simulation setups to study the production, the escape from the source and the extragalactic propagation of high-energy cosmic rays and neutrinos. We obtain the propagated neutrino flux produced by the mergers and we compare it with the observed diffuse neutrino flux. We also characterize the source environments by constraining the ratio between the cosmic ray luminosity at the acceleration and the fallback luminosity, and the event density rate.

Finally, we also consider the propagation of very-high-energy γ-rays since they also interact with background photon fields, producing an electromagnetic cascade of secondary particles. Although the development of these cascades is well understood, there are still discrepancies between the theoretical predictions and experimental observations of the photon flux from distant blazars. In particular, a suppression in the GeV photon spectrum is observed. As a possible explanation, we consider the effect of plasma instabilities on the electron-positron pairs of the cascades. We include this mechanism in the development of the electromagnetic cascades and, for the first time, we reconstruct the propagated photon spectrum, obtaining the spectral parameters at the injection for different parameterizations of the plasma instabilities. We find that, when the energy loss due to plasma instabilities is comparable to that of inverse Compton scattering, the observed photon spectrum can be reproduced.

Fate leads the willing and drags the unwilling.
— Seneca

There will come a time when you believe everything is finished.
That will be the beginning.
— Louis L'Amour

List of Publications*

Journal Papers

- L. E. E. Castro, S. Rossoni, and G. Sigl. (2024). *Influence of plasma instabilities on the propagation of electromagnetic cascades from distant blazars.* arXiv: 2405.15390 [astro-ph.HE]. Submitted for publication to **The Astrophysical Journal**.
  Author contributions: L. E. E. Castro and S. Rossoni performed the simulations, analyzed the simulation results, prepared the figures, and wrote the manuscript. G. Sigl supervised the research, provided numerical resources, contributed to the discussion of the results, and reviewed the manuscript.

- S. Rossoni, D. Boncioli, and G. Sigl. (2025). *Investigating binary-neutron-star mergers as production sites of high-energy neutrinos.* **JCAP**, 01, 009. arXiv:2407.19957 [astro-ph.HE]. https://doi.org/10.1088/1475-7516/2025/01/009.
  Author contributions: S. Rossoni performed the simulations, analyzed the simulation results, prepared the figures, and wrote the manuscript. D. Boncioli supervised the research, provided numerical resources, contributed to the discussion of the results, and reviewed the manuscript. G. Sigl supervised the research, contributed to the discussion of the results, and reviewed the manuscript.

- S. Rossoni and G. Sigl. (2025). *Anisotropy signal of UHECRs from a structured magnetized Universe.* **Phys. Rev. D**, 112, 023015. arXiv:2502.19324 [astro-ph.HE]. https://doi.org/10.1103/4zt7-s48v.
  Author contributions: S. Rossoni performed the simulations, analyzed the simulation results, prepared the figures, and wrote the manuscript. G. Sigl supervised the research, provided numerical resources, contributed to the discussion of the results, and reviewed the manuscript.

Conference Proceedings

- S. Rossoni, D. Boncioli, and G. Sigl. (2021). *Study of the production of high-energy neutrinos in the environment of binary-neutron-star mergers.* **PoS** (ICRC2021) 1004. https://doi.org/10.22323/1.395.1004.
  Author contributions: S. Rossoni performed the simulations, analyzed the simulation results, prepared the figures, and wrote the manuscript. D. Boncioli supervised the research, provided numerical resources, contributed to the discussion of the results, and reviewed the manuscript. G. Sigl supervised the research, contributed to the discussion of the results, and reviewed the manuscript.

- D. Boncioli, S. Rossoni, and C. Trimarelli. (2022). *Ultra-high-energy cosmic rays: propagation and detection.* **PoS** (CORFU2021) 320. https://doi.org/10.22323/1.406.0320.
  Author contributions: D. Boncioli prepared the figures, and wrote the manuscript. S. Rossoni and C. Trimarelli contributed to the writing and reviewed the manuscript.

- S. Rossoni and G. Sigl. (2023). *CRPropa high statistics simulations for UHECR anisotropy studies.* **EPJ Web Conf.** 283, 03010. https://doi.org/10.1051/epjconf/202328303010.
  Author contributions: S. Rossoni performed the simulations, analyzed the simulation results, prepared the figures, and wrote the manuscript. G. Sigl supervised the research, provided numerical resources, contributed to the discussion of the results, and reviewed the manuscript.

- S. Rossoni, D. Boncioli, and G. Sigl. (2023). *Production of high-energy neutrinos in binary-neutron-star merger events.* **EPJ Web Conf.** 283, 04006.
  https://doi.org/10.1051/epjconf/202328304006.
  Author contributions: S. Rossoni performed the simulations, analyzed the simulation results, prepared the figures, and wrote the manuscript. D. Boncioli supervised the research, provided numerical resources, contributed to the discussion of the results, and reviewed the manuscript. G. Sigl supervised the research, contributed to the discussion of the results, and reviewed the manuscript.

- S. Aerdker and others. (2023). *CRPropa 3.2: a public framework for high-energy astroparticle simulations.* **PoS** (ICRC2023) 1471. https://doi.org/10.22323/1.444.1471. arXiv: 2308.09532.
  Author contributions: S. Rossoni contributed to reviewing and providing comments on the manuscript.

- S. Rossoni and G. Sigl. (2023). *High-statistics CRPropa simulations for UHECR anisotropy studies.* **PoS** (ICRC2023) 433. https://doi.org/10.22323/1.444.0433.
  Author contributions: S. Rossoni performed the simulations, analyzed the simulation results, prepared the figures, and wrote the manuscript. G. Sigl supervised the research, provided numerical resources, contributed to the discussion of the results, and reviewed the manuscript.

***Excluding publications with full author list within the Pierre Auger Collaboration.**

Contents

List of Publications **i**

List of Abbreviations **vii**

1 Introduction **1**

2 Cosmic Rays **5**
2.1 Early cosmic ray observations 5
2.1.1 Cosmic rays and particle physics 8
2.1.2 The high-energy cosmic ray observatories 8
2.2 Extensive air showers 9
2.2.1 Electromagnetic showers: the Heitler model 11
2.2.2 Hadronic showers: the Heitler-Matthews model 13
2.2.3 Superposition model 14
2.2.4 EAS simulations 14
2.3 Cosmic ray energy spectrum 16

3 The Pierre Auger Observatory **21**
3.1 Hybrid detection 21
3.1.1 Surface detector 22
3.1.2 Fluorescence detector 23
3.1.3 Other detectors 24
3.1.4 Auger Prime 25
3.2 Selected scientific results 25
3.2.1 Energy spectrum 26
3.2.2 Mass composition 27
3.2.3 Anisotropies 29

4 Origin and propagation of UHECRs **35**
4.1 Cosmic rays acceleration 35
4.1.1 Stochastic acceleration: the Fermi mechanisms 36
4.1.2 Characterization of UHECR sources 39
4.1.3 Source candidates 41
4.2 Expanding Universe 42
4.3 Photohadronic interactions 45

4.3.1 Cosmic photon fields . . . 46
4.3.2 Electron-positron pair production . . . 48
4.3.3 Photopion production . . . 49
4.3.4 Photodisintegration . . . 50
4.3.5 Nuclear decay . . . 51
4.3.6 General discussion . . . 52
4.4 Interactions of electromagnetic particles . . . 53
4.5 Propagation in magnetic fields . . . 55
4.5.1 Extragalactic magnetic field . . . 57
4.5.2 Galactic magnetic field . . . 59

5 Simulation codes **63**
5.1 SimProp v2r4 . . . 63
5.2 CRPropa 3.2 . . . 65
5.3 Comparison of the codes . . . 68

6 Cosmic ray anisotropy analysis **71**
6.1 Dipole reconstruction . . . 71
6.1.1 Finite number of events . . . 72
6.1.2 Partial sky coverage . . . 73
6.2 Spherical harmonic decomposition . . . 75
6.2.1 Effect of the exposure . . . 77
6.3 Angular power spectrum expectation . . . 78
6.3.1 Infinite sky resolution . . . 79
6.3.2 Finite number of pixels . . . 81

7 UHECR anisotropies from a magnetized Universe **87**
7.1 Cosmic ray anisotropies and magnetic fields . . . 87
7.2 Extragalactic cosmic ray propagation models . . . 89
7.2.1 Constrained EGMFs . . . 90
7.2.2 Source distribution models . . . 92
7.2.3 CRPropa simulations . . . 94
7.3 Simulation analysis . . . 95
7.3.1 Anisotropies in the UHECR arrival direction distribution . . . 97
7.4 Results of the analysis . . . 98
7.4.1 Energy spectrum and mass composition . . . 98
7.4.2 Magnetic horizon . . . 100
7.4.3 Multipole analysis . . . 102
7.5 Conclusions . . . 107

8 Cosmic ray propagation in source environments **109**
8.1 Multimessenger astrophysical sources . . . 109
8.1.1 Astrophysical neutrinos . . . 110
8.2 Source model . . . 111
8.2.1 Local photon fields . . . 111
8.2.2 Escape length . . . 113

8.2.3 Interaction efficiency . . . 113
8.2.4 Numerical implementation . . . 116
8.3 Source escape and neutrino production . . . 116
8.4 Extragalactic propagation . . . 121
8.4.1 Source parameters . . . 124
8.4.2 Temporal evolution of the source environment . . . 126
8.5 Discussion and conclusions . . . 129

9 Modified electromagnetic cascades from distant blazars 133
9.1 Electromagnetic cascades and plasma instabilities . . . 133
9.2 Plasma instability energy loss model . . . 135
9.3 Cascade simulations . . . 137
9.3.1 Output analysis . . . 137
9.4 Results . . . 139
9.4.1 Standard electromagnetic cascade . . . 139
9.4.2 Modified electromagnetic cascade . . . 141
9.5 Discussion and conclusions . . . 143

10 Conclusions 145

References 149

Appendices **183**

A Sky distributions **183**
A.1 Spherical harmonics . . . 183
A.2 The von Mises-Fisher distribution . . . 186
A.3 Coordinate systems . . . 187
A.4 Rayleigh analysis . . . 188

B Cosmic ray interactions **191**
B.1 Interaction rate . . . 191
B.2 Initial state kinematics . . . 192
B.3 Connecting energy intervals . . . 193
B.4 Neutrino propagation . . . 195

C Technical details for UHECR anisotropy simulations **197**
C.1 Weighting procedure . . . 197
C.2 Arrival direction correction . . . 198
C.3 Homogeneous source scenario . . . 200

D Further scenarios for astrophysical neutrinos **207**
D.1 Cosmic ray energy spectra . . . 207
D.2 Parameter study with the SFR . . . 207

E CRPropa module for plasma instabilities in electromagnetic cascades **215**
E.1 Plasma instability module . . . 215
E.2 Testing the plasma instability module . . . 218
E.3 Dependence of the spectrum on instability parameters . . . 219

Acknowledgements **221**

Ringraziamenti **223**

List of Abbreviations

AERA	Auger engineering radio antenna
AGN	Active galactic nucleus
AMIGA	Auger muon and infilled ground array
BB	Black-body
BLS	Balloon launching station
BNS	Binary-neutron-star
CDAS	Central data acquisition system
CLF	Central laser facility
CMB	Cosmic microwave background
CNO	Carbon-Nitrogen-Oxygen
COB	Cosmic optical background
CR	Cosmic ray
CRB	Cosmic radio background
DM	Dark matter
EAS	Extensive air shower
EBL	Extragalactic background light
EGMF	Extragalactic magnetic field
EHECR	Extremely-high-energy cosmic ray
FD	Fluorescence detector
FLRW	Friedmann-Lemaître-Robertson-Walker
FWHM	Full width at half maximum
GDR	Giant dipole resonance
GMF	Galactic magnetic field
GRB	Gamma-ray burst
GUT	Grand unification theory

GW	Gravitational wave
GZK	Greisen-Zatsepin-Kuz'min
HEAT	High elevation auger telescopes
HIM	Hadronic interaction model
IGM	Intergalactic medium
IRB	Infrared background
ISM	Interstellar medium
LHC	Large hadron collider
LIV	Lorentz invariance violation
LSS	Large scale structure
NT	Non-thermal
PDG	Particle data group
PMT	Photomultiplier tube
RD	Radio detector
RM	Faraday rotation measure
SBG	Starburst galaxy
SD	Surface detector
SED	Spectral energy density
SFR	Star formation rate
SM	Standard model
SNR	Supernova remnants
SSD	Surface scintillator detectors
TA	Telescope Array
TALE	Telescope Array low-energy extension
TDE	Tidal disruption event
UHECR	Ultra-high-energy cosmic ray
UMD	Underground muon detector
UUB	Upgraded unified board
VHEGR	Very-high-energy gamma ray
XLF	eXtreme laser facility

1

Introduction

For the most of the human history, our study of the cosmos has been based on observations of light from extraterrestrial objects. However, the discoveries made in the last century have completely revolutionized the way we study the Universe beyond Earth. The change began in the 1910s, when V. F. Hess demonstrated the existence of a mysterious ionizing radiation of extraterrestrial origin [1]. Although this radiation was initially identified as very energetic photons [2], it became increasingly clear that it consisted of electrically charged particles [3–8].

Nowadays, we know that the ionizing radiation, commonly called *cosmic rays*, consists of ionized nuclei with kinetic energies from $\sim 10^6$ eV to $\sim 10^{21}$ eV[1]. The cosmic ray energy spectrum can be described approximately by a power-law of the form $J(E) \sim E^{-3}$ with a cutoff above $\sim 10^{20}$ eV [9]. The origin of these cosmic rays depends on the energy range considered. Below $\sim 10^9$ eV, most cosmic rays come from the Sun, while cosmic rays with energies up to 10^{15} eV are thought to be produced in Galactic supernova remnants. At the highest energies (above $\sim 10^{18}$ eV), cosmic rays are called ultra-high-energy cosmic rays and their origin is still a mystery. In recent decades, however, evidence has been found pointing an extragalactic origin of the ultra-high-energy cosmic rays.

Given the very large energy range, the techniques for observing cosmic rays depend on the energy interval of interest. Below $\sim 10^{15}$ eV, balloon and satellite experiments can be used to directly measure the cosmic ray flux. At the highest energies, the cosmic ray flux is extremely suppressed, down to less than 1 particle per km^2 per yr, and only indirect measurements are possible. This second type of measurement is possible because of the extensive cascades of secondary particles produced by the interaction of an ultra-high-energy cosmic ray with atmospheric constituents. Large-area ground-based detectors can measure these extensive particles showers and reconstruct the information from the primary ultra-high-energy cosmic ray. The two largest observatories for ultra-high-energy cosmic rays are the Pierre Auger Observatory [10], in Argentina, and the Telescope Array [11], in the USA.

The most important observables for ultra-high-energy cosmic rays are their energy, mass composition, and arrival direction. However, the observed values of these quantities do not correspond to those at the escape from their sources. Since the extragalactic space is populated by

[1] For reference, the same energy range in Joules would be from $\sim 2 \cdot 10^{-13}$ J to ~ 200 J.

low-energy cosmic photon fields, such as the Cosmic Microwave Background [12] and the Extragalactic Background Light [13], the ultra-high-energy cosmic rays are subject to photohadronic interactions [14, 15]. As a result, these interactions modify the energy spectrum and mass composition emitted by the cosmic ray sources. In addition, photohadronic interactions introduce a suppression of the maximum source distance depending on the observed cosmic ray energy, i.e., an interaction horizon.

In 2017, the Pierre Auger Observatory reported the first observation of a dipole component in the arrival direction distribution of the cosmic rays with energy above 8 EeV [16]. With more than $\sim 50,000$ events above 8 EeV, the actual observed dipole amplitude is $d \simeq 7.5\%$ with a 6.8σ significance, pointing more than $\sim 100^\circ$ away from the Galactic center [17], supporting the idea of an extragalactic origin above this energy. Unfortunately, the observed arrival directions may not point to the cosmic ray source, given the presence of cosmic magnetic fields. Since cosmic rays are electrically charged, galactic and extragalactic magnetic fields can deflect these particles, leading to a loss of information about the position of their sources in the sky. Moreover, the modelling of these deflections is limited by our knowledge of the galactic and extragalactic magnetism [18–20].

The cosmic ray properties at the escape from their sources, reconstructed to include the effects of the extragalactic propagation, may still not directly correspond to those at the acceleration. The local environment of candidate cosmic ray sources may be populated by matter and photon fields. Therefore, the energy spectrum and composition of the escaped cosmic rays would be given by the interplay of acceleration and local interactions. In addition, local interactions can lead to the production of neutrinos, which are neutral and weakly interacting secondary particles. Neutrinos can leave the source environment immediately after their production and propagate almost undisturbed in the extragalactic space. This means that observations of astrophysical neutrinos, such as those made by the IceCube Neutrino Observatory [21], can provide further information about interaction environments that cannot be reproduced on Earth.

The production of very-high-energy γ-rays in astrophysical environments is an additional quantity to be taken into account for a comprehensive study of astrophysical objects. However, as it happens with cosmic rays, the propagation of γ-rays in the extragalactic space is also affected by the presence of cosmic photon fields. High-energy photons will produce electron-positron pairs. These pairs will up-scatter low-energy background photons into high-energy photons. The repetition of these processes corresponds to an *electromagnetic cascade* [22].

The development of these electromagnetic cascades can be influenced by the medium in which they evolve. The electron-positron pairs produced in the cascade can be deflected by extragalactic magnetic fields, modifying the image of the source in the sky and introducing time delays with respect to rectilinear propagation. In addition, the interaction of high-energy electrons and positrons with the cosmic plasma can lead to plasma instabilities [23–25]. The effect of these instabilities on electromagnetic cascades is still under debate: further energy losses to the pair-produced electrons and positrons may suppress the production of secondary photons, and the broadening of the cascade may introduce further deflections out of the line of sight to the sources.

The overall picture of current observations in astroparticle physics is clear: cosmic ray, neutrino and γ-ray observations can be combined together to advance the study of astrophysical objects. The joint observation of all these high-energy particles has marked the beginning of the *multimessenger era* of astroparticle physics. Moreover, the first joint observations of *gravitational waves* with electromagnetic signals [26–28] have opened up new possibilities for the study

of astrophysical phenomena.

This thesis is organized as follows. Chapter 2 gives a historical introduction to cosmic ray physics and an overview of extensive air showers and the cosmic ray energy spectrum. The Pierre Auger Observatory and its main scientific results on the cosmic ray energy spectrum, mass composition and anisotropies are presented in Chapter 3. Chapter 4 gives an overview of the origin and propagation of ultra-high-energy cosmic rays. Basic acceleration mechanisms and the characterization of cosmic ray sources are discussed. In this chapter, the effects of the extragalactic propagation of high-energy particles are also presented: in particular, interactions with the background photon fields and the effect of cosmic magnetic fields are discussed. Chapter 5 introduces the most widely used simulation frameworks for ultra-high-energy cosmic ray propagation, `SimProp` and `CRPropa`.

Chapter 6 contains various methods for the study of cosmic ray anisotropies, including the effect of finite resolution in the sky, developed in this thesis. These methods are applied in Chapter 7, where the anisotropy signal obtained from three-dimensional simulations of the propagation of ultra-high-energy cosmic rays in the local Universe is discussed. These simulations are based on constrained and magnetized numerical replicas of the local cosmic web.

In Chapter 8, we study the propagation of cosmic rays in the environment of their sources and the corresponding production of astrophysical neutrinos. In particular, we consider the case of the environment produced by binary-neutron-star mergers.

The extragalactic development of electromagnetic cascades is studied in Chapter 9. We consider the cascades initiated by very-high-energy γ-rays from distant blazars, including the possible presence of plasma instabilities among the energy loss mechanisms. Finally, conclusions and future projects are discussed in Chapter 10.

2

Cosmic Rays

The history of cosmic ray physics began more than a century ago with the discovery of a mysterious ionizing radiation of unknown nature, capable of penetrating the Earth's atmosphere down to the ground. During all of these decades, cosmic ray research has developed together with many other fields, such as astronomy, astrophysics and particle physics. Moreover, cosmic rays are still nowadays the most energetic particles ever observed in the history of science. From the first balloon flights, to giant ground-based detectors, our knowledge of cosmic rays has increased enormously. But, there are still a number of questions to be answered, including perhaps the most intriguing: what are the sources capable of accelerating particles to such incredible energies.

In this chapter, a historical introduction to cosmic ray research is given in Sec 2.1. The interaction of high-energy cosmic rays with the constituents of our atmosphere is discussed in Sec. 2.2. Finally, a general overview of the energy spectrum and mass composition of cosmic rays is given in Sec. 2.3.

2.1 Early cosmic ray observations

The history of cosmic rays (CRs) began with one of the most fundamental instruments used in the development of the electromagnetic theory: the electroscope. The electroscope was the first mechanical instrument designed to measure the electric charge on a body, using the electrostatic force. In particular, the gold-leaf electroscope consists of a vertical metal rod with two parallel gold leaves hanging from the end, and a metal plate or disc at the top. A typical gold-leaf electroscope is shown in the left panel of Fig. 2.1. When an electrically charged object touches the metal plate, a charge accumulation is induced in the gold leafs which will spread apart due to Coulomb's electrostatic repulsion. However, despite the great success of the electromagnetic theory, the French physicist C. A. de Coulomb observed in the 18th century that a charged electroscope could discharge spontaneously. Unfortunately, it was not possible to attribute this phenomenon to contamination of the air inside the electroscope chamber due to defects in the insulation [29].

Another possible explanation for the spontaneous discharge of electroscopes came from the discovery of natural radioactivity (i.e. the spontaneous emission of particles from nuclei due to nuclear instability) in 1896 by A. H. Becquerel [30]. The emission of charged particles from

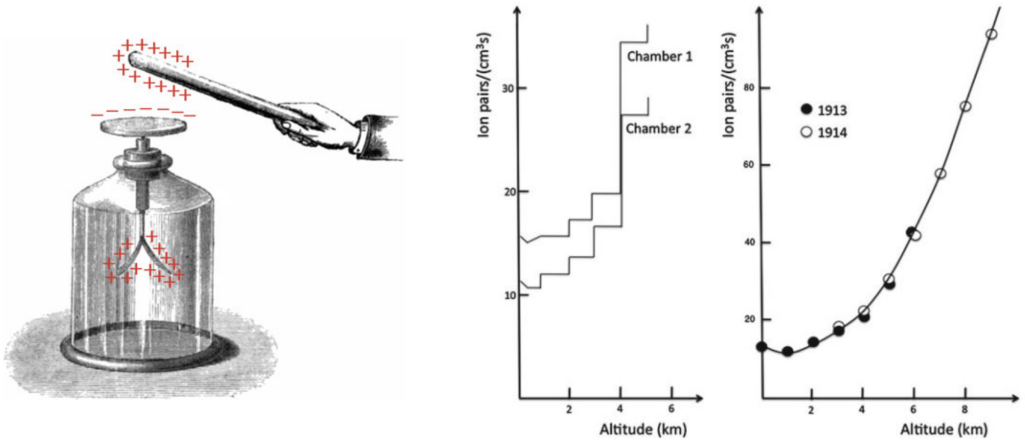

Figure 2.1: Left: illustration of a typical gold-leaf electroscope. The electrostatic repulsion of the two gold leaves can be seen when an electrically charged body is brought close to the metal disc at the top. Figure taken from [29, 38]. Right: measurements of the variation of the ionization rate by V. Hess and W. Kolhörster. Figure taken from [29].

the radioactive activity of unstable nuclei present in the environment would have induced the formation of ions in the air, causing the observed discharge. Further studies and improvements in the sensitivity and insulation of the electroscopes by H. Geitel, J. Elster [31, 32] and C. T. R. Wilson [33] led to the conclusion that this ionizing radiation came from outside the vessel of the electroscope. However, the origin of the radiation remained unclear, opening up the debate between terrestrial and extraterrestrial origins.

A number of pioneering experiments were carried out to determine the origin of this ionizing radiation. In 1909, T. Wulf measured the ionization rate at the top of the Eiffel Tower ($\sim 300\,\mathrm{m}$ height) to test its variation with height [34]. However, the measured decrease was too small to confirm the hypothesis of a terrestrial origin. In the same years, D. Pacini performed underwater measurements of the ionization rate in the Gulf of Genoa and in the Lake of Bracciano [35, 36], while A. Gockel performed balloon flights measurements over Switzerland ($\sim 4,500\,\mathrm{m}$ height) [37]. All the results obtained pointed to a possible atmospheric or extraterrestrial origin of the ionizing radiation.

The turning point in the search for the origin of the ionizing radiation came in 1912, thanks to the balloon experiments of V. F. Hess. Hess measured the ionization rate up to 5 km and showed the increase of the ionization rate up to more than the 100% compared to the ground [1]. These results were also confirmed in the following 2 years by W. Kolhörster with balloon flights up to 9 km [39, 40], where he showed that the increase of the ionization rate reached several times the value on the ground. Both Hess and Kolhörster measurements are shown in the right panel of Fig. 2.1. It was also Hess who carried out balloon measurements during a solar eclipse in 1912, without observing any decrease in the ionization rate, thus opening up the research for the source of the cosmic radiation. With several experimental confirmations of the extraterrestrial origin of this radiation, the new problem became the identification of its nature.

The first hypothesis about the nature of the ionizing radiation was proposed by R. Millikan and G. Cameron. Given the penetrating power of the radiation underwater [2], Millikan and

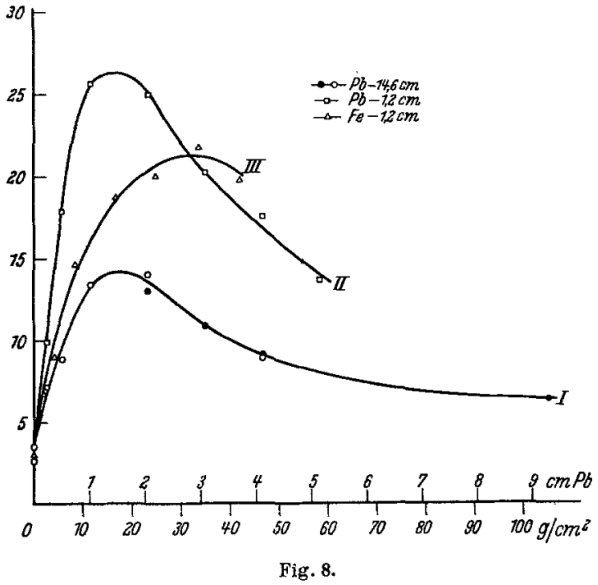

Figure 2.2: Rossi's transition curve: number of triple coincidence per hour as a function of the thickness of the shielding layer. Figure taken from [41].

Cameron concluded that it was made up of very energetic photons, more precisely γ-rays. It was Millikan and Cameron who first gave this radiation the name *cosmic rays*. However, in the same year J. Clay measured the variation of the ionization rate with the geomagnetic latitude [3], later confirmed also by W. Bothe and W. Kolhörster [4]. The interaction of the cosmic rays with the geomagnetic field proved that they did not consist of photons, but mostly of charged particles. Despite the erroneous origin of the name, the term cosmic rays is still used today.

In order to determine the dominant component of the cosmic rays, the Italian physicist B. Rossi had the idea of measuring the asymmetry in the cosmic ray flux from East and West due to the interaction with the geomagnetic field, to obtain the dominant charge [5]. Several observations by L. Alvarez, A. H. Compton, T. H. Johnson and Rossi [6–8] have shown that near the geomagnetic equator there are more cosmic rays coming from the West than from the East, nowadays called *East-West effect*. The interpretation of these results is that the cosmic rays are mostly positively charged particles, and thus probably protons.

In 1928, H. Geiger and W. Müller developed a new instrument for particles detection: the sealed Geiger-Müller tube. This device consists of a tube filled with gas and a charged metal wire. When a charged particle enters in the detector, the gas is ionized and the ions and electrons are collected by the metal wire. The electric signal collected is then amplified and read by an amperometer. The development of this instrument opened the door to the study of the secondary particles produced when cosmic rays interact with the molecules in the atmosphere. Based on the introduction of the coincidence technique with the Geiger-Müller detector by Bothe [42], Rossi noticed that even when his detectors were separated in a triangular configuration, they registered coincidence signals [43]. Subsequently, Rossi then introduced a shielding of up to 1 meter of lead over his detector array and found that the coincidence measurements increased [41]. Rossi concluded that this increase was the result of the interaction of primary particles with the

shielding material, producing secondary particles. He found out that the coincidence rate was first increasing with the thickness of the shielding layer, before falling down: this phenomenon is known as *Rossi's transition curve*, and it can be seen in Fig. 2.2.

The production of a shower of secondary particles from cosmic ray interactions was finally studied in detail by P. V. Auger in 1939. Auger and his collaborators measured showers with extensions up to 300 m, and they also estimated that the energy of the primary particle could be of the order of $O(10^{15})$ eV [44]. This value was many orders of magnitude above the energy scale of any known phenomena at the time. These enormous cascades of particles produced by the interaction of a primary cosmic ray with the atmosphere are called *extensive air showers (EASs)*.

The increase in the ionization rate measured by the Hess and Kolhörster balloon experiments was indeed consistent with an extraterrestrial origin of the cosmic radiation. However, it is important to note that due to the development of EASs in the atmosphere, these experiments did not measure the primary cosmic rays, but the secondary components of the EAS. In order to measure primary cosmic rays, it is necessary to reach the point at high altitude where the EAS begins to develop. This point is called the Regener-Pfotzer maximum [45], and it is located about 20 km above the sea level. In the 1940s, M. Schein showed with very high altitude balloon measurements that cosmic rays are mostly composed of primary protons with an energy of $10^9 - 10^{12}$ eV [46].

2.1.1 Cosmic rays and particle physics

The observation of very-high-energy cosmic rays has played a remarkable role in the development of particle physics. Before modern particle accelerators, cosmic rays were the only source of very-high-energy particles for studying the fundamental constituents of nature in detail.

The first antiparticle was discovered in 1932 when C. D. Anderson studied cosmic rays passing through a cloud chamber in a magnetic field. Anderson observed the track of a particle that behaved as an electron, but with opposite electric charge: the *positron* [47]. A few years later, in 1937, Anderson and S. Neddermeyer observed a new particle with a mass ~ 200 times that of the electron, and with both positive and negative charges: this was the first observation of the *muon* [48]. Until the 1950s, the discovery of many other particles with cosmic rays placed important milestones in the history of particle physics: among them the *pion* in 1947 by C. Lattes, G. Occhialini, and C. Powell [49], the *kaon* in 1947 by G. Rochester and C. Butler [50] and the *lambda baryon* in 1950 by V. Hopper and S. Biswas [51].

Although cosmic rays played a very important role in the understanding of particle physics, in the 1950s research began to focus more on man-made accelerators.

2.1.2 The high-energy cosmic ray observatories

The post-World War II period marked the beginning of the history of high-energy cosmic ray observatories, with attention moving over the years to higher and higher energies. An important technological advance for the study of high-energy cosmic rays was the replacement of Geiger-Müller counters by scintillation counters and water-Cherenkov detectors[1], coupled with photomultiplier tubes (PMTs) [53].

[1]The operation of water-Cherenkov detectors is based on the Cherenkov effect, observed by P. A. Cherenkov in 1937 [52], who observed flashes of blue light in a medium when high-energy electrons passed through it. These

The first ground array experiment was the Agassiz station of Harvard University, which operated from 1954 to 1957 [54]. The Agassiz station consisted of an array of 11 scintillator stations on a triangular grid covering 0.17 km^2. The largest energy detected by the Agassiz station was a primary cosmic ray with an energy of $\sim 5 \cdot 10^{18}$ eV [55]. After the Agassiz operation, the first large-scale experiment to detect cosmic ray was planned by J. Linsley and L. Scarsi in New Mexico, USA: the Volcano Ranch experiment. The area covered by Volcano Ranch was of about 8 km^2, and it operated from 1959 to 1978. It was Volcano Ranch that measured the first cosmic ray with an energy above 10^{20} eV [56, 57].

Other notable experiments operating in the same period are the Sydney University Giant Air shower Recorder (SUGAR) [58], in Australia, with a total area of 70 km^2, and the Haverah Park experiment [59], in the UK, with a total area of 34 km^2. In particular, the Haverah Park experiment used water Cherenkov detectors to measure EASs.

The first purely optical cosmic ray experiment was the Fly's Eye experiment [60], which operated from 1981 to 1993, and was subsequently updated to the High Resolution Fly's Eye (HiRes) which operated from 1997 to 2006. Fly's Eye was a fluorescence detector, able to measure the fluorescence light produced when secondary particles produced in EASs propagate in the atmosphere. It was the Fly's Eye experiment that detected the cosmic ray with the highest energy ever of $\sim 3.2 \cdot 10^{20}$ eV [61], the so-called *Fly's Eye event*. It is also important to mention the Akeno Giant Air Shower Array (AGASA) in Japan, with an extension of 100 km^2, operating between 1990 and 2004.

Modern observations are driven by the two largest cosmic ray observatories ever built: the Pierre Auger Observatory in Argentina [10] and the Telescope Array (TA) in the USA [11]. The Telescope Array is a hybrid observatory consisting of a Surface Detector (SD) array and Fluorescence Detector (FD) stations and has been operational since 2008. The SD array consists of 507 scintillation stations over an area of $\sim 700\,\mathrm{km}^2$. The FD consists of three fluorescence detector stations. The structure of the TA allows the observatory to measure the energy spectrum, mass composition and arrival directions of cosmic rays. The Telescope Array is being extended to the TAx4 experiment [62, 63]: the TAx4 extension together with the original SD stations will cover an area of $\simeq 3000\,\mathrm{km}^2$. Another important extension of TA is the Telescope Array Low-energy Extension (TALE) [64–66], which will allow the observation of EASs initiated by cosmic rays with energies down to $\sim 3 \cdot 10^{16}$ eV. The status, data acquisition and results of the Pierre Auger Observatory are described in detail in the next chapter.

2.2 Extensive air showers

Since the first observations by Rossi and Auger, it has been clear that the passage of cosmic rays through the atmosphere produces a cascade of secondary particles. These extensive air showers are produced when the cosmic ray energy is above 100 TeV [2], and their main constituents are hadrons, muons, neutrinos, electrons, positrons and photons. It is common to divide the

electrons excite the molecules in the medium, which emit photons when they return to their ground state. Since the speed of light in a medium is $v = c/n$, where c is the speed of light in vacuum, and n is the refraction index of the medium, it can happen that the particles in the medium travel at a speed v_p higher than the speed of light in the medium. The result is the emission of coherent radiation at an angle α with respect to the particle direction. The emission angle is given by $\cos\alpha = 1/\beta n$ where $\beta = v_p/c$.

[2] In this thesis the following units are often used: 1 MeV = 10^6 eV, 1 GeV = 10^9 eV, 1 TeV = 10^{12} eV, 1 PeV = 10^{15} eV, 1 EeV = 10^{18} eV and 1 ZeV = 10^{21} eV.

components of an EAS into *hadronic component*, *muonic component* (including muon neutrinos) and *electromagnetic component* (consisting of electrons, positrons and photons). A schematic representation of an EAS is shown in Fig 2.3: it can be seen that hadronic interactions are the first step in the production of the other components.

The hadronic component is dominant only during the initial development of the EAS. The main contributors to the hadronic component are protons p, neutrons n, charged pions $\pi^{\pm}$ and kaons $K^{\pm}$. The muon component of the EAS is produced by the decay of charged pions and kaons, through the following reactions:

$$\pi^+ \to \mu^+ + \nu_\mu \quad , \quad \pi^- \to \mu^- + \bar{\nu}_\mu \tag{2.1}$$

$$K^+ \to \mu^+ + \nu_\mu \quad , \quad K^- \to \mu^- + \bar{\nu}_\mu \tag{2.2}$$

$$K^+ \to \pi^0 + \mu^+ + \nu_\mu \quad , \quad K^- \to \pi^0 + \mu^- + \bar{\nu}_\mu \,. \tag{2.3}$$

Muons are characterized by a small interaction cross section, and they can penetrate the atmosphere down to the ground. The electromagnetic component of the EAS is mostly produced by the decay of neutral pions,

$$\pi^0 \to \gamma + \gamma \,. \tag{2.4}$$

The muon component can also contribute to the electromagnetic component via decay as

$$\mu^+ \to e^+ + \nu_e + \bar{\nu}_\mu \quad \text{and} \quad \mu^- \to e^- + \bar{\nu}_e + \nu_\mu \,. \tag{2.5}$$

However this is only possible for low-energy muons, due to the relativistic time dilatation of the muon lifetime. It should be remembered that the evolution of an EAS is the result of subsequent stochastic processes. Therefore, the profile of different showers is generally different, even if the first interaction is characterized by the same initial conditions.

The first hadronic interaction, which initiates the shower, occurs when the high-energy cosmic ray enters in the atmosphere at a typical altitude of 15 to 35 km [68] and interacts with one of the nuclei present in the air (usually nitrogen, oxygen or argon). The evolution of the EAS in the atmosphere is usually studied in terms of the *vertical atmospheric depth* X_v, defined as

$$X_v = \int_h^\infty \rho_{\text{air}}(h')\, dh' \,, \tag{2.6}$$

where h is the height above the sea level and ρ_{air} is the density profile of the air. X_v is usually measured in $\mathrm{g\,cm^{-2}}$. The reason why X_v is a good variable to study the evolution of particle cascades in the atmosphere is that the interaction lengths depend more on the density of the air rather than on the height. In the case where the primary cosmic ray enters in the atmosphere with an inclination angle θ, the *slant depth* is given by the approximation

$$X = X_v \cos\theta \,. \tag{2.7}$$

The point entry into the atmosphere is given by $X_0 = 0\,\mathrm{g\,cm^{-2}}$, while the point of the first interaction is given by X_1. The depth at which the shower reaches the maximum number of particles N_{max} is known as X_{max} and is commonly referred to as *shower depth*. Given the stochastic nature of the development of an EAS, the shower depth is used as a mass indicator for the primary cosmic ray. In particular, the mean value $\langle X_{\text{max}} \rangle$ and the fluctuation $\sigma(X_{\text{max}})$ are considered. The ground point of the shower is given by the detection point and it is called *column*

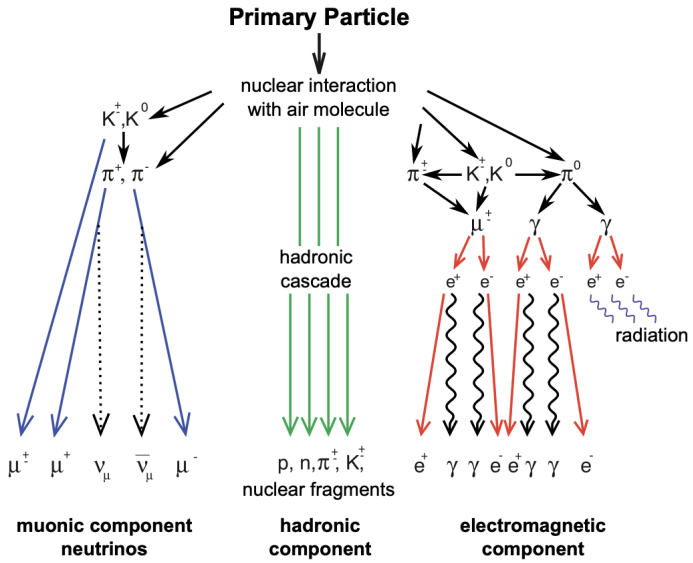

Figure 2.3: Schematic representation of an extensive air shower and its various components. Figure taken from [67].

density X_{ground}. In the case of vertical showers, for the Pierre Auger Observatory, located at 1,400 m above the sea level, this corresponds to $880\,\text{g}\,\text{cm}^{-2}$ [10], or for an observatory at the sea level to $1,030\,\text{g}\,\text{cm}^{-2}$[69].

As discussed in Sec. 2.1.1, CR physics is closely related to particle physics. This can be visualized by considering the typical center of mass energy of the first interaction in an EAS. The average atomic mass number of the air in the atmosphere is about 14, and we can assume that the nuclei in the atmosphere are basically at rest with respect to the incoming cosmic ray. Therefore, the center of mass energy $\sqrt{s}$ is given by

$$\sqrt{s} \simeq \sqrt{2 m_{\text{air}} E_{\text{CR}}} = 200 \left(\frac{m_{\text{air}}}{14 m_p}\right)^{1/2} \left(\frac{E_{\text{CR}}}{1\,\text{EeV}}\right)^{1/2} \text{TeV}\,. \tag{2.8}$$

A CR with an energy above 1 EeV is called an ultra-high-energy cosmic ray (UHECR)[3]. Thus, for a UHECR, the center of mass energy of the interaction with an air nucleon is $\sqrt{s} \simeq 50\,\text{TeV}$, which is already above the typical collision energies in accelerators.

2.2.1 Electromagnetic showers: the Heitler model

Electromagnetic showers are initiated by electrons, positrons or photons, and their development is described in terms of the Heitler model [71, 72]. Electromagnetic showers consists of two main processes: *Bremsstrahlung* (i.e. the emission of a photon from electrons and positrons) and *pair*

[3]If a UHECR has an energy above 100 EeV, the name extremely-high-energy cosmic ray (EHECR) is sometimes used.

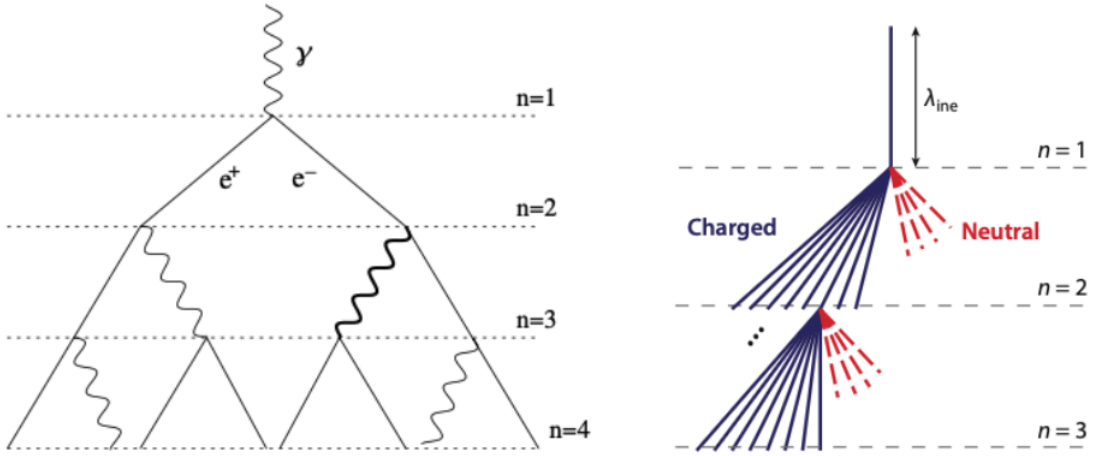

Figure 2.4: Left: schematic representation of the development of an electromagnetic shower. Figure adapted from [70]. Right: schematic representation of the development of a hadronic shower. Figure adapted from [68].

production (i.e. the production of an electron-positron pair from a photon), i.e.

$$\text{Bremsstrahlung:} \quad e^{\pm} + (A\,, Z) \to e^{\pm} + (A\,, Z) + \gamma \tag{2.9}$$

$$\text{Pair production:} \quad \gamma + (A\,, Z) \to e^{+} + e^{-} + (A\,, Z)\,. \tag{2.10}$$

In Eq. (2.9) the target nucleus is denoted by $(A\,, Z)$. The development of the electromagnetic shower can be divided into n stages in which either a photon produces an electron-positron pair, or an electron (positron) emits a photon via Bremsstrahlung. A sketch of the process is shown in the left panel of Fig. 2.4. Therefore, at a given stage n, the shower is composed of $N = 2^n$ particles.

In the Heitler model, each step occurs after the splitting mean free path (in depth) $\lambda = X_e \cdot \ln 2$, where X_e is the Bremsstrahlung depth and is equal to $X_e = 37\,\mathrm{g\,cm^{-2}}$. In general, the electron-positron pair production depth is $X_\gamma = 7/9 \cdot X_e$ and it is approximated by X_e in the simplified model. Assuming that in each interaction the energy of the initial particle is shared equally by the two particles produced, it can be seen that the an electromagnetic shower is approximated by a continuous splitting process every X_e of the energy of the initial particle [68]. Thus, after n step, the initial energy E_0 is split into N particles with energy E_0/N.

The shower stops developing when the electron and positron ionization losses become dominant over the Bremsstrahlung losses: this happens at the critical energy $E_c \simeq 86\,\mathrm{MeV}$, corresponding to the multiplication stage n_c. At this point, the shower has reached the maximum number of particles given by

$$N_{\max} = \frac{E_0}{E_c}\,, \tag{2.11}$$

at the depth

$$X_{\max} = X(N_{\max}) = \lambda \cdot n_c = X_e \ln\left(\frac{E_0}{E_c}\right)\,. \tag{2.12}$$

It is also possible to write Eq. (2.12) in physical position: the position of the maximum of the shower is then $x_{\max} = (\lambda/\ln 2) \cdot \ln(E_0/E_c)$. We obtain that the maximum number of particles in the shower is $\propto E_0$, while the position of the maximum is $\propto \ln E_0$.

2.2.2 Hadronic showers: the Heitler-Matthews model

The description of electromagnetic showers in Sec. 2.2.1 can be extended to include the hadronic component. This extension is now known as the Heitler-Matthews model [70]. As shown in the right panel of Fig. 2.4, each stage of a hadronic shower is characterized by the production of charged and neutral pions (we will restrict our attention to only pions among the produced mesons). Consider a shower initialized by a proton with energy E_0. In the Heitler-Matthews model, the multiplicity of charged particles produced $n_{\rm ch}$ is considered to be constant in hadron interactions (in particular for pp, $p\bar{p}$ and $\pi-$nucleon interactions). Since charged and neutral pions form an isospin triplet of the strong interaction[4], charged pions are produced with a branching ratio of $\sim 2/3$, while neutral pions are produced with a branching ratio of $\sim 1/3$. This means that in each interaction the number of charged pions produced is $n_{\rm ch}$ and the number of neutral pions is $(1/2) \cdot n_{\rm ch}$. Neutral pions will then decay into photons[5], initializing the electromagnetic showers described in the previous section.

As for the electromagnetic showers, after n stages the energy transferred in the hadronic and electromagnetic parts of the shower is

$$E_{\rm had} = \left(\frac{2}{3}\right)^n E_0 \,, \tag{2.13}$$

$$E_{\rm EM} = \left[1 - \left(\frac{2}{3}\right)^n\right] E_0 \,. \tag{2.14}$$

For $n = 6$, the $\sim 90\%$ of the shower energy is converted into the electromagnetic component. Charged pions continue to propagate and interact until their energy falls below the critical value $E_c^\pi \simeq 20\,\text{GeV}$, at which point they decay [68, 70]. The total number of charged pions produced after n stages is $N_{\pi^\pm} = n_{\rm ch}^n$ with an energy per charged pion of

$$E_\pi = \frac{E_0}{\left(\frac{3}{2} n_{\rm ch}\right)^n} \,. \tag{2.15}$$

We can also obtain the number of muons, since the charged pions decay when their energy falls below E_c^π, i.e. at the critical $n_c = \ln(E_0/E_c^\pi)/\ln[(3/2)n_{\rm ch}]$. Then

$$N_\mu = N_{\pi^\pm} = n_{\rm ch}^{n_c} = \left(\frac{E_0}{E_c^\pi}\right)^\beta \,, \tag{2.16}$$

where the factor β is given by

$$\beta = \frac{\ln(n_{\rm ch})}{\ln\left(\frac{3}{2} n_{\rm ch}\right)} \,. \tag{2.17}$$

[4] The pion isospin states are $|\pi^+\rangle = |u\bar{d}\rangle$, $|\pi^-\rangle = |d\bar{u}\rangle$ and $|\pi^0\rangle = (1/\sqrt{2})(|u\bar{u}\rangle - |d\bar{d}\rangle)$ [73].
[5] The lifetime of π^0 is $8.5 \cdot 10^{-17}$ s, while charged pions live $2.5 \cdot 10^6$ s.

Numerically Eq. (2.17) has values $\beta = 0.8 - 0.95$ [68, 70, 74].

Most of the energy of the hadronic shower is converted into the electromagnetic component. Therefore, we can use the results of Sec. 2.2.1 to estimate the $X_{\max}$ of the proton showers. Considering only the development of the first electromagnetic sub-shower (since this step contains most of the electromagnetic energy) given in Eq. (2.12), the shower depth in the proton scenario is

$$X^{p}_{\max} \simeq \lambda_{\rm had} + X \left(\frac{E_0}{3\, n_{\rm ch} E_c} \right) = \lambda_{\rm had} + X_e \ln \left(\frac{E_0}{3\, n_{\rm ch} E_c} \right) , \tag{2.18}$$

where $\lambda_{\rm had} \simeq 60\,{\rm g\,cm^{-2}}$ is the depth of the first hadronic interaction, and we have assumed that the energy of the neutral pion is split equally into two photons. Since we have neglected all the other electromagnetic subshowers, Eq. (2.18) is an underestimate of the real shower depth.

The treatment of hadronic interactions considered in this section is only a simplification of the air shower development. In general, both the depth of the first hadronic interaction $\lambda_{\rm had}$ and the multiplicity of charged particles produced $n_{\rm ch}$ depend on the particle energy. In Sec. 2.2.4 we briefly describe the quantities reconstructed with Monte Carlo simulations of EASs.

2.2.3 Superposition model

The development of EASs where the primary cosmic ray is not a proton can be understood by considering the fact that the binding energy of the nucleons within a nucleus is negligible with respect to the typical cosmic ray energies. It is then possible to consider the *superposition model*, where a primary nucleus with energy E_0 and atomic mass number A can be seen as a superposition of A independent nucleons with energy E_0/A [68, 74]. The shower depth is then given by

$$X^{A}_{\max} \simeq \lambda_{\rm had} + X_e \ln \left(\frac{E_0}{3A\, n_{\rm ch} E_c} \right) = \lambda_{\rm had} + X_p \ln(A) \,, \tag{2.19}$$

where $X_p = X_e \ln(E_0/3n_{\rm ch}E_c)$. Therefore, the shower of nuclei with $A > 1$ is characterized by a smaller maximum depth than that of a proton. For the number of muons we have that

$$N^{A}_{\mu} = A \cdot N_{\mu}(E_0/A) = A^{1-\beta} N_{\mu}(E_0) \,, \tag{2.20}$$

where $N_\mu(E_0)$ is given by Eq. (2.16).

The result in Eq. (2.19) can be interpreted as the effect of the *larger cross section* of a nucleus with respect to protons. It is also interesting to note that the fluctuation of different showers (i.e. $\sigma(X_{\max})$) with the same A is expected to be suppressed in the case of nuclei, since the shower of a heavy nucleus is interpreted as the average result of many proton-like showers.

2.2.4 EAS simulations

Given the complexity of the EAS development, numerical frameworks are often required for detailed studies of particle showers. Two examples of such numerical frameworks are `Corsika` [75] and `Conex` [76]. `Corsika` is a three-dimensional Monte Carlo code, while `Conex` is a one-dimensional solver of the cascade equations. The main component of all these numerical codes is the reproduction of the hadronic interactions between cosmic rays and atmospheric components. However, the parametrization of the hadronic interactions is generally extrapolated from collider measurements at lower energies. Different parameterizations then correspond to different

Hadronic Interaction Models (HIMs): the most widely used models based on measurements at the Large Hadron Collider (LHC) are EPOS-LHC [77], QGSJetII-04 [78] and Sibyll2.3 [79, 80].

The longitudinal profile of an EAS is described by the amount of energy deposited per slant depth in the atmosphere as a function of X. Alternatively, the number of particles present in the shower can also be considered. Both these quantities increase during the development of the cascade, and their reach their maximum value at $X_{\max}$. For $X > X_{\max}$ they start to decrease again. These quantities can be modelled with the *Gaisser-Hillas function* [81]. For both the number of particles $N(X)$ and the energy deposit dE/dX, the parameterization is

$$N(X) = N_{\max} \left(\frac{X - X_1}{X_{\max} - X_1} \right)^{(X_{\max} - X_1)/\lambda} \exp\left(\frac{X_{\max} - X_1}{\lambda} \right) , \tag{2.21}$$

and

$$\frac{dE}{dX} = \left(\frac{dE}{dX} \right)_{\max} \left(\frac{X - X_1}{X_{\max} - X_1} \right)^{(X_{\max} - X_1)/\lambda} \exp\left(\frac{X_{\max} - X_1}{\lambda} \right) , \tag{2.22}$$

where X_1 and λ are shape parameters, and $N_{\max}$ and $(dE/dX)_{\max}$ are the number of particles and the energy deposit at $X_{\max}$, respectively. The integral of Eq. (2.22) gives the calorimetric energy of the shower.

We have already discussed that due to the stochastic nature of hadronic interactions, the maximum depth $X_{\max}$ is described by a certain probability distribution. A commonly used parameterization of the $X_{\max}$ distribution function is given by the *generalized Gumbel distribution* [82]. For a given initial energy E and mass number A, the corresponding Gumbel function is

$$\mathcal{G}(X_{\max}|E, A) = \frac{\lambda^\lambda}{\sigma\Gamma(\lambda)} \exp\left[-\lambda \frac{X_{\max} - \mu}{\sigma} - \lambda \exp\left(-\frac{X_{\max} - \mu}{\sigma} \right) \right] , \tag{2.23}$$

where $\Gamma(x)$ is the Euler Gamma function and the values of λ, μ and σ depend on E and A and on the HIM (see [82] for the parameterization details). Some examples of the $X_{\max}$ distribution and the λ, μ and σ energy and mass dependence are shown in Fig. 2.5, top and bottom panels, respectively. Alternative parameterizations of the $X_{\max}$ distribution can also be found in [83].

The development of the EAS is also characterized by a lateral spreading around the main shower axis (mainly of the electromagnetic component). The particle density per unit area is parameterized by the Nishimura-Kamata-Greisen function [84, 85] as a function of the depth X and the distance r from the shower axis

$$n(X, r) = n_0(X, s) \left(\frac{r}{r_M} \right)^{s-2} \left(1 + \frac{r}{r_M} \right)^{s-4.5} , \tag{2.24}$$

where r_M is the Molière radius (the radius that of the area around the shower axis that contains the 90% of the shower), s is the shower age parameter defined as

$$s = \frac{3X}{X + 2X_{\max}} . \tag{2.25}$$

It can be seen that the shower age parameter is $0 \leq s \leq 3$, and $s = 1$ for $X = X_{\max}$. The normalization factor $n_0(X, s)$ is given by

$$n_0(X, s) = \frac{N_e(X)}{2\pi r_M^2} \frac{\Gamma(4.5 - s)}{\Gamma(s)\Gamma(4.5 - 2s)} , \tag{2.26}$$

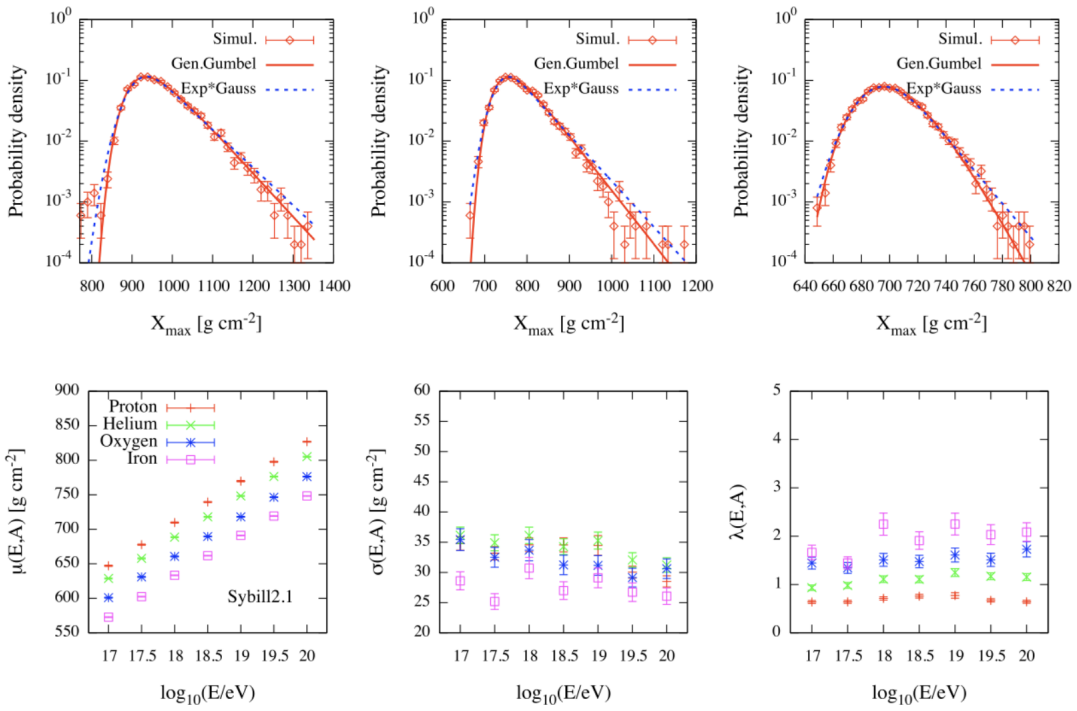

Figure 2.5: Top: $X_{\max}$ distributions from simulations with `Conex` (red circles) for photons (left), protons (middle) and iron nuclei (right) at 10 EeV with QGSJetII. The best fit obtained with the Gumbel function (red line) and with the convolution of an exponential and a Gaussian distribution (blue dashed line) are also shown. Bottom: energy dependence of the three parameters μ, σ and λ for different nuclei for the Sibyll HIM. Figure adapted from [82].

where $N_e(X)$ is the electron number at depth X and $\Gamma(x)$ is the Euler Gamma function (see also [86, 87]).

It is interesting to note that the overall profile of EASs can be described to a first approximation with only three parameters: E_0, $X_{\max}$ and N_μ (where N_μ is not necessary for pure electromagnetic showers). This general description of EAS is often referred to as *shower universality* [86].

2.3 Cosmic ray energy spectrum

The most natural quantity to study the cosmic ray flux measured at Earth is the number of particles observed at a given energy. However, the CR observatories must also take into account the *exposure* of the experiment. The exposure is defined as the time integral of the aperture of the experiment, i.e. the spatial area covered times the observed solid angle. Thus the exposure of an observatory is a quantity usually measured in $\mathrm{km}^2\,\mathrm{sr}\,\mathrm{yr}$. In this context, the differential cosmic ray energy spectrum $J(E)$ is defined as

$$J(E) = \frac{d^4N}{dE\,dA\,dt\,d\Omega}(E)\,, \tag{2.27}$$

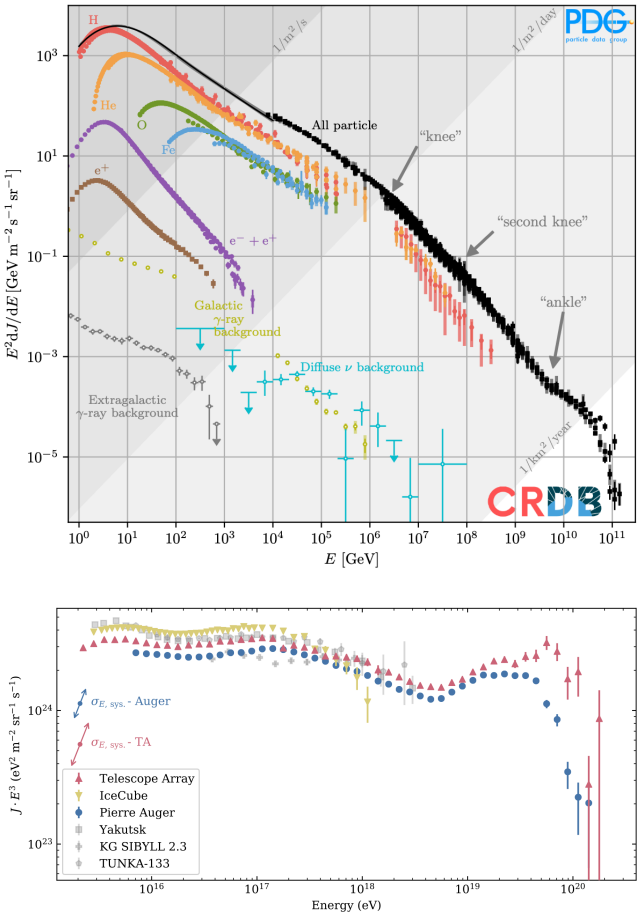

Figure 2.6: Top: cosmic ray energy spectrum together with electrons, positrons, photons and neutrinos. The energy spectrum is multiplied by the square of the kinetic energy. Figure taken from [9]. Bottom: cosmic ray energy spectrum at the highest energies. The all particle flux from TA [88], IceCube [89], Pierre Auger [90], Yakutsk [91], KASCADE-Grande [92] and TUNKA [93]. The systematics of TA and Pierre Auger are indicated by the corresponding arrows. Figure taken from [94].

where dN is the number of particles observed per unit of energy dE, unit of area dA, unit of time dt and unit of solid angle $d\Omega$. The energy spectrum in Eq. (2.27) is then often measured in $\mathrm{eV}^{-1}\,\mathrm{m}^{-2}\,\mathrm{s}^{-1}\,\mathrm{sr}^{-1}$.

The all particle cosmic ray energy spectrum[6] from GeV to ZeV energies is shown in the top panel of Fig. 2.6. The energy spectrum is multiplied by the energy E^3 in order to better visualize possible changes in the spectral features. Particles with energies below $\sim 1\,\mathrm{GeV}$ are subject to solar modulation by the solar wind: high solar activity corresponds to a decrease in the low-energy CR flux [95]. It is immediately apparent that CRs are a non-thermal population of particles with an energy spectrum well described by a power-law of the form $J(E) \sim E^{-\alpha}$, where α is the spectral index. A cutoff can be observed in the last part of the spectrum (above $100\,\mathrm{EeV}$). The cosmic ray flux varies by several orders of magnitude with energy: from more

[6] More information on the Particle Data Group (PDG) can also be found at https://pdg.lbl.gov.

than 1 particle per m^2 s at $\sim 10^3$ GeV to less than 1 particle per km^2 yr at $\sim 10^{10}$ GeV.

Given the impressive large extension of the cosmic ray spectrum, different measurement techniques are required for different energy ranges. In particular, the extremely low flux at the higher energies requires the construction of large ground-based experiments. For energies above 1 PeV, balloon or satellite cosmic ray experiments are no longer feasible. Unfortunately, this means that at the highest energies only indirect cosmic ray measurements can be made with EASs.

At a closer look, the cosmic ray energy spectrum shows several changes in the spectral shape. At $E \simeq 3$ PeV the spectral index changes from $\alpha \simeq 2.7$ to $\alpha \simeq 3.1$ [9]: this feature is called *first knee*. The first knee is followed by another change to $\alpha \simeq 3.3$ at $E \simeq 100$ PeV. Since the first observation in 1958 [96], the knee feature has been extremely important for the interpretation of the CR spectrum. As CRs are mostly electrically charged particles, their production and propagation is affected by the presence of magnetic fields. Protons at the knee energy are characterized by a Larmor radius[7] of $r_L \simeq 1$ pc[8] for the typical galactic magnetic field value ($B \sim 1\,\mu$G) [97]. It is therefore possible the PeV energy scale marks the point at which proton confinement within the galaxy is no longer efficient, since r_L would become larger than the thickness of the Galactic disk. This would lead to the steepening of the CR spectrum above the knee [98, 99].

Another possible explanation is that the knee is associated with the maximum acceleration energy in galactic supernova remnants (SNR). However, both these possible explanations suggest that if the a knee feature occurs at proton energy E_p, then the same feature is expected for a nucleus with charge number Z at the energy $E_Z = Z \cdot E_p$. This phenomenon is called *Peters cycles* [100]. The all particle spectrum will then show a smooth hardening of the spectrum for energies above the proton knee, as a result of the sum of all the mass components.

The bottom panel of Fig. 2.6 shows the cosmic ray spectrum at the highest energies. It can be seen that at $\simeq 5$ EeV there is another change in the spectral slope. This hardening of the spectrum to $\alpha \simeq 2.8$ is called the *ankle* feature and was first observed in 1963 [101]. The first interpretation of the *ankle* feature is the transition from galactic to extragalactic CRs. In this case, the suppression of the galactic component could be related to the two effects discussed above: the galactic magnetic field is no longer able to confine high-energy CRs, or galactic sources are limited in the maximum acceleration energy. Another possible explanation for this feature was given in [102, 103] in the *dip model*. In this model, the transition from galactic to extragalactic cosmic rays occurs at lower energy, and the hardening of the spectrum is the result of the electron-positron pair production of extragalactic protons with cosmic photon fields. Disintegration of CR nuclei within their source environment could also potentially explain the ankle feature [104].

At the highest energies, a suppression of the CR flux was first observed by the HiRes experiment [106] and then confirmed by the Pierre Auger Observatory [107] and the Telescope Array experiment [108] at ~ 50 EeV. Interestingly, the AGASA experiment claimed not to have observed this suppression [109]. However, given the observation of the suppression in experiments with much larger exposures, the AGASA results were probably affected by systematic errors in

[7] The Larmor radius of a charged particle with energy E and charge number Z in a magnetic field of root-mean-square strength B is given by $r_L \simeq 1.1 \left(\frac{E/Z}{1\,\text{PeV}}\right)\left(\frac{B}{1\,\mu\text{G}}\right)^{-1}$ pc. See also Sec. 4.5.

[8] In this thesis we will often use the *parsec* (pc) unit of distance. It corresponds to $1\,\text{pc} \simeq 3.26\,\text{ly} \simeq 3.09 \cdot 10^{16}$ m.

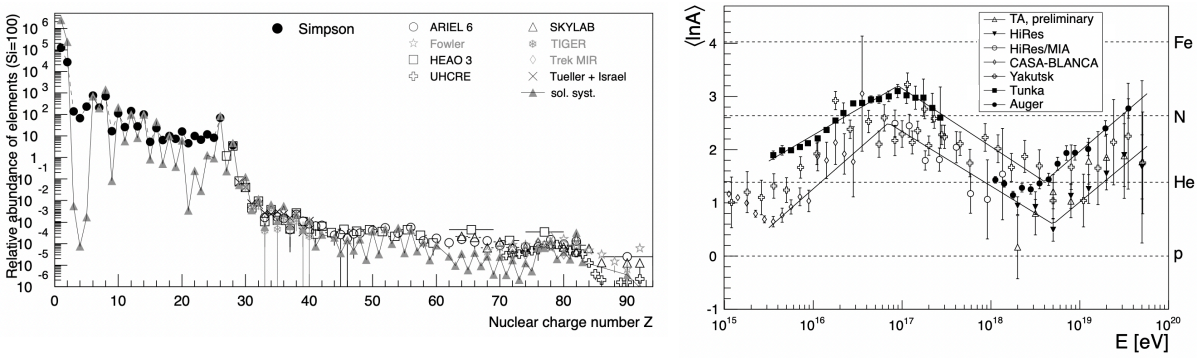

Figure 2.7: Left: cosmic ray abundances as function of their charge number Z at $\simeq 1\,\mathrm{GeV}$ per nucleon normalized to Si. The abundances of the elements in the solar system are also shown. Figure taken from [98]. Right: cosmic ray average logarithmic mass as function of their energy from $X_{\max}$ measurements. The HIM used for the reconstruction is EPOSv1.99 [105]. Figure adapted from [74].

the energy measurements. A common interpretation of this suppression in the energy spectrum is the production of pions in the interaction of UHECRs with the photons of the Cosmic Microwave Background (CMB). This effect is often referred to as the Greisen-Zatsepin-Kuz'min (GZK) cutoff [14, 15]; it is discussed in more detail in Chapter 4. The pion production energy threshold for protons interacting with CMB photons is $\simeq 34\,\mathrm{EeV}$, with a fractional of energy loss of ~ 0.2 per interaction [87]. This means that the flux of high-energy protons is affected by the presence of a horizon (the GZK horizon) of about 20 Mpc [87] beyond which CR sources can no longer contribute to the observed spectrum. However, another possible interpretation of the observed suppression could be the maximum acceleration energy of extragalactic sources, or even an interplay between these two hypotheses.

The interpretation of the CR energy spectrum is closely related to measurements of the evolution of the CR mass composition with energy. For energies below 1 PeV direct measurements of the cosmic ray mass are still possible, while above 1 PeV indirect measurements have to be made with EASs. As discussed in Sec. 2.2, the understanding of the CR composition at the highest energies is also affected by uncertainties in the HIMs. In the left panel of Fig. 2.7, the CR abundances are shown together with the solar system abundances [98]. We can see that the CR abundances follow the solar system abundances, and both show the *odd-even effect*: nuclei with even charge number Z are more tightly bound, and then more abundant. It can also be seen that the element groups $3 \leq Z \leq 5$ (Li, Be and B) and $21 \leq Z \leq 25$ (Sc, Ti, V, Cr and Mn) are more abundant in the CRs than in the solar system. This phenomenon is due to the fact that these elements are almost absent in the stellar nucleosynthesis cycle, but they are produced by heavier nuclei (such as C, N, O and Fe) as the product of the collisions with the interstellar medium (ISM): this process is called *spallation* [98].

The average logarithmic CR mass above 1 PeV as a function of the energy is shown in the right panel of Fig. 2.7. Between the first and second knee, the CR composition changes from protons to heavy nuclei. This result is consistent with the Peters cycle argument discussed for the energy spectrum. Towards the ankle region, where the transition between galactic and extragalactic CRs is thought to take place, the composition becomes lighter. The light component in this energy range should be of extragalactic origin, in order to avoid the correlation between the CR arrival direction and the Galactic plane [97]. In the end, the suppression region (above 10 EeV),

an increasingly heavy composition is visible. This transition could again be explained with a Peters cycle argument in the extragalactic sources. However, above 40 EeV the observed number of events is still too low to draw strong conclusions about the CR composition at the highest energies [94].

3

The Pierre Auger Observatory

As discussed in Chapter 2, observing of the highest energies of cosmic rays requires the construction of giant EAS detector arrays. The Pierre Auger Observatory[1] is the largest observatory of UHECRs in the world. The Pierre Auger Observatory is located in Argentina, near the city of Malargüe (Mendoza)[2], at 1400 m above the sea level [10, 110]. This region was chosen for its very low light pollution, low rainfall and large area to favor the detection of UHECRs. It was first proposed by J. Cronin and A. Watson in 1992, the construction began in 2000 and was completed in 2008, but the detection of EASs began in 2004. It is a hybrid observatory, combining different detection techniques. The observatory has exceeded a total exposure of $100,000\,\mathrm{km^2\,sr\,yr}$ [17] and it is undergoing an important upgrade phase called *Auger Prime* [111].

In Sec. 3.1 the main components of the Pierre Auger Observatory are presented, together with extensions and upgrades. In Sec. 3.2 the scientific results of the Pierre Auger Observatory are discussed.

3.1 Hybrid detection

The operation of the Pierre Auger Observatory is based on a hybrid detection technique, composed of different types of detectors. The surface array consists of 1,660 detector stations distributed on a hexagonal grid-covering an area of $3,000\,\mathrm{km^2}$ with a duty cycle of around 100%. The fluorescence detector of the observatory consists of five stations with a total of 27 fluorescence telescopes. The FD can measure the light deposited of EAS in the atmosphere only during moonless nights, which corresponds to a duty cycle of $\sim$ 15%. The amount of light is then proportional to the EAS energy deposited in the atmosphere. A schematic representation of the Pierre Auger Observatory is shown in the right panel of Fig. 3.1. In the following sections, both the SD and FD components of the Pierre Auger Observatory are described in detail.

The right panel of Fig. 3.1 also shows the two laser facilities for the atmospheric monitoring: the Central Laser Facility (CLF), the eXtreme Laser Facility (XLF) and the Balloon Launching Station (BLS). The Auger Engineering Radio Antenna (AERA) array is also visible.

[1] More information on the Pierre Auger Observatory can also be found at https://auger.org.

[2] Given the extension, the observatory lies between the latitudes 35.0° and 35.3° S, and between the longitudes 69.0° and 69.4° W.

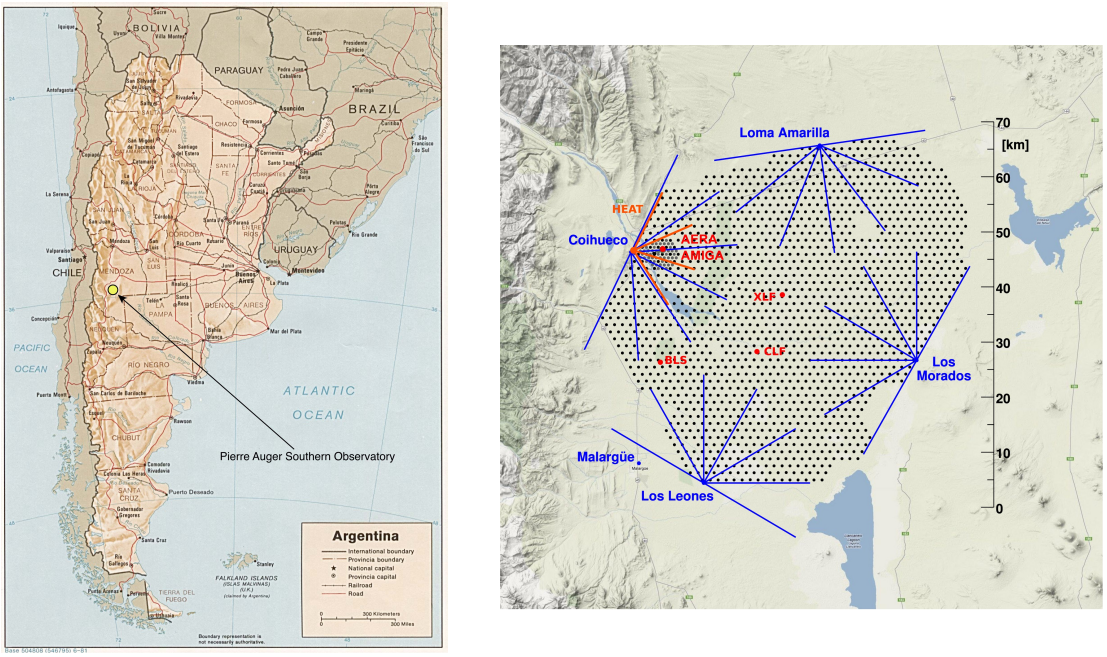

Figure 3.1: Left: map of part of South America showing the location of the Pierre Auger Observatory. Right: map of the Pierre Auger Observatory. The SD array is indicated by the black dots, the field of view of the FD stations and telescopes by the blue dots and lines. Figures taken from [112].

3.1.1 Surface detector

The SD consists of 1660 detection stations distributed in two different configurations. The SD-1500 array is composed of 1600 stations with a spacing of 1.5 km, while the SD-750 is composed of 60 stations with a spacing of 750 m and an area of 23.5 km^2 [115]. The SD-1500 is fully efficient in detecting EAS initiated by CRs with energies above 3 EeV. The SD-750 can measure down to 0.1 EeV since low-energy EASs leave a too small footprint to be detected by the SD-1500. All the SD stations are constantly monitored to control various quality factors such as temperature and humidity inside the tank.

Each SD station consists of a sealed cylindrical tank of with a diameter of 3.6 m and a height of 1.2 m [116]. Each tank is filled with 12,000 litres of ultra-purified water in order to detect the Cherenkov light produced by the passage of charged particles. The inside of the tank is covered with a reflective material. The Cherenkov light is detected by three PMTs located at the top of the inside of the tank. The SD stations are also equipped with solar panels, batteries, a radio antenna and a GPS receiver. This system is used to communicate the detection information to the Central Data Acquisition System (CDAS). A photograph and schematic representation of a SD station are shown in Fig. 3.2. The Pierre Auger SD array is characterized by a time resolution of 10 ns, which provides an angular resolution in the sky of 0.9°.

Given the large footprint of a single EAS, several SD stations may be activated during an event. An EAS is detected when a system of triggers selection is passed [117]. The first two triggers *T1* and *T2* are single station triggers and they ensure the coincidence of the signal in the three PMTs. The next trigger *T3* is a global trigger for the spatial and temporal compactness of neighbouring stations. The final triggers require that several stations to match a planar shower

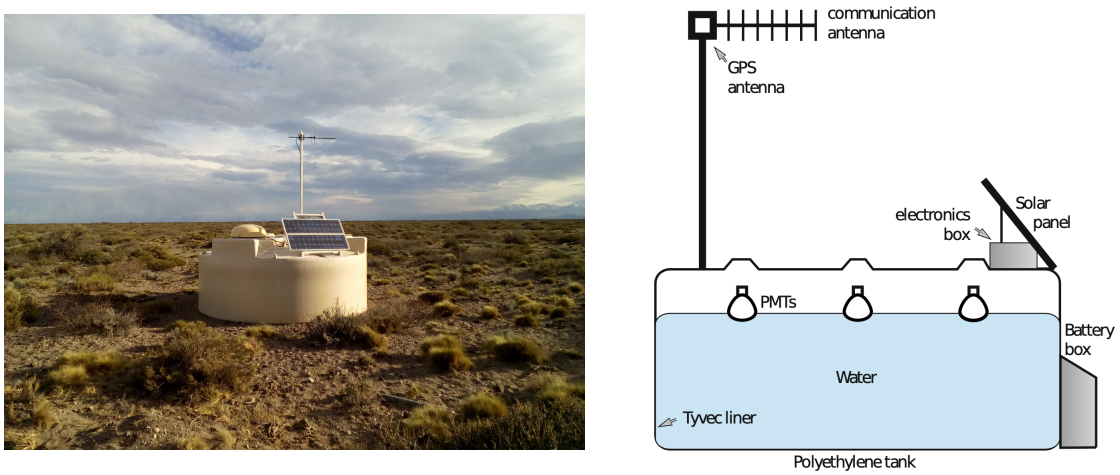

Figure 3.2: Left: photograph of a SD station. Figure taken from [112]. Right: schematic representation of a SD station. Figure taken from [113].

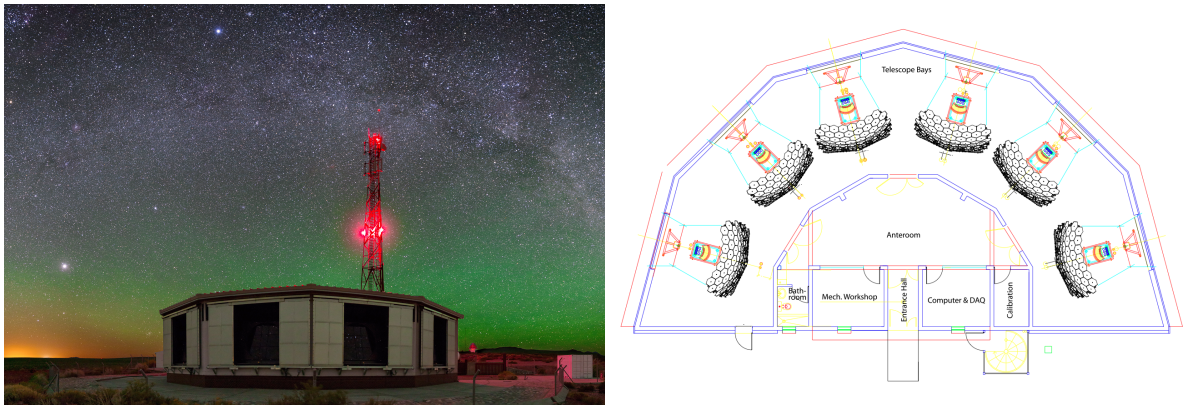

Figure 3.3: Left: photograph of the Los Morados FD station. Figure taken from [112]. Right: schematic representation of a FD station. Figure taken from [114].

front moving at the speed of light. When a signal passes this chain of triggers, the measurement of an EAS can be claimed and reconstructed. The time difference between the signals at the different SD stations is used to determine the arrival direction of the primary CR.

3.1.2 Fluorescence detector

The FD component of the Pierre Auger Observatory consists of 27 telescopes that measure the light produced during the passage of CRs in the atmosphere above the SD array. When charged particles of an EAS propagate through the atmosphere, nitrogen molecules are excited and emit UV radiation, when falling back to their ground state. The UV radiation is then detected by the fluorescence telescopes, allowing the shower depth $X_{\max}$ to be measured (see Eq. (2.22)).

As we can see in the right panel of Fig. 3.1, the FD system is composed of four stations, each with six telescopes; these sites are called *Los Leones*, *Los Morados*, *Loma Amarilla* and *Coihueco*. Each FD building is divided into six bays, each containing a fluorescence telescope

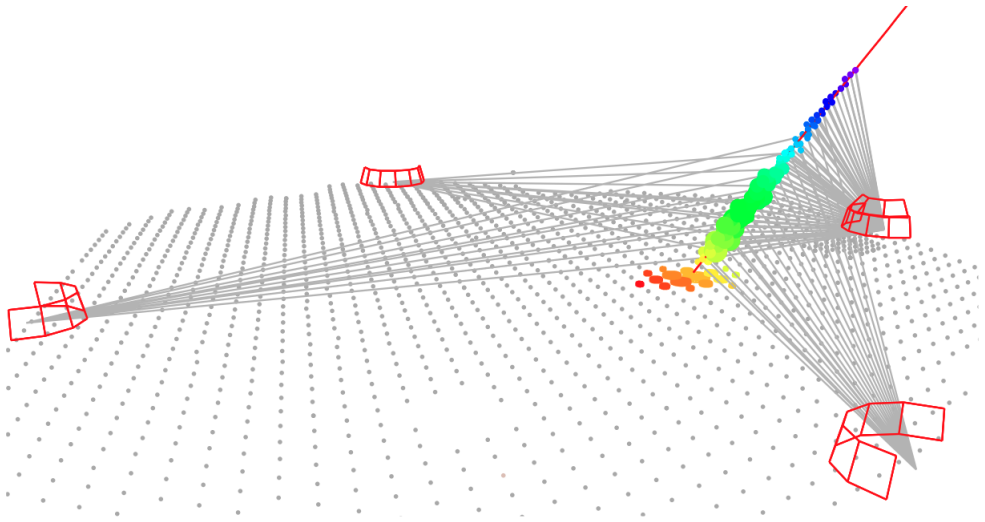

Figure 3.4: Example of a hybrid event measurement at the Pierre Auger Observatory. The red squares indicate the field of view of the FD stations and the gray dots the SD water tanks. The shower axis is given by the red line and the temporal shower development is shown by the rainbow color map. The temporal SD detection is given by the yellow-red color map. Figure taken from [121].

with a field of view of $30° \times 30°$ in azimuth and elevation, for a total of 180° in azimuth, pointing inside the SD array [114]. The external and internal layout of the Los Morados FD building is shown in Fig. 3.3. The last three telescopes are located at *Cerro Coihueco* and form the so-called High Elevation Auger Telescopes (HEAT). Each telescope is covered by a glass window with an UV filter. The UV light entering the telescope bay is then focused by a spherical mirror onto a camera of 440 hexagonal PMTs. The entire camera is given by an array of 22×20 pixels, calibrated with an external light source [118, 119].

As discussed in Sec. 2.2.2, EASs deposit $\sim 90\%$ of the atmosphere. This measurement is then used to reconstruct the primary CR energy. However, the calorimetric energy must be corrected to account for the invisible energy loss in neutrinos and muons [120].

As mentioned above, measurements with the FD can only be made on moonless nights, resulting in a duty cycle of $\sim 15\%$. Since a precise reconstruction of the EAS energy is made with FD measurements, hybrid events are essential for the *data-driven* interpretation of pure SD data.

3.1.3 Other detectors

The SD and FD of the Pierre Auger Observatory are operating simultaneously with other detectors. This allows for a better monitoring and reconstruction of the EASs produced by the CRs crossing the sky above the observatory.

EASs produced by CRs with energy below 1 EeV developed too high in the atmosphere to be measured by the FD telescopes. For this reason, the HEAT telescopes have been specially designed to measure this radiation up to 60° in elevation, thanks to a hydraulic system [122]. HEAT is then able to observe CRs with energies down to 0.1 EeV, and together with the SD-750 array allows the hybrid observation of CRs at lower energies.

The atmospheric conditions above the Pierre Auger Observatory must be monitored in order to properly reconstruct the data collected by the FD. For this purpose, two laser facilities, CLF and XLF, produce laser shots at the center of the SD array every 15 mins. These laser shots are recorded by the FD telescopes to estimate the aerosol component in the telescopes field of view [123]. Additional *lidar* stations are also present at each FD station: these stations produce UV pulses that are backscattered in the atmosphere depending on its aerosol content [124].

The muon content of EASs is further studied by the coupling of three $10\,\mathrm{m}^2$ scintillator detectors to the SD-750 water tanks. This configuration is the AMIGA extension of the Pierre Auger Observatory. An even denser array with 433 m spacing has also been installed in recent years [125].

A typical radio signal is also produced by the charged component of EASs. AERA is a system of radio antennas capable of measuring this signal [126]. It is located in the Infill region of the SD and consists of 153 antennas distributed over an area of $\sim 17\,\mathrm{km}^2$. These antennas can detect events with energies above 0.1 EeV with a duty cycle of about 100%.

3.1.4 Auger Prime

The Pierre Auger Observatory is currently undergoing an upgrade: this upgrade is called *Auger Prime* [111, 127] and it will help to better understand the origin and nature of the UHECRs. In particular, the goal of the Auger Prime upgrade is to provide an event-by event mass measurement of cosmic rays using only the SD.

Following the success of AMIGA and AERA, the SD stations will be equipped with new detectors. A plastic scintillator and a radio antenna are installed on the top of each water tank. The installation of surface scintillator detectors (SSDs) helps to discriminate between the electromagnetic and muonic components of EASs, thus improving the reconstruction of the primary CR mass. The SSDs consist of a $\sim 4\,\mathrm{m}^2$ plastic scintillator. The SD station is also equipped with radio detectors (RDs). The electromagnetic component of air showers produces a radio emission in the 30-80 MHz range, which is almost unattenuated in the atmosphere. The RDs provides a ground measurement of the electromagnetic component of the shower with a duty cycle of about 95% [128, 129].

A fourth, smaller PMT will be installed at the SD stations, together with a new Upgraded Unified Board (UUB) to improve data quality and processing [130]. Finally, an underground muon detector (UMD) is installed under 2.3 m of soil next to the SD-750 stations [131]. The UMDs are plastic scintillators and will provide direct measurements of the muon content of EASs.

3.2 Selected scientific results

The scientific output of by the Pierre Auger Observatory, which has been in operation for more than 20 years, is extremely rich. In addition to measurements strictly related to CRs, the Pierre Auger Observatory carries out studies of neutral CRs, such as neutrons [132, 133], neutral messengers such as neutrinos and photons [134–136], and also physics beyond the Standard Model (SM) such as dark matter (DM) [137–139] and Lorentz invariance violation (LIV) [140, 141]. In addition, the Pierre Auger Observatory collaborates with other observatories for joint multimessenger measurements, including also gravitational waves (GWs) [142–148]. The following sections present the main results on UHECR observables such as the energy spectrum, mass

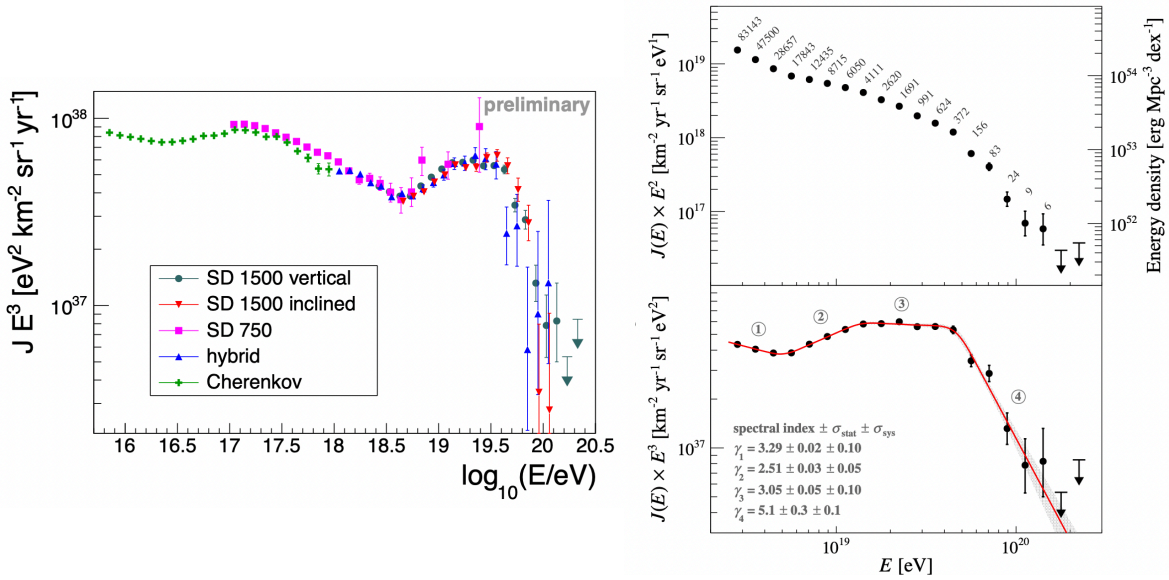

Figure 3.5: Left: CR energy spectrum multiplied by E^3 measured by the Pierre Auger Observatory using different reconstruction techniques. Figure taken from [90]. Right: UHECR energy spectrum measured by the Pierre Auger Observatory, multiplied by E^2 in the top panel and by E^3 in the bottom panel. The number of events observed is given in the upper panel. The red line in the bottom panel shows the fit curve in Eq. (3.1) and the gray band indicates the statistical uncertainty of the fit. The numbers in the circles in the bottom panel indicate the energy intervals where the energy spectrum is described by a power-law index, as in Eq. (3.1). Figure taken from [149].

composition and arrival directions.

3.2.1 Energy spectrum

We have discussed in Sec. 3.1 that the Pierre Auger Observatory can measure the UHECR energy spectrum in different energy ranges using different experimental techniques and calibration methods. The SD-1500 and SD-750 energy measurements are calibrated using high quality hybrid events observed with the FD. In addition, the HEAT telescopes provided low-energy measurements from the Cherenkov radiation produced in the EASs. The final energy spectrum obtained after taking into account detector effects is called the *unfolded* spectrum. A preliminary result of the energy spectrum obtained with all the methods mentioned above from [90] is shown in the left panel of Fig 3.5, where the different reconstruction techniques are shown in different colors.

In this work we are interested in the UHECR energy spectrum (i.e. the spectrum above 1 EeV). The Pierre Auger Observatory measurement of the UHECR energy spectrum can be found in [149, 150]. The unfolded energy spectrum is then fitted to the product of power-law functions with smooth transitions of the form

$$J(E) = J_0 \left(\frac{E}{10^{18.5}\,\mathrm{eV}}\right)^{-\gamma_1} \prod_{i=1}^{3} \left[1 + \left(\frac{E}{E_{ij}}\right)^{1/\omega_{ij}}\right]^{(\gamma_i-\gamma_j)/\omega_{ij}} , \tag{3.1}$$

where $j = i + 1$ and the factors $\omega_{ij} = 0.05$ refer to the width of the energy intervals where

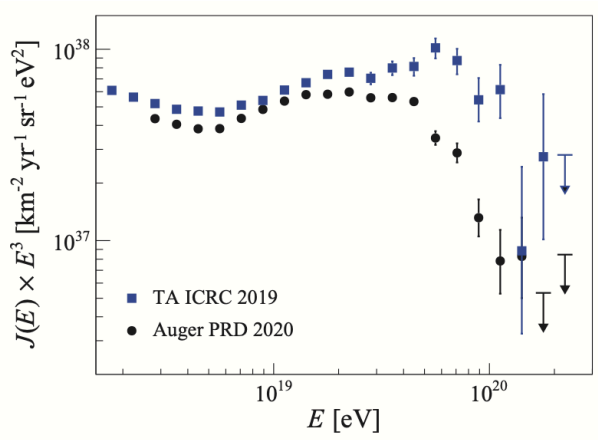

Figure 3.6: The energy spectra measured by the TA (blue squares) and Pierre Auger (black circles) observatories in the full declination bands. Figure adapted from [151].

the spectrum changes slope. The UHECR energy spectrum and the fit in Eq. (3.1) are shown in the right panels of Fig 3.5, where also the values of the indices γ_i are given. The regions corresponding to different γ_i are also indicated by the numbers in the circles. The ankle is given by the change in slope at $E_{12} = (5.0 \pm 0.1 \pm 0.5)$ EeV, while the ultra-high-energy suppression appears at $E_{34} = (46 \pm 3 \pm 6)$ EeV. In [149] the Pierre Auger Observatory has also reported the observation of a new slope change from $\gamma \simeq 2.5$ to $\gamma \simeq 3.0$ at the energy $E_{23} = (12 \pm 1 \pm 2)$ EeV. This new feature has been called the *instep* of the UHECR energy spectrum. The integral of the energy spectrum gives a measurement of the UHECR energy density of $\simeq 5.7 \cdot 10^{53}$ erg Mpc^{-3}, above the ankle[3].

In Sec. 2.1.2 the TA experiment was mentioned as the largest UHECR observatory in the northern hemisphere. Since TA also measures the cosmic ray energy spectrum with a hybrid approach, it is interesting to compare the TA and Auger energy spectra at the highest energies. This comparative analysis has been carried out by a joint TA-Auger working group since 2012. Fig. 3.6 shows both TA and Auger energy spectra: it is evident that the TA data points are systematically larger than the Auger data, and this difference increases with energy. Both the experiments are affected by systematic uncertainties (14% for Auger and 21% for TA) which are almost energy independent [151]. The difference in the normalization of the two spectra up to 10 EeV can be resolved by introducing an energy independent relative energy scale of $\simeq 10\%$, which is included in the systematic uncertainties. However, above 10 EeV an energy dependent energy shift of about $\sim 20\%$ per decade is required to restore the agreement between the two spectra. The same results have also been obtained in the common declination band of the two experiments, excluding an astrophysical origin of this discrepancy [94, 97, 151, 152].

3.2.2 Mass composition

The direct measurement of the UHECR mass composition is not possible, and then EASs have to be used to reconstruct the information about the cosmic ray entering in the atmosphere. We have seen in Sec. 2.2 that the shower depth $X_{\max}$ depends on the logarithm of the primary mass

[3]The *erg* is a unit of energy and it is equal to $1\,\text{erg} = 10^{-7}\,\text{J} = 6.2 \cdot 10^{11}\,\text{eV}$ [9].

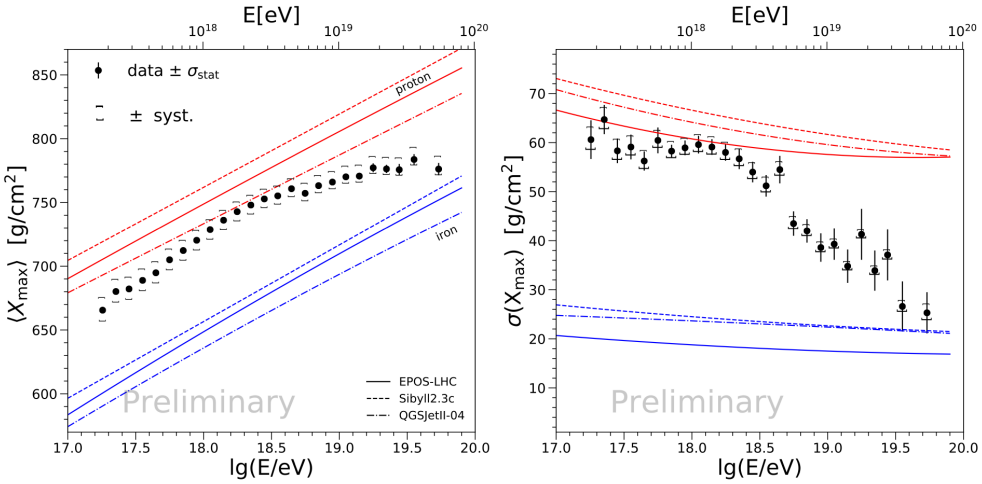

Figure 3.7: Left: measurements of $\langle X_{\max} \rangle$ by the Pierre Auger Observatory. The red and blue lines indicate the pure proton and iron composition scenarios for different HIMs. Right: same as the left panel, but for $\sigma(X_{\max})$. Figure taken from [154].

number A. For this reason, $X_{\max}$ is used as a good estimator of the cosmic ray mass composition. However, since the interactions in an EAS are stochastic processes, the $X_{\max}$ of a given nuclear species A_i is characterized by a distribution function $f_i(X_{\max})$. Then, in the case of a mixed composition with fractions p_i, the final distribution function $f(X_{\max})$ is given by

$$f(X_{\max}) = \sum_i p_i \, f_i(X_{\max}) \,, \tag{3.2}$$

where the sum is over the considered species [153]. The first two moments $\langle X_{\max} \rangle$ and $\sigma(X_{\max})$ of the distribution in Eq. (3.2) are used as indicators of the mass composition.

The Pierre Auger Observatory measures the shower development with the FD stations down to $10^{17.2}$ eV , which are then corrected for detector effects [154]. The $X_{\max}$ resolution of the FD is $\sim 20\,\mathrm{g\,cm^{-2}}$, while the shower-to-shower fluctuations are $\sim 20 - 60\,\mathrm{g\,cm^{-2}}$, making an event-by-event reconstruction impossible [153, 154]. Furthermore, the interpretation of the measured $\langle X_{\max} \rangle$ and $\sigma(X_{\max})$ is based on the comparison with Monte Carlo simulations. The predictions made with these simulations are affected by the HIM considered (see Sec. 2.2.4).

The first two moments of $X_{\max}$ measured by the Pierre Auger Observatory are shown in Fig. 3.7. As expected, $\langle X_{\max} \rangle$ increases with energy, due to the fact that high-energy showers can penetrate further into the atmosphere. The average composition becomes lighter in the beginning, then the trend is reversed at $\sim 2\,\mathrm{EeV}$, after which it becomes heavier. We can also observe a similar trend also in the second moment $\sigma(X_{\max})$. Since heavy primary nuclei corresponds to less fluctuations in the shower maximum, it can be seen that below $\sim 2\,\mathrm{EeV}$ the UHECR composition is quite mixed, while at the highest energies it becomes more pure [154, 155].

The information obtained from the $X_{\max}$ distribution can be converted into the mass fractions in Eq. 3.2, assuming a HIM. The evolution of the CR mass fractions with energy is shown in Fig. 3.8. It can be seen that the composition changes from a proton dominated knee, to a heavier

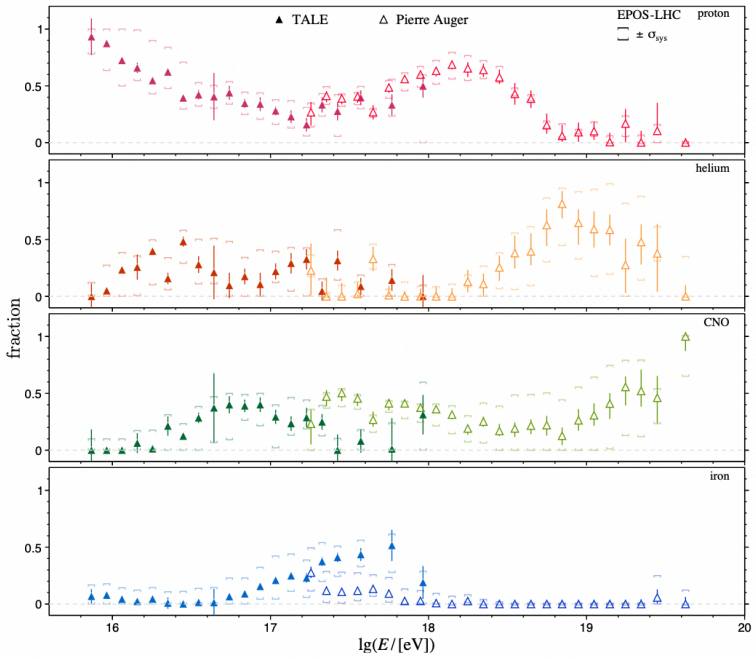

Figure 3.8: Fractions of the primary cosmic rays as a function of the energy from the TA and Pierre Auger observatories. Fractions obtained with the HIM EPOS-LHC. Figure taken from [94].

composition towards the second knee, then the proton component increases again at the ankle. The highest energies are first dominated by helium, then by nuclei of the CNO group, and finally a possible iron contribution could maybe become important [94, 97].

3.2.3 Anisotropies

The last observable measured by the Pierre Auger Observatory is the UHECR arrival direction at the top of the atmosphere. The precise determination of the arrival directions is a key measurement in the search for UHECR sources. The Pierre Auger Observatory has achieved an angular resolution in the sky of $1° - 2°$ degrees, depending on the number of SD stations triggered by the EAS [156]. However, the observed arrival directions do not point directly back to the CR sources. Since cosmic rays are charged particles, their propagation is affected by the presence of the galactic and extragalactic magnetic fields (GMF and EGMF), which can obscure the true position of the source in the sky. Moreover, this magnetic deflection depends on the magnetic rigidity $R = E/Z$ of the particle, where E is the energy and Z is the charge number, which is affected by the interactions during the extragalactic propagation (see Sec. 2.3). Once all of these effects are taken into account, the analysis of the UHECR arrival directions can help for the localization of their sources.

Before presenting the anisotropy results by the Pierre Auger Observatory, it is necessary to define some fundamental quantities. Given the unitary vector on a sphere $\hat{\mathbf{n}}$, the cosmic ray flux $\Phi(\hat{\mathbf{n}})$ is defined as the number of particles per unit of area, unit of time and unit of solid angle, i.e.

$$\Phi(\hat{\mathbf{n}}) = \frac{d^3N}{dA\, dt\, d\Omega}(\hat{\mathbf{n}})\,. \tag{3.3}$$

It is also common to the define the flux in Eq. (3.3) only for particles above a given energy threshold $E_{\rm th}$. Since the flux $\Phi(\hat{\mathbf{n}})$ is a function of the arrival direction, it can be expanded in spherical harmonics $Y_{lm}(\hat{\mathbf{n}})$ as

$$\Phi(\hat{\mathbf{n}}) = \sum_{l=0}^{+\infty} \sum_{m=-l}^{l} a_{lm} Y_{lm}(\hat{\mathbf{n}}) \,, \tag{3.4}$$

where the spherical harmonic expansion is defined in Appendix A.1. The spherical coefficients a_{lm} are then used to define the angular power spectrum of the flux function

$$\mathcal{C}_l = \frac{1}{2l+1} \sum_{m=-l}^{l} |a_{lm}|^2 \,, \tag{3.5}$$

where $|a_{lm}|^2 = a_{lm}^* a_{lm}$ is the modulus square of the complex spherical coefficients. The angular power spectrum is then used to study the angular features in the sky of the observed flux. In particular, a given power mode l can be associated with an angular scale in the sky of the order of $\sim 180°/l$. These angular scales can then be associated with specific quantities by rewriting the expansion in Eq. (3.4) as

$$\Phi(\hat{\mathbf{n}}) = \Phi_0 \left(1 + \mathbf{d} \cdot \hat{\mathbf{n}} + \frac{1}{2} \hat{\mathbf{n}} \cdot \mathbf{Q} \cdot \hat{\mathbf{n}} + ... \right) \,, \tag{3.6}$$

where Φ_0 is the monopole, $\mathbf{d}$ is the dipole vector and $\mathbf{Q}$ is the quadrupole tensor. The dipole and quadrupole strengths are defined as $d^2 = \sum_{i=1}^{3} d_i$ and $Q^2 = \sum_{i,j=1}^{3} Q_{ij}/9$. We will show in detail in Chapter 6 that the dipole vector is given by the coefficients a_{1m}, while the quadrupole tensor is given by the coefficient a_{2m}. Therefore, when we talk about large angular scale anisotropies, we refer to the dipolar and quadrupolar components of the flux. When we talk about small and intermediate angular scale anisotropies, we refer to angular scales smaller than the the dipolar and quadrupolar ones.

The Pierre Auger Observatory reported the first observation of a large angular scale deviation from isotropy in the UHECR sky above 8 EeV in 2017 [16]. This result is based on the Rayleigh analysis [157, 158] of the right ascension[4] α_i of the observed events (see Appendix A.4 for more details). The first harmonic Fourier coefficients are given by

$$a_\alpha = \frac{2}{\mathcal{N}} \sum_{i=1}^{N} \omega_i \cos \alpha_i \quad \text{and} \quad b_\alpha = \frac{2}{\mathcal{N}} \sum_{i=1}^{N} \omega_i \sin \alpha_i \,, \tag{3.7}$$

where N is the total number of events, $\mathcal{N} = \sum_{i=1}^{N} \omega_i$ and ω_i are weights to account for the experiment exposure. The amplitude r_α and the phase φ_α of the harmonic are given by

$$r_\alpha = \sqrt{a_\alpha^2 + b_\alpha^2} \quad \text{and} \quad \tan \varphi_\alpha = \frac{b_\alpha}{a_\alpha} \,. \tag{3.8}$$

[4]For the definition of the right ascension and other quantities related to celestial coordinate systems, see Appendix A.3.

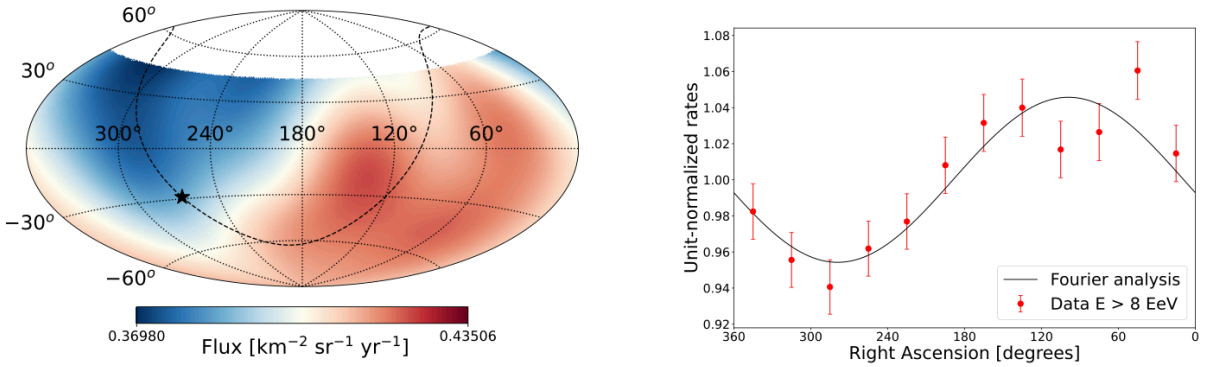

Figure 3.9: Left: cosmic ray flux above 8 EeV measured by the Pierre Auger Observatory in equatorial coordinates. The flux is smoothed using a von Mises-Fisher distribution with a mean cosine equal to that of a top-hat distribution with radius of 45°. The Galactic plane and the Galactic center are indicated by the dashed black line and the black star. Right: distribution in right ascension of the normalized UHECR rate, the black line represents the analysis done with a pure dipolar flux. Figure taken from [17].

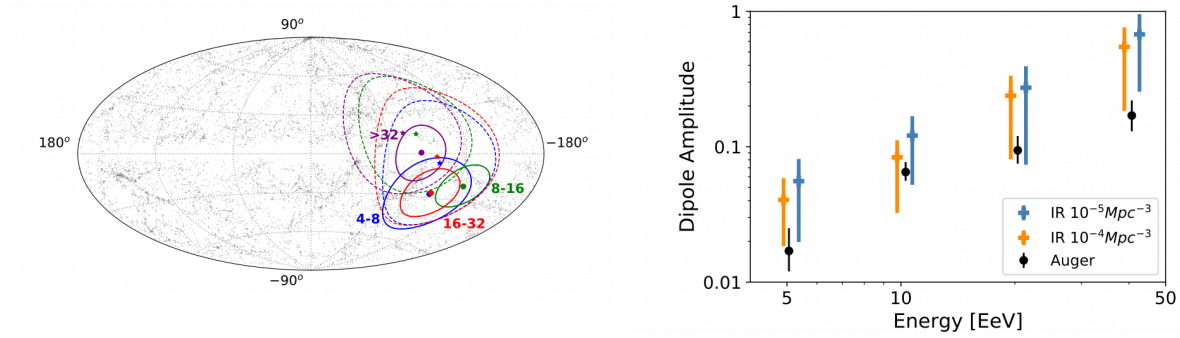

Figure 3.10: Left: prediction in Galactic coordinates of the mean dipole direction (stars) and the 68% confidence level contour (dashed lines) obtained with 10^3 realizations of UHECR sources with density 10^{-4} Mpc^{-3} in different energy bins. The sources are extracted from the infrared galaxies in the 2MASS catalogue [159], up to 120 Mpc from the Earth. The observed dipole data are indicated by the solid lines. Right: same as the left panel, but for the dipole amplitude. Figures adapted from [17].

The results obtained in [16] with $\sim 30,000$ events were $r_\alpha = 4.7^{+0.8}_{-0.7}\%$ and $\varphi_\alpha = 100° \pm 10°$. The reconstructed three-dimensional dipole amplitude was $d = 6.5^{+1.3}_{-0.9}\%$, pointing in the Galactic coordinates $(l, b) = (233°, -13°)$ with a significance level of 5.2σ. Since the observed dipole pointed more than 100° away from the Galactic center, this result provided the first evidence for an extragalactic origin of the UHECRs above 8 EeV. In the following years, the Pierre Auger Observatory continued to monitor the cosmic ray sky at the ultra-high energies to study the observed dipole modulation [17, 160, 161]. The last published dipole amplitude with $\sim 50,000$ events above 8 EeV is $d = 7.4^{+1.0}_{-0.8}\%$ with a 6.8σ significance [17]. The cosmic ray flux and the Rayleigh analysis results from [17] are shown in Fig. 3.9.

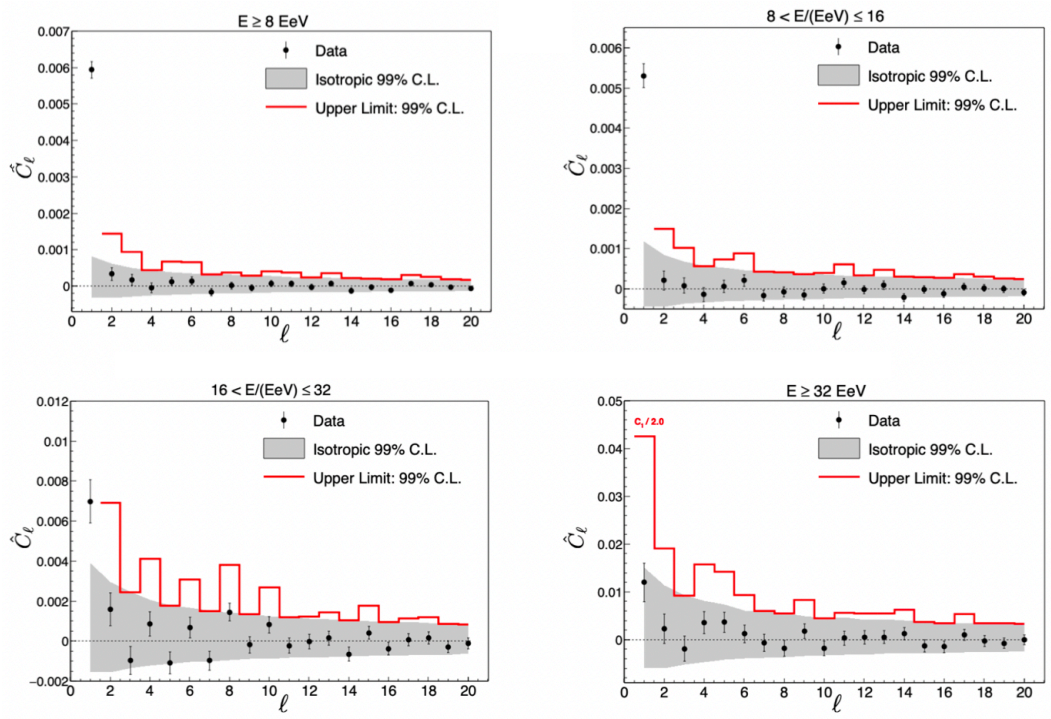

Figure 3.11: Angular power spectrum measured by the Pierre Auger Observatory for the energy bins ≥ 8 EeV (top left), 8-16 EeV (top right), 16-32 EeV (bottom left) and ≥ 32 EeV (bottom right). The gray area correspond to the 99% CL fluctuations from an isotropic distribution and the red lines correspond to the 99% CL upper limits. In the lower right panel, the upper limit for $\mathcal{C}_1$ was divided by 2. Figure adapted from [17].

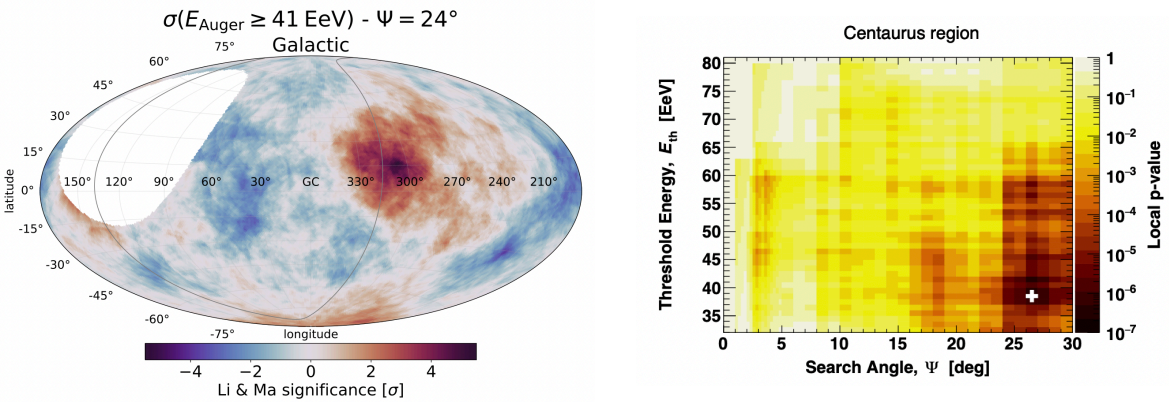

Figure 3.12: Left: Li-Ma significance in Galactic coordinates of the excess of UHECRs with energy $E \geq 41$ EeV, with the Supergalactic plane indicated by the gray line. Right: local p-value of the excess in the Centaurus A region. The minimum is marked by the white cross. Figures adapted from [162].

A first prediction for the observed dipolar anisotropy could come from the relative motion of the Earth in the CR reference frame (i.e. the CMB reference frame): this phenomenon is called

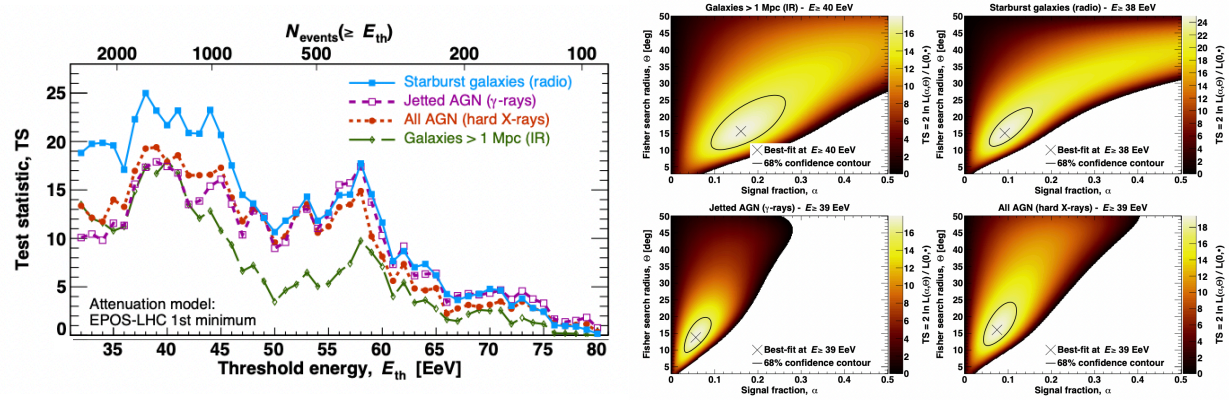

Figure 3.13: Left: test statistic TS as a function of the energy threshold for the correlations of the observed UHECRs with the source catalogues considered in [162]. Right: same test statistic as in the left panel, but as a function of the signal fraction α and the smearing angle Θ. The best-fit parameters are indicated by the cross, together with the 68% C.L. contour. Figures adapted from [162].

the *Compton-Getting effect* [163]. However, the corresponding dipole due to the Compton-Getting effect would only be of $\sim 0.6\%$ [164, 165], and then too small compared to observations. Therefore, the origin of the UHECR dipole could be related to an inhomogeneous distribution of UHECR sources. If the cosmic ray sources follow the local baryon distribution, or also the Large Scale Structure (LSS) distribution, and if the deflections are not too large, a correlation between the UHECR and source distribution dipoles is expected. Furthermore, interactions of UHECRs during the extragalactic propagation would correspond to an increase in the dipole amplitude with energy. These energy dependencies of the dipole amplitude and direction are shown in Fig. 3.10.

Due to the only partial sky coverage of the Pierre Auger Observatory, a joint working group with the TA Collaboration has been also established in the context of UHECR arrival direction studies [166, 167]. The combination of the field of view the two observatories is then crucial to achieve a full sky coverage. As expected, this joint working group has confirmed Auger results on the large angular scale anisotropies.

Despite the observation of the dipole, all the higher order multipoles observed by the Pierre Auger Observatory show no statistically significant deviation from isotropy in all the energy bins considered, as shown in Fig. 3.11 from [17]. However, small and intermediate angular scale anisotropy searches can be carried out by looking for UHECR overdensities in the sky and for correlations with real source catalogues. This has been done in [162], where more than 2.600 UHECRs above 32 EeV are considered. The search for local excesses is done by comparing the number of observed events in a given circular window with the expected number of events from an isotropic distribution. These windows have radii from 1° to 30° in steps of 1°, and their are centered on a $1^\circ \times 1^\circ$ grid in the sky. Different energy thresholds are considered, from 32 EeV to 80 EeV with 1 EeV steps. The significance of the excess is evaluated with the Li-Ma significance [168]. The most significant excess was found above 41 EeV with a window of 24° centered in Galactic coordinates $(l, b) = (305^\circ, 16^\circ)$. The significance of this excess was found to be 5.4σ, as can be seen in Fig. 3.12. However, the post-trial p-value is ~ 0.03, so the excess is not statistically significant. Similar results were obtained when looking for correlations with structures such as

the Galactic center, the Galactic plane and the Supergalactic plane. Another interesting region considered in this analysis is the direction of Centaurus A, the nearest radio galaxy at $\sim 4\,\mathrm{Mpc}$ and in equatorial coordinates $(\alpha, \delta) = (201.4°, -43.0°)$. The same analysis described above found an excess above 38 EeV in an angular window of 27° with a post-trial p-value of $4.5 \cdot 10^{-5}$.

In [162] a search for correlations of the UHECR arrival direction above 32 EeV with real source catalogues was also done. In particular, jetted and all Active Galactic Nuclei (AGNs), Starburst Galaxies (SBGs) are considered along with the LSS distribution of matter (see [162] for more details on the catalogues). This is done by constructing two signal functions, one based on the flux from the source in the catalogue and a purely isotropic one, and performing a likelihood ratio analysis. However, the signal function obtained with the catalogues is generically given by the combination of the catalogue contribution and an isotropic component. The amplitude of the catalogue contribution is given by the signal fraction α. The flux of each component of a catalogue is modelled with a von Mises-Fisher distribution with a smearing angle Θ (see Appendix. A.2). The results are shown in Fig. 3.13. The global maximum for the test statistic is obtained for the SBG catalogue for $E_{\mathrm{th}} = 38\,\mathrm{EeV}$ with a signal fraction of $\alpha = 9^{+6}_{-4}\%$ and a post-trial p-value of $3.2 \cdot 10^{-5}$ ($\simeq 4\sigma$). Similar results are also obtained for the jetted-AGN catalogue ($\simeq 3\sigma$). This result is mainly due to the presence of an excess of events in the Centaurus region, where strong sources such as the SBG NGC 4945 and Centaurus A are located.

4

Origin and propagation of UHECRs

The observation of UHECRs with energies up to 100 EeV leads to the question of where these extremely energetic particles are accelerated. The observation of a dipolar component in the UHECR flux reported in [17] points in the direction of an extragalactic origin. However, even if several classes of sources could be responsible for the observed dipole, a definitive answer has not yet been found. Furthermore, as UHECRs propagate in the extragalactic space, interactions with the cosmic background photon fields become possible, due to the large Lorentz boost of these photons in the cosmic ray reference frame. These interactions introduce an additional difficulty in the identification of the CR sources, since the energy spectrum and mass composition of the observed cosmic rays do not correspond to that leaving the source environment. We will see that this is also a problem when considering the propagation of very-high-energy $\gamma-$rays. Finally, the presence of galactic and extragalactic magnetic fields affects the observed UHECR arrival directions.

In this chapter, the possible acceleration sites and mechanisms are presented in Sec. 4.1. In Secs. 4.2 and 4.3 the main energy loss mechanisms during the UHECR extragalactic propagation are discussed. In Sec. 4.4 we also discuss the interactions of high-energy $\gamma-$rays with cosmic photon fields. Finally, in Sec. 4.5 the effect of the galactic and extragalactic magnetic fields is considered.

4.1 Cosmic rays acceleration

One of the most puzzling questions in CR physics is the origin of such extremely energetic particles. Even after decades of observations, the astrophysical sources and the acceleration mechanisms that produce the UHECRs are still unknown. In view of the experimental results discussed in Sec. 3.2, UHECR sources must be characterized by acceleration mechanisms capable of reaching energies of the order of $\sim 10^{20}$ eV, way beyond the maximum energy produced in ground-based accelerators.

Two main scenarios of CR acceleration mechanisms can be considered: the *top-down* scenario and the *bottom-up* scenario. In the top-down scenario, UHECRs are produced as the decay prod-

uct of heavy exotic particles with masses from $\sim 1\,\text{TeV}$ to $M_{\text{GUT}} \sim 10^{24}\,\text{eV}$[1] [29]. Experimental constraints on top-down mechanisms obtained by the Pierre Auger Observatory can be found in [139, 169]. In the bottom-up scenario, UHECRs are accelerated to ultra-high energies in astrophysical sources. Let us make some general considerations: given the electric field vector $\mathbf{E}$ and the magnetic field vector $\mathbf{B}$, the force electromagnetic force on a particle with electric charge q and velocity vector $\boldsymbol{\beta}$ is given by the Lorentz force

$$\mathbf{F} = q\,(\mathbf{E} + \boldsymbol{\beta} \times \mathbf{B})\,, \tag{4.1}$$

which depends only on the particle rigidity vector $\mathbf{R} = \mathbf{p}/q$ such that

$$\frac{d\mathbf{R}}{dt} = \mathbf{E} + \boldsymbol{\beta} \times \mathbf{B}\,. \tag{4.2}$$

We can use Eq. (4.2) to obtain the time evolution of the rigidity $R^2 = \mathbf{R} \cdot \mathbf{R}$, which is

$$\frac{dR^2}{dt} = 2\mathbf{R} \cdot \frac{d\mathbf{R}}{dt} = 2\mathbf{R} \cdot \mathbf{E}\,. \tag{4.3}$$

The result in Eq. (4.3) is particularly interesting because in astrophysical plasmas local electric fields are normally rapidly suppressed due to the high conductivity. However, electric and magnetic fields can transform into each other when different reference frames are considered[2]. Therefore, even if no energy change is possible in the rest frame of the plasma, an energy gain can be obtained by changing the reference frame.

In the context of the bottom-up acceleration mechanisms, two main sub-scenarios can be considered. In the *on-shot* or *direct* scenarios, charged particles are accelerated directly by an electric field: this is the case of the so-called *unipolar inductors*. In this case, rapidly rotating and strongly magnetized astrophysical objects can induce an electric field capable of extracting and accelerating particles from the surface of the object. Examples of unipolar inductors are white dwarfs [170, 171] and neutron stars (such as pulsars and magnetars) [172–175]. The second scenario is called *stochastic acceleration*: in this case, particles gain small amounts of energy during multiple scattering with magnetic turbulence. We will describe stochastic acceleration in detail in the next section.

4.1.1 Stochastic acceleration: the Fermi mechanisms

The idea of stochastic acceleration is based on the fact that particles gain a constant fraction of energy ξ in each acceleration cycle [29, 176, 177]. If we consider a particle with initial energy E_0, after one acceleration cycle the energy will be $E_1 = E_0(1+\xi)$, and after two cycles the energy will be $E_2 = E_1(1+\xi) = E_0(1+\xi)^2$. Therefore, after n cycles, the energy of the particle will be

$$E_n = E_0(1+\xi)^n\,, \tag{4.4}$$

from which we can write the number of cycles n as

$$n = \frac{\ln\left(E_n/E_0\right)}{\ln\left(1+\xi\right)}\,. \tag{4.5}$$

[1] GUTs stands for *Grand Unification Theories*.

[2] Electric and magnetic fields are different manifestations of the electromagnetic field tensor $F_{\mu\nu}$, whose components transform under Lorentz transformations from one reference frame to another.

We can now define the probability P that the particle will leave the acceleration region, ending the acceleration process. If N_0 is the initial number of particles, then the number of particles accelerated to an energy $E \geq E_n$ after n cycles is given by

$$N(E \geq E_n) = N_0 \sum_{k=n}^{+\infty} (1-P)^k \,, \tag{4.6}$$

and since $|1-P| < 1$, we can use the geometric series to calculate the sum. Then, the number of particles with $E \geq E_n$ can be written as

$$\begin{aligned} N(E \geq E_n) &= N_0 \left[\sum_{k=0}^{+\infty} (1-P)^k - \sum_{k=0}^{n-1} (1-P)^k \right] \\ &= N_0 \left[\frac{1}{1-(1-P)} - \frac{1-(1-P)^n}{1-(1-P)} \right] \\ &= N_0 \left[\frac{1}{P} - \frac{1-(1-P)^n}{P} \right] \\ &= N_0 \frac{(1-P)^n}{P} \,. \end{aligned} \tag{4.7}$$

If we consider the result in Eq. (4.5), we can write $N(E \geq E_n)$ as

$$N(E \geq E_n) \propto \left(\frac{E_n}{E_0} \right)^{-\gamma} \,, \tag{4.8}$$

where the index γ is given by

$$\gamma = -\frac{\ln(1-P)}{\ln(1+\xi)} \simeq \frac{P}{\xi} \,. \tag{4.9}$$

We can see that stochastic acceleration leads to a power law spectrum of the form $dN/dE \propto E^{-\alpha}$, where $\alpha = 1+\gamma$ is the spectral index, such that $\alpha \simeq 1 + P/\xi \simeq 1 + \xi^{-1}(\tau_{\text{cycle}}/\tau_{\text{esc}})$, where τ_{cycle} and τ_{esc} are the typical time scales of an acceleration cycle and of the escale from the acceleration region, respectively. We can also see that, given the lifetime of the accelerator τ_{acc}, the maximum energy the particles can reach is limited by $E \lesssim E_0(1+\xi)^{\tau_{\text{acc}}/\tau_{\text{cycle}}}$.

The first stochastic acceleration mechanism for cosmic rays was proposed by E. Fermi in [178]: the idea is that charged particles interact with the magnetic field frozen in interstellar clouds of plasma moving in random directions with velocity $V = |\mathbf{V}|$. A representation of this scenario is shown in the left panel of Fig. 4.1. We can then consider an ultrarelativistic particle with initial energy E_1 that enters in the cloud and begins to propagate diffusively in its magnetic field. The energy of the particle in the rest frame of the cloud is given by the Lorentz transformation

$$E_1' = \Gamma E_1 \left(1 - \beta \cos\theta_1\right) \,, \tag{4.10}$$

where $\Gamma = (1-\beta^2)^{-1/2}$ and β are the Lorentz factor and the velocity of the cloud and θ_1 is the entering angle with respect to the velocity of the cloud. We assume that the mass of the plasma cloud is much larger than the mass of the particle. The energy of the particle at the escape E_2 can be obtained considering the opposite Lorentz transformation

$$E_2 = \Gamma E_2' (1 + \beta \cos\theta_2') \,, \tag{4.11}$$

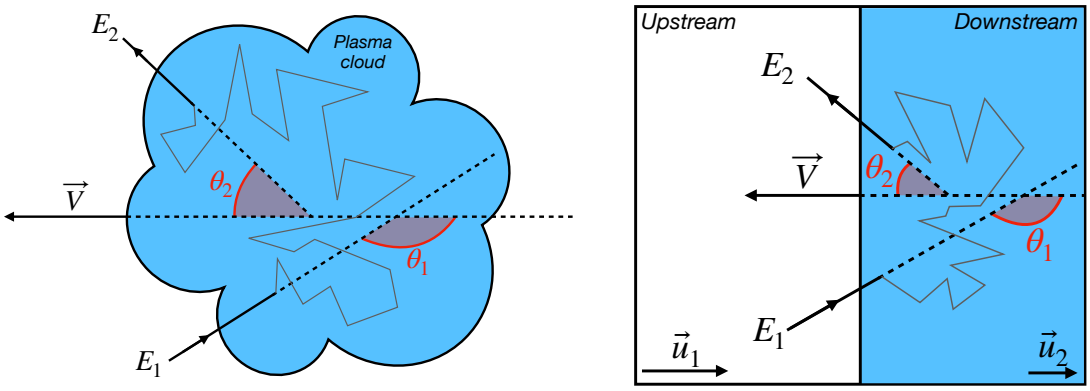

Figure 4.1: Left: schematic representation of the second-order Fermi mechanism of charged particle scattering from a plasma cloud. Right: schematic representation of the first-order Fermi mechanism of a shock front.

where E_2' is the energy of the particle at the escape and θ_2' is the escape angle, both in the reference frame of the cloud. Since $E_1' = E_2'$, we can then write the energy gain as

$$\frac{\Delta E}{E} = \frac{E_2 - E_1}{E_1} = \frac{1 + \beta\cos\theta_2' - \beta\cos\theta_1 - \beta^2\cos\theta_1\cos\theta_2'}{1-\beta^2} - 1\,. \tag{4.12}$$

We can now calculate the energy gain factor ξ by considering the mean value of Eq. (4.12). The probability of having a collision with a plasma cloud is proportional to the relative velocity of the cloud and must be maximal for $\theta_1 = \pi$. This means that

$$\mathcal{P}(\cos\theta_1) = \frac{1-\beta\cos\theta_1}{2}\,, \tag{4.13}$$

while the probability distribution for the angle θ_2' is uniform, since the escape from the plasma cloud is the result of a large number of scatterings, $\mathcal{P}(\cos\theta_2') = 1/2$. We then obtain that

$$\langle\cos\theta_1\rangle = \int_{-1}^{1} x\cdot\frac{1-\beta x}{2}\,dx = -\frac{\beta}{3}\,, \tag{4.14}$$

$$\langle\cos\theta_2'\rangle = \int_{-1}^{1}\frac{x}{2}\,dx = 0\,, \tag{4.15}$$

from which the average energy gain

$$\xi = \left\langle\frac{\Delta E}{E}\right\rangle = \frac{1+\frac{1}{3}\beta^2}{1-\beta^2} - 1 \simeq \frac{4}{3}\beta^2\,, \tag{4.16}$$

where we have assumed that $\beta \ll 1$. This result is known as *second-order Fermi mechanism*, since the energy gain is proportional to the second power of the cloud velocity β. Unfortunately, second-order acceleration is not very efficient, since the typical velocity of interstellar clouds is $\beta \sim 10^{-4}$, giving an average energy gain of $\xi \sim 10^{-8}$.

In the second-order Fermi mechanism, the plasma clouds act like a magnetic mirror moving in random directions. However, another possible situation is given by the case where the magnetic

mirror is characterized by a specific geometrical structure. This is the case of a planar magnetized shock front: this case is referred to as *first-order Fermi mechanism* [179]. We consider the reference frame in which the shock front is at rest, as shown in the right panel of Fig. 4.1. In this reference frame, the plasma on the upstream side moves towards the shock front with velocity $\mathbf{u}_1$, while on the downstream side the plasma moves away from the shock front with velocity $\mathbf{u}_2$, so that $u_2 < u_1$. In the case of non-relativistic shock we have that $V \simeq u_1 - u_2$. We can then use the same formalism as for the second-order Fermi mechanism, but consider that one acceleration cycle is given by the particle crossing the shock front from the upstream side to the downstream side and then crossing back to the upstream side. The energy change in one cycle is then still given by Eq. (4.12), where the prime quantities are calculated in the downstream side of the shock front. However, the probability distributions of the two angles are now given by

$$\mathcal{P}(\cos\theta_1) = -2\cos\theta_1 \qquad \text{for} \quad -1 \leq \cos\theta_1 \leq 0\,, \tag{4.17}$$

$$\mathcal{P}(\cos\theta_2') = 2\cos\theta_2' \qquad \text{for} \quad 0 \leq \cos\theta_2' \leq 1\,, \tag{4.18}$$

from which we can see that

$$\langle\cos\theta_1\rangle = -\frac{2}{3} \quad \text{and} \quad \langle\cos\theta_2'\rangle = \frac{2}{3}\,. \tag{4.19}$$

The average energy gain for the first-order Fermi mechanism is then given by

$$\xi = \left\langle\frac{\Delta E}{E}\right\rangle = \frac{1 + \frac{4}{3}\beta + \frac{4}{9}\beta^2}{1-\beta^2} - 1 \simeq \frac{4}{3}\beta\,. \tag{4.20}$$

We can see that the first-order Fermi mechanism leads to an average energy gain that is linear in the shock velocity β, and then more efficient than the scattering on random interstellar plasma clouds. This mechanism, also called *shock acceleration*, is characterized by a spectral index $\alpha \simeq 2$ for non-relativistic shocks and $\alpha \simeq 2.3$ for ultra-relativistic shocks [180].

4.1.2 Characterization of UHECR sources

The acceleration processes described above are based on the assumption that UHECRs are accelerated by electromagnetic mechanisms. However, for an acceleration process to be efficient, the particles must be confined within the accelerator site. The typical length scale for the characterization of the propagation of charged particles in a magnetic field is the Larmor radius r_L, which is given by

$$r_L \simeq 1.1 \left(\frac{E/Z}{1\,\text{EeV}}\right)\left(\frac{B}{1\,\mu\text{G}}\right)^{-1}\,\text{kpc}\,, \tag{4.21}$$

where E/Z is the particle rigidity and B is the magnetic field strength. If R is the typical size of the accelerator, then the condition $r_L \lesssim R$ must be satisfied. Given Eq. (4.21), we obtain the condition for the maximum acceleration energy as

$$E_{\max} \lesssim 1 \cdot Z \left(\frac{R}{1\,\text{kpc}}\right)\left(\frac{B}{1\,\mu\text{G}}\right)\,\text{EeV}\,. \tag{4.22}$$

The condition in Eq. (4.22) is known as the *Hillas criterion* [181] and it constrains the product $R{\cdot}B$ that characterizes the acceleration region. As expected, the Hillas criterion shows that heavy

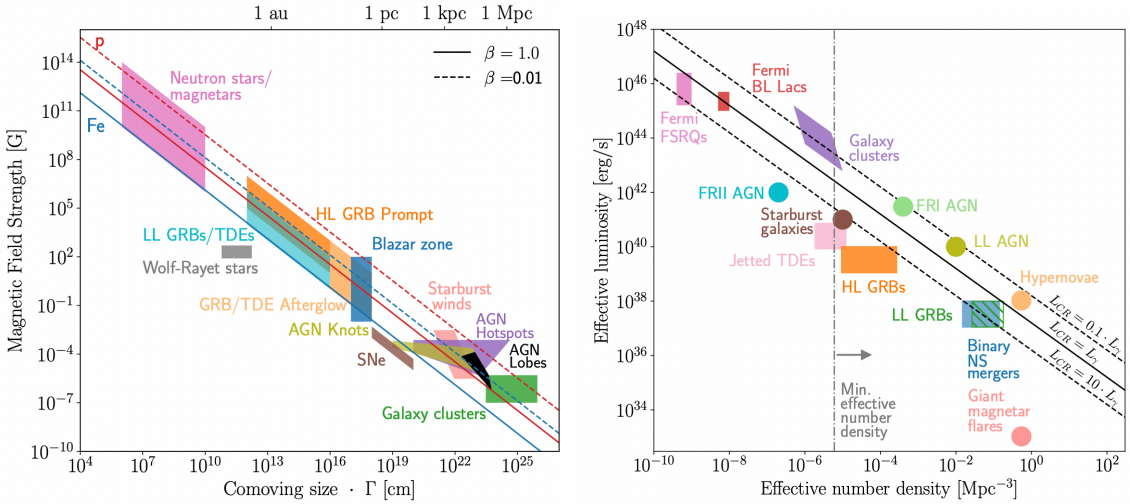

Figure 4.2: Left: Hillas diagram for several source classes as a function of their characteristic size and magnetic field strength. The condition in Eq. (4.23) for protons (red lines) and iron nuclei (blue lines) is shown for $E = 100\,\mathrm{EeV}$ and different values of β. Right: characteristic source luminosity as a function of the characteristic source number density for steady sources and the effective source luminosity as a function of the effective source number density for transient sources with $\tau \simeq 10^5\,\mathrm{yr}$. Different assumptions for the CR luminosity are shown (continuous and dashed lines). Figures taken from [94].

nuclei can be accelerated to higher energies than protons within the same source environment, due to the rigidity dependence, as already shown in Eq. (4.3). A more stringent condition is given by the *Lagage-Cesarsky limit* [182] of the Hillas criterion for shock accelerations. Given the shock velocity β, the Lagage-Cesarsky limit is given by

$$E_{\mathrm{max}} \lesssim 1 \cdot Z \cdot \beta \left(\frac{R}{1\,\mathrm{kpc}}\right)\left(\frac{B}{1\,\mu\mathrm{G}}\right)\,\mathrm{EeV}\,, \tag{4.23}$$

where for $\beta = 1$ it corresponds to the Hillas criterion. Inefficiency in the acceleration process and ultrarelativistic flow can also be taken into account by multiplying Eq. (4.23) by Γ/η, where Γ is the boost factor and $\eta \leq 1$ parameterizes the efficiency of the acceleration process [94, 97, 183, 184]. An example of Hillas diagram is shown in the left panel of Fig. 4.2 for protons and iron nuclei with energy $E = 100\,\mathrm{EeV}$ and different values of β and in the ideal limit $\eta = 1$. The classes of objects located to the left of the lines do not satisfy the acceleration criterion. As expected, for a lower value of β, a higher value of $R \cdot B$ is required to reach a given maximum energy.

The Hillas criterion (or equivalently one of the other formulations given above) is a necessary condition for the production of UHECRs, but it is not sufficient. Astrophysical sources must also be characterized by an energy budget capable of providing the observed UHECR flux. Given the observed cosmic ray emissivity $\mathcal{E}_{\mathrm{CR}}$ (i.e. the CR energy per unit of volume and unit of time), continuous sources with number density n_{S} and mean cosmic ray luminosity L_{CR} must be such that $\mathcal{E}_{\mathrm{CR}} \approx n_{\mathrm{S}} L_{\mathrm{CR}}$. In the case of transient sources, given the event density rate $\dot{n}_{\mathrm{S}}$ (i.e. the number of transient events per unit of volume and unit of time) and the average emitted cosmic ray energy E_{CR} per event, we obtain that $\mathcal{E}_{\mathrm{CR}} \approx \dot{n}_{\mathrm{S}} E_{\mathrm{CR}}$. In this case, an effective number

density can be defined such as $n_S^{\rm eff} \approx \dot{n}_S \tau$, where τ is the characteristic arrival time spread of the emitted UHECRs [97, 184]. We then have that $\mathcal{E}_{\rm CR} \approx n_S^{\rm eff} L_{\rm CR}^{\rm eff}$, where $L_{\rm CR}^{\rm eff} = E_{\rm CR}/\tau$ is the effective mean luminosity in cosmic rays. These conditions are shown in the right panel of Fig. 4.2 for several astrophysical sources, where it is assumed that the cosmic ray luminosity is proportional to the photon luminosity L_γ. As for the Hillas diagram, sources to the left of the lines do not provide enough power to produce UHECRs.

4.1.3 Source candidates

In Fig. 4.2, it is shown how several classes of astrophysical objects can satisfy the condition given by the Hillas criterion and the source energy budget. In the following, several classes of UHECR source candidates are presented in more detail.

Active Galactic Nuclei: AGNs consist of a supermassive black hole at the center of a Galaxy surrounded by an accretion disk. Sometimes, AGNs also present jets with lobes: these lobes can emit in the radio band, defining the classification in *radio loud* and *radio quiet* AGNs. Another historical classification of AGN was based on the observation of different frequency bands. However, this classification was unified in [185], where the viewing angle was identified as the cause of the different observed emissions. Thus, AGNs are called *blazars* when viewed in the direction of the jet, *radio galaxies* when viewed perpendicular to the jet, and *quasars* for the angles in between. AGNs have been suggested as possible UHECR sources, also because of the correlation with the Pierre Auger Observatory events in the early stages of the experiment [186]. UHECR acceleration is in principle possible both the AGN core and in the jets [187–191]. However, energy losses in the inner part of the core are expected to have an important effect, limiting the maximum acceleration energy. On the contrary, particle acceleration in the AGN jet, which can extend to ∼Mpc scales, is a promising mechanism for UHECR acceleration, especially in the case of blazars, where secondary messengers can also be produced [192].

Starburst Galaxies: SBGs are galaxies characterized by a high star formation rate up to $\sim 10^2\,{\rm M}_\odot\,{\rm yr}^{-1}$[3] [193], which corresponds to a high supernova rate [194–196]. The internal environment of SBGs is characterized by a particle number density above $10^2\,{\rm cm}^{-3}$ and a very strong infrared emission [196]. Since the interstellar environment of SBGs is perturbed by a strong magnetized wind with velocity up to thousands of km/s, UHECR acceleration up to very high energies may be possible in the SBG environment [197–199]. However, energy losses could still limit the acceleration efficiency also in the case of SBGs.

Gamma-ray Bursts: GRBs are the most powerful transient events in the Universe and consist of a very energetic burst of $\gamma-$rays in the MeV energy range, which can last from $\lesssim 1\,{\rm s}$ (short-GRBs) to $\gtrsim 1\,{\rm s}$ (long-GRBs). Phenomenologically, GRBs can be modelled as a relativistic expanding wind, and due to their very high luminosity they have been considered as a possible UHECR source since their first detection [200–204]. Due to the strong radiation field present in high-luminosity GRBs, low-luminosity GRBs would guarantee a higher survival rate of UHECR nuclei. Moreover, low-luminosity GRBs are also more numerous than the high-luminosity ones [205, 206]. However, neutrino production in GRBs could also limit the possibility of considering

[3]The quantity $M_\odot$ indicates the Solar mass and is equal to $M_\odot \simeq 2 \cdot 10^{30}\,{\rm kg}$ [9].

GRBs as UHECR sources.

Galaxy clusters: Galaxy clusters are the largest gravitationally bound structures in the Universe, with sizes up to $\sim 10\,\mathrm{Mpc}$ and magnetic field strengths of $\sim 1\,\mu\mathrm{G}$ [207]. Because of their large size, they may be able to confine CRs at the ultra-high energies. The extremely large structures could host several candidate source classes (e.g. AGNs), and due to the long residence time of UHECRs within the cluster, secondary particles may also be produced [208, 209].

Tidal Disruption Events: TDEs are transient events caused by the passage of a star very close to a supermassive black hole. The star is then disrupted by the tidal force of the black hole, producing debris that becomes part of the accretion disk [210]. TDEs have been proposed as possible sources of UHECRs [171, 183, 211–213]. However, given the low rate of TDEs, the relation between the radiative TDE luminosity and the UHECR luminosity is the main parameter to constrain the cosmic ray energy budget. TDEs have also recently been associated with observations of high-energy neutrinos [214, 215].

Compact objects: compact and extremely magnetized astrophysical objects, such as pulsars and magnetars, may be able to accelerate CRs to extremely high energies. Magnetars can reach magnetic field values of $\sim 10^{14}\,\mathrm{G}$ and rotation periods of $\sim 1\,\mu\mathrm{s}$ [207], inducing then strong electric fields. Since these objects are the result of the collapse of massive stars, heavy nuclei may also be present and accelerated [174]. All these properties make magnetized compact objects interesting candidates UHECR production [172, 175, 216].

4.2 Expanding Universe

UHECRs can travel cosmological distances ($\sim O(100\,\mathrm{Mpc})$) from their source to Earth. Therefore, describing their extragalactic propagation requires taking into account the properties of the Universe on such scales. The description of the Universe on cosmological scales is obtained starting from the *cosmological principle*: the spatial distribution of matter in the Universe is isotropic and homogeneous at cosmological distances.

Under the assumptions of the cosmological principle, the overall geometry and evolution of the Universe is described by the Friedmann-Lemaître-Robertson-Walker (FLRW) metric [217–220], where the Lorentz-invariant distance element ds^2 is given by[4]

$$ds^2 = dt^2 - R^2(t)\left[\frac{dr^2}{1-kr^2} + r^2\left(d\theta^2 + \sin^2\theta d\phi^2\right)\right], \tag{4.24}$$

where t is the cosmic time, (r, θ, ϕ) are comoving spherical coordinates (see Appendix A.1), $R(t) = R_0\, a(t)$ is the time-dependent scale factor, $a(t)$ is the dimensionless scale factor, and k is the curvature parameter, which can take the values $k = -1, 0, 1$. The scale factor is normalized to the present time t_0 so that the dimensionless scale factor is $a(t_0) = 1$ and $R(t_0) = R_0$. The value of the curvature parameter k defines the geometry of the Universe: $k = -1$ is a hyperbolic open Universe, $k = 0$ is a flat Universe and $k = 1$ is a spherical closed Universe. The FLRW metric in Eq. (4.24) represents the possible cases of maximally symmetric three-dimensional space.

[4] The convention $c = 1$ is used in this section.

The propagation of a light ray along the radial direction in the FLRW metric is such that $ds^2 = 0$, and then

$$dt = R_0 a(t) \frac{dr}{\sqrt{1-kr^2}} \,. \tag{4.25}$$

So if λ_0 is the wavelength of a photon at the time t_0, then the wavelength at a generic time t is given by

$$\lambda = \lambda_0 \, a(t) \,. \tag{4.26}$$

We can then define the *redshift* variable z so that

$$a(t) = \frac{1}{1+z} \qquad \Rightarrow \qquad \lambda = \frac{\lambda_0}{1+z} \,. \tag{4.27}$$

Eq. (4.27) can also be written as $z = (\lambda_0 - \lambda)/\lambda = \Delta\lambda/\lambda$. This last result is the first observation of the fact that the Universe is expanding. In 1929, E. Hubble observed that the wavelength of the light emitted by distant galaxies was shifted towards the red direction and that the shift $\Delta\lambda$ was proportional to the distance d of the source [221]. This result was interpreted in the terms of a Doppler effect [222]: this would correspond to a recession velocity v of all the galaxies such that

$$v = H_0 \cdot d \,, \tag{4.28}$$

where H_0 is the Hubble's constant. The relation in Eq. 4.28 is called *Hubble's law*. H_0 is often written as $H_0 = 100\, h \,\mathrm{km\,s^{-1}\,Mpc^{-1}}$, where $h \simeq 0.67$ is the dimensionless Hubble constant [9]. The modern interpretation of the Hubble's law is that the source distribution is static in time, but the scale factor $a(t)$ evolves to describe the expansion of the Universe. In particular, to account for the redshift effect described above, the scale factor $a(t)$ increases with time. The definition of the Hubble parameter can be obtained by considering two points, separated by a fixed comoving distance $R_0\, r$, moving away from each other at a velocity $v(t) = \dot{a}(t) R_0\, r = (\dot{a}(t)/a(t)) a(t) R_0\, r = H(t) r(t)$, where

$$H(t) = \frac{\dot{a}(t)}{a(t)} \,, \tag{4.29}$$

is the *Hubble rate*. The Hubble constant is given by the condition $H(t = t_0) = H_0$.

The evolution of the Universe, and hence of the scale factor $a(t)$, can be obtained by applying Einstein's field equations to the FLRW metric: the resulting equations are called the *Friedmann equations* [217, 223]. In particular, the Hubble rate is given by

$$H(z) = H_0 \, E(z) = H_0 \sqrt{\Omega_m (1+z)^3 + \Omega_r (1+z)^4 + \Omega_k (1+z)^2 + \Omega_\Lambda} \,, \tag{4.30}$$

where the dimensionless quantities Ω_i are given by the ratio of the corresponding energy densities ρ_i with the critical density $\rho_{c,0} = 3H_0^2/8\pi G$, where G is the Newtonian gravitational constant[5]. The values of the dimensionless densities are: $\Omega_m = 0.31$ for non-relativistic matter, $\Omega_r \sim 10^{-5}$ for relativistic matter (or radiation), $\Omega_\Lambda = 0.68$ for the dark energy and $\Omega_k \sim 0.001$ for the curvature energy density [9]. These quantities follow the summation rule $\Omega_m + \Omega_r + \Omega_\Lambda = 1 - \Omega_k$. The relation between the cosmic time t and the redshift parameter z is

$$\left(\frac{dt}{dz}\right)^{-1} = -(1+z) H(z) \,. \tag{4.31}$$

[5]The numerical value of the critical density is $\rho_{c,0} = 1.54 \cdot 10^4 \, h^2 \,\mathrm{eV\,cm^{-3}} = 4.96 \cdot 10^{65} \, h^2 \,\mathrm{erg\,Mpc^{-3}}$ [87].

The result in Eq. (4.26) can be applied to the energy of relativistic particles. If E_0 is the particle energy at present time t_0, then the energy at a given redshift z is $E(z) = E_0(1+z)$. We can then obtain the energy loss rate due to the expansion of the Universe (also called the *adiabatic* energy loss rate) by considering Eq. 4.31, i.e.

$$\beta_{\rm ad}(z) = \left(-\frac{1}{E}\frac{dE}{dt}\right)_{\rm ad} = H(z)\,. \tag{4.32}$$

The numerical value of the adiabatic energy loss length at $z = 0$ is $\beta_{\rm ad}^{-1} = H_0^{-1} \simeq 4\,{\rm Gpc}$. We will see that adiabatic losses are only important for low-energy UHECRs.

The fact that the Universe is expanding introduces some important new concepts, namely the definition of time and distance scales. From Eq. (4.31) it is possible to define the expansion age of the Universe at redshift z as

$$t(z) = \int_0^t d\tau = \int_z^{+\infty} \frac{dz'}{(1+z')H(z')}\,, \tag{4.33}$$

and then the age of the Universe t_0 is given by

$$t_0 = \int_0^{t_0} d\tau = \int_0^{+\infty} \frac{dz'}{(1+z')H(z')}\,, \tag{4.34}$$

which corresponds to $t_0 \simeq 13.8 \cdot 10^9\,{\rm yr}$ [9]. The maximum distance a particle can travel between the cosmic time t_1 and $t_2 > t_1$ is called *proper distance* $d_p(t_1, t_2)$ and it is given by the condition $ds^2 = 0$.

$$d_p(t_1, t_2) = \int_{t_1}^{t_2} \frac{d\tau}{a(\tau)} = R_0 \int_0^r \frac{dr'}{\sqrt{1-kr'^2}}\,, \tag{4.35}$$

where we have assumed that $r(t_1) = 0$ and $r(t_2) = r$. We can see that the proper distance depends on the value of k. In particular, we obtain that the proper distance depends on the coordinate distance r such that

$$r = S_k(d_p/R_0) = \begin{cases} \sin(d_p/R_0) & \text{for } k = 1 \\ d_p/R_0 & \text{for } k = 0 \\ \sinh(d_p/R_0) & \text{for } k = -1 \end{cases}\,. \tag{4.36}$$

Since no signal can travel faster than light, from Eq. (4.35) we can determine the *physical causal horizon*[6] $d_H(z)$ at redshift z as

$$d_H(z) = \int_0^t \frac{d\tau}{a(\tau)} = \int_z^{+\infty} \frac{dz'}{H(z')}\,, \tag{4.37}$$

which defines the distance beyond which events cannot be causally correlated.

In a static Universe, the distance of an astrophysical object is defined in terms of its intrinsic luminosity L and its apparent luminosity F (or flux) such that

$$F = \frac{L}{4\pi d_L^2} \quad \Rightarrow \quad d_L = \sqrt{\frac{L}{4\pi F}}\,, \tag{4.38}$$

[6] $d_H(z)$ is also called the *event horizon*.

where d_L is called *luminosity distance*. To derive the same quantity in an expanding Universe we can consider the FLRW metric and note that the solid angle element is $R^2(t)r^2\left(d\theta^2+\sin^2\theta d\phi^2\right)$. Thus, the area of the sphere surrounding a source at redshift z today is $4\pi R_0^2 r^2$. Since the photon energies and the time scales are redshifted, the apparent luminosity is given by

$$F=\frac{L}{(1+z)^2 4\pi R_0^2 r^2}\,, \tag{4.39}$$

from which we obtain the luminosity distance

$$d_L(z)=(1+z)R_0 r=(1+z)R_0 S_k(d_p/R_0)=(1+z)R_0 S_k\left[\frac{1}{R_0}\int_0^0\frac{dz'}{H(z')}\right]\,. \tag{4.40}$$

If we now consider an object with a comoving length scale l_0, its physical length scale at redshift z would be $l(z)=l_0/(1+z)$. It will therefore appear under the angle

$$\alpha=\frac{\lambda_0}{R_0 r}=\frac{l}{(1+z)R_0 r}\,. \tag{4.41}$$

We can then define the *angular diameter distance* $d_A(z)$ as

$$d_A(z)=\frac{l}{\alpha}=\frac{d_L(z)}{(1+z)^2}\,. \tag{4.42}$$

Finally, the comoving volume element in the FLRW metric can be written as

$$dV=\frac{R_0^3 r^r\,dr\,d\Omega}{\sqrt{1-kr^2}}=S_k^2\left[\frac{1}{R_0}\int_0^0\frac{dz'}{H(z')}\right]\frac{R_0^2 dz\,d\Omega}{H(z)}\,, \tag{4.43}$$

where $d\Omega=\sin\theta d\theta\,d\psi$ is the differential of the solid angle. The corresponding physical volume is given by the comoving volume divided by a factor $(1+z)^3$.

4.3 Photohadronic interactions

As anticipated in Chapter 2, the propagation of UHECRs in the extragalactic space is affected by stochastic interactions with background photon fields. These interactions will result in the reduction of the primary UHECR energy and the production of secondary particles, such as neutrinos and photons. If we consider the rest frame of the photon field, where a given photon has energy ε, the CR Lorentz factor is then Γ. We can now calculate the Lorentz boost of the photon energy in the CR rest frame as

$$\varepsilon'=\Gamma\varepsilon(1-\cos\theta)\,, \tag{4.44}$$

where θ is the angle between the CR and the photon momentum. We can see that, for a head-on collision $\theta=\pi$, the photon energy seen by the cosmic ray is $\varepsilon'=2\Gamma\varepsilon$. It is clear that also a microwave photon with energy $\varepsilon=1\,\mathrm{meV}$ in the reference frame of an UHECR with Lorentz factor $\Gamma=10^9$ will appear as a γ-ray with energy $\varepsilon'\simeq 1\,\mathrm{MeV}$.

The typical time scale of an interaction process is given by $\tau\simeq(n\sigma)^{-1}$, where n is the number density of the target particles and σ is the cross section of the interaction process. However, if

we consider that the target particles (in our case target photons) are characterized by a certain spectral energy density (SED), i.e. the number of photons per unit energy and per unit volume, the interaction rate τ^{-1} is given by

$$\tau^{-1}(\Gamma) = \frac{1}{2\Gamma^2} \int_{\varepsilon'_{\rm th}}^{+\infty} \sigma(\varepsilon')\varepsilon' \int_{\varepsilon'/2\Gamma}^{\infty} \frac{n(\varepsilon)}{\varepsilon^2}\, d\varepsilon\, d\varepsilon' \,, \tag{4.45}$$

where $\sigma(\varepsilon')$ and $\varepsilon'_{\rm th}$ are the cross section and the photon energy threshold of the considered process in the CR reference frame and $n(\varepsilon)$ is the photon SED in the laboratory frame. A full derivation of Eq. (4.45) is given in Appendix B.1.

The energy loss rate of a CR undergoing a given interaction process can be obtained by considering the average fraction of energy lost during an interaction. This quantity, called *inelasticity*, is given by

$$\nu(\varepsilon') = \left\langle \frac{E_{\rm in} - E_{\rm out}}{E_{\rm in}} \right\rangle = \frac{1}{\sigma(\varepsilon')} \int (1-x) \frac{d\sigma}{dx}\, dx \,, \tag{4.46}$$

where $E_{\rm in}$ and $E_{\rm out}$ are the cosmic ray energies before and after the interaction, $x = E_{\rm out}/E_{in}$ and $d\sigma/dx$ is the differential cross section [177]. The energy loss rate is then given by

$$-\frac{1}{E}\frac{dE}{dt} = \frac{1}{2\Gamma^2} \int_{\varepsilon'_{\rm th}}^{+\infty} \sigma(\varepsilon')\nu(\varepsilon')\varepsilon' \int_{\varepsilon'/2\Gamma}^{\infty} \frac{n(\varepsilon)}{\varepsilon^2}\, d\varepsilon\, d\varepsilon' \,, \tag{4.47}$$

The energy loss rate in Eq. (4.47) is often also written as

$$-\frac{1}{E}\frac{dE}{dt} = \beta_0(E) \,, \tag{4.48}$$

where the subscript 0 refers to the fact that these quantities are defined at redshift $z = 0$. From $\beta_0(E)$ the following quantity is also defined

$$b_0(E) = -\frac{dE}{dt} = E\,\beta_0(E) \,. \tag{4.49}$$

The next sections describe the cosmic photon fields relevant to the photohadronic interactions of UHECRs.

4.3.1 Cosmic photon fields

The state of the primordial Universe is described by a fully ionized plasma in which photons and electrons are strongly coupled. However, due to the cosmological expansion, the temperature of the Universe decreased over time, until it dropped below the hydrogen ionization energy of $\sim 13.6\,\text{eV}$. When the temperature dropped below $\sim 0.3\,\text{eV}$ ($\sim 3,000\,\text{K}$), electrons and protons recombined into hydrogen atoms and the Universe became transparent to photons[7]. This relic radiation, produced at redshift $z \simeq 1,100$ (or when the Universe was $380,000\,\text{yr}$ old) is still visible today as the Cosmic Microwave Background (CMB).

The CMB radiation was first measured in 1964 by A. A. Penzias and R. W. Wilson [12] as an isotropic background noise in their instrumentation, and then interpreted in [224]. Today we

[7] The recombination temperature is smaller than the hydrogen binding energy and it is given by the presence of enough photons with energy $> 13.6\,\text{eV}$ to reionize the plasma.

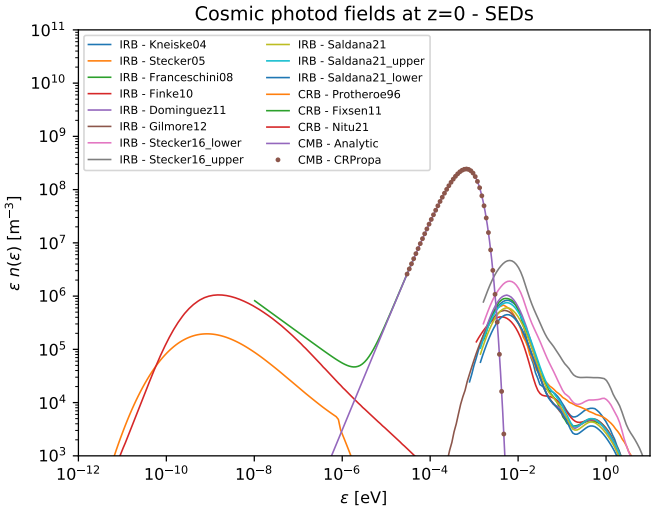

Figure 4.3: Spectral energy densities multiplied by the photon energy ε for the CMB, the EBL models from [225–232] and the CRB models from [233–235] at $z = 0$. The analytical form of the CMB spectral energy density from Eq. (4.50) is also shown for comparison. All the SEDs shown have been extracted from the simulation code `CRPropa` [236].

know that the CMB is the dominant radiation field present in the Universe, and it is described as a black-body photon field with the present temperature $T_{\rm CMB,0} = 2.725\,\mathrm{K}$ [9]. The spectral energy density of the CMB at $z = 0$ is given by

$$n_{\rm CMB}(\varepsilon) = \frac{1}{\pi^2}\frac{\varepsilon^2}{\exp(\varepsilon/k_B T_{\rm CMB,0}) - 1}\,, \tag{4.50}$$

where $k_B = 8.617 \cdot 10^{-5}\,\mathrm{eV\,K^{-1}}$ is the Boltzmann constant [9]. The CMB spectral energy density at $z = 0$ is shown in Fig. 4.3: we can see that the CMB radiation peaks at $\varepsilon \simeq 1\,\mathrm{meV}$.

The CMB temperature evolves with redshift as $T_{\rm CMB}(z) = (1+z)\cdot T_{\rm CMB,0}$, and since this photon field receives no feedback from astrophysical sources, the cosmological evolution of the SED is given by

$$n_{\rm CMB}(\varepsilon, z) = (1+z)^2 n_{\rm CMB}\left(\frac{\varepsilon}{1+z}\right)\,, \tag{4.51}$$

where $n_{\rm CMB}(\varepsilon/(1+z))$ is the SED at the present time and the prefactor $(1+z)^2$ is due to the combination of the volume evolution factor $(1+z)^3$ and the energy redshift factor $(1+z)^{-1}$. We can then obtain the CMB number density as

$$\begin{aligned} n_{\rm CMB}(z) &= \int_0^{+\infty} n_{\rm CMB}(\varepsilon, z)\, d\varepsilon = \frac{(1+z)^3 (k_B T_{\rm CMB,0})^3}{\pi^2}\int_0^{+\infty}\frac{x^2}{e^x - 1}\,dx \\ &= (1+z)^3 (k_B T_{\rm CMB,0})^3 \frac{2\zeta(3)}{\pi^2} = (1+z)^3 n_{\rm CMB,0}\,, \end{aligned} \tag{4.52}$$

where $\zeta(3) = 1.20$ is the Riemann zeta function and $n_{\rm CMB,0} = 2\zeta(3)(k_B T_{\rm CMB,0})^3/\pi^2 \simeq 400\,\mathrm{cm^{-3}}$ is the CMB number density at $z = 0$. Similarly, the energy density of the CMB radiation is

given by

$$\rho_{\rm CMB}(z) = \int_0^{+\infty} \varepsilon n_{\rm CMB}(\varepsilon, z)\, d\varepsilon = \frac{(1+z)^4 (k_B T_{\rm CMB,0})^4}{\pi^2} \int_0^{+\infty} \frac{x^3}{e^x - 1}\, dx$$
$$= (1+z)^4 (k_B T_{\rm CMB,0})^4 \frac{\pi^2}{15} = (1+z)^4 \rho_{\rm CMB,0}\,, \tag{4.53}$$

where $\rho_{\rm CMB,0} = \pi^2 (k_B T_{\rm CMB,0})^4/\pi^2 \simeq 0.26\,{\rm eV\,cm^{-3}}$ is the energy density at $z = 0$. Given the simple cosmological evolution of the CMB field, we can immediately see that the interaction rate in Eq. (4.45) and the energy loss rate in Eq. (4.47) at a given redshift z are given by

$$\tau^{-1}(\Gamma, z) = (1+z)^3 \tau^{-1}((1+z)\Gamma)\,, \tag{4.54}$$
$$\beta(E, z) = (1+z)^3 \beta_0((1+z)E)\,. \tag{4.55}$$

Another important background photon field for UHECRs is the Extragalactic Background Light (EBL): this radiation field is composed of photons from infrared to ultraviolet wavelengths emitted by astrophysical objects [13, 237]. The EBL is divided into two components: the Infrared Background (IRB), which peaks at $\simeq 10\,{\rm meV}$, and the Cosmic Optical Background (COB), which peaks at 1 eV. The COB peak is due to the direct emission from stars and galaxies, while the IRB peak is due to the absorption and re-emission of radiation by the interstellar dust. Since the number density at the peak of the IRB is about 100 greater than the number density at the peak of the COB [237], the IRB is the most relevant for UHECR propagation and it is often used as representative of the EBL. The cosmological evolution of this photon field is not as trivial as that of the CMB, since it depends on the evolution of source luminosities and dust emission. However, the cosmological expansion of the Universe still affects the EBL, and for this reason the SED can be written as

$$n_{\rm EBL}(\varepsilon, z) = (1+z)^2 n_{\rm EBL}\left(\frac{\varepsilon}{1+z}, z\right)\,, \tag{4.56}$$

where the term $n_{\rm EBL}(\varepsilon/(1+z), z)$ contains the information about the cosmological evolution of the emission. Several EBL models can be found in the literature: in Fig. 4.3 the SEDs of the EBL models from [225–232] are shown.

The last background field presented is the Cosmic Radio Background (CRB), which is mostly produced by radio galaxies. The CRBs from [233–235] are also shown in Fig. 4.3.

4.3.2 Electron-positron pair production

The first photohadronic interaction between UHECRs and cosmic photon fields is the production of electron-positron pairs (also called Bethe-Heitler pair production [238, 239]). Given a CR nucleus (A, Z) and a background photon $\gamma_{\rm bg}$, the reaction is given by

$$(A, Z) + \gamma_{\rm bg} \to (A, Z) + e^+ + e^-\,, \tag{4.57}$$

and the CR energy threshold can be calculated as

$$E_{\rm th} = \frac{m_e(m + m_e)}{\varepsilon} \simeq 5 \cdot 10^{17} A \left(\frac{\varepsilon}{1\,{\rm meV}}\right)^{-1} {\rm eV}\,, \tag{4.58}$$

where m_e is the electron mass, $m \simeq A m_p$ is the CR mass, m_p is the proton mass, ε is the energy of the background photon and we have assumed a head-on collision. If we consider a CMB photon with a typical energy of $\sim 1\,\mathrm{meV}$, we obtain that $E_{\rm th}/A \sim 5 \cdot 10^{17}\,\mathrm{eV}$, or $\Gamma_{\rm th} \sim 10^9$. The same calculation with EBL photons of energy $\sim 10\,\mathrm{meV}$ corresponds to $\Gamma_{\rm th} \sim 10^8$. However, at this low Lorentz factor, the energy loss due to pair production with EBL photons is negligible, since adiabatic losses dominate [240].

The inelasticity of electron-positron pair production at the threshold is given by $\nu_{\rm th} = 2m_e/(m_p + 2m_e) \simeq 10^{-3}$ for protons, and it decreases at higher energies [241]. For this reason this process is often approximated as a continuous energy loss. The parameterization of the energy loss of pair production with CMB photons is given by

$$-\frac{dE}{dt} = \frac{3\alpha_{\rm em} Z^2 \sigma_{\rm T} (m_e k_{\rm B} T)^2}{(2\pi)^3} f(\Gamma)\,, \tag{4.59}$$

where $\alpha_{\rm em}$ is the fine structure constant, $\sigma_{\rm T} \simeq 0.7 \cdot 10^{-24}\,\mathrm{cm}^2$ is the Thomson cross section and $f(\Gamma)$ is a function of the nucleus Lorentz factor [239]. Given the scaling of the inelasticity of CR nuclei $\nu_A = \nu_p/A$, the energy loss rate at zero redshift is such that

$$\beta_0^A(E) = \frac{Z^2}{A}\beta_0^p(E)\,, \tag{4.60}$$

where $\beta_0^p(E)$ is the energy loss rate for protons at $z = 0$. For the redshift dependence, Eq. (4.54) can be used.

4.3.3 Photopion production

Another interaction process between cosmic background photons and UHECRs is the production of pions

$$(A, Z) + \gamma_{\rm bg} \to (A, Z) + \pi\,, \tag{4.61}$$

where the number of pions produced depends on the center of mass energy of the process. The energy threshold in a head-on collision for single pion production is given by

$$E_{\rm th} = \frac{m_\pi(m + 2m_\pi)}{4\varepsilon} = 3.5 \cdot 10^{19} A \left(\frac{\varepsilon}{1\,\mathrm{meV}}\right)^{-1} \mathrm{eV}\,, \tag{4.62}$$

where $m_\pi \simeq 140\,\mathrm{MeV}$ is the pion mass [9]. We can see that pion production is a very important process in the propagation of cosmic rays with energies above $\sim 10\,\mathrm{EeV}$. The influence of photopion production between UHECRs and CMB photons was predicted in the 1960s in the context of the so-called GZK effect [14, 15]. In the case of nucleons, photopion production is given by

$$p + \gamma_{\rm bg} \to p + \pi^0 \quad , \quad n + \gamma_{\rm bg} \to n + \pi^0 \tag{4.63}$$

$$p + \gamma_{\rm bg} \to n + \pi^+ \quad , \quad n + \gamma_{\rm bg} \to p + \pi^-\,. \tag{4.64}$$

We can see that the production of pions in the extragalactic propagation of UHECRs also corresponds to the production of secondary particles as decay products of the pions (see Sec. 2.2). These particles produced during the extragalactic propagation are often called *cosmogenic*. Cosmogenic neutrinos typically have the $\simeq 5\%$ of the energy of the primary nucleon, while cosmogenic photons have $\simeq 10\%$ of the energy of the primary nucleon [242].

Photopion production involves both electromagnetic and strong interactions. In the reference frame of a CR nucleon, the threshold photon energy is $\varepsilon' \sim 150\,\mathrm{MeV}$ and the first (and most important) peak in the cross section is at $\varepsilon' \sim 350\,\mathrm{MeV}$ with a value of $\sigma \sim 600\,\mu\mathrm{b}$[8] [176, 243]. This peak corresponds to the production of the Δ^+ resonance, which subsequently decays with the emission of a pion. With increasing energy, the cross section converges to the almost energy independent values of $\sigma \sim 150\,\mu\mathrm{b}$, in the multi-pion production regime. The inelasticity of pion production at the threshold energy is $\sim 20\%$, but it increases with energy up to almost $\sim 50\%$ [87].

Since the photon energy involved in pion production in the reference frame of a nucleus is much larger than the binding energy, the process can be described within the superposition model. In this case, a nucleus (A, Z) with energy E is equivalent to Z protons and $A - Z$ neutrons with energy E/A. Therefore, the inelasticity also scales as $\nu_A = \nu_p/A$ and we can write the energy loss rate at zero redshift as

$$\beta_0^A(E) = \frac{Z}{A}\beta_0^p(E) + \frac{A-Z}{Z}\beta_0^n(E)\,, \tag{4.65}$$

where $\beta_0^n(E)$ is the energy loss rate for neutrons.

4.3.4 Photodisintegration

The last important process in the propagation of ultra-high-energy nuclei is photodisintegration, which consists of the emission of one or more nuclear fragments (which can be both nucleons and light nuclei). The photodisintegration process for a nucleus (A, Z) can be written as

$$(A, Z) + \gamma_{\mathrm{bg}} \to (A - n, Z - n') + nN\,, \tag{4.66}$$

where n is the number of emitted nucleons N and n' is the number of emitted protons. Since the recoil energy of the nucleus in its rest frame is negligible compared to the rest mass, the Lorentz factor of the nuclei involved is conserved.

Nuclei are complex objects and the emission of nucleons per photodisintegration depends on the energy of the absorbed photon [244, 245]. In particular, photodisintegration becomes relevant for photon energies $\varepsilon' \gtrsim 8\,\mathrm{MeV}$ in the nucleus rest frame. In the low-energy regime, $\varepsilon' \lesssim 30\,\mathrm{MeV}$, the leading process is given by the emission of one or two nucleons. This regime is also called the *Giant Dipole Resonance* (GDR) [246] which can be interpreted as the global vibration of protons and nucleons due to the absorption of the radiation, resulting in resonant states. For $30\,\mathrm{MeV} \lesssim \varepsilon' \lesssim 150\,\mathrm{MeV}$, photons interact with nucleon pairs: this regime is called the *quasi-deuteron* regime [247] where multiple nucleons and light nuclear fragments can be emitted. Above 150 MeV the photoproduction of mesons (such as pions) begins to dominate over photodisintegration.

Since photodisintegration is only relevant for $\varepsilon' \lesssim 150\,\mathrm{MeV}$, we obtain that nuclei with Lorentz factor $\Gamma \lesssim 10^{10}$ (see Eq. (4.44)) will undergo photodisintegration with CMB photons. Interestingly, if we consider that EBL photons have energies $10^{-2}\,\mathrm{eV} \lesssim \varepsilon \lesssim 1\,\mathrm{eV}$, we obtain that nuclei with Lorentz factor $10^7 \lesssim \Gamma \lesssim 10^9$ will photodisintegrate due to the interaction with EBL photons.

[8] A *barn* (b) is a metric unit of area and it is equal to $10^{-24}\,\mathrm{cm}^2$.

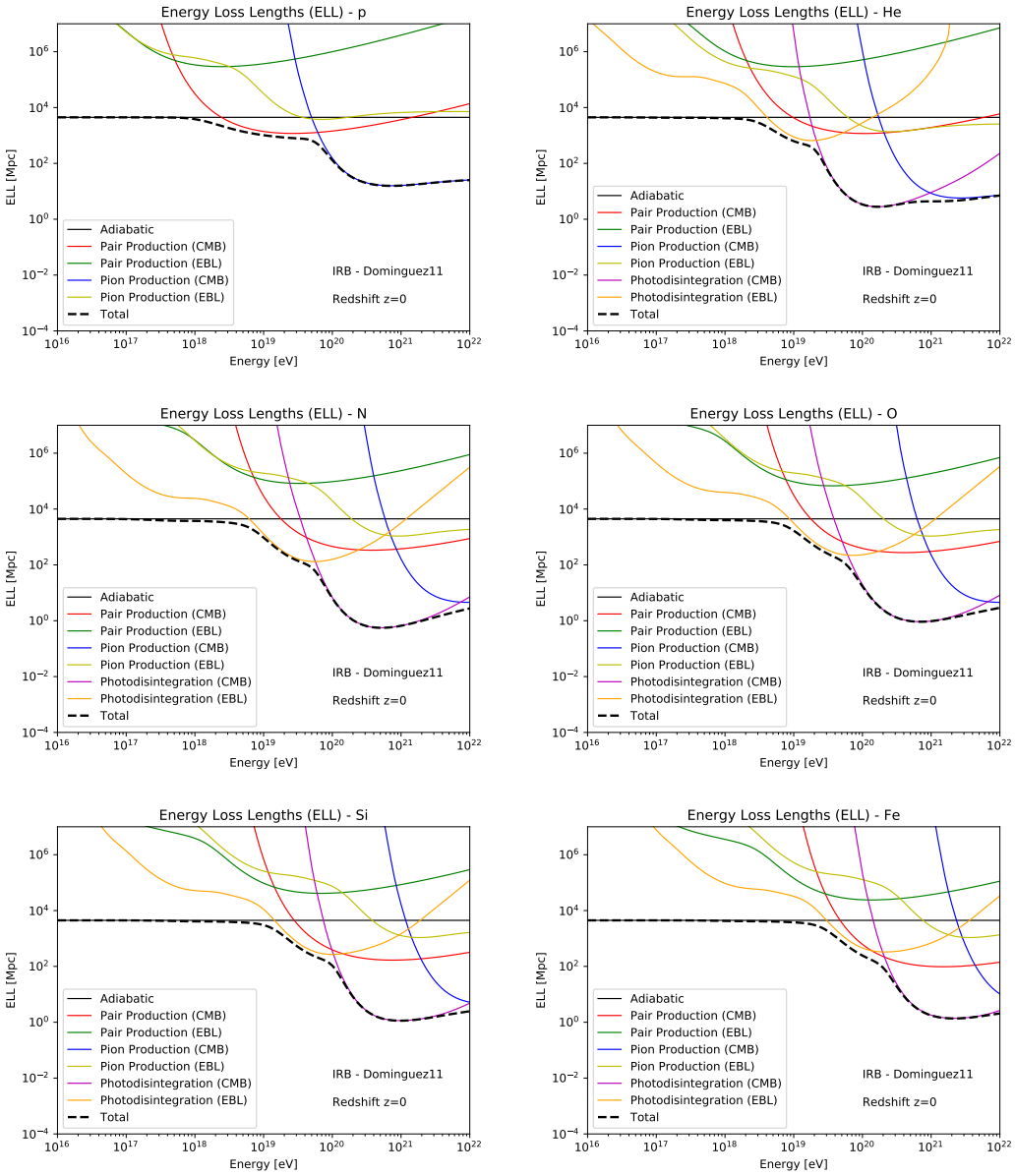

Figure 4.4: Energy loss lengths for p, ^{4}He, ^{14}N, ^{16}O, ^{28}Si and ^{56}Fe nuclei for the interaction with CMB and EBL photons from [229] at $z = 0$. Different energy loss processes are shown in different colors. The thick dashed black line represents the total energy loss length. All the energy loss length values have been obtained with the simulation code `CRPropa` [236].

4.3.5 Nuclear decay

Given the processes described above, unstable nuclei can also be produced during UHECR propagation. Since nuclear decay can change both the energy and mass of a nucleus, it must be taken into account when studying the path of cosmic rays from their sources to the Earth. However, given the extremely high energies involved, time dilation plays an important role. In particular,

if τ is the proper lifetime of an unstable nucleus with Lorentz factor Γ, then the mean free path that the nucleus will travel before decaying is given by $\lambda = \Gamma\tau$.

4.3.6 General discussion

As we have discussed above, the observed UHECR energy spectrum is given by the injected spectrum from cosmic ray sources, modified by the presence of adiabatic and stochastic energy losses during the propagation. In particular, the presence of interactions with background photon fields leads to changes in the slope of the energy spectrum. In Fig. 4.4, the different contributions to the total energy loss length are shown for different nuclei at $z = 0$. In all the panels, the thick dashed black line indicates the total energy loss length when adiabatic losses and interactions with CMB and EBL photons from [229] are taken into account.

In the top left panel of Fig. 4.4, the proton case is shown. We can immediately see two main facts: protons only interact with CMB photons, and when their energy is below 1 EeV only the expansion of the Universe affects their propagation. This last point is particularly important: from Eq. (4.32) we can see that the adiabatic energy loss length does not depend on the proton energy, and this means that the observed spectrum $\lesssim 1$ EeV has the same shape as the injected spectrum. The energy loss for protons with energy $1\,\text{EeV} \lesssim E \lesssim 50\,\text{EeV}$ is dominated by electron-positron pair production, while above $\simeq 50$ EeV photopion production is the main energy loss mechanism. We can see how the interactions introduce a maximum horizon for the sources: for $E \gtrsim 1$ EeV pair production sets a horizon of $\simeq 4$ Gpc, while at the highest energies ($E \gtrsim 100$ EeV) only sources at a distance of $\lesssim 100$ Mpc can contribute to the proton flux.

The signatures of photohadronic interactions in the propagated proton spectrum has been extensively discussed in [102, 103, 241, 248]. At the highest energies, the GZK cutoff introduces a strong suppression of the proton spectrum above $\simeq 50$ EeV. The spectral shape of the cutoff depends on the astrophysical model considered (spectral index at the acceleration, typical source separation distance, redshift evolution of the sources, and maximum acceleration energy). It is important to note that the high-energy suppression could also be mimicked by a maximum energy value at the acceleration. In the propagated spectrum from single sources, protons undergoing photopion production accumulate at energies just below the GZK cutoff, producing a *bump* in the spectrum. However, since sources at different distances produce bumps at different energies, this feature is smoothed out in the diffuse energy spectrum. Finally, in the energy range where pair production dominates, a *dip* in the proton spectrum is obtained, independent of the details of the astrophysical model. In this scenario, the ankle in the cosmic ray spectrum (see Sec. 2.3) can be associated with the dip produced by pair production. However, this scenario is in tension with the observed UHECR composition [154] and with limits on the cosmogenic neutrino flux [249].

The signature of photohadronic interactions in the energy spectrum of cosmic ray nuclei is substantially different from that of the proton case [240, 241, 250]. As we can see in Fig. 4.4, adiabatic losses become dominant for $E \lesssim 1 - 10$ EeV, depending on the nuclear species. In addition, photodisintegration completely dominates the total energy loss length at high energies. In contrast to proton propagation, pair production is negligible for nuclei, and photopion only becomes relevant above $10^3 - 10^4$ EeV. Interestingly, photodisintegration due to EBL photons is a dominant process in the propagation of nuclei for $10\,\text{EeV} \lesssim E \lesssim 100\,\text{EeV}$, while photodisintegration due to CMB photons dominates at higher energies. Similar to protons, heavy nuclei

are also characterized by an interaction horizon which can go down to $\simeq 1\,\mathrm{Mpc}$ in the case of N nuclei. We can also see that the smallest horizon is given by intermediate atomic masses, while heavy nuclei such as silicon and iron have larger energy loss lengths.

Since pair production is negligible in the propagation of nuclei, the interpretation of the ankle in the cosmic ray spectrum requires a different explanation when nuclei are accelerated by UHECR sources. It has been suggested in the past that the ankle feature indicates the transition between galactic and extragalactic CRs. However, this scenario requires a light cosmic ray component of galactic origin just below the ankle energy, which is disfavoured by the anisotropy measurements. An additional light extragalactic component around the ankle energy and a mixed composition component above the second knee have been proposed in several models [104, 251–254] in order to fully reproduce the observed UHECR energy spectrum.

4.4 Interactions of electromagnetic particles

In Sec. 4.3, we have seen that the presence of cosmic photon fields plays a fundamental role in describing the extragalactic propagation of UHECRs. We have also seen that photohadronic processes such as the photopion production of neutral pions and the nuclear decay of unstable isotopes during the UHECR propagation can be natural sources of very-high-energy gamma rays (VHEGRs). These energetic photons can also be produced directly in the environment of CR sources via photohadronic or hadron-hadron interactions. Unlike cosmic rays, photons are not deflected by magnetic fields, which makes it much easier to identify their sources. However, photons can also interact with background photon fields, producing secondary leptons, such as electrons and positrons, and initiating an electromagnetic cascade. Moreover, these charged leptons can be deflected by magnetic fields, changing the geometry of the cascade. It is then clear that even if VHEGRs can potentially carry with them further information about both the extragalactic space and the local environment of astrophysical objects, their propagation in highly non-trivial and requires taking into account several effects.

The same formalism discussed for photohadronic interactions can also be used for the interaction of VHEGRs with cosmic photon fields, with the only difference that the projectile particles are now also photons. We first consider the production of an electron-positron pair (simply called pair production or Breit–Wheeler process [255]). Given the VHEGR γ and a background photon γ_{bg}, the process is given by

$$\gamma + \gamma_{\mathrm{bg}} \to e^+ + e^- \,, \tag{4.67}$$

where the photon energy threshold is given by

$$E_{\mathrm{th}} = \frac{m_e^2}{\varepsilon} \,, \tag{4.68}$$

which corresponds to $E_{\mathrm{th}} \simeq 200\,\mathrm{TeV}$ with CMB photons of energy $\varepsilon \simeq 1\,\mathrm{meV}$, and to $E_{\mathrm{th}} \simeq 200\,\mathrm{GeV}$ with EBL photons of energy $\varepsilon \simeq 1\,\mathrm{eV}$. The total cross section for pair production is given by [256]

$$\sigma_{\mathrm{PP}} = \frac{3\sigma_{\mathrm{T}}}{16}\left(1-\beta^2\right)\left[\left(3-\beta^4\right)\ln\left(\frac{1+\beta}{1-\beta}\right) - 2\beta\left(2-\beta^2\right)\right] \,, \tag{4.69}$$

where $\beta = \sqrt{1-4m_e^2/s}$ is the velocity of the outgoing electron in the center of mass frame and s is the squared center of mass energy. In the high-energy limit $s \gg m_e^2$, the cross section

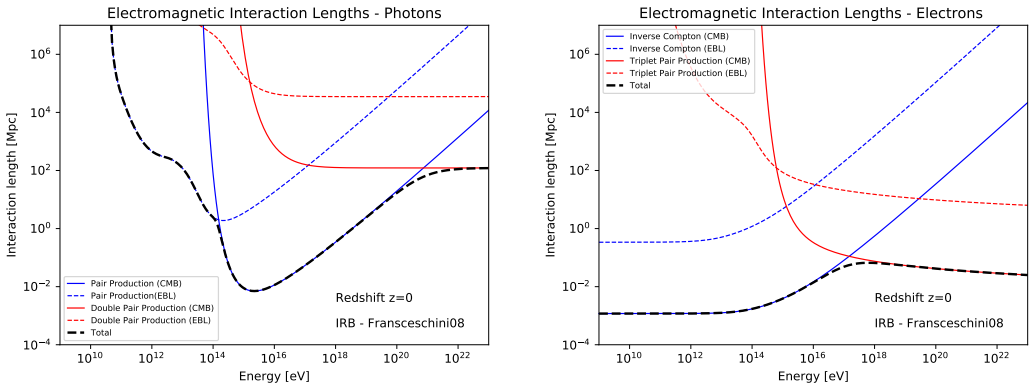

Figure 4.5: Left: interaction lengths for photons interacting with CMB (continuous lines) and EBL (dashed lines) photons from [227] at $z = 0$. Different processes are represented by different colors. The thick dashed black line represents the total interaction length. Right: same as left panel, but for electrons and positrons. All the interaction length values have been obtained with the simulation code `CRPropa` [236].

converges to

$$\sigma_{\rm KS} \simeq \frac{3\sigma_{\rm T}}{2}\frac{m_e^2}{s}\ln\left(\frac{s}{2m_e^2}\right) , \tag{4.70}$$

where $\sigma_{\rm KS}$ is also known as *Klein-Nishina limit* [257]. In the low-energy limit $s - m_e^2 \ll m_e^2$ (also called *Thomson limit*, where $\beta \ll 1$) the cross section in Eq. (4.69) becomes proportional to β. At even higher photon energies, higher order processes, with more than two particles in the final state, start to become relevant. The first higher order process is double pair production and it is given by

$$\gamma + \gamma_{\rm bg} \to e^+ + e^- + e^+ + e^- , \tag{4.71}$$

where the energy threshold is given by $E_{\rm th} = 4m_e^2/\varepsilon$. The cross section of double pair production quickly approaches the value $\sigma_{\rm DPP} \simeq 172\alpha_{\rm em}^4/36\pi m_e^2 \simeq 6.5\,\mu$b [87, 256].

The interaction lengths of VHEGRs for pair and double pair production with CMB and EBL photons from [227] are shown in the left panel of Fig. 4.5. We can see that the propagation of photons with energy $\lesssim 100$ TeV is only affected by pair production with EBL photons on distance scales of $\gtrsim 1$ Mpc. At photon energies $\simeq 1$ PeV, pair production with CMB photons becomes the most relevant process, and it corresponds to the strongest limit of the propagation distance at $\lesssim 10$ kpc. We can see that double pair production becomes dominant only at very high energies, i.e. $E \gtrsim 10^3$ EeV.

The propagation of the electrons and positrons produced in VHEGR interactions is also affected by the presence of photon fields. High-energy electrons (and positrons) can up-scatter background photons in what is known as inverse Compton scattering[9], in the process

$$e^\pm + \gamma_{\rm bg} \to e^\pm + \gamma\,. \tag{4.72}$$

[9]It is interesting to note that although inverse Compton scattering is called differently from the ordinary Compton scattering [258], it is essentially the same process. The only difference is that in the Compton scattering the electrons are the the target particles of the process, whereas in the inverse Compton scattering the target particles are background photons.

In the right panel of Fig. 4.5, the interaction lengths for inverse Compton scattering are shown for different background photon fields. We can see that for electrons with energy $E \lesssim 100\,\mathrm{PeV}$ the only relevant process is inverse Compton scattering with CMB photons. Furthermore, below 100 TeV the inverse Compton interaction length is approximately constant at the value $\lambda_{\mathrm{IC}} \simeq 1\,\mathrm{kpc}$. In the Thomson regime $s - m_e^2 \ll m_e^2$, valid for electron energies $E \lesssim 1\,\mathrm{PeV}$, the energy of the up-scattered photon is given by

$$\varepsilon_{\mathrm{up}} \simeq \frac{4\varepsilon E_e^2}{3m_e^2} \simeq 1.0 \left(\frac{\varepsilon}{1\,\mathrm{meV}}\right)\left(\frac{E}{10\,\mathrm{TeV}}\right)^2 \mathrm{TeV}\,, \tag{4.73}$$

which is the average energy lost by the electrons. Therefore, the energy loss length of inverse Compton scattering in the Thomson regime with CMB photons is given by [87, 259, 260]

$$\left(-\frac{1}{E}\frac{dE}{dx}\right)^{-1}_{\mathrm{IC}} \simeq 400 \cdot \left(\frac{E}{10^3\,\mathrm{TeV}}\right)^{-1} \mathrm{pc}\,. \tag{4.74}$$

For electrons and positrons, the first relevant high order process is the triplet pair production and it is given by

$$e^{\pm} + \gamma_{\mathrm{bg}} \to e^{\pm} + e^{+} + e^{-}\,. \tag{4.75}$$

In the right panel of Fig. 4.5, we can see that the only relevant background field for triplet pair production is again the CMB, and this process starts to become a relevant energy loss mechanism for electron and positron only above 10 EeV.

We can now consider the chain of reactions produced by all the processes described above. If we consider an astrophysical source of photons with an energy of $\sim$ TeV, we can see from Eq. (4.68) that these photons will interact with EBL photons, producing pairs of electrons and positrons. Since we are in the Klein-Nishina regime $s \gg m_e^2$, most of the energy of the primary photon will be carried by the produced leptons. At this point, electrons and positrons will interact with the CMB up-scattering background low-energy photons to high-energy γ-rays (see Eq. (4.73)). This cycle will then start again until the point where photons have an energy below the pair production threshold. Therefore, similar to what we discussed in Sec. 2.2.1, this chain of interactions takes the name of *electromagnetic cascade*. Two important consequences of electromagnetic cascades are: the low-energy part ($E \lesssim 100\,\mathrm{GeV}$) of the energy spectrum of TeV γ-ray sources can also be populated by secondary photons produced during the propagation of the primary γ-rays. The second consequence is that the penetration depth of the electromagnetic cascade is much larger than the interaction length of the primary photons.

In this discussion of the interaction of electromagnetic particles, we have neglected the fact that particles heavier than electrons, such as muons, tauons, pions or nuclei, could also be produced. The reason for this simplification is that the energy threshold in Eq. (4.68) grows with the square of the mass of the particles produced and the cross section is reduced by the same amount. Similarly, the contributions from other processes such as double Compton scattering or $\gamma\gamma$ scattering are also negligible [87, 256].

4.5 Propagation in magnetic fields

UHECRs are mostly electrically charged particles and they are deflected when propagating in a magnetic field. The propagation of an electric charge in a magnetic field $\mathbf{B}$ is described by the

Lorentz force in Eq. (4.1). If we consider a uniform magnetic field $\mathbf{B}_0$, the component $\mathbf{p}_\perp$ of the particle momentum perpendicular to $\mathbf{B}_0$ will gyrate around the field line with the angular frequency given by

$$\omega_g = \frac{|q|B_0}{E}\,, \tag{4.76}$$

where q is the electric charge and E is the energy of the particle and $B_0 = |\mathbf{B}_0|$. The gyration radius of the particle, also known as the *Larmor radius*, is then given by

$$r_L = \frac{|\boldsymbol{\beta}_\perp|}{\omega_g} = \frac{|\mathbf{p}_\perp|}{E\,\omega_g} = \frac{|\mathbf{p}_\perp|}{|q|B_0}\,. \tag{4.77}$$

As already discussed, the propagation depends only on the rigidity of the particle , and in particular on its transverse component with respect to the magnetic field vector. The parallel component $\mathbf{p}_\parallel$ is conserved and the motion is linear. If we consider a particle of energy E and charge number Z propagating in a magnetic field with root-mean-square strength $B_{\rm rms}$[10], we can write Eq. (4.77) in the ultra-relativistic limit as

$$r_L \simeq 1.1 \left(\frac{E/Z}{1\,\mathrm{PeV}}\right)\left(\frac{B_{\rm rms}}{1\,\mu\mathrm{G}}\right)^{-1} \mathrm{pc}\,, \tag{4.78}$$

where we have used that $|\mathbf{p}| = p \simeq E$.

The propagation of UHECRs in a generic magnetic field depends strongly on the details of the field spatial structure, and in particular on its irregularities. The type of propagation of a charged particle can be studied by considering the ratio of the spatial size of the field irregularities with the Larmor radius of the particle. If the Larmor radius is much larger than the spatial size of the magnetic field irregularities, then the nucleus will continue to gyrate around the mean magnetic field line as if there were no irregularities. In the opposite case, the propagation will be sensible to the field line of the irregularity. If we consider a statistically uniform turbulent magnetic field with root-mean-square strength $B_{\rm rms}$ and coherence length λ_c[11], we can define the critical energy E_c as the energy at which $r_L \simeq \lambda_c$. The critical energy is then given by

$$E_c \simeq 1 \cdot Z \left(\frac{\lambda_c}{1\,\mathrm{Mpc}}\right)\left(\frac{B_{\rm rms}}{1\,\mathrm{nG}}\right) \mathrm{EeV}\,. \tag{4.79}$$

For $E < E_c$ (and then $r_L < \lambda_c$), cosmic rays can resolve the structure of the magnetic turbulence and their propagation is characterized by scattering on the field components. In this case, the propagation is called *resonant diffusion* and it is possible to define the *diffusion length* λ_D as the distance corresponding to a deflection of 1 rad. The diffusion length is such that $\lambda_D \simeq \lambda_c (E/E_c)^\alpha$, where the index α depends on the magnetic field spectrum [261–265].

In the case of $E > E_c$ (and then $r_L > \lambda_c$) the propagation is characterized by small deflections $\delta\theta \simeq \lambda_c/r_g$ in a magnetic domain of size λ_c. The total deflection angle over a distance d is given by the accumulation of $\delta\theta$ over several magnetic domains. We have that $\theta_{\rm rms} \simeq \sqrt{N}\delta\theta$ where $N = d/\lambda_c$ and it corresponds to [266]

$$\theta_{\rm rms} \simeq 0.8^\circ \cdot Z \left(\frac{E}{100\,\mathrm{EeV}}\right)^{-1}\left(\frac{d}{10\,\mathrm{Mpc}}\right)^{1/2}\left(\frac{\lambda_{\rm c}}{1\,\mathrm{Mpc}}\right)^{1/2}\left(\frac{B_{\rm rms}}{1\,\mathrm{nG}}\right)\,. \tag{4.80}$$

[10] The root-mean-square strength of a magnetic field is defined as $B_{\rm rms} = \sqrt{\langle|\mathbf{B}|^2\rangle}$, where $\langle ...\rangle$ denotes the spatial average of the field strength $|\mathbf{B}|^2$.

[11] The coherence length of the magnetic field is the typical distance over which the magnetic field maintains the same structure, i.e. the typical distance over which the magnetic field does not fluctuate.

We can also obtain the diffusion length by considering the condition $\theta_{\rm rms} = 1\,{\rm rad}$, and it corresponds to $\lambda_D \simeq \lambda_c (E/E_c)^2$. The corresponding time delay due to the magnetic deflection is given by [267]

$$\tau \simeq 1.5 \cdot 10^3 Z^2 \left(\frac{E}{100\,{\rm EeV}}\right)^{-2} \left(\frac{d}{10\,{\rm Mpc}}\right)^2 \left(\frac{\lambda_{\rm c}}{1\,{\rm Mpc}}\right) \left(\frac{B_{\rm rms}}{1\,{\rm nG}}\right)^2 {\rm yr}\,. \tag{4.81}$$

It is important to note that the effect of the magnetic field on the CR observables, such as the energy spectrum and mass composition, also depends on the source density considered. Given the source number density n_s, the typical source distance is given by $d_s \simeq (n_s)^{-1/3}$. Therefore, if the distance of a cosmic ray source from Earth is such that $d_s \gtrsim \lambda_D$, diffusion will occur as long as

$$E \lesssim E_s = 1 \cdot Z \left(\frac{d_s\,\lambda_c}{1\,{\rm Mpc}^2}\right)^{1/2} \left(\frac{B_{\rm rms}}{1\,{\rm nG}}\right) {\rm EeV}\,. \tag{4.82}$$

CRs satisfying the condition in Eq. (4.82) will still propagate in a diffusive regime, while for $E \gtrsim E_s$ the propagation is quasi-rectilinear with no significant magnetic deflection [265].

When charged particles propagate in a magnetic field, they lose energy by emitting *synchrotron radiation*. The synchrotron energy loss rate for a particle with mass m, energy E and electric charge q is given by

$$\left(-\frac{dE}{dt}\right)_{\rm sync} = \frac{4}{3}\sigma_{\rm T}\frac{B^2}{8\pi}\left(\frac{q m_e}{m}\right)^4 \left(\frac{E}{m_e}\right)^2\,, \tag{4.83}$$

where $\sigma_{\rm T}$ is the Thomson cross section (see Eq. (4.59)), $B^2/8\pi$ is the magnetic energy density and m_e is the electron mass [239, 256, 259, 268]. We can immediately see that synchrotron losses are negligible for protons and nuclei because of the m^{-4} factor. On the contrary, the development of electromagnetic cascades (see Sec. 4.4) is modified by synchrotron emission when it becomes comparable to inverse Compton, since electrons and positrons will lose energy before up-scattering background photons. For very-high-energy electrons, we obtain that synchrotron cooling becomes dominant for [87]

$$B_{\rm rms} \gtrsim 3 \left(\frac{E}{1\,{\rm EeV}}\right)^{-1} {\rm nG}\,. \tag{4.84}$$

We can see that in the case of Eq. (4.84), the penetration power of an electromagnetic cascade is reduced by synchrotron emission, which will populate the low-energy part of the propagated γ-ray spectrum.

4.5.1 Extragalactic magnetic field

The current knowledge of the extragalactic magnetic field (EGMF) is rather limited, and its origin is still an open problem in astrophysics and cosmology. Two main classes of magnetogenesis scenarios can be identified: the *astrophysical* scenario and the *primordial* scenario [18–20]. In the astrophysical scenario, the EGMF is generated locally by the feedback of astrophysical processes into the extragalactic space, which generate the seed field, which is then amplified by a dynamo mechanism. However, in this scenario, a very weak EGMF is expected in the cosmic voids (i.e.

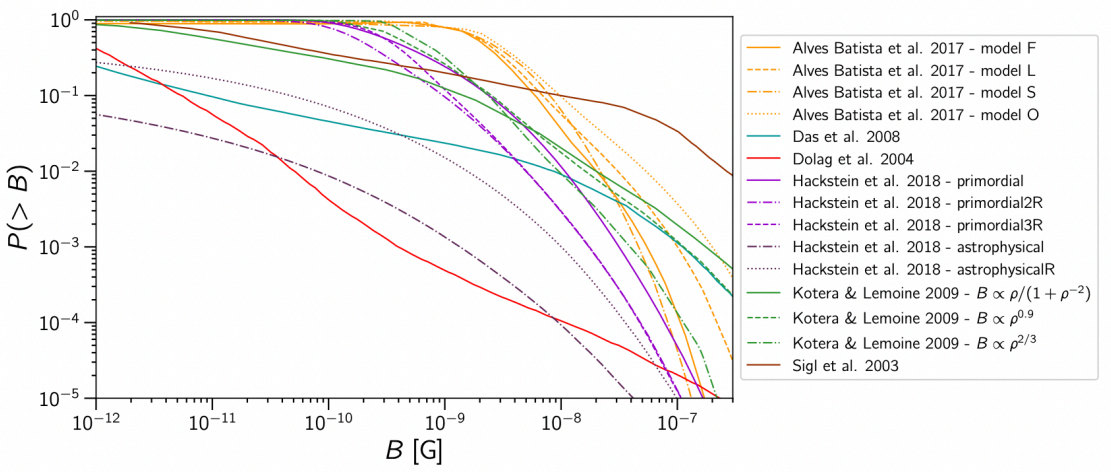

Figure 4.6: Cumulative volume filling factor for different EGMF models from numerical simulations. Figure taken from [94].

the regions where the matter density is close to zero). In contrast, in the primordial scenario, the seed of the EGMF was generated in earlier stages of the Universe. The field is then amplified in the regions with higher matter density, but may still be different from zero in cosmic voids. A combination of the two scenarios described above is also possible.

The large uncertainties present in the understanding of the EGMF can be observed in Fig. 4.6, where the cumulative volume filling factor (i.e. the percentage of the simulation volume where the magnetic field strength is greater than a given value) of different EGMF models from numerical simulations are shown. We can see that most of the cosmic volume (between 10% and 90% is characterized by the presence of a very weak field, below $\sim 1\,\mathrm{nG}$. Since cosmic voids represent the largest part of the extragalactic space, the propagation of CRs is expected to be particularly sensitive to the magnetization of these regions. Moreover, experimental observations of the EGMF in cosmic voids (mostly obtained indirectly from γ-ray observations) provide lower limits of $B > 10^{-15} - 10^{-13}\,\mathrm{G}$ [269–272] (see also the left panel of Fig. 4.7). Upper limits have also been obtained by studying the effect of the EGMF on the CMB spectrum; the limit of $\lesssim 0.1 - 1\,\mathrm{nG}$ was obtained in [273, 274].

A very small fraction of the extragalactic volume is filled with matter structures: galaxy clusters fill $\lesssim 0.1\%$ of the volume and filaments fill $\sim 0.1 - 10\%$ of the volume. In Galaxy clusters, Faraday rotation measurements show a magnetic field value from $\sim 1\,\mu\mathrm{G}$ to $\sim 10\,\mu\mathrm{G}$ in the center of the cluster [275–278], while cosmic filaments are characterized by a magnetic field strength from $\sim 0.1\,\mathrm{nG}$ to $\sim 100\,\mathrm{nG}$ [278–280].

The study of the extragalactic propagation of UHECRs in the EGMF is based on the use of cosmological simulations of the magnetization of the local Universe. However, given the large uncertainties (see Fig. 4.6), very different conclusions have been obtained. In Chapter 7, we will discuss these results and we will see how the magnetization of the cosmic voids plays a fundamental role in the UHECR deflection.

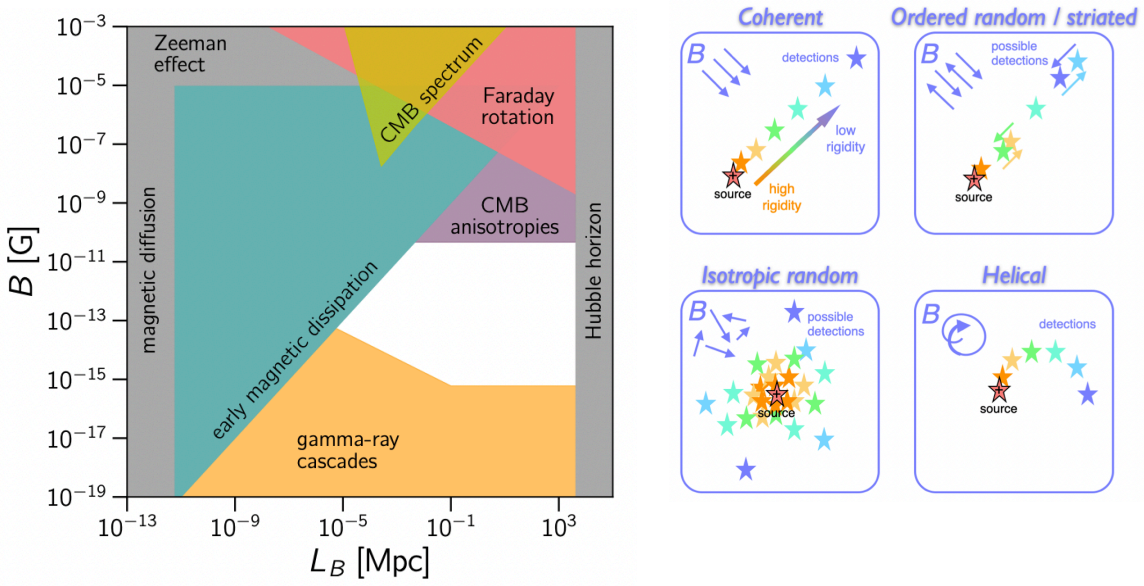

Figure 4.7: Left: limits of the magnetic field strength $B_{\rm rms}$ and coherence length λ_c of the EGMF. Figure taken from [97]. Right: representation of the effect of different components of the GMF on the observed arrival directions of UHECRs. Figure taken from [94].

4.5.2 Galactic magnetic field

After propagating through extragalactic space, CRs will eventually enter in the environment of our Galaxy, where they will be further deflected by the Galactic magnetic field. Therefore, a complete reconstruction of the UHECR arrival directions must to take into account the magnetic field of the Milky Way.

Several techniques can be used to measure and reconstruct the GMF [281]. One of the first observations of the GMF [282, 283] was based on the *Zeeman effect* [284]: when an atom or a molecule is in the presence of a magnetic field, the energy levels are split in proportion to the magnetic field strength. This type of measurement is very useful for measuring the magnetic field in specific regions. More modern techniques for measuring the GMF are given by the *Faraday rotation measure* (RM) and synchrotron emission. Faraday RMs are based on the fact that the plane of polarization of light is rotated as it propagates in a magnetic field. However, Faraday RMs depend only on the magnetic field component parallel to the line of sight to the source. Similarly, synchrotron emission from electrons gyrating around the magnetic field lines only provides information about the magnetic field component perpendicular to the line of sight. Moreover, although Faraday RMs and synchrotron emission provide complementary information on the GMF, they are both integrated measurements over the line of sight. This makes the reconstruction of the three-dimensional structure of the GMF more challenging and sensitive to possible uncertainties.

A GMF model is typically characterized by three effective components [94, 281], as shown in the right panel of Fig. 4.7. The first component is given by the *coherent field* (or mean field), which is such that the magnetic field is coherent over large spatial scales ($\sim O(1\,\mathrm{kpc})$). The *isotropic random component* is a stochastic field that points in all directions with equal

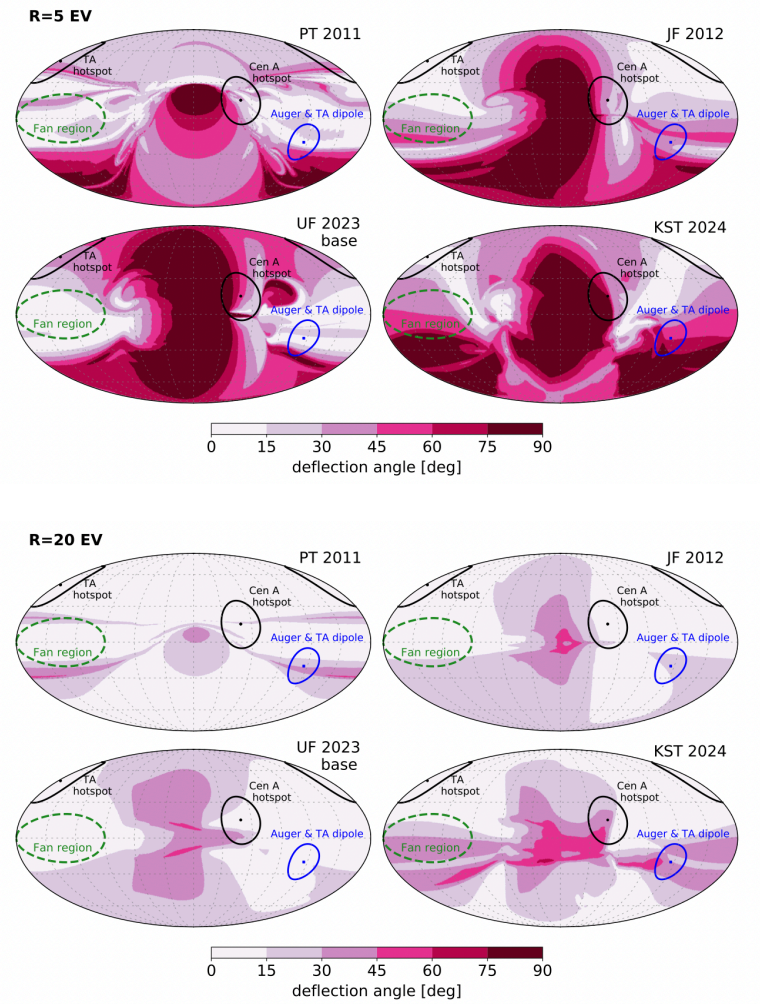

Figure 4.8: Angular deflection of CRs with rigidity $R = 5\,\mathrm{EV}$ (top panels) and $R = 20\,\mathrm{EV}$ (bottom panels) for different GMF models. The maps are shown in Galactic coordinates with increasing longitude to the left. Figure adapted from [285].

probability. The third component is an *anisotropic random component* (or striated field), which is still a stochastic field, but with preferred orientations, but not directions. We can see that the coherent component generates a shift in one direction of the UHECR arrival directions, while the random components are responsible for a scattering of the arrival directions around the direction of the source. The GMF can also be characterized by the *magnetic helicity*[12] H_B, which is related to the topology of the magnetic field, in particular to the twisting of the field lines.

One of the most comprehensive and widely used GMF models is that developed in [286, 287],

[12]The helicity of a magnetic field is defined as

$$H_B = \int_V \mathbf{A} \cdot \mathbf{B}\, dV\,, \tag{4.85}$$

where V is the integration volume and $\mathbf{A}$ is the magnetic vector potential such that $\mathbf{B} = \nabla \times \mathbf{A}$.

referred to as JF12. Other GMF models can be found in [288, 289], while more recent models can be found in [290, 291]. Unfortunately, the effect of different GMF models on the UHECR arrival directions can be very different, introducing another source of uncertainty in anisotropy studies. This can be seen in Fig. 4.8, where the angular deflection of cosmic rays with different rigidities is obtained with different GMF models. We can clearly see that, although the mean deflection decreases as the rigidity increases, very different deflection patterns are obtained even for cosmic rays with $R = 20\,\mathrm{EV}$. We can also see that, even at the highest rigidities, deflections above $\simeq 45^\circ$ are still possible.

5

Simulation codes

In Chapter 4 we have discussed the propagation of UHECRs in the extragalactic space. We have seen that, in order to fully reconstruct the journey of cosmic rays from their sources to the Earth, several processes of different types have to be taken into account. Continuous and stochastic energy losses, the production of secondary particles, and the deflections in magnetic fields are key elements to interpret the UHECR observations. Moreover, given the current uncertainties in the modelling of the astrophysical propagation, numerical simulations are fundamental to test predictions made by different assumptions on the propagation model. In this thesis, two widely used simulation codes have been used: `SimProp v2r4` [292] and `CRPropa 3.2` [236]. This chapter is dedicated to the description of these simulation frameworks.

5.1 SimProp v2r4

`SimProp` [292–295] is a Monte Carlo code for the extragalactic propagation of UHECRs. The propagation is simulated in a fully one-dimensional framework and then no magnetic deflections are taken into account. The adiabatic and photohadronic energy losses described in Sec. 4.3 with cosmic photon fields such as the CMB and the EBL are implemented in the code. These interactions include the decay of unstable particles and the production of secondary particles (such as photons, electrons, positrons and neutrinos). The code is written in `C++` and uses the `ROOT` [296] framework[1].

A typical `SimProp v2r4`[2] [292] run consists of N simulated events with energy $E_{\rm inj}$ and with mass number $A_{\rm inj}$. The initial energy is sampled from an energy distribution $dN/dE_{\rm inj} \propto E_{\rm inj}^{-\gamma}$ from $E_{\rm min}$ to $E_{\rm max}$. The initial redshift $z_{\rm inj}$ of the injected particles is sampled uniformly between $z_{\rm min}$ and $z_{\rm max}$. As it can be seen in the right panel of Fig. 5.1, the parameters N, $A_{\rm inj}$, γ, $E_{\rm min}$, $E_{\rm max}$, $z_{\rm min}$ and $z_{\rm max}$ are input parameters of the simulation and they can be specified in the input command line. Since the default sampling of the source locations is uniform in redshift, in order to reproduce the distribution of a source class, it is assigned to each particle

[1] More information can be found at `https://cplusplus.com` and `https://root.cern`.
[2] The code is available at `https://github.com/SimProp/SimProp-v2r4`.

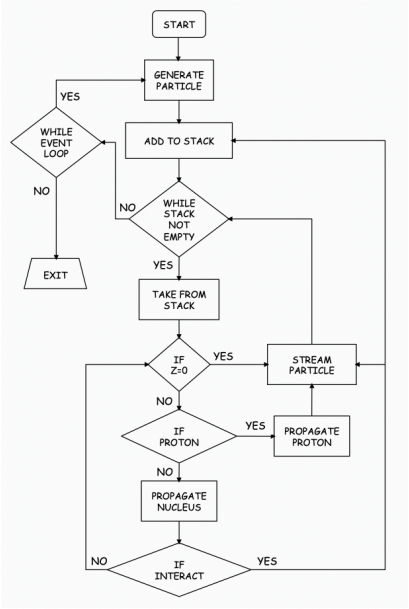

SimProp v2r4 recognizes the following command-line options:

option	description	default
`-h`	prints the help and exits	none
`-s`	seed of the random number generator	65539
`-N`	number of events to be generated	100
`-A`	mass number of primary nuclei, $A_{\rm inj}$ (chosen at random for each event with `-A 0`)	56
`-e`	$\log_{10}(E_{\rm min}/{\rm eV})$, where $E_{\rm min}$ is the minimum injection energy	17
`-E`	$\log_{10}(E_{\rm max}/{\rm eV})$, where $E_{\rm max}$ is the maximum injection energy	21
`-g`	injection spectral index, γ	1
`-z`	minimum source redshift, $z_{\rm min}$	0
`-Z`	maximum source redshift, $z_{\rm max}$	1
`-r`	distance between sources, $L_{\rm s}$,[5] in Mpc	0
`-L`	EBL model, see section 4.1	1
`-M`	photodisintegration model, see section 4.2	0
`-n`	nucleon ejection scaling factor (only with `-M 3` and `-M 4`)	1
`-a`	alpha-particle ejection scaling factor (only with `-M 3` and `-M 4`)	1
`-D`	beta decay: `0` disabled, all nuclei treated as their respective beta-decay stable isobars; `1` enabled, treated as instantaneous	1

Figure 5.1: Left: flowchart of `SimProp`. Figure taken from [293]. Right: command line options of `SimProp v2r4`. Figure taken from [292].

a weight factor of the form

$$\omega_{\rm inj}(z_{\rm inj}) \propto \frac{S(z_{\rm inj})}{(1+z_{\rm inj})H(z_{\rm inj})}\,, \tag{5.1}$$

where the denominator ensures a uniform distribution in the comoving volume and $S(z)$ characterizes the source class evolution. Usually the source class evolution function is a power law of the form $S(z) \propto (1+z)^m$, where m depends on the source class.

In `SimProp v2r4`, energy losses can be both continuous and stochastic. The redshift interval between the production of a particle and a stochastic process (or the condition $z = 0$) is called *branch*. During a branch, the particle type does not change, but its energy is reduced by the continuous energy losses. Each time a new particle is produced, a new branch starts. The end of the simulation of a particle is given by the condition $z = 0$. Electromagnetic particles such as photons, electrons and positrons are not propagated in `SimProp v2r4`, but their production information is recorded in the output file in order to allow their propagation to be simulated with other tools. Since the propagation of neutrinos is only affected by adiabatic losses, they are propagated to $z = 0$ immediately after their production and their final energy is given by

$$E_{\nu,{\rm Earth}} = \frac{E_{\nu,{\rm prod}}}{1+z_{\rm prod}}\,, \tag{5.2}$$

where $E_{\nu,{\rm prod}}$ and $z_{\rm prod}$ are the energy and the redshift at the production, respectively.

Adiabatic energy losses and electron-positron pair production are always treated as continuous processes in `SimProp v2r4`, while photodisintegration is always treated stochastically. Photopion production can be treated as either continuous or stochastic, depending on the user's requirements (see right panel of Fig. 5.1). The nuclear decay of unstable particles (nuclei, pions and muons) is always treated as an instantaneous process.

The photohadronic interaction rate of UHECRs with background photon fields in Eq. (4.45) is linear in both the SED of the radiation and the cross section of the interaction process. This means that if the interaction rate of the process i with the photon filed j is given by τ_{ij}^{-1}, then the total interaction rate is given by

$$\tau^{-1} = \sum_{i,j} \tau_{ij}^{-1} \,. \tag{5.3}$$

The sampling of the interaction process is then done by considering the interaction probability $p_{ij} = \tau_{ij}^{-1}/\tau^{-1}$. The kinematics of the interaction process is described in Appendix B.2.

The characterization of the extragalactic propagation is affected by uncertainties due to the knowledge of the components required by the astrophysical models. The first uncertainty is given by the EBL model considered in the simulation (see Sec. 4.3.1). Several EBL models are implemented in `SimProp v2r4` [225, 226, 229, 230] and can be selected from the command line. A power law approximation or no EBL field are also possible simulation scenarios in `SimProp v2r4`.

The second source of uncertainty is the photohadronic cross sections. The photopion production cross section from protons is taken from `SOPHIA` [243]. Photopion production from heavy nuclei is obtained in the superposition model, where a nucleus (A, Z) is equivalent to A protons with the same Lorentz factor of the nucleus. The interacting nucleon is randomly sampled from the nucleus. In `SimProp v2r4` single pion production is considered with probability 2/3 for neutral pions and probability 1/3 for charged pions. Several photodisintegration models are implemented in the code [244, 297, 298]: the photodisintegration channel is randomly chosen with a probability proportional to the branching ratio, and all the fragments are produced with the same Lorentz factor of the primary nucleus.

We can see that a very large number of possible astrophysical scenarios can be simulated if all the uncertainties are taken into account. However, this process can be numerically expensive and very time consuming. A very useful strategy for optimizing numerical simulations is the creation of a simulation database. For a given choice of injection energy $E_{\rm inj}$, atomic mass $A_{\rm inj}$ and maximum redshift $z_{\rm max}$, the propagation of the CRs to the Earth is fully characterized by the assumed source evolution, EBL and cross section models. After the propagation, a certain distribution of observed energies $E_{\rm obs}$ and atomic masses $A_{\rm obs}$ at $z = 0$ is obtained from the considered astrophysical scenario. By repeating this scheme for all the values of interest of $E_{\rm inj}$ and $A_{\rm inj}$, a database of propagation matrices $M(E_{\rm obs}, A_{\rm obs}; E_{\rm inj}, A_{\rm inj})$ containing the probabilities of observing cosmic rays of energy $E_{\rm obs}$ and mass $A_{\rm obs}$ from the injection of cosmic rays of energy $E_{\rm inj}$ and mass $A_{\rm inj}$ can be created for each astrophysical scenario. In this way, different assumptions about source energetics and mass composition can be tested by reweighing the matrix database. This technique is particularly useful for one-dimensional simulations; the situation is different for three-dimensional simulations, where the number of degrees of freedom (such as the relative position in the volume of the source and observer) can become so large that creating a propagation database is impractical.

5.2 CRPropa 3.2

`CRPropa` [236, 299–302] is also a Monte Carlo code for simulating the propagation of CRs, electromagnetic particles and neutrinos in various astrophysical scenarios. All the interaction processes

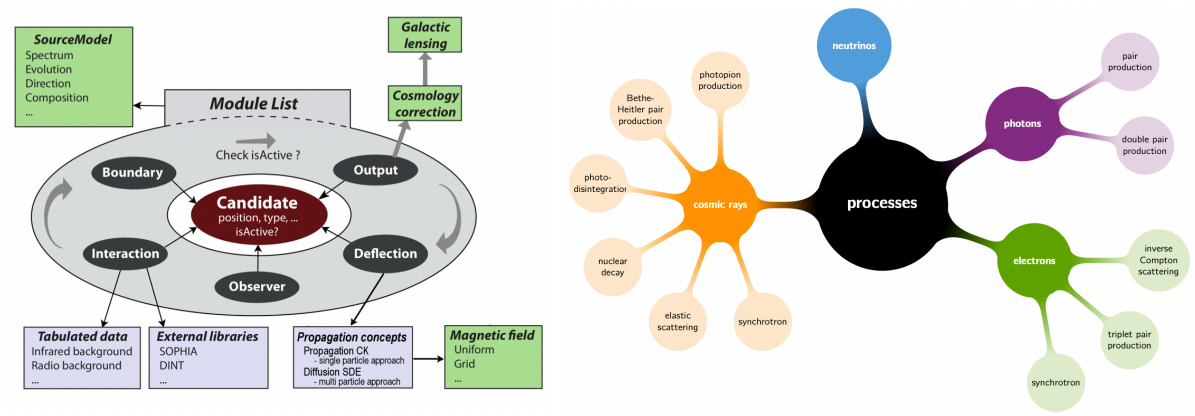

Figure 5.2: Left: modular structure of `CRPropa`. Figure taken from [302]. Right: schematic representation of the interaction processes implemented in CRPropa 3.2. Figure taken from [236].

present in `SimProp v2r4` are also present in `CRPropa`, with the addition of the electromagnetic processes described in Sec. 4.4 (see also the right panel of Fig. 5.2). The latest released version of the code is `CRPropa 3.2` [3] and it is written in `C++` with a `Python` interface based on `SWIG`[4]. Starting from `CRPropa 3`, the code structure is fully modular: different components of a simulation (e.g. interactions, sources and observers) are defined in specific independent modules. This structure also allows for implementation of new modules by users.

A simulation run consists of the propagation of several candidate particles. Since each particle simulation is independent, the propagation of several candidates can be parallelized, thus reducing the computational time. This is done in `CRPropa 3.2` with `OpenMP`[5] which allows shared-memory multiprocessing.

The simulated particle is defined by the *candidate class*, which contains all the relevant information about the simulated event such as particle type, energy, momentum and position vectors. These properties are updated at each propagation step until a breaking condition, defined by the user, is satisfied. Secondary particles are also included in the candidate class, if their propagation is requested in the simulation. The creation of a simulation candidate can be done directly by the user, or by defining an element of the *source class*. In this second scenario the candidate properties are obtained from the source characterization parameters such as energy spectrum, mass composition, spatial distribution and injection configuration.

The end condition of the simulation of a given candidate can be defined in different ways, depending on the scenario considered. Several conditions are available for single candidates, such as a minimum energy or a maximum trajectory length. If the user is interested in the particles collected in specific spatial and temporal windows, one or more observers can also be defined. The `CRPropa 3.2` *observer class* consists of a specific geometrical condition (from point-like to three-dimensional volume) where particles are collected (possibly also in a specific time range). In this case, the end condition of a candidate is given by its detection by the observer.

In `CRPropa 3.2`, one-dimensional and three-dimensional simulations can be performed. The

[3] The code is available at `https://crpropa.desy.de`.
[4] More information can be found at `https://www.python.org` and `https://www.swig.org`.
[5] For more details, visit `https://www.openmp.org`.

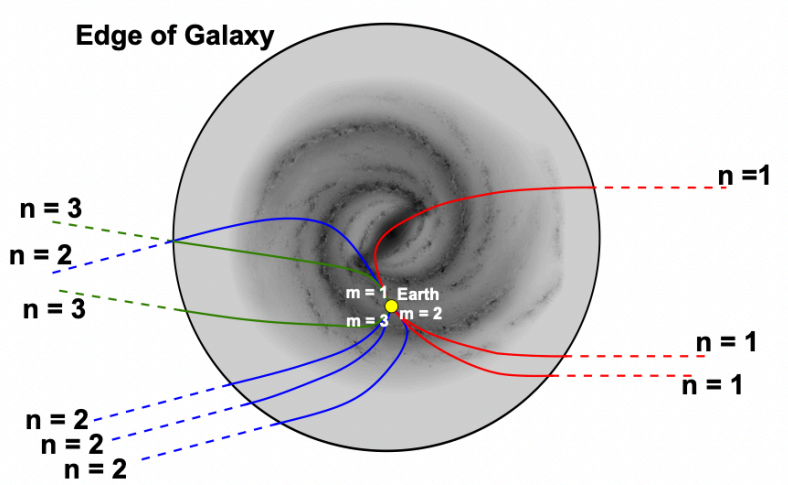

Figure 5.3: Schematic representation of the creation of a magnetic lens from backtracking simulations. CRs are emitted at Earth in directions $\boldsymbol{p}_m$ and they leave the galactic edge in the directions $\boldsymbol{p}_n$. Figure taken from [304].

three-dimensional framework allows the use of both three-dimensional source distributions and magnetic fields. In principle, any type of magnetic field can be used by implementing the appropriate function in the *Magnetic Field class*. However, some general classes of magnetic fields are already implemented in the code such as homogeneous, dipolar, helical and turbulent. Several models of GMF are also implemented in the code, such as the JF12 [286, 287] and the TF17 [303] models.

As we can see from the discussion in Sec. 4.3, photohadronic interactions can be neglected in the propagation of UHECRs in the Milky Way. Therefore, the forward and backward tracking of CRs in the Milky Way can be studied with `CRPropa 3.2`. However, the forward propagation of cosmic rays from the edge of the Galaxy to the Earth can be computationally inefficient since most of the particles will not reach the observer. For this reason, the lensing technique developed in the `PARSEC` code [304] is also available in `CRPropa 3.2`. The use of *magnetic lenses* allows a numerically efficient reproduction of the galactic deflection in the propagation of UHECRs to the Earth. The magnetic lens is obtained by considering particles at a given rigidity value $R_i = E_i/Z_i$ and backtracking their trajectory from an isotropic distribution at Earth to the edge of the Milky Way. The probability of observing a particle at Earth from a given direction $\boldsymbol{p}_m$ given the entrance direction $\boldsymbol{p}_n$ at the edge of the Galaxy is given by $l_{mn,i}$. These probabilities are then collected in the matrix $\mathcal{L}_i$. The magnetic lens is then given by the collection of matrices $\mathcal{L}_i$, ..., $\mathcal{L}_N$, where N is the number of the rigidity values considered. A schematic representation of the creation of a magnetic lens is shown in Fig. 5.3. Therefore, a probability vector $\mathcal{P}_i^{\text{edge}}$ of observing particles with rigidity R_i from a given direction at the edge of the Galaxy from an extragalactic simulation can be mapped into the corresponding probability vector at Earth $\mathcal{P}_i^{\text{Earth}}$ by the matrix multiplication

$$\mathcal{L}_i \cdot \mathcal{P}_i^{\text{edge}} = \mathcal{P}_i^{\text{Earth}} \,. \tag{5.4}$$

Photohadronic processes are implemented in `CRPropa` for the interaction with several photon fields: the CMB field, the EBL models from [225–232] and the CRB models from [233–235].

Photopion production in CRPropa 3.2 is done via a direct interface with SOPHIA, which simulates the interaction between photons and nucleons. The rescaling for primary nuclei is done as in the previous versions of the code [300, 301]. The photodisintegration implementation is based on the TALYS 1.8 code [305] for a total of more than 2.000 disintegration channels. Nuclear decay of unstable species and the elastic scattering of background photons are also implemented in the code.

In the latest released versions of CRPropa, some features not directly related to the extragalactic propagation of UHECRs have also been implemented, making the code more complete for modelling high-energy astrophysical phenomena. In CRPropa 3.2, the development of electromagnetic cascades in the extragalactic space (see Sec. 4.4) has been fully implemented in the modular structure of the code. In particular, the electromagnetic processes of pair production, double pair production, inverse Compton scattering and synchrotron radiation are present as independent modules that can be included in the propagation script. Since the number of secondary particles produced in electromagnetic cascades in the extragalactic space grows very rapidly, a *thinning* procedure for the sampling of secondary particles [306] has been implemented, mainly inspired by the ELMAG code [307, 308].

Among the latest developments in CRPropa 3.2, CR acceleration is also present in the simulation framework. In particular, second- and first-order Fermi mechanisms (see Sec. 4.1.1) are implemented. Finally, from CRPropa 3.1, the code has also been extended to study problems where a transport-equation-based approach is more convenient (e.g. galactic propagation of CRs with energy $\lesssim 1\,\mathrm{PeV}$). In particular, an ensemble-average approach is implemented in the code for simulating the evolution of phase-space elements (or pseudo-particles). The equation of motion is then solved by considering a set of *stochastic differential equations* in which the diffusion term is implemented. In CRPropa 3.2, this framework has been extended to include advection and adiabatic energy change.

5.3 Comparison of the codes

In the previous sections, we have seen that the implementation of the extragalactic propagation of UHECRs is very different in the numerical frameworks of SimProp and CRPropa. In particular, different results can be obtained due to the different treatment of uncertainties affecting the propagation, such as the EBL field and photodisintegration. These differences between the two codes have been studied first in [309], and then again in [310], using the latest versions of the codes: SimProp v2r4 and CRPropa 3.

The difference in the propagated UHECR spectrum obtained with the two codes, assuming the same EBL and photodisintegration models, has been studied in [309]. It has been shown that, in general, the differences are always less than $\sim 10\%$ for proton propagation and always less than $\sim 30\%$ for heavier nuclei. These differences are mainly due to the simplified treatment of the EBL redshift evolution in CRPropa and from the simplified treatment of the photohadronic interactions in SimProp. In particular, in CRPropa the redshift dependence of the interaction rates with the EBL is parameterized by a global scaling factor, while in SimProp the interaction rates are calculated at each redshift value. Furthermore, in SimProp photopion production is always approximated as single pion production, while in CRPropa multiple particle production channels are possible. Simplifications in the treatment of photodisintegration in SimProp are also relevant.

In [310], the impact of these uncertainties on the production of secondary neutrinos and photons has also been investigated. Differences of more than $\sim 50\%$ have been found in the simulated neutrino fluxes, again caused by the different implementations of the cosmological evolution of the EBL and the pion production. Similar results have also been obtained for the production rate of high-energy photons.

6

Cosmic ray anisotropy analysis

Sec. 6.3 of this chapter is based on the publication:

- S. Rossoni and G. Sigl. (2025). *Anisotropy signal of UHECRs from a structured magnetized Universe*. **Phys. Rev. D**, 112, 023015. arXiv:2502.19324 [astro-ph.HE]. https://doi.org/10.1103/4zt7-s48v.

The first observation of an anisotropic component in the UHECR flux was reported by the Pierre Auger Observatory in 2017. Since the first observation, the dipole component in the UHECR flux above 8 EeV has grown in significance to the current value of $d \simeq 7.5\%$ with a 6.8σ significance. As we have discussed in Sec. 3.2.3, the observation of CR arrival directions is fundamental to continue the search of their astrophysical sources. This chapter presents the mathematical framework for the study of CR arrival directions and anisotropies. In Sec. 6.1 the reconstruction of a purely dipolar cosmic ray flux is discussed. The more general case of a flux characterized by higher order multipoles than the dipole is discussed in Sec. 6.2. Finally, in Sec. 6.3 the expected angular power spectrum of a distribution of N cosmic rays is discussed in different scenarios.

6.1 Dipole reconstruction

In this section, a purely dipolar CR flux is considered. In particular, given the unit vector on the sphere $\hat{\mathbf{n}}$ a purely dipolar flux[1] is given by

$$\Phi(\hat{\mathbf{n}}) = \Phi_0(1 + \mathbf{d}\cdot\hat{\mathbf{n}}) = \Phi_0(1 + \alpha\,\hat{\mathbf{d}}\cdot\hat{\mathbf{n}})\,, \tag{6.1}$$

where the dipole vector is given by $\mathbf{d} = \alpha\,\hat{\mathbf{d}}$, the unit vector $\hat{\mathbf{d}} = (d_x, d_y, d_z)$ is such that $d_x^2 + d_y^2 + d_z^2 = 1$ and α is the dipole amplitude. The normalization factor Φ_0 corresponds to the average value of $\Phi(\hat{\mathbf{n}})$ in the sky, in fact,

$$\overline{\Phi(\hat{\mathbf{n}})} = \frac{1}{4\pi}\int d\hat{\mathbf{n}}\,\Phi(\hat{\mathbf{n}}) = \frac{\Phi_0}{4\pi}\int d\hat{\mathbf{n}}\,(1 + \alpha\,\hat{\mathbf{d}}\cdot\hat{\mathbf{n}}) = \Phi_0\,, \tag{6.2}$$

[1] The CR flux $\Phi(\hat{\mathbf{n}})$ is defined in Eq. (3.3), while the spherical coordinates are discussed in Appendix A.1.

where $d\hat{\mathbf{n}} = d\Omega = \sin\theta d\theta d\phi$ is the solid angle. It is also easy to see that the integral of $\Phi(\hat{\mathbf{n}})$ over the whole sky is equal to the CR intensity $4\pi\Phi_0$. We can now define the moments of order zero and one of $\Phi(\hat{\mathbf{n}})$ as in [311, 312]

$$I_0 = \int d\hat{\mathbf{n}}\, \Phi(\hat{\mathbf{n}}) \qquad \text{and} \qquad \mathbf{I} = \int d\hat{\mathbf{n}}\, \hat{\mathbf{n}}\, \Phi(\hat{\mathbf{n}})\,. \tag{6.3}$$

For a dipolar flux we obtain that

$$I_0 = \Phi_0 \int d\hat{\mathbf{n}}\, (1 + \alpha\, \hat{\mathbf{d}} \cdot \hat{\mathbf{n}}) = 4\pi\, \Phi_0\,, \tag{6.4}$$

$$\begin{aligned} I_x &= \Phi_0 \int d\hat{\mathbf{n}}\, \sin\theta \cos\phi (1 + \alpha\, \hat{\mathbf{d}} \cdot \hat{\mathbf{n}}) \\ &= \alpha\, d_x\, \Phi_0 \int d\hat{\mathbf{n}}\, \sin^2\theta \cos^2\phi = \frac{4\pi}{3} \alpha\, d_x\, \Phi_0 = \frac{I_0}{3} \alpha\, d_x\,. \end{aligned} \tag{6.5}$$

Similarly to I_x, we also obtain that

$$I_y = \frac{I_0}{3} \alpha\, d_y\,, \tag{6.6}$$

$$I_z = \frac{I_0}{3} \alpha\, d_z\,. \tag{6.7}$$

Then, we can write the first moment as $\mathbf{I} = (I_0\alpha/3)\, \hat{\mathbf{d}}$, from which we obtain the dipole amplitude and direction as

$$\alpha = 3\frac{I}{I_0} \qquad \text{and} \qquad \hat{\mathbf{d}} = \frac{\mathbf{I}}{I}\,, \tag{6.8}$$

where $I = \sqrt{I_x^2 + I_y^2 + I_z^2}$. The relations in Eq. (6.8) can then be used for actual CR measurements. In the next section, we will discuss the dipole reconstruction considering experimental effects as the fact that we have a finite number of events in observations and how to take into account the exposure of the observatory.

6.1.1 Finite number of events

We can now consider a set of N observed CR arrival directions $\hat{\mathbf{n}}_1$, $\hat{\mathbf{n}}_2$, ..., $\hat{\mathbf{n}}_N$. These arrival directions are observed from a CR observatory with exposure $0 < \mathcal{E}(\hat{\mathbf{n}}) \leq 1$: we consider the case of non-uniform but complete sky coverage for the exposure function (the case of partial sky coverage will be discussed in the next section). The observed CR flux is given by

$$\Phi(\hat{\mathbf{n}}) = \sum_{i=1}^{N} \frac{\delta(\hat{\mathbf{n}} - \hat{\mathbf{n}}_i)}{\mathcal{E}(\hat{\mathbf{n}}_i)}\,, \tag{6.9}$$

where $\delta(x - x')$ is the Dirac delta function and $\mathcal{E}(\hat{\mathbf{n}}_i)$ is the exposure in the direction $\hat{\mathbf{n}}_i$. We can see that the average value of $\Phi(\hat{\mathbf{n}})$ in the sky is given by

$$\overline{\Phi(\hat{\mathbf{n}})} = \frac{1}{4\pi} \int d\hat{\mathbf{n}}\, \Phi(\hat{\mathbf{n}}) = \frac{1}{4\pi} \sum_{i=1}^{N} \frac{1}{\mathcal{E}(\hat{\mathbf{n}}_i)} \int d\hat{\mathbf{n}}\, \delta(\hat{\mathbf{n}} - \hat{\mathbf{n}}_i) = \frac{\mathcal{N}}{4\pi}\,, \tag{6.10}$$

where $\mathcal{N} = \sum_{i=1}^{N} \mathcal{E}^{-1}(\hat{\mathbf{n}}_i)$. Instead, the total number of events is given by

$$\int d\hat{\mathbf{n}}\, \mathcal{E}(\hat{\mathbf{n}})\Phi(\hat{\mathbf{n}}) = \sum_{i=1}^{N} \frac{1}{\mathcal{E}(\hat{\mathbf{n}}_i)} \int d\hat{\mathbf{n}}\, \mathcal{E}(\hat{\mathbf{n}})\delta(\hat{\mathbf{n}} - \hat{\mathbf{n}}_i) = N\,. \tag{6.11}$$

We can now obtain the first two moments of our observed flux by using the definitions in Eq. (6.4). We obtain that

$$S_0 = \int d\hat{\mathbf{n}}\, \Phi(\hat{\mathbf{n}}) = \sum_{i=1}^{N} \frac{1}{\mathcal{E}(\hat{\mathbf{n}}_i)}\,, \tag{6.12}$$

$$\mathbf{S} = \int d\hat{\mathbf{n}}\, \hat{\mathbf{n}}\, \Phi(\hat{\mathbf{n}}) = \sum_{i=1}^{N} \frac{1}{\mathcal{E}(\hat{\mathbf{n}}_i)} \int d\hat{\mathbf{n}}\, \hat{\mathbf{n}}\, \delta(\hat{\mathbf{n}} - \hat{\mathbf{n}}_i) = \sum_{i=1}^{N} \frac{\hat{\mathbf{n}}_i}{\mathcal{E}(\hat{\mathbf{n}}_i)}\,. \tag{6.13}$$

The sums in Eqs. (6.12) and (6.13) can be compared with the results obtained for I_0 and $\mathbf{I}$ to reconstruct the dipole parameters. As discussed in [312], these estimates of the dipole parameters will become accurate as the number of observed arrival directions increases.

The flux function $\Phi(\hat{\mathbf{n}})$ can be rewritten using the definition of $\mathcal{N}$ as

$$\Phi(\hat{\mathbf{n}}) = \mathcal{N} \cdot \phi(\hat{\mathbf{n}})\,, \tag{6.14}$$

where the function $\phi(\hat{\mathbf{n}})$ is given by

$$\phi(\hat{\mathbf{n}}) = \frac{1}{\mathcal{N}} \sum_{i=1}^{N} \frac{\delta(\hat{\mathbf{n}} - \hat{\mathbf{n}}_i)}{\mathcal{E}(\hat{\mathbf{n}}_i)}\,, \tag{6.15}$$

and it corresponds to the normalized observed flux. It is easy to show that

$$\int d\hat{\mathbf{n}}\, \phi(\hat{\mathbf{n}}) = 1 \qquad \text{and} \qquad \overline{\phi(\hat{\mathbf{n}})} = \frac{1}{4\pi} \int d\hat{\mathbf{n}}\, \phi(\hat{\mathbf{n}}) = \frac{1}{4\pi}\,. \tag{6.16}$$

The definition of $\phi(\hat{\mathbf{n}})$ will be useful in the following sections.

6.1.2 Partial sky coverage

As discussed in [311], the results obtained in Eqs. (6.12) and (6.13) cannot be used if the exposure is zero in some regions of the sky. However, the procedure described above can be generalized to the case of partial sky coverage, as shown in [312]. In particular, if the exposure in a region of the sky is zero, this means that no events arriving from that region can be observed. Therefore, the momenta I_0 and $\mathbf{I}$ must be calculated only in the region of the sky where it is possible to observe events. This new set of momenta is still invertible and it can be used to find the expressions for α and $\hat{\mathbf{d}}$. The estimate of the dipole parameters is still given by the values of S_0 and $\mathbf{S}$, but in a different combination than Eq. (6.8).

Given the fact that the Earth rotates on its axis, it is clear that the field of view of a CR observatory will be limited in declination, but not in right ascension (see Appendix A.3). In spherical coordinates, the field of view and then the exposure will be different from zero for

$0 \leq \phi \leq 2\pi$ and $\theta_{\rm min} \leq \theta \leq \theta_{\rm max}$ (see Appendix A.1). Therefore, the moments of order zero and one of the flux $\Phi(\hat{\mathbf{n}})$ are given by

$$I_0 = \int_{\theta_{\rm min}}^{\theta_{\rm max}} d\theta \, \sin\theta \int_0^{2\pi} d\phi \, \Phi(\hat{\mathbf{n}}) \qquad \text{and} \qquad \mathbf{I} = \int_{\theta_{\rm min}}^{\theta_{\rm max}} d\theta \, \sin\theta \int_0^{2\pi} d\phi \, \hat{\mathbf{n}} \, \Phi(\hat{\mathbf{n}}) \, . \tag{6.17}$$

These integrals can be solved analytically to obtain

$$I_0 = \Phi_0 \pi d (2 + \alpha d_z s) \, , \tag{6.18}$$
$$I_x = \Phi_0 \pi d (1 - \gamma) \alpha d_x \, , \tag{6.19}$$
$$I_y = \Phi_0 \pi d (1 - \gamma) \alpha d_y \, , \tag{6.20}$$
$$I_z = \Phi_0 \pi d (s + 2\gamma \alpha d_z) \, , \tag{6.21}$$

where $d = \cos\theta_{\rm min} - \cos\theta_{\rm max}$, $s = \cos\theta_{\rm min} + \cos\theta_{\rm max}$, $p = \cos\theta_{\rm min} \cdot \cos\theta_{\rm max}$ and $\gamma = (s^2 - p)/3$. We can now invert the relations for I_0 and $\mathbf{I}$ to find the dipole parameters as

$$\alpha d_x = \frac{I_x}{s I_z - 2\gamma I_0} \frac{\gamma - p}{\gamma - 1} \, , \tag{6.22}$$
$$\alpha d_y = \frac{I_y}{s I_z - 2\gamma I_0} \frac{\gamma - p}{\gamma - 1} \, , \tag{6.23}$$
$$\alpha d_z = \frac{s I_0 - 2 I_z}{s I_z - 2\gamma I_0} \, . \tag{6.24}$$

The dipole parameters can then be evaluated by considering the values of S_0 and $\mathbf{S}$ obtained from the observed events. In particular, the dipole amplitude is given by

$$\alpha = \sqrt{\frac{\left(\frac{\gamma - p}{\gamma - 1}\right)^2 (S_x^2 + S_y^2) + (s S_0 - 2 S_z)^2}{(2\gamma S_0 - s S_z)^2}} \, , \tag{6.25}$$

and the dipole direction is given by the angles

$$\phi_d = \arctan\left(\frac{d_y}{d_x}\right) = \arctan\left(\frac{S_y}{S_x}\right) \, , \tag{6.26}$$

and

$$\theta_d = \arcsin\left(\frac{d_z}{d}\right) = \arcsin\left(\frac{2 S_z - s S_0}{\sqrt{\left(\frac{\gamma - p}{\gamma - 1}\right)^2 (S_x^2 + S_y^2) + (s S_0 - 2 S_z)^2}}\right) \, . \tag{6.27}$$

In this way, all the three-dimensional information about the dipole vector can be reconstructed even with a partial sky coverage.

6.2 Spherical harmonic decomposition

In Sec. 6.1, we have assumed that the CR flux is given by a purely dipolar distribution of arrival directions. However, higher order features, such as a quadrupolar component, are also possible. In general, the flux function $\Phi(\hat{\mathbf{n}})$ can be written as in Eq. (3.6)

$$\Phi(\hat{\mathbf{n}}) = \Phi_0 \left(1 + \mathbf{d}\cdot\hat{\mathbf{n}} + \frac{1}{2}\hat{\mathbf{n}}\cdot\mathbf{Q}\cdot\hat{\mathbf{n}} + ...\right) , \tag{6.28}$$

where $\mathbf{d}$ is the dipole vector and $\mathbf{Q}$ is the symmetric quadrupole tensor. Moreover, the flux $\Phi(\hat{\mathbf{n}})$ can also be decomposed into spherical harmonics as in Eq. (3.4). It is then clear that $\mathbf{d}$ and $\mathbf{Q}$ can be written as functions of the spherical coefficients a_{lm}. Similarly, the factor Φ_0 will also be proportional to the coefficient a_{00}. In this section, we derive the expressions for Φ_0, $\mathbf{d}$ and $\mathbf{Q}$ as functions of the spherical coefficients a_{lm}.

Before starting with the derivation, two things need to be clarified. We use the spherical harmonic normalization so that

$$\int d\hat{\mathbf{n}}\, Y_{lm}(\hat{\mathbf{n}}) Y^*_{l'm'}(\hat{\mathbf{n}}) = \delta_{ll'}\delta_{mm'} , \tag{6.29}$$

from which we see that the first harmonic is given by $Y_{00}(\hat{\mathbf{n}}) = 1/\sqrt{4\pi}$. Second, since our flux function $\Phi(\hat{\mathbf{n}})$ is a real value function, the property $a_{l-m} = (-1)^m a^*_{lm}$ holds and, in particular, it implies that the coefficients a_{l0} are always real numbers.

We can now write Eq. (6.28) explicitly as

$$\begin{aligned}\Phi(\hat{\mathbf{n}}) = \Phi_0 \Big(1 &+ d_x \sin\theta\cos\phi + d_y \sin\theta\sin\phi + d_z\cos\theta + \frac{Q_{xx}}{2}\sin^2\theta\cos^2\phi \\ &+ Q_{xy}\sin^2\theta\cos\phi\sin\phi + Q_{xz}\sin\theta\cos\theta\cos\phi \\ &+ \frac{Q_{yy}}{2}\sin^2\theta\sin^2\phi + Q_{yz}\sin\theta\cos\theta\sin\phi + \frac{Q_{zz}}{2}\cos^2\theta + ...\Big) .\end{aligned} \tag{6.30}$$

We can compute the same expression, but taking into account the decomposition into spherical harmonics up to $l = 2$. We obtain that

$$\begin{aligned}\Phi(\hat{\mathbf{n}}) = &\frac{a_{00}}{\sqrt{4\pi}} - \frac{a_{11}}{2}\sqrt{\frac{3}{2\pi}}\sin\theta e^{i\phi} + \frac{a_{10}}{2}\sqrt{\frac{3}{\pi}}\cos\theta + \frac{a_{1-1}}{2}\sqrt{\frac{3}{2\pi}}\sin\theta e^{-i\phi} \\ &+ \frac{a_{22}}{4}\sqrt{\frac{15}{2\pi}}\sin^2\theta e^{2i\phi} - \frac{a_{21}}{2}\sqrt{\frac{15}{2\pi}}\sin\theta\cos\theta e^{i\phi} + \frac{a_{20}}{4}\sqrt{\frac{5}{\pi}}\left(3\cos^2\theta - 1\right) \\ &+ \frac{a_{2-1}}{2}\sqrt{\frac{15}{2\pi}}\sin\theta\cos\theta e^{-i\phi} + \frac{a_{2-2}}{4}\sqrt{\frac{15}{2\pi}}\sin^2\theta e^{-2i\phi} + ...\end{aligned} \tag{6.31}$$

We can now use the property of a^*_{lm} considering that, given a complex number z, the sum $z + z^*$

is equal to $2\Re(z)$ and the difference $z - z^*$ is equal to $2i\Im(z)$[2]. We obtain that

$$\begin{aligned}\Phi(\hat{\mathbf{n}}) = \frac{a_{00}}{\sqrt{4\pi}} \Bigg[& 1 - \sqrt{6}\frac{\Re(a_{11})}{a_{00}} \sin\theta\cos\phi + \sqrt{6}\frac{\Im(a_{11})}{a_{00}} \sin\theta\sin\phi + \sqrt{3}\frac{a_{10}}{a_{00}}\cos\theta \\ & + \left(\sqrt{\frac{15}{2}}\frac{\Re(a_{22})}{a_{00}} - \frac{\sqrt{5}}{2}\frac{a_{20}}{a_{00}}\right)\sin^2\theta\cos^2\phi - 2\sqrt{\frac{15}{2}}\frac{\Im(a_{22})}{a_{00}}\sin^2\theta\cos\phi\sin\phi \\ & - 2\sqrt{\frac{15}{2}}\frac{\Re(a_{21})}{a_{00}}\sin\theta\cos\theta\cos\phi - \left(\sqrt{\frac{15}{2}}\frac{\Re(a_{22})}{a_{00}} + \frac{\sqrt{5}}{2}\frac{a_{20}}{a_{00}}\right)\sin^2\theta\sin^2\phi \\ & + 2\sqrt{\frac{15}{2}}\frac{\Im(a_{21})}{a_{00}}\sin\theta\cos\theta\sin\phi + \sqrt{5}\frac{a_{20}}{a_{00}}\cos^2\theta + \ldots\Bigg] \,. \end{aligned} \tag{6.32}$$

By comparing the decompositions in Eqs. (6.30) and (6.32) we can write the expressions for Φ_0, $\mathbf{d}$ and $\mathbf{Q}$ as

$$\Phi_0 = \frac{a_{00}}{\sqrt{4\pi}} \,, \tag{6.33}$$

$$\mathbf{d} = \begin{pmatrix} -\sqrt{6}\dfrac{\Re(a_{11})}{a_{00}} \\ \sqrt{6}\dfrac{\Im(a_{11})}{a_{00}} \\ \sqrt{3}\dfrac{a_{10}}{a_{00}} \end{pmatrix} \,, \tag{6.34}$$

and

$$\mathbf{Q} = \begin{pmatrix} 2\sqrt{\dfrac{15}{2}}\dfrac{\Re(a_{22})}{a_{00}} - \sqrt{5}\dfrac{a_{20}}{a_{00}} & -2\sqrt{\dfrac{15}{2}}\dfrac{\Im(a_{22})}{a_{00}} & -2\sqrt{\dfrac{15}{2}}\dfrac{\Re(a_{21})}{a_{00}} \\ & -2\sqrt{\dfrac{15}{2}}\dfrac{\Re(a_{22})}{a_{00}} - \sqrt{5}\dfrac{a_{20}}{a_{00}} & 2\sqrt{\dfrac{15}{2}}\dfrac{\Im(a_{21})}{a_{00}} \\ & & 2\sqrt{5}\dfrac{a_{20}}{a_{00}} \end{pmatrix} \,. \tag{6.35}$$

As we have seen in Sec. 3.2.3 and Appendix A.1, the spherical coefficients a_{lm} can be combined to obtain the angular power spectrum of $\Phi(\hat{\mathbf{n}})$, defined as

$$\mathcal{C}_l = \frac{1}{2l+1}\sum_{m=-l}^{l} |a_{lm}|^2 \,. \tag{6.36}$$

[2]Given a complex number $z = a + ib$, we have that $\Re(z) = a$ and $\Im(z) = b$.

We can see that each multipole l in $\mathcal{C}_l$ can be associated with a term in Eq. (6.28). In particular

$$\mathcal{C}_0 = |a_{00}|^2 = 4\pi\Phi_0^2\,, \tag{6.37}$$

$$\mathcal{C}_1 = \frac{|a_{10}|^2 + 2|a_{11}|^2}{3} = \frac{d^2|a_{00}|^2}{9} = \frac{4\pi}{9}\Phi_0^2 d^2\,, \tag{6.38}$$

$$\mathcal{C}_2 = \frac{|a_{20}|^2 + 2|a_{21}|^2 + 2|a_{22}|^2}{5} = \frac{3Q^2|a_{00}^2|}{50} = \frac{12\pi}{50}\Phi_0^2 Q^2\,, \tag{6.39}$$

where $d^2 = \sum_{i=1}^{3} d_i^2$ and $Q^2 = \sum_{i,j} Q_{ij}^2/9$. We can then write the dipole and quadrupole strengths as

$$d = \sqrt{\frac{9\,\mathcal{C}_1}{4\pi\Phi_0^2}} = 3\sqrt{\frac{\mathcal{C}_1}{\mathcal{C}_0}}\,, \tag{6.40}$$

$$Q = \sqrt{\frac{50\,\mathcal{C}_2}{12\pi\Phi_0^2}} = \sqrt{\frac{50}{3}\frac{\mathcal{C}_2}{\mathcal{C}_0}}\,. \tag{6.41}$$

The results in Eqs. (6.40) and (6.41) give the connection between the angular power spectrum of $\Phi(\hat{\mathbf{n}})$ and the strengths of the dipole and quadrupole components.

6.2.1 Effect of the exposure

In the previous section we considered the decomposition of the flux function $\Phi(\hat{\mathbf{n}})$ into spherical harmonics. This decomposition is characterized by the spherical coefficients a_{lm}, given by

$$a_{lm} = \int d\hat{\mathbf{n}}\,\Phi(\hat{\mathbf{n}}) Y_{lm}^*(\hat{\mathbf{n}})\,. \tag{6.42}$$

However, CR observatories usually have only a partial and non-uniform view of the sky. As we introduced in Sec. 6.1.1, the field of view of a CR experiment is characterized by the exposure function $\mathcal{E}(\hat{\mathbf{n}})$. This means that the flux $\Phi(\hat{\mathbf{n}})$ cannot be observed directly. The observable quantity is the function

$$n(\hat{\mathbf{n}}) = \mathcal{E}(\hat{\mathbf{n}}) \cdot \Phi(\hat{\mathbf{n}}) \tag{6.43}$$

is the observable quantity. The function $n(\hat{\mathbf{n}})$ represents the sky distribution of the number of events, and its spherical decomposition is given by

$$b_{lm} = \int d\hat{\mathbf{n}}\, n(\hat{\mathbf{n}}) Y_{lm}^*(\hat{\mathbf{n}})\,. \tag{6.44}$$

We can then find the connection between the two sets of coefficients a_{lm} and b_{lm} as done in [313, 314] by inserting the definition into Eq. (6.43) in Eq. (6.44) as

$$\begin{aligned} b_{lm} &= \int d\hat{\mathbf{n}}\, n(\hat{\mathbf{n}}) Y_{lm}^*(\hat{\mathbf{n}}) = \int d\hat{\mathbf{n}}\, \mathcal{E}(\hat{\mathbf{n}})\Phi(\hat{\mathbf{n}}) Y_{lm}^*(\hat{\mathbf{n}}) \\ &= \sum_{l'=0}^{+\infty} \sum_{m'=-l'}^{l'} a_{l'm'} \int d\hat{\mathbf{n}}\, Y_{l'm'}(\hat{\mathbf{n}})\mathcal{E}(\hat{\mathbf{n}}) Y_{lm}^*(\hat{\mathbf{n}}) \\ &= \sum_{l'=0}^{+\infty} \sum_{m'=-l'}^{l'} a_{l'm'} [K]_{l'm'lm}\,, \end{aligned} \tag{6.45}$$

where we have defined the kernel tensor components as

$$[K]_{l'm'lm} = \int d\hat{\mathbf{n}}\, Y_{l'm'}(\hat{\mathbf{n}})\mathcal{E}(\hat{\mathbf{n}})Y^*_{lm}(\hat{\mathbf{n}})\,. \tag{6.46}$$

The inversion of Eq. (6.45) (which involves the calculation of $[K^{-1}]_{l'm'lm}$, see [314] for more details) gives the relation between the flux coefficients a_{lm} and the coefficients b_{lm} obtained when the exposure is taken into account. In practice, since only a finite number of events can be observed, an estimate $\bar{b}_{lm}$ of the coefficients b_{lm} is obtained. However, this estimate can be used to find the estimate $\bar{a}_{lm}$ of the flux coefficients a_{lm} as in Eq. (6.45) [314].

6.3 Angular power spectrum expectation

In Sec. 6.1.1 we have defined the normalized flux function $\phi(\hat{\mathbf{n}})$ given by a sequence of N arrival directions $\hat{\mathbf{n}}_1$, $\hat{\mathbf{n}}_2$, ..., $\hat{\mathbf{n}}_N$. This function, also called signal function [311, 312, 315], can be written as

$$\phi(\hat{\mathbf{n}}) = \frac{1}{\mathcal{N}}\sum_{i=1}^{N}\omega(\hat{\mathbf{n}}_i)\delta(\hat{\mathbf{n}}-\hat{\mathbf{n}}_i)\,, \tag{6.47}$$

where $\mathcal{N} = \sum_{i=1}^{N}\omega(\hat{\mathbf{n}}_i)$ and $\omega(\hat{\mathbf{n}}_i)$ is the weight factor of the event i. In general, the weight factor can be written as $\omega(\hat{\mathbf{n}}_i) = \omega_i/\mathcal{E}(\hat{\mathbf{n}}_i)$, where the arrival direction dependent exposure $\mathcal{E}(\hat{\mathbf{n}}_i)$ is separated from the arrival direction independent factor ω_i, which can be different for different events. The weight factor ω_i may be given by some weighting procedure in UHECR simulations such as different injection scenarios (see Sec. 5.1) or the use of a magnetic lens (see Sec. 5.2).

The signal function defined in Eq. (6.47) is characterized by the assumption that different arrival directions can be distinguished regardless of their angular separation in the sky (i.e. an infinite sky resolution is assumed). If this assumption is not fulfilled (as is often the case when considering the sky map distribution of simulated UHECRs), the definition of $\phi(\hat{\mathbf{n}})$ will be different. If we consider a finite number of pixels in the sky centered in the direction $\hat{\mathbf{p}}_i$, where $i = 1, ..., N_p$, and N_p is the total number of pixels, then the signal function $\phi(\hat{\mathbf{n}})$ is given by

$$\phi(\hat{\mathbf{n}}) = \frac{1}{\mathcal{N}}\sum_{i=1}^{N_p}\mathcal{N}(\hat{\mathbf{p}}_i)\,\Delta(\hat{\mathbf{n}}-\hat{\mathbf{p}}_i)\,, \tag{6.48}$$

where $\mathcal{N} = \sum_{i=1}^{N_p}\mathcal{N}(\hat{\mathbf{p}}_i)$ and $\mathcal{N}(\hat{\mathbf{p}}_i)$ is defined as the sum of the particle weights $\omega(\hat{\mathbf{n}}_j)$ within the pixel i. The function $\Delta(\hat{\mathbf{n}}-\hat{\mathbf{p}}_i)$ is defined as

$$\Delta(\hat{\mathbf{n}}-\hat{\mathbf{p}}_i) = \begin{cases} \dfrac{1}{\Delta\Omega_i} & \text{for } \hat{\mathbf{n}} \text{ in the pixel } \hat{\mathbf{p}}_i; \\ 0 & \text{otherwise,} \end{cases} \tag{6.49}$$

where $\Delta\Omega_i$ is the angular size of the pixel $\hat{\mathbf{p}}_i$. Note that $\phi(\hat{\mathbf{n}})$ is still normalised to 1. The quantity $\mathcal{N}(\hat{\mathbf{p}}_i)$ can then be written as

$$\mathcal{N}(\hat{\mathbf{p}}_i) = \Delta\Omega_i\sum_{j=1}^{N}\omega(\hat{\mathbf{n}}_j)\,\Delta(\hat{\mathbf{n}}_j-\hat{\mathbf{p}}_i)\,. \tag{6.50}$$

In the following sections we discuss the calculation of the angular power spectrum of the signal functions in Eqs. (6.47) and (6.48). In particular, given a probability distribution function in the sky, $\Psi(\hat{\mathbf{n}})$, and considering each arrival direction as an independent event, the total probability distribution of N events is given by

$$\Psi_N(\hat{\mathbf{n}}_1,\, \hat{\mathbf{n}}_2,\, ...,\, \hat{\mathbf{n}}_N) \prod_{i=1}^{N} d\hat{\mathbf{n}}_i = \prod_{i=1}^{N} \Psi(\hat{\mathbf{n}}_i) d\hat{\mathbf{n}}_i \,. \tag{6.51}$$

We then obtain the expected values of the signal functions and their angular power spectra, assuming the probability distribution $\Psi_N(\hat{\mathbf{n}})$.

6.3.1 Infinite sky resolution

We start by considering the case of infinite sky resolution, where the signal function is given by Eq. (6.47). We consider the case of N events obtained with a full sky and uniform exposure[3], i.e. $\omega(\hat{\mathbf{n}}_i) = \omega_i$. The signal function is then given by

$$\phi(\hat{\mathbf{n}}) = \frac{1}{\mathcal{N}} \sum_{i=1}^{N} \omega_i \, \delta(\hat{\mathbf{n}} - \hat{\mathbf{n}}_i) \,, \tag{6.52}$$

where $\mathcal{N} = \sum_{i=1}^{N} \omega_i$. The expected value of $\phi(\hat{\mathbf{n}})$ with respect to the distribution function $\Psi(\hat{\mathbf{n}})$ is given by

$$\langle \phi(\hat{\mathbf{n}}) \rangle_{\Psi_N} = \int ... \int \left(\prod_{i=1}^{N} \Psi(\hat{\mathbf{n}}_i) d\hat{\mathbf{n}}_i \right) \phi(\hat{\mathbf{n}}) = \frac{1}{\mathcal{N}} \sum_{i=1}^{N} \omega_i \int d\hat{\mathbf{n}}_i \, \Psi(\hat{\mathbf{n}}_i) \delta(\hat{\mathbf{n}} - \hat{\mathbf{n}}_i) = \Psi(\hat{\mathbf{n}}) \,. \tag{6.53}$$

The expected value of the signal function is independent of the number of arrival directions and the relative weight of the events.

To obtain the angular power spectrum of the signal function, we must first compute the spherical decomposition. The coefficients a_{lm} are given by

$$a_{lm} = \int d\hat{\mathbf{n}} \, \phi(\hat{\mathbf{n}}) Y^*_{lm}(\hat{\mathbf{n}}) = \frac{1}{\mathcal{N}} \sum_{i=1}^{N} \omega_i \int d\hat{\mathbf{n}} \, Y^*_{lm}(\hat{\mathbf{n}}) \delta(\hat{\mathbf{n}} - \hat{\mathbf{n}}_i) = \frac{1}{\mathcal{N}} \sum_{i=1}^{N} \omega_i \, Y^*_{lm}(\hat{\mathbf{n}}_i) \,, \tag{6.54}$$

which is the weighted average of the corresponding spherical harmonic in the direction of the event. The expected value of a_{lm} is then given by

$$\langle a_{lm} \rangle_{\Psi_N} = \frac{1}{\mathcal{N}} \sum_{i=1}^{N} \omega_i \, \langle Y^*_{lm}(\hat{\mathbf{n}}_i) \rangle_{\Psi_N} \,. \tag{6.55}$$

If we consider an isotropic sky distribution, we have that $\Psi^{\rm iso} = (4\pi)^{-1}$, and then $\Psi^{\rm iso}_N = (4\pi)^{-N}$, from which we have that

$$\langle Y^*_{lm}(\hat{\mathbf{n}}_i) \rangle_{\Psi^{\rm iso}_N} = \frac{1}{(4\pi)^N} \int ... \int \left(\prod_{j=1}^{N} d\hat{\mathbf{n}}_j \right) Y^*_{lm}(\hat{\mathbf{n}}_i) = \frac{1}{4\pi} \int d\hat{\mathbf{n}}_i \, Y^*_{lm}(\hat{\mathbf{n}}_i) = \frac{\delta_{l0}\delta_{m0}}{\sqrt{4\pi}} \,, \tag{6.56}$$

[3] This is the usual scenario in UHECR simulation. However, it is important to note that the results obtained under this assumption can only be compared with experimental results already corrected for exposure effects. For a direct comparison with experimental data, which are usually measured by observatories with partial and highly non-uniform exposure, the effect of $\mathcal{E}(\hat{\mathbf{n}})$ has to be included in the simulated signal function.

where we have used the property in Eq. (A.1.18). The expected spherical coefficients are given by

$$\langle a_{lm} \rangle_{\Psi_N^{\rm iso}} = \frac{1}{\mathcal{N}} \sum_{i=1}^{N} \frac{\omega_i \, \delta_{l0} \delta_{m0}}{\sqrt{4\pi}} = \frac{\delta_{l0} \delta_{m0}}{\sqrt{4\pi}} \,. \tag{6.57}$$

As expected, in the case of an isotropic distribution, the only coefficient different from zero is $a_{00} = (4\pi)^{-1/2}$.

The angular power spectrum of the signal function in Eq. (6.47) is given by

$$\mathcal{C}_l = \frac{1}{2l+1} \sum_{m=-l}^{l} |a_{lm}|^2 = \frac{1}{2l+1} \frac{1}{\mathcal{N}^2} \sum_{m=-l}^{l} \left| \sum_{i=1}^{N} \omega_i \, Y_{lm}^*(\hat{\mathbf{n}}_i) \right|^2 \,. \tag{6.58}$$

We can now use the result in Eq. (6.54) to calculate the value of $|a_{lm}|^2$ in order to obtain the expected value of the angular power spectrum. We have that

$$\begin{aligned} |a_{lm}|^2 = a_{lm} a_{lm}^* &= \frac{1}{\mathcal{N}^2} \sum_{i,j} \omega_i \, \omega_j \, Y_{lm}^*(\hat{\mathbf{n}}_i) Y_{lm}(\hat{\mathbf{n}}_j) \\ &= \frac{1}{\mathcal{N}^2} \left[\sum_{i=1}^{N} \omega_i^2 \, |Y_{lm}(\hat{\mathbf{n}}_i)|^2 + \sum_{i \neq j} \omega_i \, \omega_j \, Y_{lm}^*(\hat{\mathbf{n}}_i) Y_{lm}(\hat{\mathbf{n}}_j) \right] \,. \end{aligned} \tag{6.59}$$

The expected value of $|a_{lm}|^2$ under isotropy can be obtained by considering the quantities

$$\begin{aligned} \left\langle |Y_{lm}(\hat{\mathbf{n}}_i)|^2 \right\rangle_{\Psi_N^{\rm iso}} &= \frac{1}{(4\pi)^N} \int \ldots \int \left(\prod_{j=1}^{N} d\hat{\mathbf{n}}_j \right) |Y_{lm}(\hat{\mathbf{n}}_i)|^2 \\ &= \frac{1}{4\pi} \int d\hat{\mathbf{n}}_i \, |Y_{lm}(\hat{\mathbf{n}}_i)|^2 = \frac{1}{4\pi} \,, \end{aligned} \tag{6.60}$$

and

$$\begin{aligned} \langle Y_{lm}^*(\hat{\mathbf{n}}_i) Y_{lm}(\hat{\mathbf{n}}_j) \rangle_{\Psi_N^{\rm iso}} &= \frac{1}{(4\pi)^N} \int \ldots \int \left(\prod_{k=1}^{N} d\hat{\mathbf{n}}_k \right) Y_{lm}^*(\hat{\mathbf{n}}_i) Y_{lm}(\hat{\mathbf{n}}_j) \\ &= \frac{1}{(4\pi)^2} \int \int d\hat{\mathbf{n}}_i \, d\hat{\mathbf{n}}_j \, Y_{lm}^*(\hat{\mathbf{n}}_i) Y_{lm}(\hat{\mathbf{n}}_j) = \frac{\delta_{l0} \delta_{m0}}{4\pi} \,. \end{aligned} \tag{6.61}$$

We then obtain that

$$\left\langle |a_{lm}|^2 \right\rangle_{\Psi_N^{\rm iso}} = \frac{1}{4\pi \mathcal{N}^2} \left[\sum_{i=1}^{N} \omega_i + \delta_{l0} \delta_{m0} \sum_{i \neq j} \omega_i \, \omega_j \right] \,, \tag{6.62}$$

from which the angular power spectrum is given by

$$\langle \mathcal{C}_l \rangle_{\Psi_N^{\rm iso}} = \begin{cases} \dfrac{1}{4\pi} & l = 0; \\ \dfrac{1}{4\pi \mathcal{N}^2} \displaystyle\sum_{i=1}^{N} \omega_i^2 & l \neq 0. \end{cases} \tag{6.63}$$

The angular power spectrum in Eq. (6.63) is characterized by a constant monopole component, while the components for $l \neq 0$ depend on the combination of the weight factors ω_i. The fact that $\mathcal{C}_{l\neq 0}$ are different from zero, unlike the spherical coefficients a_{lm}, is due to the fact that the angular power spectrum is linear in $|a_{lm}|^2$ and not in the spherical coefficients. However, the components $\mathcal{C}_{l\neq 0}$ converge to zero for a large number of events since the denominator contains the mixed products $\omega_i\,\omega_j > 0$. In the simple case of $\omega_i = 1$, and then $\mathcal{N} = N$, we obtain that

$$\langle \mathcal{C}_l \rangle_{\Psi_{\rm iso}} = \begin{cases} \dfrac{1}{4\pi} & l = 0; \\ \dfrac{1}{4\pi N} & l \neq 0; \end{cases} \tag{6.64}$$

where it is clear that $\mathcal{C}_{l\neq 0} \simeq 0$ for $N \gg 1$.

6.3.2 Finite number of pixels

We can now repeat the analysis described in the previous section in the case of finite sky resolution, where the signal function is given by Eqs. (6.48) and (6.50), and we assume that $\omega(\hat{\mathbf{n}}_i) = \omega_i$. The expected value of $\phi(\hat{\mathbf{n}})$ with respect to the distribution function $\Psi(\hat{\mathbf{n}})$ is now given by

$$\begin{aligned} \langle \phi(\hat{\mathbf{n}}) \rangle_{\Psi_N} &= \frac{1}{\mathcal{N}} \sum_{i=1}^{N_p} \sum_{j=1}^{N} \omega_j \, \Delta\Omega_i \int \ldots \int \left(\prod_{k=1}^{N} \Psi(\hat{\mathbf{n}}_k) d\hat{\mathbf{n}}_k \right) \Delta(\hat{\mathbf{n}}_j - \hat{\mathbf{p}}_i) \Delta(\hat{\mathbf{n}} - \hat{\mathbf{p}}_i) \\ &= \frac{1}{\mathcal{N}} \sum_{i=1}^{N_p} \sum_{j=1}^{N} \omega_j \, \Delta\Omega_i \Delta(\hat{\mathbf{n}} - \hat{\mathbf{p}}_i) \int d\hat{\mathbf{n}}_j \, \Psi(\hat{\mathbf{n}}_j) \Delta(\hat{\mathbf{n}}_j - \hat{\mathbf{p}}_i) \\ &= \frac{1}{\mathcal{N}} \sum_{i=1}^{N_p} \sum_{j=1}^{N} \omega_j \, \Delta\Omega_i \Delta(\hat{\mathbf{n}} - \hat{\mathbf{p}}_i) \overline{\Psi}(\hat{\mathbf{p}}_i) \\ &= \sum_{i=1}^{N_p} \Delta\Omega_i \Delta(\hat{\mathbf{n}} - \hat{\mathbf{p}}_i) \overline{\Psi}(\hat{\mathbf{p}}_i) \, , \end{aligned} \tag{6.65}$$

where we have defined the mean value of $\Psi(\hat{\mathbf{n}})$ within the pixel in direction $\hat{\mathbf{p}}_i$ as $\overline{\Psi}(\hat{\mathbf{p}}_i)$. We can see that, given a generic direction $\hat{\mathbf{v}}$ contained in the pixel $\hat{\mathbf{p}}_k$ the expected value of the signal function is given by $\langle \phi(\hat{\mathbf{v}}) \rangle_{\Psi_N} = \overline{\Psi}(\hat{\mathbf{p}}_k)$.The effect of a finite sky resolution is already visible in the expected value of the signal function, which corresponds to the average value of the expected distribution function within the pixellation of the sky. In the case of an isotropic distribution, we obtain that $\langle \phi(\hat{\mathbf{n}}) \rangle_{\Psi_N^{\rm iso}} = (4\pi)^{-1}$.

The spherical decomposition of (6.48) can be obtained as

$$a_{lm} = \int d\hat{\mathbf{n}} \, \phi(\hat{\mathbf{n}}) Y^*_{lm}(\hat{\mathbf{n}}) = \frac{1}{\mathcal{N}} \sum_{i=1}^{N_p} \mathcal{N}_i \int d\hat{\mathbf{n}} \, \Delta(\hat{\mathbf{n}} - \hat{\mathbf{p}}_i) Y^*_{lm}(\hat{\mathbf{n}}) \, . \tag{6.66}$$

We can define the coefficients $f^*_{lm,i}$ as

$$f^*_{lm,i} = \int d\hat{\mathbf{n}} \, \Delta(\hat{\mathbf{n}} - \hat{\mathbf{p}}_i) Y^*_{lm}(\hat{\mathbf{n}}) = \frac{1}{\Delta\Omega_i} \int_{\Delta\Omega_i} d\hat{\mathbf{n}} \, Y^*_{lm}(\hat{\mathbf{n}}) \, , \tag{6.67}$$

and then

$$a_{lm} = \frac{1}{\mathcal{N}} \sum_{i=1}^{N_p} \mathcal{N}_i f^*_{lm,i} \,. \tag{6.68}$$

From Eq. (6.67) we can see that the coefficient $f_{lm,i}$ corresponds to the average value of the spherical harmonic $Y_{lm}(\hat{\mathbf{n}})$ within the pixel in the direction $\hat{\mathbf{p}}_i$. Given the spherical harmonic normalization used in this thesis, we have that $f^*_{00,i} = (4\pi)^{-1/2}$, and then $a_{00} = (4\pi)^{-1/2}$, independent of the number of pixels. The expected value of the spherical coefficients is given by

$$\langle a_{lm} \rangle_{\Psi_N} = \frac{1}{\mathcal{N}} \sum_{i=1}^{N_p} \langle \mathcal{N}_i \rangle_{\Psi_N} f^*_{lm,i} \,, \tag{6.69}$$

where the quantity $\langle \mathcal{N}_i \rangle_{\Psi_N}$ can be obtained as

$$\begin{aligned} \langle \mathcal{N}_i \rangle_{\Psi_N} &= \Delta\Omega_i \sum_{j=1}^{N} \omega_j \int \dots \int \left(\prod_{k=1}^{N} d\hat{\mathbf{n}}_k \Psi(\hat{\mathbf{n}}_k) \right) \Delta(\hat{\mathbf{n}}_j - \hat{\mathbf{p}}_i) \\ &= \Delta\Omega_i \sum_{j=1}^{N} \omega_j \int d\hat{\mathbf{n}}_j \, \Delta(\hat{\mathbf{n}}_j - \hat{\mathbf{p}}_i) \Psi(\hat{\mathbf{n}}_j) = \mathcal{N} \Delta\Omega_i \overline{\Psi}(\hat{\mathbf{p}}_i) \,, \end{aligned} \tag{6.70}$$

and then

$$\langle a_{lm} \rangle_{\Psi_N} = \sum_{i=1}^{N_p} \Delta\Omega_i \overline{\Psi}(\hat{\mathbf{p}}_i) f^*_{lm,i} \,. \tag{6.71}$$

In the case of an isotropic distribution, we can then calculate the expected value of the spherical coefficients as

$$\langle a_{lm} \rangle_{\Psi_N^{\rm iso}} = \frac{1}{4\pi} \sum_{i=1}^{N_p} \Delta\Omega_i f^*_{lm,i} = \frac{1}{4\pi} \sum_{i=1}^{N_p} \int_{\Delta\Omega_i} d\hat{\mathbf{n}} \, Y^*_{lm}(\hat{\mathbf{n}}) = \frac{1}{4\pi} \int d\hat{\mathbf{n}} \, Y^*_{lm}(\hat{\mathbf{n}}) = \frac{\delta_{l0}\delta_{m0}}{\sqrt{4\pi}} \,. \tag{6.72}$$

As expected, under the assumption of an isotropic sky, the only spherical coefficient different from zero is again $a_{00} = (4\pi)^{-1/2}$.

The angular power spectrum of the signal function in Eq. (6.48) is now given by

$$\mathcal{C}_l = \frac{1}{2l+1} \sum_{m=-l}^{l} |a_{lm}|^2 = \frac{1}{2l+1} \frac{1}{\mathcal{N}^2} \sum_{m=-l}^{l} \left| \sum_{i=1}^{N_p} \mathcal{N}_i f^*_{lm,i} \right|^2 \,. \tag{6.73}$$

The expectation value of the angular power spectrum can be obtained by estimating the modulus square of the angular coefficients, as done in the case of infinite sky resolution. The modulus square of the spherical coefficients is now given by

$$\begin{aligned} |a_{lm}|^2 &= \frac{1}{\mathcal{N}^2} \sum_{i,j=1}^{N_p} \mathcal{N}_i \mathcal{N}_j f^*_{lm,i} f_{lm,j} \\ &= \frac{1}{\mathcal{N}^2} \left[\sum_{i=1}^{N_p} \mathcal{N}_i^2 \, |f_{lm,i}|^2 + \sum_{i \neq j} \mathcal{N}_i \mathcal{N}_j f^*_{lm,i} f_{lm,j} \right] \,. \end{aligned} \tag{6.74}$$

We can write the two factors $\mathcal{N}_i^2$ and $\mathcal{N}_i\mathcal{N}_j$ in a unique way as

$$\begin{aligned}\mathcal{N}_i\mathcal{N}_j &= \Delta\Omega_i\Delta\Omega_j \sum_{s,t=1}^{N} \omega_s\,\omega_t\,\Delta(\hat{\mathbf{n}}_s - \hat{\mathbf{p}}_i)\Delta(\hat{\mathbf{n}}_t - \hat{\mathbf{p}}_j) \\ &= \delta_{ij}\Delta\Omega_j \sum_{s=1}^{N} \omega_s^2\,\Delta(\hat{\mathbf{n}}_s - \hat{\mathbf{p}}_j) + \Delta\Omega_i\Delta\Omega_j \sum_{s\neq t} \omega_s\,\omega_t\,\Delta(\hat{\mathbf{n}}_s - \hat{\mathbf{p}}_i)\Delta(\hat{\mathbf{n}}_t - \hat{\mathbf{p}}_j)\,. \end{aligned} \tag{6.75}$$

where the value of $\mathcal{N}_i^2$ corresponds to the case $i = j$. The expected values of $\mathcal{N}_i^2$ and $\mathcal{N}_i\mathcal{N}_j$ are then given by

$$\begin{aligned}\langle N_i N_j\rangle_{\Psi_N} &= \delta_{ij}\Delta\Omega_j \sum_{s=1}^{N} \omega_s^2 \int d\hat{\mathbf{n}}_s\,\Psi(\hat{\mathbf{n}}_s)\Delta(\hat{\mathbf{n}}_s - \hat{\mathbf{p}}_j) \\ &\quad + \Delta\Omega_i\Delta\Omega_j \sum_{s\neq t} \omega_s\,\omega_t \int d\hat{\mathbf{n}}_s\,\Psi(\hat{\mathbf{n}}_s)\,\Delta(\hat{\mathbf{n}}_s - \hat{\mathbf{p}}_i)\Delta(\hat{\mathbf{n}}_t - \hat{\mathbf{p}}_j) \\ &= \delta_{ij}\Delta\Omega_j \sum_{s=1}^{N} \omega_s^2\,\overline{\Psi}(\hat{\mathbf{p}}_i) + \Delta\Omega_i\Delta\Omega_j \sum_{s\neq t} \omega_s\,\omega_t\,\overline{\Psi}(\hat{\mathbf{p}}_i)\overline{\Psi}(\hat{\mathbf{p}}_j)\,, \end{aligned} \tag{6.76}$$

from which we obtain the expected value of the modulus square of the spherical coefficients

$$\left\langle |a_{lm}|^2 \right\rangle_{\Psi_N} = \frac{\sum_{j=1}^{N}\omega_j^2}{\mathcal{N}^2} \sum_{i=1}^{N_p} \Delta\Omega_i\overline{\Psi}(\hat{\mathbf{p}}_i)\,|f_{lm,i}|^2 + \frac{\sum_{j\neq k}^{N}\omega_j\omega_k}{\mathcal{N}^2} \left| \sum_{i=1}^{N_p} \Delta\Omega_i\overline{\Psi}(\hat{\mathbf{p}}_i) f_{lm,i}^* \right|^2 . \tag{6.77}$$

If we consider again the prediction under an isotropic sky distribution, and we also assume that the sky is divided into pixels with the same angular size $\Delta\Omega$, we obtain that

$$\left\langle |a_{lm}|^2 \right\rangle_{\Psi_N^{\rm iso}} = \frac{\Delta\Omega}{4\pi}\frac{\sum_{j=1}^{N}\omega_j^2}{\mathcal{N}^2} \sum_{i=1}^{N_p} |f_{lm,i}|^2 + \frac{1}{4\pi}\frac{\sum_{j\neq k}\omega_j\omega_k}{\mathcal{N}^2}\delta_{l0}\delta_{m0}\,, \tag{6.78}$$

and then the angular power spectrum

$$\langle \mathcal{C}_l\rangle_{\Psi_{\rm iso}} = \begin{cases} \dfrac{1}{4\pi} & l = 0; \\ \dfrac{1}{2l+1}\dfrac{\Delta\Omega}{4\pi}\dfrac{\sum_{j=1}^{N}\omega_j^2}{\mathcal{N}^2} \displaystyle\sum_{m=-l}^{l}\sum_{i=1}^{N_p} |f_{lm,i}|^2 & l \neq 0. \end{cases} \tag{6.79}$$

As expected, the monopole component of (6.79) does not depend on the number of pixels neither on the number of arrival directions. The components for $l \neq 0$ go to zero for N going to infinity and depend on the pixelation used. If we consider the scenario where $\omega_i = 1$ for all the particles, the prediction of the angular power spectrum becomes

$$\langle \mathcal{C}_l\rangle_{\Psi_{\rm iso}} = \begin{cases} \dfrac{1}{4\pi} & l = 0; \\ \dfrac{1}{2l+1}\dfrac{\Delta\Omega}{4\pi N} \displaystyle\sum_{m=-l}^{l}\sum_{i=1}^{N_p} |f_{lm,i}|^2 & l \neq 0. \end{cases} \tag{6.80}$$

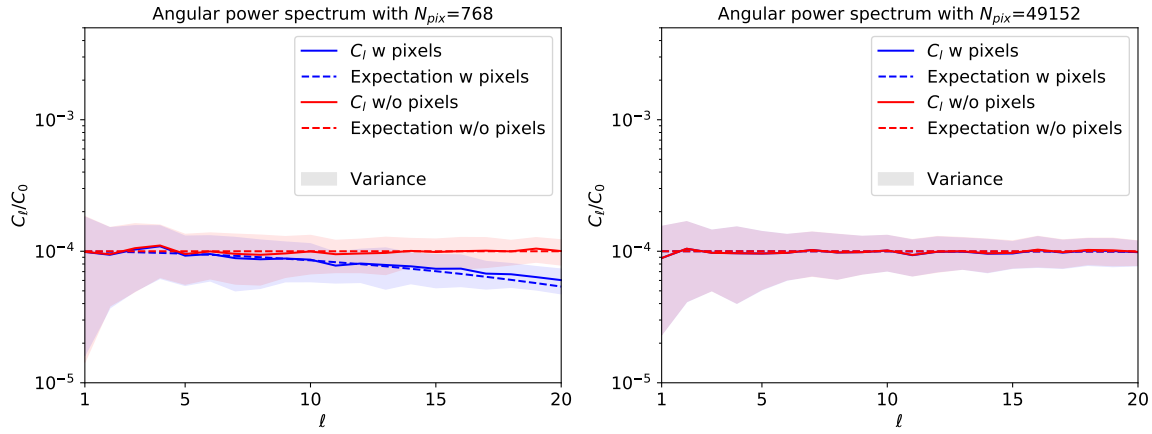

Figure 6.1: Left: Mean angular power spectra normalized to the monopole (i.e. $\mathcal{C}_l/\mathcal{C}_0$) of 100 isotropic arrival direction distributions with 15,000 events each with $N_{\rm pix} = 768$ pixels. The angular power spectra of (6.73) (blue line) and (6.58) (red line) are shown, assuming all weighting factors $\omega_i = 1$, together with the isotropic predictions (6.80) (blue dashed line) and (6.64) (red dashed line). The shaded areas indicate the estimated variance of the angular power spectra. Right: same as left panel, but for $N_{\rm pix} = 49,152$ pixels. Figure taken from [316].

As the number of pixels goes to infinity, the sum of the coefficients $f_{lm,i}$ is such that $\sum_{i=1}^{N_p} |f_{lm,i}|^2 \to \Delta\Omega$. Therefore, the predictions in Eqs. (6.79) and (6.80) converge to the results in Eqs. (6.63) and (6.64), respectively.

The required angular resolution on the sky is related to the maximum spherical coefficient considered in the analysis. In particular, each spherical parameter l is related to the angular scale $\theta \sim \pi/l$ and the corresponding solid angle is given by

$$\Delta\Omega = 4\pi \sin^2\left(\frac{\theta}{2}\right) \simeq \pi\,\theta^2\,, \tag{6.81}$$

where the last equality holds for small angles. Therefore, for the solid angle we obtain that $\Delta\Omega \simeq \pi^3/l^2$. In this thesis, we analyse the sky map distributions by using the `Python` package `HEALPY`[4] [317], based on the Hierarchical Equal Area isoLatitude Pixellization (`HEALPix`[5]) scheme [318]. In the `HEALPix` scheme, the spherical surface is divided into quadrilaterals of equal area and different shapes. The basic resolution of the spherical grid in the `HEALPix` scheme is 12 pixels. The parameter $N_{\rm side}$, usually defined as a power of 2, gives the number of divisions along the side of a fundamental quadrilateral. Therefore, the final number of pixels is given by

$$N_{\rm pix} = 12 \cdot N_{\rm side}^2, \tag{6.82}$$

and the corresponding angular size of a single pixel is

$$\Delta\Omega_{\rm pix} = \frac{4\pi}{N_{\rm pix}} = \frac{\pi}{3 \cdot N_{\rm side}^2}. \tag{6.83}$$

[4]The package is available at `https://healpy.readthedocs.io/en/latest/index.html`
[5]More information can be found at `https://healpix.sourceforge.io`

In the study of UHECR anisotropies presented in the next chapter, we consider a maximum spherical parameter $l_{\max} = 20$, which corresponds to an angular resolution of $\Delta\Omega \sim 7.8 \cdot 10^{-2}\,\mathrm{sr}$. This means that the minimum number of pixels is given by the inverse of the relation (6.83), where $\Delta\Omega_{\mathrm{pix}}$ is given by π^3/l^2. This corresponds to a minimum number of pixels of $N_{\mathrm{pix}} = 4\pi/\Delta\Omega_{l=20} \simeq 160$. We will consider a division parameter of $N_{\mathrm{side}} = 64$, which corresponds to $N_{\mathrm{pix}} = 49,152$ with an angular size of $\Delta\Omega_{\mathrm{pix}} \sim 2.6 \cdot 10^{-4}\,\mathrm{sr}$, or $\theta \sim 0.5°$, well above the minimum number of pixels required for $l_{\max} = 20$.

Since the introduction of a finite sky resolution implies a maximum resolvable angular scale in the sky, given by the spherical parameter $l_{\max} \sim \sqrt{\pi^3/\Delta\Omega}$, the angular power spectrum is also be affected by this limitation. Fig. 6.1 shows the mean angular power spectrum of 100 isotropic arrival direction distributions with $15,000$ events each. The angular power spectra of (6.73) (blue line) and (6.58) (red line) are shown assuming all weight factors $\omega_i = 1$, along with the isotropic predictions (6.80) (blue dashed line) and (6.64) (red dashed line), respectively. The left panel of Fig. 6.1 shows the case of $N_{\mathrm{pix}} = 768$. In this case, the maximum spherical parameter is $l_{\max} \sim 13$. It can be seen that both the angular power spectrum and the isotropic prediction deviate from the results obtained with infinite resolution. In particular, for $l \gtrsim 15$ the deviation becomes larger than the estimated variance. This is due to the fact that the coefficients $f_{lm,i}$ correspond to the average value of the spherical harmonic $Y_{lm}(\hat{\mathbf{n}})$ in the pixel. Therefore, if the angular size of the pixel is larger than the solid angle associated with the spherical parameter l, several oscillations of the spherical harmonic are contained within the pixel, leading to a decrease in the mean value of the spherical harmonic $Y_{lm}(\hat{\mathbf{n}})$. In the right panel of Fig. 6.1 we consider $N_{\mathrm{pix}} = 49,152$, which corresponds to $l_{\max} \sim 348$. We can see that all the predictions for $l \leq 20$ agree with the angular power spectra obtained from the isotropic arrival direction distributions.

7

UHECR anisotropies from a magnetized Universe

This chapter is based on the publication:

- S. Rossoni and G. Sigl. (2025). *Anisotropy signal of UHECRs from a structured magnetized Universe*. **Phys. Rev. D**, 112, 023015. arXiv:2502.19324 [astro-ph.HE]. https://doi.org/10.1103/4zt7-s48v.

In Chapter 4, we have seen that the extragalactic propagation of UHECRs is affected by interactions with the background photon fields and cosmic magnetic fields. Furthermore, the cosmic rays observables such as the energy spectrum, mass composition and arrival directions are affected by these interactions, making it difficult to identify their sources. In this chapter, we present our simulations of the propagation of UHECRs with energies above 8 EeV in magnetized replicas of the local Universe. In particular, we study the arrival direction distribution of the propagated CRs for different assumptions on the UHECR source distribution and density. We compute the angular power spectrum, and in particular the dipole and quadrupole moments, of the simulated CRs. In this way, we study the impact of the different propagation scenarios considered on the UHECR anisotropy signal.

The state of research on the effect of EGMF and GMF on UHECR anisotropies is discussed in Sec. 7.1. The details of our simulation setup are presented in Sec. 7.2. The analysis of the simulation results is described in Sec. 7.3 and the results are presented in Sec. 7.4. The discussion of the results and conclusions are given in Sec. 7.5.

7.1 Cosmic ray anisotropies and magnetic fields

We have discussed in Chapter 3 the observation of a large scale dipole anisotropy in the UHECR sky above 8 EeV observed by the Pierre Auger Observatory [16, 319]. The analyses of the UHECRs detected during the Phase 1 of the Pierre Auger Observatory have shown a dipole with a strength of $\sim 7\%$ for the arrival direction distribution of the UHECRs above 8 EeV with a significance of 6.9σ [17, 320]. Furthermore, the significance of the dipole in the energy range

$8 - 16$ EeV has reached 5.7σ. Telescope Array has also performed similar analyses to search for large scale anisotropy signals, also observing a dipolar component. However, due to the limited statistics, this result is compatible with both Pierre Auger results and an isotropic UHECRs arrival direction distribution [321]. The observed quadrupole and higher multipole moments are not statistically significant, being consistent with isotropy in the combined Pierre Auger Observatory and Telescope Array analysis [167].

The correlation analyses between AGN and SBG catalogues and the UHECR arrival directions with energy above 32 EeV [162, 322] has shown that the SBG catalogue is the most statistically significant, presenting a $\sim 4\sigma$ deviation from isotropy for energies above 40 EeV. Telescope Array has also reported the presence of hotspots in the northern sky that deviate from isotropy [323–327]. An excess of events with energy $\gtrsim 60$ EeV in Equatorial coordinates $(144°, 41°)$ has been observed at $\sim 20°$ away from the supergalactic plane with 4.8σ Li-Ma significance. The presence of a new hotspot of events with energies between $\sim 30 - 60$ EeV has also recently been observed in the direction of the *Perseus-Pisces* supercluster. The origin of these UHECR hotspots has been studied in [328], where the most massive galaxies in the *Local Group* (referred to as *Council of Giants*) were considered. An early UHECR pulse from Centaurus A, scattered by other galaxies, could cause multiple UHECR excesses in the sky, while late echoes propagate out into the local extragalactic space. Recently, a hotspot associated with the Sombrero galaxy was claimed to have a global significance of 3.3σ [329].

In Sec. 4.5, we have seen that the search for UHECR sources is further complicated by the presence of galactic and extragalactic magnetic fields. In particular, the spatial distribution of the EGMF is characterized by various structures such as clusters, filaments and cosmic voids. Moreover, the EGMF is still poorly understood and its inclusion in CR simulations could be one of the main sources of uncertainties, as shown in Fig. 4.6. Unconstrained simulations of the local cosmic web have been considered in [330–332] to study the anisotropy signal of UHECRs above 10 EeV. Large deflections up to $\sim 20°$ have been observed even for cosmic rays with energy above 100 EeV. Therefore, UHECR astronomy would not be possible even at such high energies. Similarly, in [333], large deflections up to $\sim 50°$ have also been obtained in the case of a single nearby source. However, in the simulations of UHECR propagation in constrained replicas of the local Universe performed in [334, 335], it was found that large deflections occur only when particles pass through magnetised clusters, which consist of a very small fraction of the volume. In particular, UHECRs with energy above 40 EeV are expected to be deflected less than $\sim 1°$ in most cases. This implies that cosmic ray astronomy would be possible. Similar results were also found in [336], where above 60 EeV the deflections are small enough to allow for cosmic ray astronomy.

In the more recent constrained simulations in [337, 338], it was shown that the anisotropy signal of UHECRs with energy $\gtrsim 1$ EeV is not affected by the different magnetogenesis scenarios and is nearly compatible with ballistic propagation. However, the source distribution and the relative position of the cosmic ray observer within the simulation volume are important factors in distinguishing the observed anisotropies from the isotropic prediction. In particular, sources within ~ 50 Mpc dominate the anisotropies, and show a deviation from the isotropic scenarios when their position is inferred from the local matter distribution. Similarly, in [339], propagation in highly magnetised cosmic voids ($B \sim 1$ nG) shows small deflections in most of the sky. UHECR anisotropy studies have also been used to constrain EGMF parameters, as done for example in [340, 341].

We have discussed the GMF in Sec. 4.5.2, where we have seen that one of the most comprehensive and widely used models is the JF12 [286, 287]. Galactic deflection of UHECRs in the JF12 model was studied in [342] for several cosmic ray energies and source directions. It was found that below rigidities of $\sim 10\,\mathrm{EeV}$, galactic deflections can also reach $\sim 90°$. In [343], the energy and mass dependence of the elongation of cosmic ray hotspots in the sky due to the GMF for $E > 40\,\mathrm{EeV}$ from different candidate sources was studied. The propagation of cosmic rays in the GMF can also be associated to modifications in the observed anisotropy signal at relatively low [344] and very high energies [285, 345]. In [345], it was shown how different models of GMF introduce dipole amplitude suppression and dipole direction shifts. It has also been shown in [346] how large multipole moments, such as the quadrupole, can also be affected by the propagation in the Galactic halo.

An useful quantity for the study of UHECR deflection in extragalactic magnetic field is the magnetization parameter, and it is defined as

$$\beta_{\mathrm{EGMF}} = B_{\mathrm{rms}}\sqrt{\lambda_{\mathrm{c}}}\,, \tag{7.1}$$

where B_{rms} is the root-mean-square of the field strength and λ_{c} is the coherence length of the magnetic field. We can then write the deflection angle in Eq. (4.80) as

$$\theta_{\mathrm{rms}} \simeq 0.8° \cdot Z \left(\frac{E}{100\,\mathrm{EeV}}\right)^{-1} \left(\frac{r}{10\,\mathrm{Mpc}}\right)^{1/2} \left(\frac{\beta}{1\,\mathrm{nG\,Mpc}^{1/2}}\right)\,, \tag{7.2}$$

where Z and E are the charge number and the energy of the cosmic ray and r is the propagation distance. The magnetization parameter β_{EGMF} is often constrained together with the UHECR source number density n_s. One of the most general assumption about the distribution of the UHECR sources is that they follow the local baryon distribution, also called the Large Scale Structure (LSS) [17, 347–353]. In [352], the interplay between EGMF and n_s has been studied in detail and it was shown that for a small magnetic deflection (i.e. $\beta_{\mathrm{EGMF}} \lesssim 0.1\,\mathrm{nG\,Mpc}^{1/2}$) a source density $n_s > 10^{-3}\,\mathrm{Mpc}^{-3}$ is required to reproduce the observed multipoles. Furthermore, scenarios characterized by $\beta_{\mathrm{EGMF}} \geq 3\,\mathrm{nG\,Mpc}^{1/2}$ or a homogeneous source distribution would be excluded. A similar study, considering local SBGs as UHECR sources, was performed in [354], where upper limits on the source density $n_s \lesssim 9 \cdot 10^{-2}\,\mathrm{Mpc}^{-3}$ and $\beta_{\mathrm{EGMF}} \lesssim 20\,\mathrm{nG\,Mpc}^{1/2}$ have been obtained. In [355], different source densities and newly developed GMF models were considered to reproduce the observed dipole and quadrupole moments. The authors have shown that the continuous source scenario (i.e. $n_s = \infty$) cannot reproduce the observed dipole, and a source density of $n_s \simeq 10^{-4}\,\mathrm{Mpc}^{-3}$ seems to be favored. Transient sources of cosmic rays were considered in [356], finding that the turbulent magnetic field strength in the Local Sheet should be of $0.5 - 20\,\mathrm{nG}$ with a coherence length of $10\,\mathrm{kpc}$, and identifying long gamma-ray bursts as possible source candidates. Interestingly, it was also shown in [357] that the EGMF-induced time delay in the propagation of UHECRs from AGNs can be comparable to or even larger than the source duty cycle. This would make the correlation of the arrival directions of UHECRs and their sources very difficult.

7.2 Extragalactic cosmic ray propagation models

Given the current uncertainties in the cosmic ray source density and the limited knowledge of the EGMF, we consider several propagation scenarios to study the produced anisotropy signal, taking

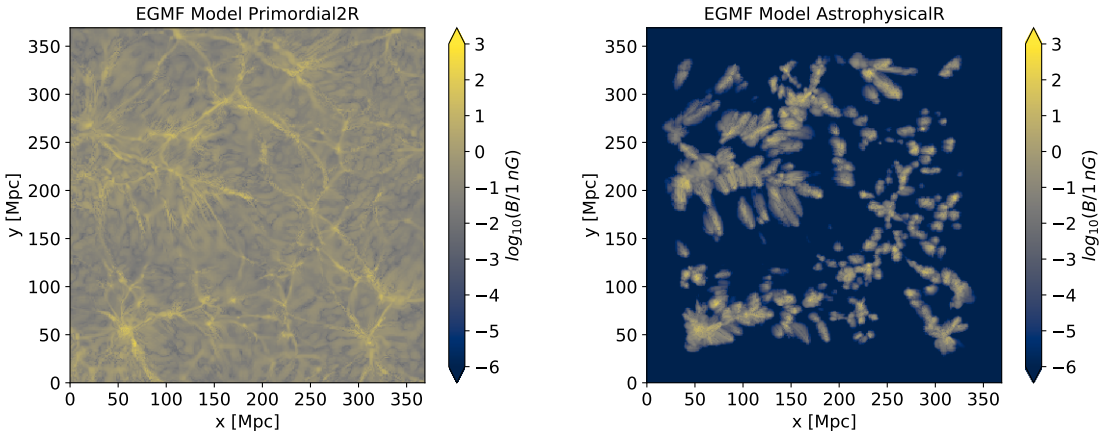

Figure 7.1: Left: magnetic field strength in nG of the EGMF model *primordial2R* in Supergalactic coordinates at redshift $z = 0$. The Supergalactic plane orthogonal to the Z-axis including the Milky Way at the center is shown. Right: same as left panel, but for the *astrophysicalR* mode. The EGMF models are taken from [338]. Figure taken from [316].

into account the different possible UHECR trajectories to Earth. The propagation scenarios considered are described in the following sections.

7.2.1 Constrained EGMFs

We consider constrained MagnetoHydroDynamics simulations of the local cosmic web to investigate realistic magnetic deflections. In particular, the evolved EGMF models described in [338] are considered for our UHECR propagation simulations. These magnetic field models were obtained with the cosmological grid code `ENZO`[1] [358], where a numerical replica of the local Universe at redshift $z = 0$ is obtained by initializing a volume of $(500\,\mathrm{Mpc}/h)^3$ (with the Hubble parameter $h = 0.677$) at $z = 60$, where only the internal subregion with the Milky Way in the center is constrained. The evolution of the cosmic baryonic structures and the EGMF are then simulated together[2].

We consider the EGMF models called *primordial2R* and *astrophysicalR* in [338]. As discussed in Sec.4.5.1, we consider these two models to be representative of the two main magnetogenesis scenarios. The *primordial2R* model consists of an EGMF obtained from a power-law spectrum with spectral index $n_\mathrm{B} = -3$ at $z = 60$. The normalization of this model is such that the root-mean-square value of the field is 1 nG at $z = 0$. In the *astrophysicalR* model, the magnetic field has astrophysical origin, and the magnetic energy is assumed to be 50% of the injected thermal energy. The magnetic field is released as a dipole around halos where the physical gas density exceeds the density value $n_\mathrm{crit} = 10^{-2}\,\mathrm{cm}^{-3}$. These EGMF models are shown in Fig. 7.1 in Supergalactic coordinates (see Appendix A.3) within a length scale of $250\,\mathrm{Mpc}/h$ each side (the plane orthogonal to the Z-axis including the Milky Way is shown). Note that the volume of the cosmological simulations described above was $(500\,\mathrm{Mpc}/h)^3$ in order to remove numerical

[1] More information can be found at https://enzo-project.org.

[2] The evolved EGMF models and the baryon distribution can be found in https://crpropa.github.io/CRPropa3/pages/AdditionalResources.html.

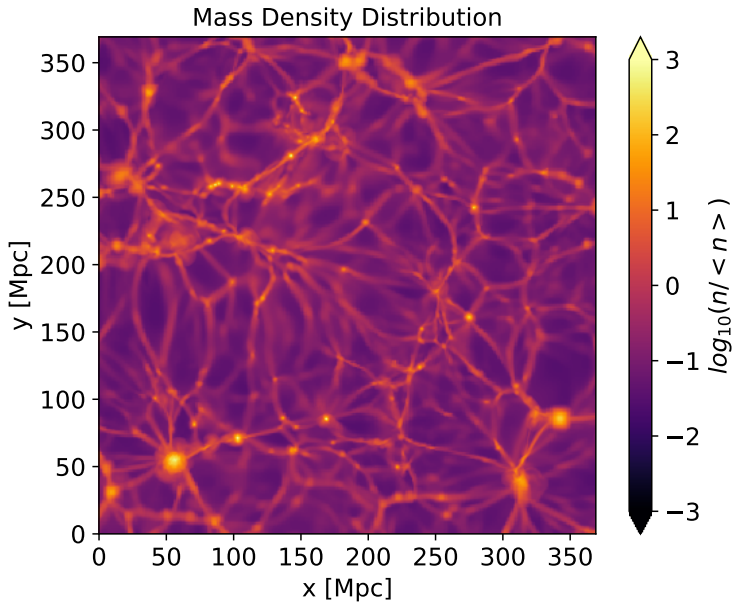

Figure 7.2: Mass number density n normalized to the average value in the simulation volume, $\langle n \rangle$, in Supergalactic coordinates at redshift $z = 0$. The panels show the Supergalactic plane orthogonal to the Z-axis including the Milky Way at the center. Mass density distribution from [338]. Figure taken from [316].

effects due to periodic boundary conditions. For this reason, UHECR simulations are performed within a smaller internal volume of $(250\,\mathrm{Mpc}/h)^3$.

We can see that both models show a spatial distribution characterised by the cosmic structures mentioned above. We can also see that the EGMF is clearly correlated with the baryon density distribution at $z = 0$, shown in Fig. 7.2. The different magnetization of the cosmic voids is given by the different assumptions on the field origin. In the *astrophysicalR* model, the magnetic field is only produced where the matter density if different from zero. Therefore, this model is characterized by magnetized clusters and filaments, but voids do not show any magnetization. On the contrary, the seed field of the *primordial2R* model is uniformly present throughout the simulation volume at $z = 60$. Therefore, during the evolution of cosmic structures, the EGMF correlates with the matter density, giving rise to the structures observed in Fig. 7.1, and also keeping magnetised *baryon-empty* regions.

The deflection angle in Eq. (7.2) can be used to estimate how the values of B_{rms} and λ_{c} affect the multipole distribution. Since the multipole parameter l is related to the angular scale $\theta \sim 180^\circ/l$ (see Sec. 6.3.2), we obtain that, for cosmic ray energies $E \geq 8\,\mathrm{EeV}$, the magnetization parameter must be such that

$$\beta \gtrsim 2 \cdot Z^{-1} \left(\frac{10}{l}\right) \left(\frac{r}{10\,\mathrm{Mpc}}\right)^{-1/2} \mathrm{nG\,Mpc}^{1/2}\,. \tag{7.3}$$

Above 8 EeV, we expect that the UHECR flux is mostly produced by sources within a distance of $r \lesssim 100\,\mathrm{Mpc}$. Furthermore, the average observed UHECR mass composition in this energy

range is $\langle A \rangle \sim 10$ [155, 359]. Under these conditions, we obtain that

$$\beta \gtrsim 10^{-1} \left(\frac{10}{l} \right) \text{nG}\,\text{Mpc}^{1/2}\,. \tag{7.4}$$

For $l = 1, 2$ (i.e. for the dipole and quadrupole components), this is equal to

$$B_{\text{rms}} \gtrsim 1 \cdot \left(\frac{\lambda_{\text{c}}}{1\,\text{Mpc}} \right)^{-1/2} \text{nG}\,. \tag{7.5}$$

The result in Eq. (7.5) cannot be applied to the structured field models described above. In these cases, the B_{rms} and λ_{c} can only be defined locally within cosmic structures, and they do not describe the properties of the magnetic field in the entire simulation volume. However, in both structured models, large deflections are expected to occur at most within cosmic structures.

In order to better understand the effects due to the spatial distribution of the EGMF models, we also consider two other propagation scenarios: the *ballistic* scenario and the *statistical* scenario. In the *ballistic* case, the propagation of the cosmic rays is purely ballistic (i.e. no EGMF). In the *statistical* scenario, the extragalactic field is given by a statistically homogeneous Kolmogorov-like power-law spectrum [360] with root-mean-square field strength $B_{\text{rms}} = 1\,\text{nG}$ and coherence length $\lambda_{\text{c}} = 1\,\text{Mpc}$. We chose these parameters because of the result on the effect of the EGMF on the dipole and quadrupole moments in Eq. (7.5). The *ballistic* and *statistical* scenarios give us the opportunity to study the effects not only of the presence of an EGMF, but also of the influence of a structured magnetic field configuration.

7.2.2 Source distribution models

The distribution of the source positions in the extragalactic space can strongly influence the observed anisotropies, in particular at the highest energies, due to the presence of the interaction horizon (see Sec. 4.3). For this reason, we consider two different values for the source number density: in the first case, we consider a synthetic catalogue of $5 \cdot 10^3$ point-like sources, corresponding to a source number density of $n_s = 10^{-4}\,\text{Mpc}^{-3}$, while the second case is given by $5 \cdot 10^5$ point-like sources, corresponding to a source number density of $n_s = 10^{-2}\,\text{Mpc}^{-3}$ [352, 354, 355]. These density values can be related to real candidate source classes. In particular, $n_s \simeq 10^{-2}\,\text{Mpc}^{-3}$ corresponds to the number density of Milky Way-like galaxies [361], while infrared starburst galaxies (SBGs) are characterized by a number density of $n_s \simeq 10^{-4}\,\text{Mpc}^{-3}$[94, 196, 362]. We then define two different classes of catalogues of source locations for each density value, called *homogeneous* and *mass density*. In the first class, we obtain the source positions with a homogeneous sampling in the simulation volume. On the other hand, the *mass density* class is obtained by sampling the source positions with a probability density proportional to the baryon density distribution from [338], as shown in Fig. 7.2.

It has to be noted that a single sample of source positions represents only one possible discrete realization of a continuous distribution. Given that the location of the UHECR sources is still unknown, our results could be affected by the cosmic variance associated with the synthesised source catalogue. For this reason, we consider $N_{\text{R}} = 10$ different realizations of the two classes of source catalogues. The number of sources as a function of the distance from the Milky Way is shown in the bottom panel of Fig. 7.3: the *homogeneous* catalogues are shown in green and the *mass density* catalogues are shown in red. The solid lines correspond to source number density

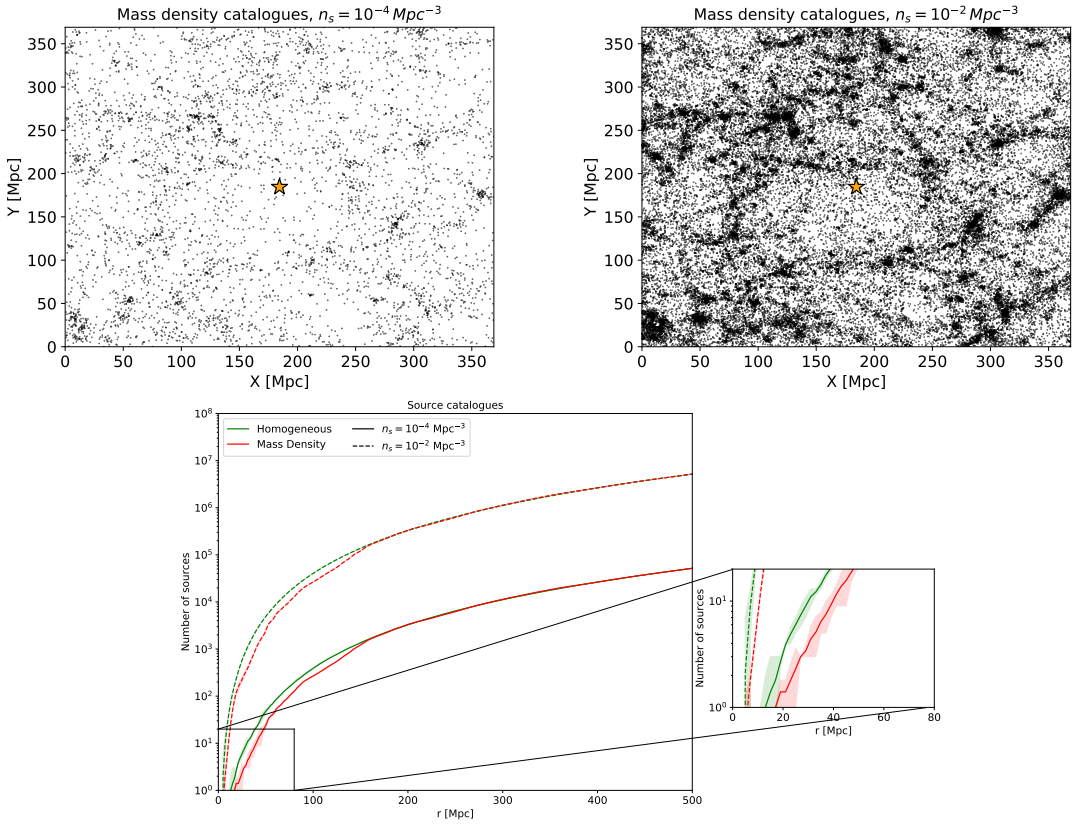

Figure 7.3: Top: scatter plot of a catalogue of source locations in the low density (left) and high density (right) scenarios. Both panels show the positions of the sources projected onto the Supergalactic plane orthogonal to the Z-axis, including the Milky Way (yellow star) in the center. In the high density scenario, only 10% of the sources in the catalogue are shown. Bottom: number of sources as a function of the distance from the Milky Way for the two catalogues. The *homogeneous* catalogues are in green and the *mass density* catalogues are in red. Solid lines correspond to the source number density $n_s = 10^{-4}\,\mathrm{Mpc}^{-3}$ and dashed lines correspond to $n_s = 10^{-2}\,\mathrm{Mpc}^{-3}$. The shaded areas represent the cosmic variance multiplied by three. A zoom is shown for $r \leq 80\,\mathrm{Mpc}$. Figure taken from [316].

$n_s = 10^{-4}\,\mathrm{Mpc}^{-3}$ and the dashed lines correspond to $n_s = 10^{-2}\,\mathrm{Mpc}^{-3}$, while the shaded red and green areas represent the cosmic variance (here estimated by simply calculating the sample variance) multiplied by three, for better visualization. We can see that the number of sources in the two classes of catalogues differs for distances $r \lesssim 150\,\mathrm{Mpc}$. In particular, the *homogeneous* catalogue contains more sources at small distances than the *mass density*. This is due to the structure of the baryon density in the local Universe, where sources are more concentrated in regions of high density (i.e. clusters and filaments). However, at a distance of $r \gtrsim 200\,\mathrm{Mpc}$, the difference between the two catalogues is negligible, as predicted by the cosmological principle, where both of them show a trend like $N_{\mathrm{source}} \propto r^3$. Moreover, the cosmic variance also becomes negligible, and we can also see that the cosmic variance becomes negligible when a high density of sources is considered. The spatial distributions of one of the *mass density* catalogues for each number density are also shown in the top panels of Fig. 7.3, where the positions of the sources

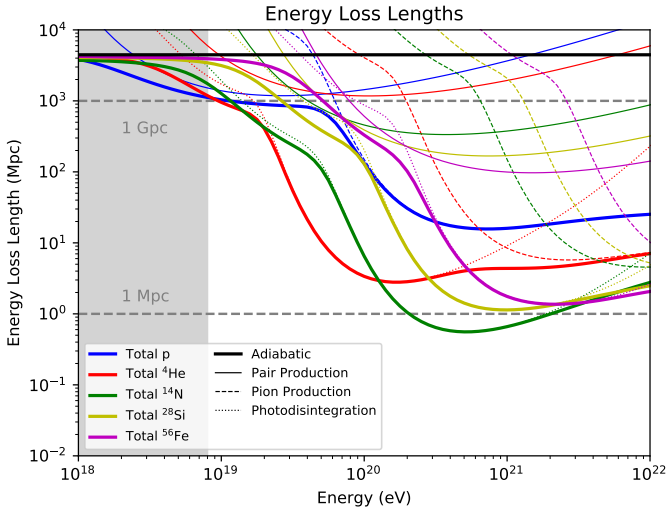

Figure 7.4: Energy loss lengths corresponding to the interactions with both the CMB and the EBL [230] photon fields for different nuclei: p in blue, ^{4}He in red, ^{14}N in green, ^{28}Si in yellow, and ^{56}Fe in purple. The adiabatic energy loss length is given by the black thick line. Different photohadronic interactions are shown with different line styles: thin continuous for pair production, dashed for pion production and dotted for photodisintegration. The total energy loss length of a given nucleus is given by the colored thick lines. All the energy loss lengths have been obtained with the simulation code `CRPropa` [236]. Figure taken from [316].

are projected onto the Supergalactic plane orthogonal to the Z-axis, including the Milky Way (yellow star) in the center.

7.2.3 CRPropa simulations

To reproduce all the physical processes occurring during the extragalactic propagation, we use the Monte Carlo code `CRPropa 3`, described in Sec. 5.2, and, in particular, we consider the released version `CRPropa 3.2`. The propagation is simulated by calculating the actual extragalactic magnetic deflection, and by taking into account interactions with the background photon fields (we consider the CMB and the EBL model from [230]). Photohadronic interactions include Bethe-Heitler pair production, pion production, and photodisintegration. Nuclear decay of unstable species and adiabatic energy loss due to the expansion of the Universe are also considered. However, since the adiabatic energy loss rate is 3 to 4 times smaller than the total photohadronic energy loss rate at 8 EeV, as shown in Fig. 7.4, cosmological effects are not larger than other uncertainties of the model.

Given the simulation volume of 250 Mpc/h on each side, we use the condition that when a particle leaves the volume, its trajectory is continued on the opposite side, and the injection position is changed accordingly, i.e. we use *periodic boundary conditions*. Therefore, the maximum observed source distance does not depend on the size of the simulation volume, but it is given by the physical processes included in the simulations. Periodic boundary conditions also allow us to account for the contribution of sources at distances larger than the sources in the catalogues. Moreover, the use of periodic boundary conditions corresponds to the position of a CR observer

in each virtual replica of the simulation volume.

We have introduced two possible *end-conditions* in our simulations. Since we are interested in anisotropies in the UHECR arrival directions with energy above 8 EeV, we terminate the simulation when the cosmic ray energy falls below this value. The second condition is based on the fact that the EGMF models in [338] are produced with constrained cosmological simulations. Since we can then identify the position of the Milky Way in the center of the simulation volume, we place in that position our UHECR observer, which is given by a spherical surface with radius $R_{\rm O} = 1\,{\rm Mpc}$. When particle intersects this sphere, the event is recorded and the simulation ends.

We simulate the propagation of five different species: protons p, helium ^{4}He, nitrogen ^{14}N, silicon ^{28}Si, and iron ^{56}Fe nuclei. The initial energy is extracted from an injection rate of the form $Q_A(E) \propto E^{-1}$, between 8 EeV and 10^3 EeV. We consider this energy spectrum at the escape from the sources to increase the probability of recording high-energy particles at the end of the simulation. The simulated species are injected with equal probability and the initial momentum direction is chosen to be isotropic at the injection position.

The combinations of EGMF models, source catalogues and injected species define our simulation database. If $N_{\rm B}$ is the number of EGMF models, $N_{\rm S}$ is the number of source models, $N_{\rm A}$ is the number of injected species and $N_{\rm R}$ is the number of source catalogue realizations, then the total number of simulated scenarios in our database is given by

$$N_{\rm scenarios} = N_{\rm B} \cdot N_{\rm S} \cdot N_{\rm R} \cdot N_{\rm A} = 4 \cdot 4 \cdot 10 \cdot 5 = 800\,, \tag{7.6}$$

where 400 simulations are in the low density scenarios and 400 are in the high density scenarios. For each simulated scenario in our database, we obtained $N = 5 \cdot 10^4$ observed events above 8 EeV, as in [17]. We want to highlight an important fact: in the high source density scenario the number of sources present in a catalogue is $5 \cdot 10^5$, which is one order of magnitude larger than the final number of events collected by the observer. However, since the propagation of the UHECRs is simulated in a three-dimensional volume, to obtain such a statistic we had to inject $4 \cdot 10^7$ particles for each species, for a total of $2 \cdot 10^8$ simulated particles for each combination of source distribution and EGMF model.

7.3 Simulation analysis

In order to reproduce a realistic injection scenario, we reweighted our simulations database. For this procedure, we consider the scenario where the UHECR emissivity at the escape from the source[3] is described by a power-law with a broken exponential cutoff following the Peters cycle [100], as already described in [254, 363–365]. Therefore, the injection rate takes the form

$$Q_A(E) = Q_0\, a_A \left(\frac{E}{1\,{\rm EeV}}\right)^{-\gamma} f_{{\rm cut},A}(E)\,, \tag{7.7}$$

where the cutoff function is given by the broken exponential

$$f_{{\rm cut},A}(E) = \begin{cases} 1 & E < Z_A R_{\rm cut}\,; \\ \exp\left(1 - \dfrac{E}{Z_A R_{\rm cut}}\right) & E \geq Z_A R_{\rm cut}\,, \end{cases} \tag{7.8}$$

[3] In this chapter, we do not study the possible change in the emissivity of accelerated UHECR due to *in-source* interactions. Therefore, we do not distinguish between accelerated and escaped cosmic rays from the source environment.

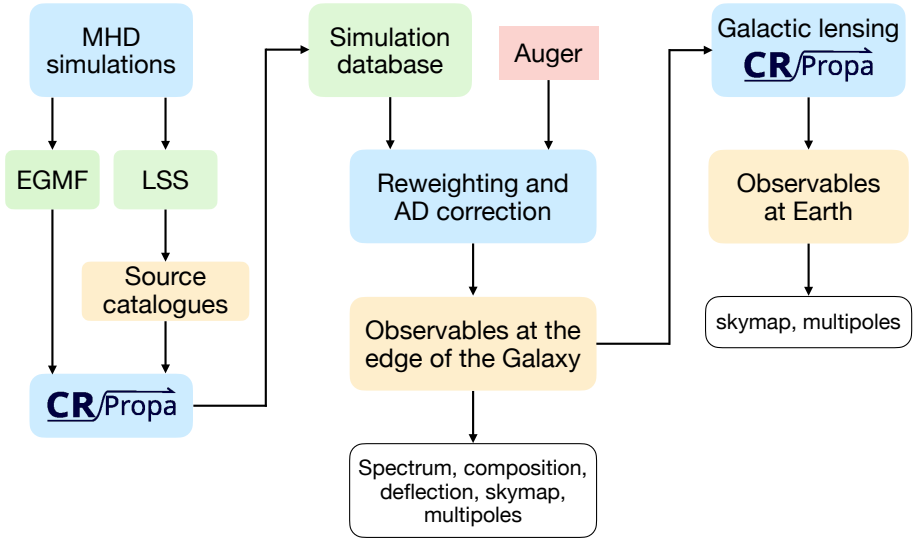

Figure 7.5: Schematic representation of the structure of the study presented in this chapter. The creation of the source catalogues, the simulations database and the analysis of the obtained scenarios are shown.

where Q_0 is a normalization constant, γ is the spectral index, $R_{\rm cut}$ is the maximum rigidity, Z_A is the atomic number of the injected species with mass number A and a_A is the fraction of injected particles of the same species. In particular, the coefficients a_A are such that $\sum_A a_A = 1$. We have assumed that the injection rate of all the sources is characterized by the same maximum rigidity $R_{\rm cut}$. This is justified by the results obtained in [366], where it was shown that a very small variance of $R_{\rm cut}$ is expected in order to reproduce the available data. The set of coefficients a_A can also be expressed as integral functions $I_A = a_A Z_A^{2-\gamma} / \sum_{A'} a_{A'} Z_{A'}^{2-\gamma}$, which correspond to the emitted energy fractions of the element A. Details about the weighting procedure of our simulations can be found in Appendix C.1.

To find the set of injection parameters γ, $R_{\rm cut}$ and I_A that reproduces the observed energy spectrum and mass composition of the UHECRs above 8 EeV, we define the variable χ^2 as the sum of the spectral component χ^2_J and the mass component $\chi^2_{\langle A\rangle}$,

$$\chi^2 = \chi^2_J + \chi^2_{\langle A\rangle} = \sum_i \left(\frac{J_{i,\rm Auger} - J_{i,\rm sim}}{\sigma^J_{i,\rm Auger}} \right)^2 + \sum_j \left(\frac{\langle A\rangle_{j,\rm Auger} - \langle A\rangle_{j,\rm sim}}{\sigma^{\langle A\rangle}_{j,\rm Auger}} \right)^2 , \tag{7.9}$$

where the summations are over different energy bins, and $J_{i,\rm sim}$ and $\langle A\rangle_{j,\rm sim}$ refer to the energy spectrum and average mass number of a given simulated scenario. The quantities obtained from real data are indicated with the subscript *Auger*: the energy spectrum above 8 EeV is taken from [367] and the mass composition from [155, 359] for the hadronic interaction model EPOS-LHC [77]. The values $\sigma^J_{i,\rm Auger}$ and $\sigma^{\langle A\rangle}_{j,\rm Auger}$ indicate the statistical variance of $J_{i,\rm Auger}$ and $\langle A\rangle_{j,\rm Auger}$, respectively. We therefore find the set of injection parameters that minimize Eq. (7.9) for our simulated scenarios.

The trajectory of the UHECRs registered by the observer is finally modified by the GMF, as

we have discussed in Sec. 4.5.2. We assume that the observer's surface represents the edge of the Milky Way, and we apply a magnetic lens to the observed arrival directions (Eq. (5.4)). However, before applying the magnetic lens, we correct the recorded arrival directions for the finite size of the observer. The correction procedure is described in Appendix C.2. Several magnetic lenses are implemented in `CRPropa 3`: here we use the magnetic lens based on the JF12 model.

For each simulated scenario, we compute the energy spectrum, mass composition, mean angular deflection, sky map and angular power spectrum of the recorded UHECRs. In addition, the sky distributions are constructed at the edge of the Milky Way and at Earth. We compute the relevant observables for each realization of the source catalogue: we calculate the cosmic average, and we estimate the cosmic variance by calculating the sample variance of the observables. A summary scheme of the simulation and analysis procedures discussed in this chapter is shown in Fig. 7.5.

7.3.1 Anisotropies in the UHECR arrival direction distribution

In our anisotropies analysis, we consider a finite number of pixels in the sky centered in the direction $\hat{\mathbf{p}}_i$, where $i = 1, ..., N_p$, and N_p is the total number of pixels. Then, we define the UHECR arrival direction distribution of a given scenario as done in Eq. (6.48). We analyze these distributions by using the `Python` package `HEALPY` [317], based on the Hierarchical Equal Area isoLatitude Pixellization (`HEALPix`) scheme [318]. We consider the division parameter $N_{\rm side} = 64$, which corresponds to $49,152$ pixels with angular size $\theta \simeq 0.5°$. The dependency of the maximum spherical parameter $l_{\rm max}$ on the number of pixels is discussed in Sec. 6.3.2.

We compute the angular power spectrum in Eq. (6.73) and we compare it to the one expected for an isotropic distribution in the case of a finite number of recorded particles and pixels in the sky, given by Eq. (6.79). We also compute the statistical variance of the multipole moments $\mathcal{C}_l$ as done in [315, 337, 368], and it is equal to

$$\sigma_{\mathcal{C}_l} = \sqrt{\frac{2}{2l+1}}\,\mathcal{C}_l\,. \tag{7.10}$$

Given the normalization used in this study, the monopole component of the angular power spectrum is $\mathcal{C}_0 = (4\pi)^{-1}$. To be independent of the chosen normalization, we will consider the angular power spectrum normalized to the monopole component, i.e. $\mathcal{C}_l/\mathcal{C}_0$. This quantity is also a better choice for studying dipole and quadrupole amplitudes since, as we have shown in Sec. 6.2, the dipole and quadrupole amplitudes are given by

$$d = \sqrt{\sum_i d_i^2} = 3\sqrt{\frac{\mathcal{C}_1}{\mathcal{C}_0}}\,, \tag{7.11}$$

$$Q = \sqrt{\sum_{i,j} \frac{Q_{ij}^2}{9}} = \sqrt{\frac{50}{3}\,\frac{\mathcal{C}_2}{\mathcal{C}_0}}\,. \tag{7.12}$$

For the definition of the quadrupole strength Q, see also [17].

$n_s = 10^{-4}\,\mathrm{Mpc}^{-3}$

	ballistic	*astrophysicalR*	*primordial2R*	*statistical*
γ	-2.81	-1.53	-2.53	-3.03
$\log(R_{\mathrm{cut}}/1\,\mathrm{EV})$	0.07	0.30	0.12	0.08
I_p	$1.3 \cdot 10^{-1}$	$8.6 \cdot 10^{-2}$	$6.6 \cdot 10^{-2}$	$1.5 \cdot 10^{-1}$
I_{He}	$1.2 \cdot 10^{-1}$	$9.1 \cdot 10^{-2}$	$8.4 \cdot 10^{-2}$	0.0
I_N	$3.7 \cdot 10^{-1}$	$3.5 \cdot 10^{-1}$	$4.4 \cdot 10^{-1}$	$5.3 \cdot 10^{-1}$
I_{Si}	$3.3 \cdot 10^{-1}$	$3.8 \cdot 10^{-1}$	$3.3 \cdot 10^{-1}$	$2.6 \cdot 10^{-1}$
I_{Fe}	$5.1 \cdot 10^{-2}$	$8.8 \cdot 10^{-2}$	$8.3 \cdot 10^{-2}$	$6.0 \cdot 10^{-2}$

$n_s = 10^{-2}\,\mathrm{Mpc}^{-3}$

	ballistic	*astrophysicalR*	*primordial2R*	*statistical*
γ	-1.88	-2.50	-2.18	-1.76
$\log(R_{\mathrm{cut}}/1\,\mathrm{EV})$	0.26	0.18	0.11	0.29
I_p	$2.3 \cdot 10^{-1}$	$1.1 \cdot 10^{-1}$	$3.4 \cdot 10^{-2}$	$1.8 \cdot 10^{-1}$
I_{He}	0.0	0.0	$1.6 \cdot 10^{-1}$	0.0
I_N	$2.6 \cdot 10^{-1}$	$4.6 \cdot 10^{-1}$	$4.0 \cdot 10^{-1}$	$3.2 \cdot 10^{-1}$
I_{Si}	$5.0 \cdot 10^{-1}$	$4.2 \cdot 10^{-1}$	$2.7 \cdot 10^{-1}$	$4.4 \cdot 10^{-1}$
I_{Fe}	$3.8 \cdot 10^{-3}$	$1.8 \cdot 10^{-2}$	$1.3 \cdot 10^{-1}$	$5.9 \cdot 10^{-2}$

Table 7.1: Minimization results of Eq. (7.9) for the *mass density* source scenarios. Different columns correspond to different EGMF models. The source number density of a given model is indicated at the top of the table. Table taken from [316].

7.4 Results of the analysis

In the following, the results of the analysis of the simulated scenario described above are presented for the *mass density* source catalogues. The *homogeneous* source scenarios are discussed in Appendix C.3. We recall once again that, given the observation of a dipole component in the UHECR sky above 8 EeV by the Pierre Auger Observatory, we will only focus on this energy range.

7.4.1 Energy spectrum and mass composition

The results of the minimization of the χ^2 in Eq. (7.9) for the *mass density* catalogues are given in Table 7.1. The results for both the source number densities considered are shown. We found that a hard spectral index up to $\gamma \simeq -3$ and an average rigidity cutoff of $\log(R_{\mathrm{cut}}/1\,\mathrm{EV}) \simeq 0.2$ is required to reproduce observations, as also found in [254, 352, 364, 365]. We found that the mass composition is dominated by the nitrogen and silicon components in all the scenarios. This is due to the fact that the lightest components are already suppressed above 8 EeV since ($E_{\mathrm{cut},p} = Z_p R_{\mathrm{cut}} \simeq 1.5\,\mathrm{EeV}$ and $E_{\mathrm{cut,He}} = Z_{\mathrm{He}} R_{\mathrm{cut}} \simeq 3\,\mathrm{EeV}$). Moreover, a dominant iron

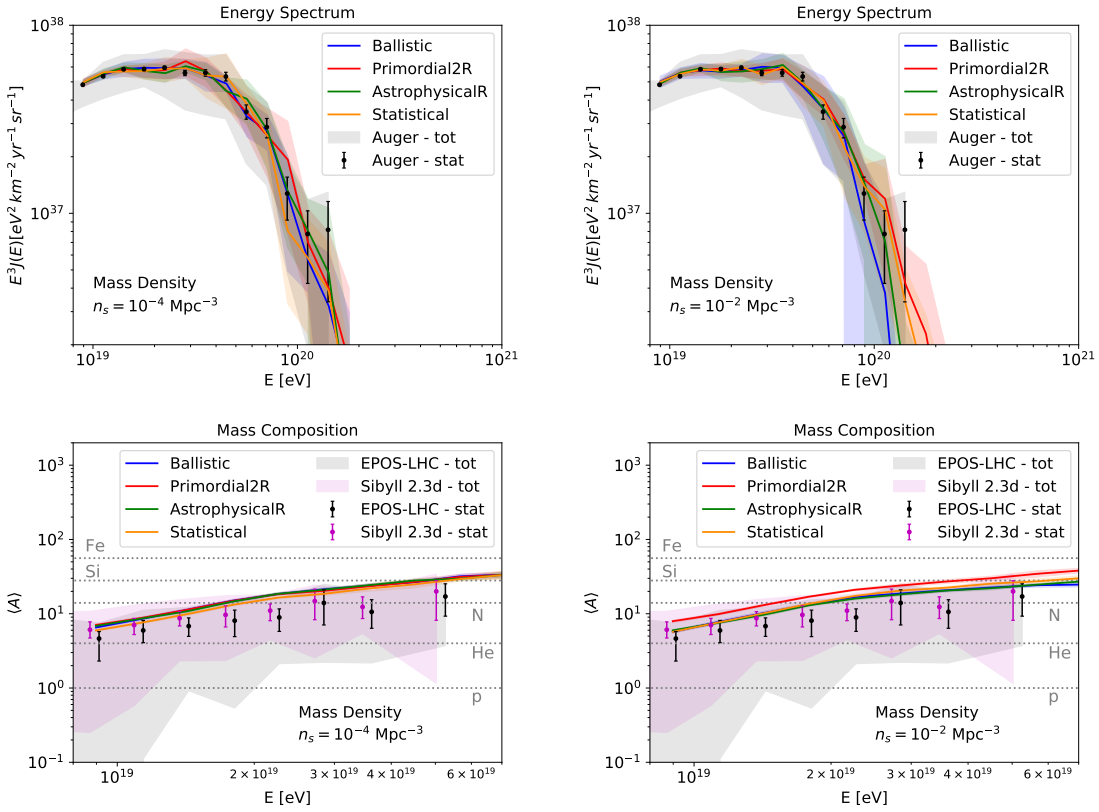

Figure 7.6: Top: simulated energy spectrum at Earth for the *mass density* catalogues. Different colors correspond to different EGMF models and the shaded areas indicate the cosmic variance of the model. The simulated energy spectra are compared with the observed energy spectrum above 8 EeV from [367] shown as black points: the black error bars indicate the statistical variance, and the gray shaded areas correspond to the total variance (statistical and systematic) of the data. Bottom: simulated mass compositions compared with the observed composition from [155, 359] shown as black points for the hadronic interaction model EPOS-LHC [77], and as purple points for Sibyll 2.3d [80]: Error bars and shaded areas indicate the same uncertainties as for the energy spectrum. The left panels refer to the source density $n_s = 10^{-4}\,\mathrm{Mpc}^{-3}$ and the right panels to $n_s = 10^{-2}\,\mathrm{Mpc}^{-3}$. Figure taken from [316].

component would give rise to a too heavy mass composition at the highest energy.

The propagated energy spectra and mass compositions are shown in Fig. 7.6 for the parameters in Table 7.1. The colored lines and shaded areas correspond to the cosmic average and cosmic variance of the simulated scenarios. We also show the observed energy spectrum above 8 EeV by the Pierre Auger Observatory [367] as black points. The statistical variance is indicated by black error bars, while the total variance (statistical and systematic) is indicated by the gray shaded area. The simulated mass compositions are also compared with the observed composition from [155, 359] for the hadronic interaction models EPOS-LHC [77] (black points) and Sibyll 2.3d [80] (purple points). The error bars and shaded areas denote again the statistical and total variance, respectively. We can see that our simulated scenarios are compatible with observations within the current systematic uncertainties and the cosmic variance of our simulated scenarios.

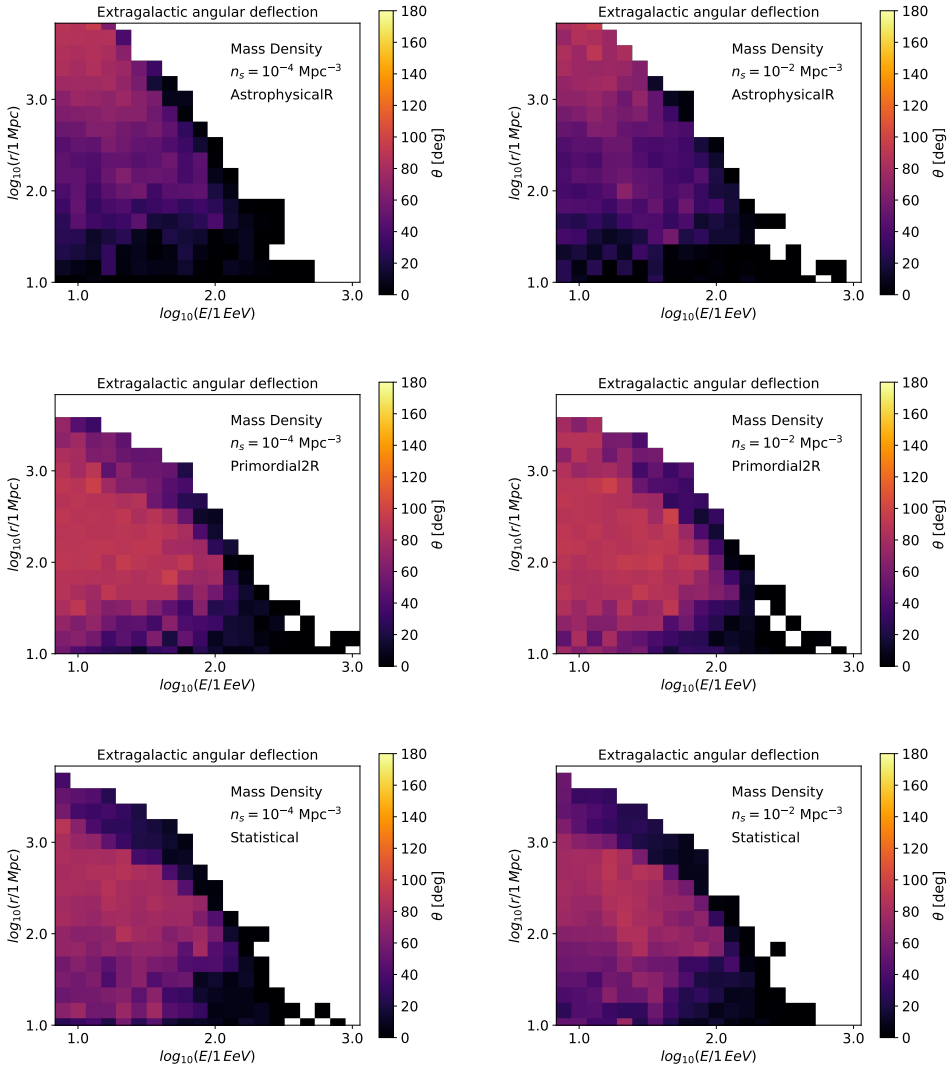

Figure 7.7: Cosmic average of the total angular deflection distribution of the observed UHECRs above 8 EeV for the *mass density* source catalogues. The *astrophysicalR* (top), *primordial2R* (middle) and *statistical* (bottom) EGMF models are shown. The deflection angle is given in degrees and it is indicated in the color bar. The axes show the observed energy (x-axis) and the source distance (y-axis). The left panels refer to the source density $n_s = 10^{-4}\,\mathrm{Mpc}^{-3}$ and the right panels to $n_s = 10^{-2}\,\mathrm{Mpc}^{-3}$. Figure taken from [316].

7.4.2 Magnetic horizon

The maximum observable UHECR source distance may be affected by magnetic deflections during the extragalactic propagation. In order to evaluate this effect, we compute the angular deflection of the simulated UHECRs as the angle between the momentum of the particle at the injection and at the observation at the observer's surface. In this way, we can consider the effect of the EGMF alone. The distributions of the angular deflection for the *mass density* source catalogues are

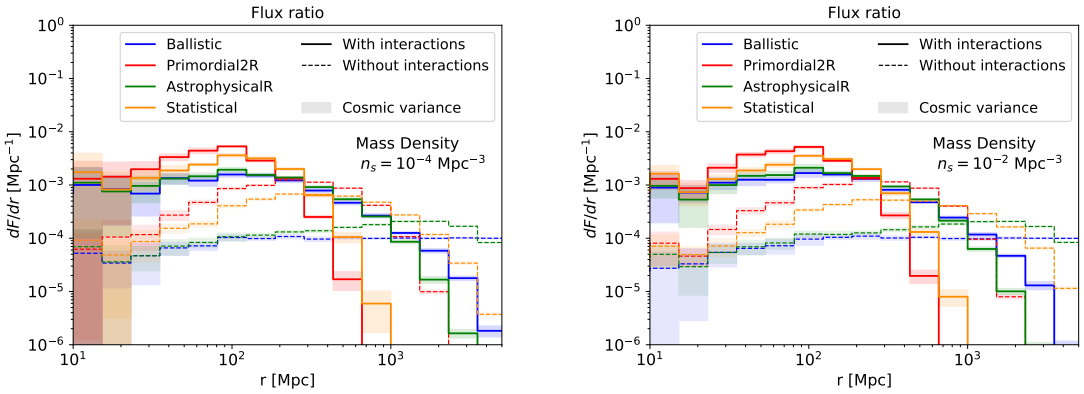

Figure 7.8: Distribution of the relative UHECR flux contribution dF above 8 EeV from sources within distance interval dr with distance to the observer r, for the *mass density* source catalogues. Different colors correspond to different EGMF models. The low density scenario is shown in the left panel and high density scenario in the right panel. The same scenarios, but without photohadronic interactions are shown as dashed lines. The shaded areas represent the cosmic variance. Figure taken from [316].

shown in Fig. 7.7 for all EGMF and source density scenarios. The distributions of the deflection angle are shown as functions of the observed cosmic ray energy and source distance.

We obtained large deflection angles up to $\sim 90°$ in all EGMF models considered, although different magnetization scenarios of the cosmic voids correspond to different distributions. In the *astrophysicalR* model, magnetic deflections are expected to occur only in regions where a high baryonic density is present. This can be seen by comparing the right panel of Fig. 7.1 and Fig. 7.2. In the top panels of Fig. 7.7, it can be seen that deflection angles $\gtrsim 90°$ are obtained for UHECR sources at distance $r \gtrsim 1$ Gpc. These large deflections from very distant sources are due to the fact that UHECRs have to pass through several magnetized regions separated by large unmagnetized cosmic voids in order to collect enough small angle deflections.

In contrast, in the *primordial2R* and *statistical* scenarios, the magnetization of the cosmic voids is such that large deflections are observed even for sources at $r \sim 100$ Mpc. The magnetization of the voids is also such that the maximum distance of the observed sources decreases. This is due to the fact that particles from very distant sources suffer greater energy losses and are therefore deflected more strongly until they enter the diffusive regime and are no longer able to reach the observer within the maximum propagation time. This leads to the formation of a *magnetic horizon*, regardless of the source density considered.

To better quantify the dependence of this magnetic horizon on the EGMF model, we show in Fig. 7.8 the relative contribution dF to the UHECR flux per source distance interval dr as a function of the distance r to the observer for all the EGMF models as colored lines. We also show the dF/dr obtained with simulations where photohadronic interactions are neglected, as dashed lines in Fig. 7.8. In this way, it is possible to see the magnetic horizon suppression given by the EGMF alone. As expected, the scenarios without both interactions and magnetic field show the same contribution from near and distant sources (i.e. flux contributions per distance bin that are roughly constant). A small suppression is obtained at small distances: it is due to the finite value of the source number density, which corresponds to a minimum source distance. However, we can see that the more magnetized models introduce a suppression of the maximum source distance,

which becomes stronger as the magnetization of the voids increases, as in the *primordial2R* and *statistical* scenarios. This effect becomes more pronounced when photohadronic interactions are included in the simulations, due to the production of low rigidity particles during the extragalactic propagation. We have obtained that the maximum source distance of the ballistic case of few Gpc is reduced to $\sim O(100\,\mathrm{Mpc})$. Correspondingly, an increased contribution from sources at distances $10\,\mathrm{Mpc} \lesssim r \lesssim 100\,\mathrm{Mpc}$ is also observed, which is almost independent of the source distribution model or number density considered. We have also obtained that, for distances $r \lesssim 20\,\mathrm{Mpc}$, the cosmic variance of the source catalogues strongly affects the contribution of nearby sources to the UHECR flux. This effect is particularly strong when $n_s = 10^{-4}\,\mathrm{Mpc}^{-3}$.

7.4.3 Multipole analysis

The deviation from a purely isotropic sky distribution $\Psi^{\mathrm{iso}} = (4\pi)^{-1}$ of the arrival direction distribution $\phi(\hat{\mathbf{n}})$ can be evaluated by considering the fractional deviation function, defined as

$$\delta_\phi(\hat{\mathbf{n}}) = \frac{\phi(\hat{\mathbf{n}}) - \Psi^{\mathrm{iso}}}{\Psi^{\mathrm{iso}}} \,. \tag{7.13}$$

The average map of the fractional deviations $\delta_\phi(\hat{\mathbf{n}})$ on the observer surface obtained with the 10 realizations of the *mass density* scenarios are shown in Fig 7.9 for all the propagation scenarios considered, in Galactic coordinates. The *astrophysicalR* (second row), *primordial2R* (third row) and *statistical* (fourth row) EGMF models are shown together with the ballistic case (first row). We apply a Gaussian smoothing to the sky maps in Fig. 7.9 with a full width at half maximum (FWHM) of 45° to remove small scale anisotropies while preserving the large scale structure. The deviations from the isotropic expectation observed in the ballistic scenarios in Fig. 7.9 are due to the combined effect of the intrinsic structure of the source distribution and the interaction horizon, as shown in Fig. 7.8. We obtain a hotspot of UHECRs at Galactic coordinates $\sim (-60°, 30°)$ with $\delta_\phi \gtrsim 0.25$. The position and structure of this hotspot are modified by the magnetization of the cosmic voids. In fact, in the *astrophysicalR* model this deviation is reduced to $\delta_\phi \simeq 0.15$ when $n_s = 10^{-4}\,\mathrm{Mpc}^{-3}$, while it is almost unchanged in the high density scenario, due to the number of nearby sources. The *primordial2R* EGMF introduces a general shift of the hotspot to Galactic coordinates $\sim (-90°, 45°)$, independent of the source density. Finally, when we consider the *statistical* scenario, we obtain that the UHECR excess is scattered across the sky: the excess remains clearly visible only in the case of high source density, with a value of $\delta_\phi \simeq 0.15 - 0.20$.

We quantify the anisotropy signal by calculating the angular power spectrum $\mathcal{C}_l$ of the sky distributions $\phi(\hat{\mathbf{n}})$. We consider the ratio $\mathcal{C}_l/\mathcal{C}_0$, in oder to be independent from the UHECR flux normalization. Fig. 7.10 shows the angular power spectra $\mathcal{C}_l/\mathcal{C}_0$ for the *mass density* scenarios. We show the cosmic variance (shaded areas) and the total variance (error bars, cosmic and statistical variance from Eq. (7.10)). The low source density scenarios correspond to a slightly higher angular power spectrum and its cosmic variance. This effect is particularly visible for $l \lesssim 3$, due to the smaller number of nearby sources and their intrinsically structured distribution. Interestingly, we also observe this feature in the *homogeneous* scenarios, when ballistic propagation is considered (Fig. C.3.6). As shown in Fig. 7.3, the *homogeneous* source catalogues contain more sources at small distances than the *mass density* catalogues. Despite the structured distribution of the *mass density* catalogues, the larger number of local sources in the *homogeneous* catalogues has a direct impact on the UHECR multipole distribution.

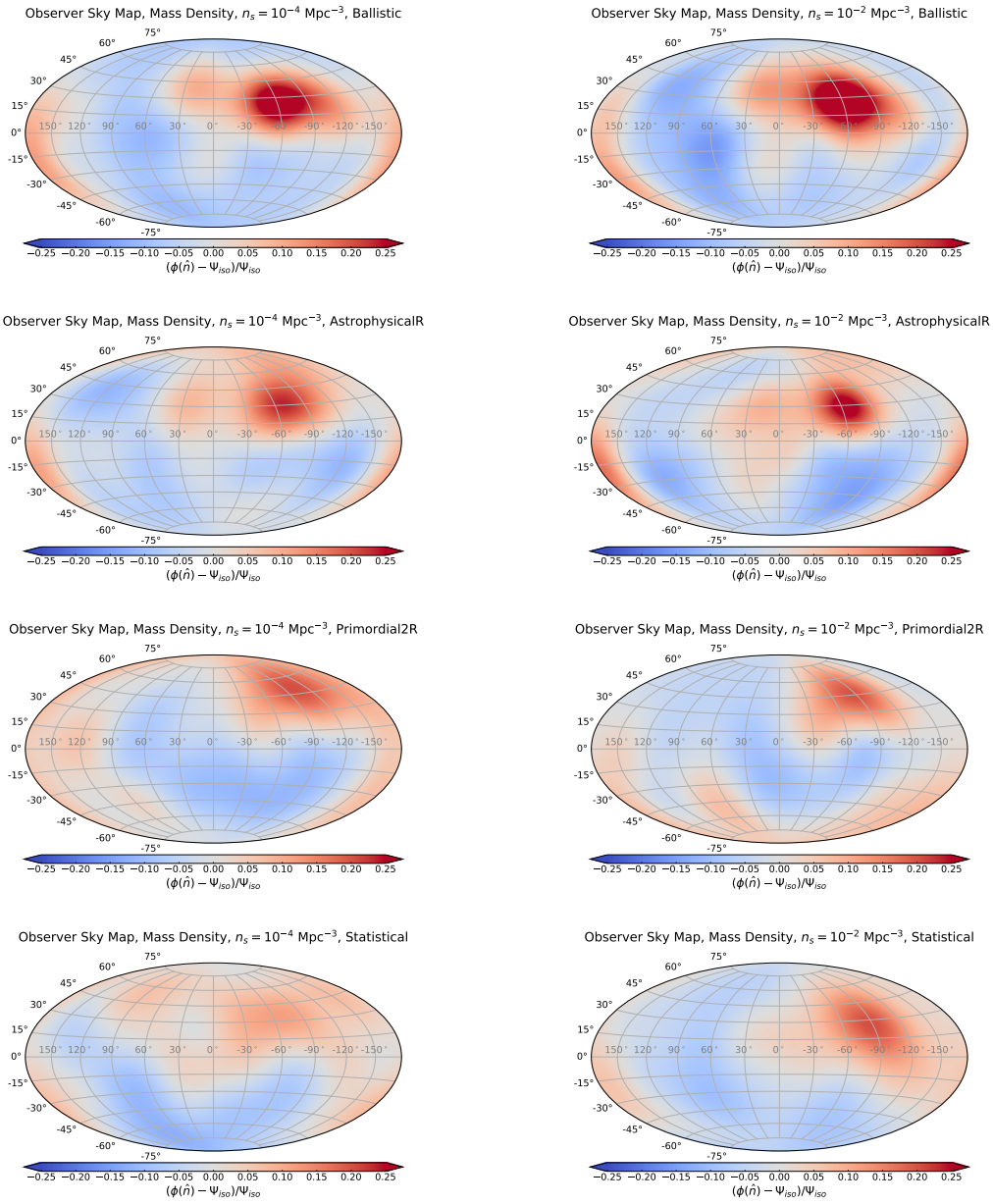

Figure 7.9: Average maps of the fractional deviation from isotropy in Eq. (7.13) of UHECRs above 8 EeV obtained with the 10 realizations of the *mass density* source catalogues. Sky maps obtained at the surface of the observer (i.e. at the edge of the galaxy) in Galactic coordinates. The *astrophysicalR* (second row), *primordial2R* (third row) and *statistical* (fourth row) EGMF models are shown together with the ballistic case (first row). The left panels refer to the source density $n_s = 10^{-4}\,\mathrm{Mpc}^{-3}$ and the right panels to $n_s = 10^{-2}\,\mathrm{Mpc}^{-3}$. We apply a Gaussian smoothing to the sky maps with a full width at half maximum (FWHM) of 45°. The color bar indicates the fractional deviation from isotropy from -0.25 to 0.25. Figure taken from [316].

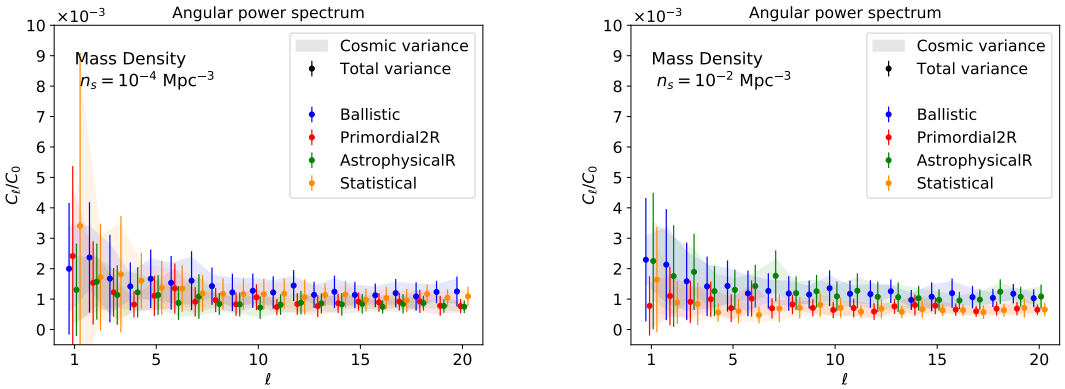

Figure 7.10: Angular power spectra normalized to the monopole (i.e. $\mathcal{C}_l/\mathcal{C}_0$) of the UHECR arrival direction distributions above 8 EeV for the *mass density* source catalogues. The left panel refers to the source density $n_s = 10^{-4}\,\mathrm{Mpc}^{-3}$ and the right panel to $n_s = 10^{-2}\,\mathrm{Mpc}^{-3}$. Different EGMF models are shown in different colors. The shaded areas correspond to the cosmic variance and the error bar to the total variance (cosmic and statistical variance from Eq. (7.10)). Figure taken from [316].

Regarding the fluctuations in the angular power spectra, we observer that the cosmic variance of the source catalogues is the main source of fluctuations in the multipoles. In general, the statistical fluctuation due to the finite number of observed UHECRs has a minor effect on the multipoles variance. In all the scenarios considered here, the angular power spectra decrease at small angular scales (i.e. large values of l) because on small scales the average source distribution is rather smooth and only varies significantly on relatively larger scales. This effect also propagates to the cosmic variance, due to the cosmological principle. In fact, as we look at larger and larger cosmic volumes around the UHECR observer, the differences in multiple samples of the source catalogues become negligible.

We account for the influence of the Galactic magnetic field by applying the magnetic lensing based on the JF12 GMF model to the arrival direction distribution at the edge of the Galaxy. In Fig. 7.11 the fractional deviation from isotropy of the lensed distributions are shown in Galactic coordinates (as in Fig. 7.9). We can see that the main hotspot present in the sky at the edge of the Galaxy is still present after the propagation in the GMF, with basically the same relative excess. We obtain that the GMF introduces a general shift of the hotspot towards lower Galactic latitudes and a smearing of the hotspot angular size. Furthermore, we can also see that most of the small angular scale deviations present in Fig 7.9 are suppressed after propagating in the Galactic field. Only the large angular scale deviations are still present in the UHECR sky above 8 EeV.

The effect of the GMF is also visible in the angular power spectra of the lensed arrival direction distributions, as shown in Fig. 7.12. The angular power spectra are shown together with the theoretical prediction for an isotropic sky obtained with Eq. (6.79) (dashed lines) and the observed multipoles from [17] (black squares). The propagation in the Milky Way introduces a strong suppression of multipoles, especially for $l > 5$. We can clearly see how the large multipole components of the lensed angular power spectra converge to the expected angular power spectrum for an isotropic distribution as l increases. However, the small multipole components, such as the dipole and the quadrupole, are larger than those observed by the Pierre Auger Observatory.

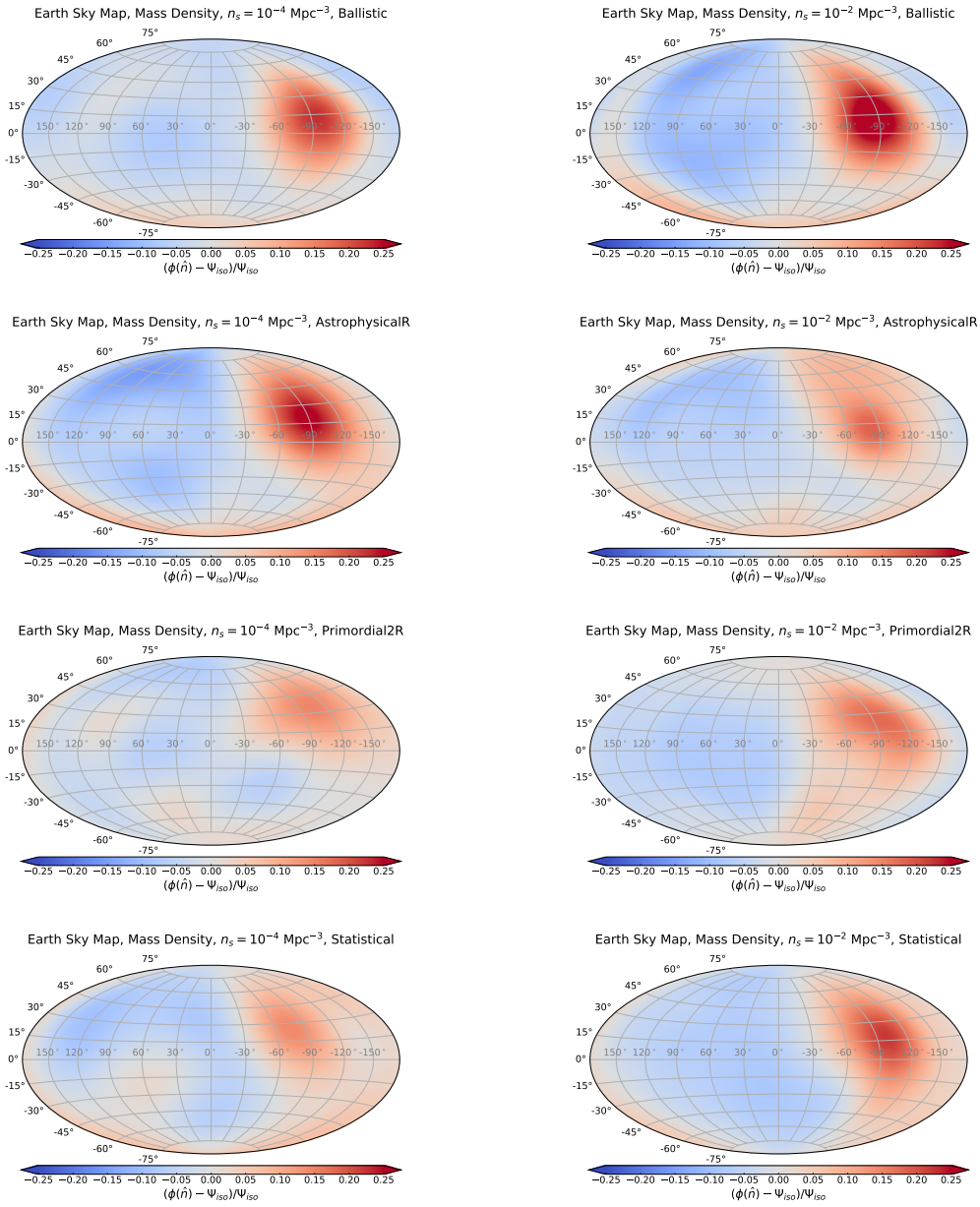

Figure 7.11: Average maps of the fractional deviation from isotropy (7.13) of UHECRs above 8 EeV obtained with the 10 realizations of the *mass density* source catalogues. Sky maps obtained at Earth after the propagation in the JF12 GMF model. Maps in Galactic coordinates. The *astrophysicalR* (second row), *primordial2R* (third row) and *statistical* (fourth row) EGMF models are shown together with the ballistic case (first row). The left panels refer to the source density $n_s = 10^{-4}\,\mathrm{Mpc}^{-3}$ and the right panels to $n_s = 10^{-2}\,\mathrm{Mpc}^{-3}$. We apply a Gaussian smoothing to the sky maps with a full width at half maximum (FWHM) of 45°. The color bar indicates the fractional deviation from isotropy from -0.25 to 0.25. Figure taken from [316].

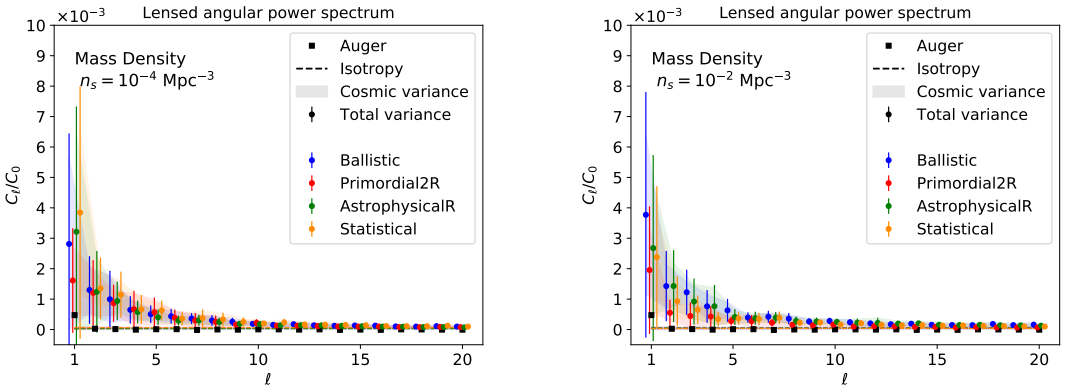

Figure 7.12: Lensed angular power spectra normalized to the monopole (i.e. $\mathcal{C}_l/\mathcal{C}_0$) of the UHECR arrival direction distributions above 8 EeV for the *mass density* source catalogues. The left panel refers to the source density $n_s = 10^{-4}\,\mathrm{Mpc}^{-3}$ and the right panel to $n_s = 10^{-2}\,\mathrm{Mpc}^{-3}$. Different EGMF models are shown in different colors. The shaded areas correspond to the cosmic variance and the error bar to the total variance (cosmic and statistical variance from Eq. (7.10)). The dashed lines correspond to the isotropic theoretical predictions from Eq. (6.79) of the scenarios considered. The black squares correspond to the observed angular power spectrum above 8 EeV from [17]. Figure taken from [316].

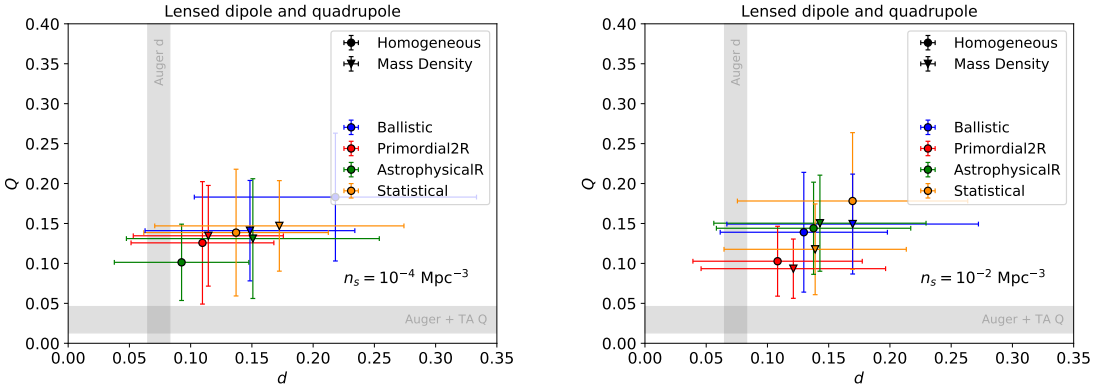

Figure 7.13: Simulated lensed dipoles and quadrupoles above 8 EeV obtained with Eqs. (7.11) and (7.12) shown as circles for the *homogeneous* scenarios and triangles for the *mass density*. The left panel refers to the source density $n_s = 10^{-4}\,\mathrm{Mpc}^{-3}$ and the right panel to $n_s = 10^{-2}\,\mathrm{Mpc}^{-3}$. Different EGMF models are shown in different colors. The error bars correspond to the total variance. The gray regions correspond to the observed dipole and quadrupole from [320] and [167], respectively. Figure taken from [316].

Fig. 7.13 shows the obtained dipole and quadrupole moments for the simulated scenarios after accounting for the galactic deflection. The dipoles and quadrupoles are obtained from the lensed angular power spectra in Figs. 7.12 and C.3.7 with Eqs. (7.11) and (7.12), respectively. The error bars indicate the total variance and the gray areas the observed dipole from [320] and quadrupole from [167]. We can see that in the *mass density* scenarios larger dipole values are obtained on average than in the *homogeneous* cases for $n_s = 10^{-4}\,\mathrm{Mpc}^{-3}$. This effect is less

present in the high source density case due to the much larger number of local sources. This is again the result of the structured distribution of the local sources in our catalogues. We do not observe any significant effect due to the EGMF model on the predicted dipole and quadrupole moments. We have obtained that most of the dipoles are compatible with observations only within the total variance, while the quadrupole moments are generally too large.

7.5 Conclusions

We have studied the propagation of UHECRs in constrained replicas of the local cosmic web by taking into account the effect of different structured EGMF and source distribution models. We have simulated the injection of five different nuclear species at the locations of sources with identical properties. We also account for the effect of the GMF by lensing the corrected arrival directions at the edge of the Milky Way halo.

To account for the cosmic variance in our results, we have considered $N_{\rm R} = 10$ realizations of the synthetic source catalogues. Although a larger number of realizations is possible in principle, three-dimensional simulations of UHECR propagation in structured magnetic fields are very time consuming. As shown in Fig. 7.3, the cosmic variance of the number of sources within $\sim 100\,\mathrm{Mpc}$ from the observer is very small, and basically negligible for larger distances. Indeed, we find that the cosmic variance of the simulated UHECR observables does not affect the robustness of our results. The average number of sources within 100 Mpc from the observer is $N_{\rm source,low} \simeq 4 \cdot 10^2$ for the low density catalogues and $N_{\rm source,high} \simeq 4 \cdot 10^4$ for the high density catalogues. Since the corresponding fluctuations in the number of sources within 100 Mpc from the observer can be estimated as $\sqrt{N_{\rm source,low}} \simeq 20$ and $\sqrt{N_{\rm source,high}} \simeq 200$, we do not expect rare catalogue realizations characterized by large source overdensities to substantially change our conclusions.

We have found that, in order to reproduce the observed UHECR energy spectrum and mass composition above 8 EeV, a hard spectral index from $\gamma \simeq -1$ to $\gamma \simeq -3$ and a rigidity cutoff of $\log\left(R_{\rm cut}/1\,\mathrm{EV}\right) \simeq 0.2$ are needed at the escape from the source environments (see Tables 7.1 and C.1). Furthermore, the composition must be dominated by nitrogen and silicon nuclei. However, the variance observed in the injection parameters among different propagation scenarios shows how different assumptions can strongly affect the predictions at the escape from the sources.

Very large deflections, due to the EGMF, up to $\sim 90^\circ$ have been observed in Figs. 7.7 and C.3.3. We found that the level of magnetization of the cosmic voids plays the main role in the distribution of the deflection angles in energy and source distance. In the case of an astrophysical EGMF, large deflections are observed only for very-low-energy nuclei coming from distant sources. On the contrary, in primordial scenarios, very large deflections are observed even for cosmic rays emitted at $\sim 100\,\mathrm{Mpc}$ from the observer.

The magnitude of the magnetization of the cosmic voids also affects the maximum source distance of the observed UHECR above 8 EeV. We have found that the horizon resulting from the interaction with background photon fields is further reduced by the EGMF, depending on the level of magnetization of the cosmic voids. In particular, the suppression is due to the large deflection experienced by the cosmic rays as they propagate through the magnetized voids. In the *primordial2R* and *statistical* cases, we find a suppression of the interaction horizon from $\sim 500\,\mathrm{Mpc}$ to $\sim 100\,\mathrm{Mpc}$. Correspondingly, the contribution of sources at distance $r \lesssim 100\,\mathrm{Mpc}$ increases with respect to the *astrophysicalR* and ballistic cases. These results are independent

on the cosmic variance of the source catalogues.

We have evaluated the probability distributions $\phi(\hat{\mathbf{n}})$ of the recorded UHECR arrival directions for our simulated scenarios and the corresponding angular power spectra. We have seen in Figs. 7.10 and C.3.6 that a structured source distribution corresponds to larger values of low multipoles ($l \lesssim 3$) than in the *homogeneous* scenarios. We have also confirmed that the main source of fluctuation in the multipole distribution is the cosmic variance of the source catalogues, which increases as the source density value decreases. Unfortunately, no effects of the EGMF models have been found in the multipole expansions. We have repeated the same analysis taking into account the deflection due to the GMF, considering the magnetic lens of the JF12 model. The main effects observed in the arrival direction distributions are the suppression of the small angular scale deviations observed at the edge of the Galaxy, and a general shift of the main UHECR excess towards lower Galactic latitudes. We have also found that all the angular power spectra of the considered scenarios converge to their corresponding isotropic prediction for $l > 5$.

However, in all the simulated scenarios, we found too large low multipoles compared to the results of the Pierre Auger Observatory. In particular, as it can be seen in Fig. 7.13, the dipole components are compatible with the observations only within the total variance, while the quadrupole components are generally too large, independently on the source density, distribution and EGMF model. This discrepancy between the simulated quadrupole moments and the observations indicates the need to refine the assumptions of the model. We have considered one GMF model and found that its main effect is to suppress the large multipole components of the simulated angular power spectra. The deflection angle of UHECRs with energies above 8 EeV in the GMF is $\theta \lesssim 20^\circ$, corresponding to mutipoles of order $l \gtrsim 10$. Therefore, we do not expect that different GMF models would lead to a strong suppression of the quadrupole amplitude. Therefore, since the obtained dipole and quadrupole moments are independent of the EGMF model, one possible explanation for the observed anisotropies could be an intrinsic and almost purely dipolar distribution of their sources. This would put constraints on the general assumption that the UHECR sources follow the baryonic distribution in the local Universe.

8

Cosmic ray propagation in source environments

This chapter is based on the publication:

- S. Rossoni, D. Boncioli, and G. Sigl. (2025). *Investigating binary-neutron-star mergers as production sites of high-energy neutrinos.* **JCAP**, 01, 009. arXiv:2407.19957 [astro-ph.HE]. https://doi.org/10.1088/1475-7516/2025/01/009.

The presence of photon fields in the environment in which UHECRs propagate leads to stochastic interactions and production of secondary particles. However, this can occur both during the extragalactic propagation and within source environments. Moreover, the production of neutral and stable secondary particles, such as neutrinos, which leave the source region immediately after production, can be used to study the local UHECR source environment.

An interesting site for the production of high-energy neutrinos is the end state of a binary-neutron-star merger. Inspired by the event GW170817, we investigate a scenario in which CRs are accelerated in a population of mergers in the energy range from the knee to the ankle of the CR energy spectrum. In Sec. 8.2, we model the interactions and, in Sec. 8.3, we study the resulting neutrino production of CRs with the local photon fields. In Sec. 8.4, we study the extragalactic propagation of the escaped CR and neutrino fluxes and compare the expected diffuse fluxes with experimental data and current limits. We then discuss the predicted diffuse neutrino flux associated with this class of astrophysical objects, as a function of the details of the accelerated CR energy spectrum, the photon field characterizing the post-merger stage, and the time evolution of the interaction region. Finally, in Sec. 8.5, we constrain the fraction of accelerated baryons at the source site given the merger rate per volume, taking into account at the same time the constraints from the measured cosmic ray and neutrino fluxes.

8.1 Multimessenger astrophysical sources

The observed energy spectrum and mass composition of the UHECRs detected by cosmic ray observatories do not correspond to that at the escape from their sources. We have discussed in

Sec. 4.3 that this is due to the photohadronic interactions between UHECRs and the background photon fields that are present during the extragalactic propagation. We have also seen that these interactions lead to the production of secondary cosmogenic particles, such as neutrinos and photons, which carry useful information for the characterization of the primary UHECR sources.

The typical length scales for the production of cosmogenic particles can be obtained with Eq. (4.45), which is linear in both the SED of the photon fields and the cross section of the interaction processes. However, if we consider the derivation of the UHECR interaction rate τ^{-1} given in Appendix B.1, we can immediately see that the same result can also be applied in a context other than the extragalactic propagation. Since the only assumption made is that the interactions occur between a projectile particle propagating in an isotropic photon field, Eq. (4.45) can be used to calculate the interaction rate with a generic photon field. In particular, local photon fields present in source environments can be considered to study the propagation of CRs before they escape from their accelerators.

Two main results can be obtained by considering the propagation of cosmic rays before they escape from the source environment. Since the energy spectrum and mass composition obtained by considering the effects of the extragalactic propagation correspond to those at the escape from the source, the same spectrum and composition also correspond to those produced by the interplay of acceleration and interactions within the sources. This means that *in-source* simulations can be combined with observations to characterize the local environment of UHECR sources. In addition, secondary particles produced in local photohadronic interactions could escape from the source region and propagate to the Earth. Observations of the astrophysical flux of these secondary particles could provide further information for the search of cosmic ray sources and for the characterization of the acceleration region. The combined study of different astrophysical particles, such as cosmic rays, neutrinos and γ-rays is called *multimessenger astrophysics* [369, 370].

8.1.1 Astrophysical neutrinos

Neutrinos and other neutral and stable messengers could be very important for studying the sources and the acceleration mechanisms of UHECRs. Neutrinos can escape from dense astrophysical environments that are opaque to nuclei and γ-rays. Furthermore, because neutrinos are neutral particles, they are not deflected by cosmic magnetic fields and they point back to their sources. This means that astrophysical neutrinos can be used for spatial and temporal coincidence studies with other particles in a multimessenger framework.

The IceCube Neutrino Observatory [21] has reported the observation of a diffuse neutrino flux in the TeV - PeV energy range [371]. The muon-neutrino (ν_μ) flux from the IceCube muon-track data is consistent with an energy spectrum of the form $E_\nu^{-\gamma}$, with normalization at 100 TeV of $\phi_{\nu_\mu+\bar{\nu}_\mu} \simeq 1.5 \cdot 10^{-18}\,\mathrm{GeV}^{-1}\,\mathrm{cm}^{-2}\,\mathrm{s}^{-1}\,\mathrm{sr}^{-1}$ and spectral index $\gamma \simeq 2.4$ [372] . Moreover, the flux of neutrinos from cascade events has also been shown to be consistent with a single power-law with normalization of $\phi_{\nu+\bar{\nu}} \simeq 1.7 \cdot 10^{-18}\,\mathrm{GeV}^{-1}\,\mathrm{cm}^{-2}\,\mathrm{s}^{-1}\,\mathrm{sr}^{-1}$ at 100 TeV, and spectral index $\gamma \simeq 2.5$ [373]. Upper limits for the contributions of different classes of sources, such as for distant blazars in [374], have been obtained. In the context of multimessenger astrophysics, the successful observation of neutrinos and γ-rays from the blazar TXS 0506+056 [192], and the association of 79 neutrino events to the Seyfert galaxy NGC 1068 [375] show the advantage of considering neutral and stable cosmic messengers . It has also been shown that IceCube neutrino events can

be associated with the optical counterparts of the emission from TDEs [214, 215, 376]. Non-jetted sources are also becoming interesting as possible sites for high-energy neutrino production [377]. Phenomenological models have been developed to explain the simultaneous electromagnetic and neutrino production, as in [378] for the blazar TXS 0506+056, in [379] for NGC 1068, and in [380] for the TDE AT2019aalc.

In 2017, the first joint observation of a GW signal and its electromagnetic counterpart occurred [26–28]. Even if no evidence of correlations between high-energy neutrinos and GWs has been established yet [381], the sources responsible for GW signals are considered to be of great interest for the study of high-energy interactions, as shown in [173]. An interesting class of GW sources are binary systems of coalescing neutron stars: the probable end state of binary-neutron-star (BNS) mergers is a black hole with a relativistic jet, powered by the material in the accretion disk. The formation of the jet gives rise to a short-GRB, where the production of high-energy neutrinos might be possible [184]. Another possible mechanism for the production of astrophysical neutrinos has been described in [382], where a small fraction of the ejected material falls back to the central compact object produced after the merger. This fallback outflow encounters the earlier ejected mass shell, producing a shock wave where particles can be accelerated [216, 383–386]. In particular, in [386] it has been shown how the local magnetic field might allow cosmic rays to reach the energy of the ankle in the CR energy spectrum, contributing to the energy spectrum beyond the Galactic contribution.

We therefore consider the scenario of a population of BNS merger remnants, as described in [382], to study the interaction of cosmic rays with local photon fields. We consider the presence of a thermal field produced by the nuclear decay of synthesized nuclei in the ejecta and a non-thermal synchrotron component [386, 387].The interactions of the UHECRs with these local fields will produce high-energy neutrinos, which will leave the production region undisturbed and travel through the extragalactic space without undergoing any interaction or magnetic deflection. Since the propagation of the escaped UHECRs in the extragalactic space will give rise to the production of a second population of neutrinos (i.e. the cosmogenic neutrinos), we will refer to neutrinos produced in the source as source neutrinos, and neutrinos produce during the propagation as cosmogenic neutrinos.

8.2 Source model

In Chapter 5, we have described the most used numerical frameworks for the extragalactic propagation of high-energy particles. As mentioned in Sec. 8.1, the structure of the calculation of interaction processes with cosmic photon fields can be also used for studying the interactions with the photon field within possible CR sources. In this section, the modelling of the remnant of a BNS merger as cosmic ray source is described. Moreover, the numerical implementation of the in-source propagation in the Monte Carlo framework of `SimProp v2r4` is presented.

8.2.1 Local photon fields

We define the time t as the time after the coalescence, so that $t = 0$ corresponds to the merger event. Due to the nuclear decay of the unstable species synthesized in the ejecta by the merger, a thermal photon field is produced in the source environment. Assuming that the heat from nuclear decays is homogeneously distributed, the photon emission can be modeled as a black-

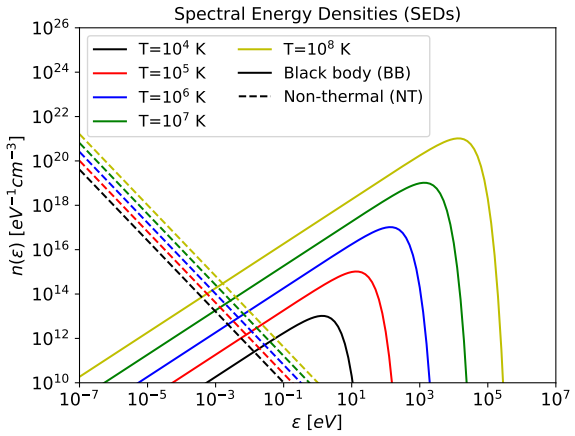

Figure 8.1: SEDs of the thermal photon field (solid lines) and the non-thermal field (dashed lines) in Eq. (8.4). Different times after the merger (corresponding to different temperatures of the black body) are shown in different colors. Figure taken from [388].

body (BB) photon field. The SED of a BB photon field is given in Eq. (4.50). We modeled the temporal evolution of the BB photon field density as done in [382]. Therefore, the time after the merger t and the BB temperature T are such that

$$T = 10^6 \cdot \left(\frac{t}{10^3\,\mathrm{s}}\right)^{-2} \mathrm{K}\,. \tag{8.1}$$

As expected, when time increases after the merger, the temperature of the BB decreases. The number density of the BB photons is given by the integral in the photon energy ε of the SED (see Sec. 4.3.1), and it corresponds to

$$n_{\mathrm{BB}} \simeq 20 \cdot \left(\frac{T}{1\,\mathrm{K}}\right)^3 \mathrm{cm}^{-3}\,. \tag{8.2}$$

Several days after the merger, the thermal photon field is not the dominant background anymore and it is replaced by a non-thermal (NT) component, mainly due to synchrotron emission. We consider the radio-to-X-ray emission of the merger event GW170817 described in [387], where the flux density function is assumed to be of the form $\phi_{\mathrm{NT}}(\nu) \propto \nu^{-\beta}$, where ν is the photon frequency and the index β is fixed to the value 0.6. From [387], we obtain the flux density function[1] as

$$\phi_{\mathrm{NT}}\,(\nu) = 0.76 \cdot \left(\frac{t}{1\,\mathrm{s}}\right)^{1.2} \left(\frac{\nu}{1\,\mathrm{Hz}}\right)^{-0.6} \mu\mathrm{Jy}\,, \tag{8.3}$$

where t is the time after the merger. The flux density in Eq. (8.3) can be then converted to the SED of the non-thermal component as

$$n_{\mathrm{NT}}\,(\varepsilon) = 1.2 \cdot 10^{27} \cdot \left(\frac{V}{1\,\mathrm{km}^3}\right)^{-1} \left(\frac{t}{1\,\mathrm{s}}\right)^{2.2} \left(\frac{\varepsilon}{1\,\mathrm{eV}}\right)^{-1.6} \mathrm{eV}^{-1}\mathrm{cm}^{-3}\,, \tag{8.4}$$

[1] We use the flux unit μJy, which corresponds to $1\,\mathrm{Jy} = 10^{-23}\,\mathrm{erg\,s^{-1}\,cm^{-2}\,Hz^{-1}}$.

where V is the volume of the source environment. The SED in Eq. (8.4) and the thermal SED are shown in Fig. 8.1, where solid lines correspond to the BB component and the dashed lines correspond to the NT component. Different colors are used for different temperatures (or times) after the merger. We can see that the BB component is the dominant background for $\varepsilon \gtrsim 0.01\,\text{eV}$. For $T \lesssim 10^4\,\text{K}$ (i.e. $t \gtrsim 3\,\text{h}$) the non-thermal field becomes dominant.

8.2.2 Escape length

We approximate the size of the neutrino production site by taking into account the radius of the ejected material, in free expansion after the merger. In particular, we make the simplistic assumption that the typical escape length for UHECRs is given by the radius of the ejected material, given by

$$\lambda_{\text{esc}}(t) = \beta_{\text{ej}}\, t\,, \tag{8.5}$$

where β_{ej} is the speed of the ejected material in units of speed of light. The typical escape rate is thus

$$\tau_{\text{esc}}^{-1}(t) = \frac{1}{\lambda_{\text{esc}}(t)} = \frac{1}{\beta_{\text{ej}} t}\,. \tag{8.6}$$

We assume $\beta_{\text{ej}} = 0.3$, as done in [382].

The assumption we made on the escape length may influence the neutrino production efficiency of the source. A higher value of β_{ej} corresponds to a lower escape rate, and thus accelerated CRs may produce more neutrinos. Moreover, the confinement of a nucleus in Eq. (8.6) is only due to the dimension of the source, and does not depend on the rigidity of the nucleus, i.e. we are assuming that the propagation is ballistic. The validity of the ballistic approximation is given by the condition $\lambda_{\text{esc}}(t) \lesssim r_L$, where r_L is the Larmor radius of the nucleus (see Sec. 4.5). Therefore, the condition on the CR Lorentz factor Γ is

$$\Gamma \gtrsim 3 \cdot 10^5 \left(\frac{Z}{A}\right) \left(\frac{t}{10^2\,\text{s}}\right) \left(\frac{B}{1\,\text{G}}\right)\,, \tag{8.7}$$

where A is the mass number and Z is the atomic number. If we consider that $Z/A \sim 1/2$ and that the neutrino production is maximal for $t \sim 10^2\,\text{s}$, considering a limiting magnetic field strength value equal to $B \sim 1\,\text{G}$ [382, 386], we obtain that the ballistic approximation can be used for $\Gamma \gtrsim 10^5$. This corresponds to $E \gtrsim 10^{14}\,\text{eV}$ for protons and $E \gtrsim 6 \cdot 10^{15}\,\text{eV}$ for iron nuclei.

8.2.3 Interaction efficiency

In this section, we obtain the photohadronic interaction lengths of protons and iron nuclei ^{56}Fe at different times after the merger. Bethe-Heitler pair production, photopion production and photodisintegration are taken into account. However, as shown in [382], the energy loss length of pair production is always several orders of magnitude greater than the one associated with photopion production. Therefore, Bethe-Heitler pair production has a major effect on the total interaction efficiency and escape conditions of the accelerated nuclei.

In the left panel of Fig. 8.2, the photopion interaction lengths (solid lines) of protons interacting with the BB photon field are shown, as a function of the proton Lorentz factor Γ. Different colors correspond to different BB temperatures. The dashed lines correspond to the source typical lengths as defined in Eq. (8.5) at the corresponding temperatures. We can see that both

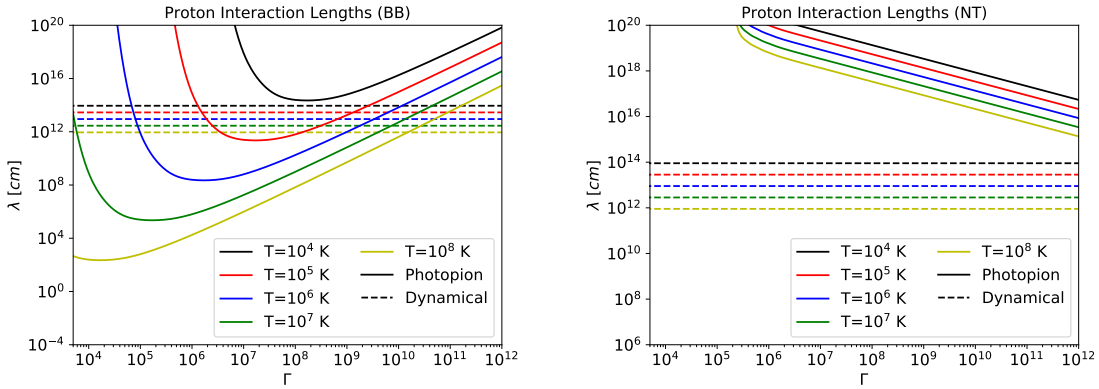

Figure 8.2: Left: interaction lengths for protons for photopion production with the BB photon field (solid lines), as a function of the Lorentz factor Γ. The size of the source radii is indicated with dashed lines. Different colors refer to the BB temperatures as indicated in Fig. 8.1. Right: same as left panel, but for the NT photon field. Note the different ranges of the y-axis. Figure taken from [388].

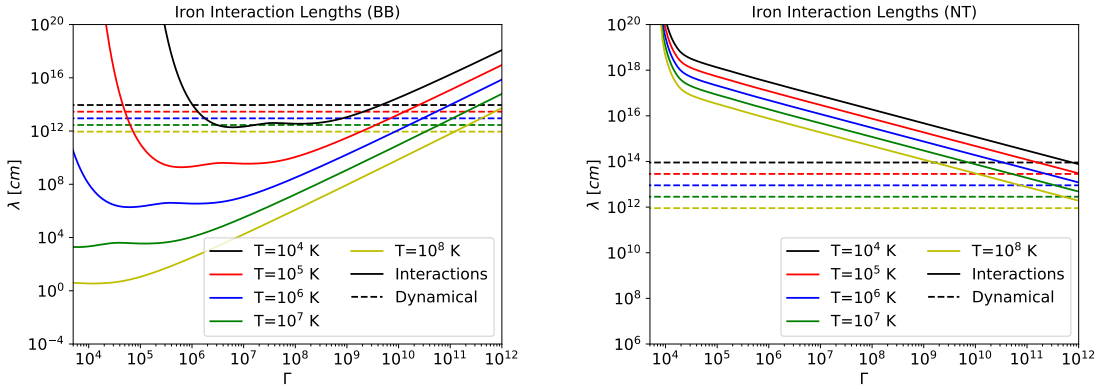

Figure 8.3: Same as Fig. 8.2, but for iron nuclei. Note the different ranges of the y-axis. Figure taken from [388].

the interaction lengths $\lambda_{\rm p}$ and the source radii $\lambda_{\rm esc}$ increase as the BB temperature decreases. We also obtain that $\lambda_{\rm p} > \lambda_{\rm esc}$ for each value of Γ only when $T \sim 10^4$ K. After the merger, the BB temperature decreases and the number of available high-energy photons decreases, making photopion production less efficient. At the same time, the expansion of the source environment is not fast enough to compensate for the field dilution. Therefore, for $T \gtrsim 10^4$ K, protons no longer interact with the local field and they can escape from the source environment. Conversely, in the early stages after the merger, protons interact frequently with the local field, and only very-high-energy protons leave the source undisturbed. The same effect is also obtained for protons of very-low-energy, for which the escape energy threshold increases rapidly as the temperature of the BB decreases, to the point where protons escape for any energy value. In the right panel of Fig. 8.2 the interaction lengths with the NT component are shown. In this case, the photopion production is never an efficient process since the number of high-energy photons is highly suppressed, even when the source temperature is $T = 10^8$ K.

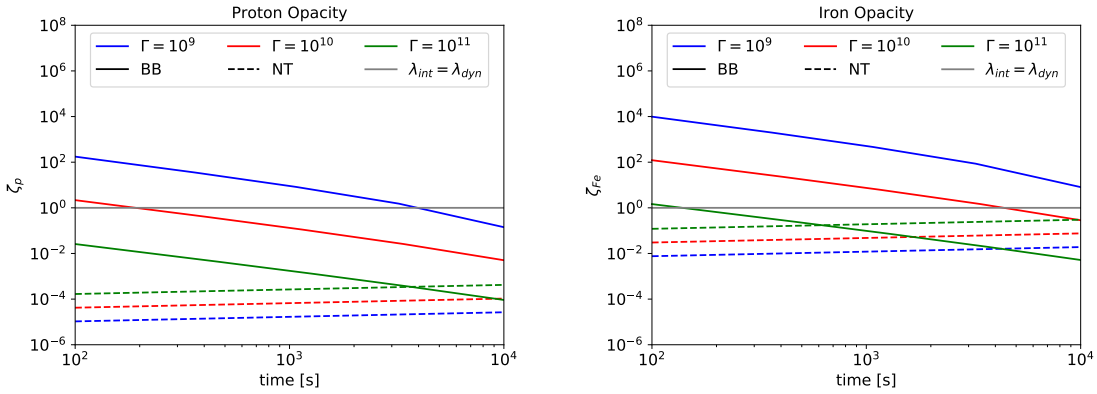

Figure 8.4: Left: source opacity for protons with Lorentz factors $\Gamma = 10^9$ (blue), $\Gamma = 10^{10}$ (red) and $\Gamma = 10^{11}$ (green) as a function of time. Solid lines corresponds to the BB field, dashed lines to the NT field, and the solid gray line represents the condition $\lambda_A = \lambda_{\rm esc}$. Right: same as left panel, but for iron nuclei. Figure taken from [388].

The propagation of iron nuclei in the source environment is also affected by photodisintegration. In the left panel of Fig. 8.3, the total interaction length for iron nuclei is shown together with the typical source radius. We can see that the total interaction length is characterized by two minima: the low-energy minimum can be attributed to the photodisintegration while the high-energy minimum to the photopion production. In general, the interaction versus escape dynamics with the BB temperature is similar to the proton scenario. However, for iron nuclei, interactions are still possible for $T \sim 10^4\,\mathrm{K}$. The total interaction length of iron nuclei with NT photons is slightly smaller than in the case of protons, although interactions with this component are still very inefficient.

We consider only photohadronic interactions because, as shown in [382], photopion production is the dominant process for neutrino production, for both protons and iron nuclei, with respect to hadronic interactions. This can be seen by considering the hadronic cross-section of $\sigma \sim 10^{-25}\,\mathrm{cm}^2$ and inelasticity $\kappa \sim 0.5$ at 1 EeV: we obtain that, for $t \simeq 10^2\,\mathrm{s}$ and the baryon density from [382], the hadronic energy loss length is $\sim 2 \cdot 10^{10}\,\mathrm{cm}$. Comparing this estimate to the photohadronic interaction lengths shown in the left panels of Figs. 8.2 and 8.3, it can be seen that photohadronic interactions are the main neutrino production processes.

We can characterize the efficiency of the photohadronic interactions with time by considering the opacity of the source environment $\zeta_A(\Gamma, t)$ for a nucleus of mass A defined as

$$\zeta_A(\Gamma, t) = \frac{\lambda_{\rm esc}(t)}{\lambda_A(\Gamma, t)}\,, \tag{8.8}$$

where λ_A is the total interaction length and $\lambda_{\rm esc}$ is defined in Eq. (8.5). From the definition in Eq. (8.8), we have that for $\zeta_A > 1$ (< 1) interactions dominate (are suppressed) over the escape. The opacity is shown in the left panel of Fig. 8.4 for protons and in the right panel for iron nuclei. Different fixed values of the Lorentz factor are shown with different colors. The solid lines refer to the opacity of the BB, and dashed lines to the opacity of the NT field. We can see again that the NT component is always transparent for protons and iron nuclei, while the BB opacity is greater than 1 for $\Gamma \lesssim 10^8$ for protons, and $\Gamma \lesssim 10^{10}$ for iron nuclei, for a considerable amount of

time after the merger. As also discussed in [386], very-high-energy CRs ($\Gamma \gtrsim 10^{12}$) will undergo interactions with local photon fields when $t \lesssim 10^4$ s. At later times, the source opacity becomes smaller than 1, and the nuclei are free to escape from the source region without interacting. We find again that the NT photon field is not relevant for CR interaction, and therefore for the production of astrophysical neutrinos. We will then consider only the interactions in the BB field in the study of the production of astrophysical neutrinos.

8.2.4 Numerical implementation

In order to simulate the propagation of UHECRs in the source environment, we have modified the Monte Carlo code `SimProp v2r4` for the extragalactic propagation of UHECRs. We named this modified version as `SimProp in-source`. Since all the interaction processes present in `SimProp v2r4` involve cosmic rays and the cosmic photon fields, the first modification concerns the target photon fields for photohadronic interactions. We replaced the cosmic fields with the local fields described in Sec. 8.2.1. As discussed earlier, the non-thermal component of the source environment is not considered in the simulations. In the original version of `SimProp`, particles propagate from the source until they reach the redshift condition $z = 0$. In the modified version, we implemented an escape condition based on a leaky-box model, where the escape rate in Eq. (8.6) is compared to the total interaction rate. The escape condition is then given by the random sampling of the escape rate among all the possible processes.

The CR and neutrino energy spectra at the escape from the source environment described in Sec. 8.2 will represent the input spectra for the extragalactic propagation. In order to compute the expected diffuse spectra at Earth from a population of BNS mergers, we use the original version of `SimProp v2r4`. A schematic representation of the simulation procedures used in this chapter is shown in Fig. 8.5.

8.3 Source escape and neutrino production

We present and discuss in this section he propagation of cosmic rays in the source environment, taking into account pair production, photopion production, and photodisintegration processes occurring in interactions with the BB local field. We consider the post BNS merger times corresponding to the temperatures between 10^8 K and 10^4 K, as shown in Fig. 8.1. Since the temperature of the source environment is a fixed parameter in every simulation, the other source properties, such as the source radius, the SEDs and escape rate, are also fixed. The photodisintegration of nuclei heavier than protons is simulated considering the default option of `SimProp v2r4` with the parametrization of the cross sections from [244, 297].

It was shown in [382] that, assuming that the magnetic energy in the acceleration site is a fraction of the kinetic energy of the fallback, the only limiting process to the acceleration of nuclei is synchrotron cooling. However, since hadronic and photohadronic interaction processes occur on a large time scales, we can separate the acceleration phase from the neutrino production phase. Furthermore, assuming an equipartition between magnetic and kinetic energy, a maximum acceleration energy of $\sim 10^{19}$ eV can be reached for proton and iron nuclei. The maximum acceleration energy depends slightly on time, as shown in [382]. We assume that $E_{\rm cut}$ does not change over time. For these reasons, we study the production of high-energy neutrinos by considering the injection, into the source environment, of CRs with energy between 10^{14} eV and

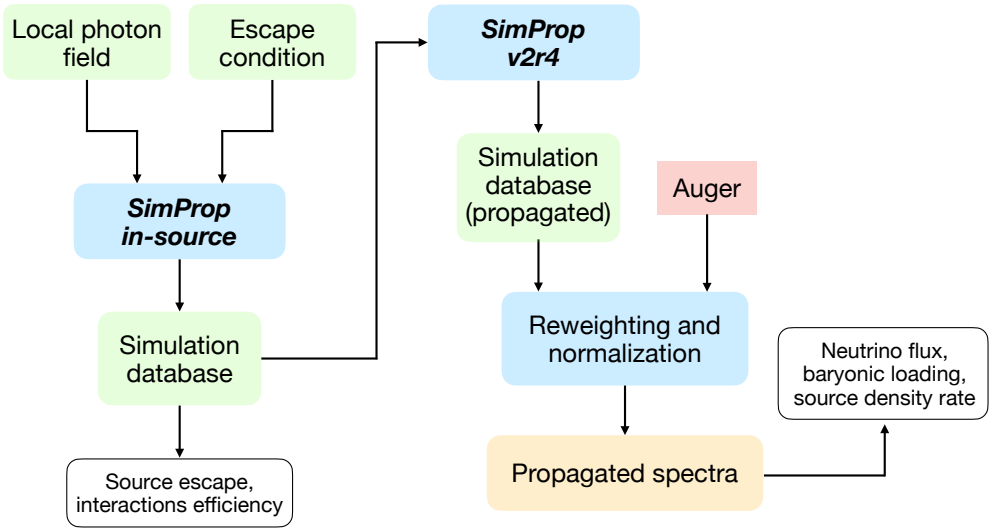

Figure 8.5: Schematic representation of the structure of the study presented in this chapter. The propagation in the source model and in the extragalactic space, the creation of the simulations database, and the obtained propagated spectra are shown.

10^{20} eV. The injection rate at the acceleration of the nuclear species with mass number A is

$$Q^A_{\rm acc}(E) = Q^A_{0,\rm acc} \left(\frac{E}{1\,\rm EeV}\right)^{-\gamma} \exp\left(-\frac{E}{E_{\rm cut}}\right) , \tag{8.9}$$

where γ is the spectral index and $E_{\rm cut}$ is the high-energy cutoff. The normalization constant $Q^A_{0,\rm acc}$ will be obtained by comparing the propagated cosmic rays to the observed energy spectrum by the Pierre Auger Observatory. For the spectral parameters at the injection we consider $\gamma = 0.5, ..., 2.5$ with steps of $\Delta\gamma = 0.25$, and $\log(E_{\rm cut}/1\,\rm eV) = 17.0, ..., 19.0$ with steps of $\Delta \log(E_{\rm cut}/1\,\rm eV) = 0.1$.

The escaped cosmic ray and neutrino spectra for a pure proton injection are shown in Fig. 8.6 in arbitrary units. Several injection configurations are shown: $\gamma = 1.5$ and $E_{\rm cut} = 10^{18.5}$ eV in the top panels, $\gamma = 1.5$ and $E_{\rm cut} = 10^{17.5}$ eV in the central panels and $\gamma = 0.75$ and $E_{\rm cut} = 10^{18.5}$ eV in the bottom panels. Different colors correspond to different BB temperatures while the dashed black line in the cosmic ray spectra corresponds to the injected energy spectrum. We obtain that photohadronic interactions systematically suppress the injected proton spectrum. When the BB field cools down, the escaped spectrum converges to the injected spectrum. This is due to the fact that the total interaction length $\lambda_p(\Gamma, t)$ increases faster than the escape length $\lambda_{\rm esc}(t)$ with time. The injected spectrum at $E \lesssim 10^{19}$ eV is, in general, more suppressed than the high-energy part. This is because the condition $\lambda_p \gtrsim \lambda_{\rm esc}$ is satisfied for almost all the temperatures when $E \gtrsim 10^{19}$ eV. For the neutrino energy spectra, shown in the right panels of Fig. 8.6, the opposite behavior can be observed. When the temperature of the photon field is high, interactions are more efficient, and the production of high-energy neutrinos is favored, until the saturation level is reached. We can also see that the peak in the neutrino spectra is at $E_\nu \sim 5\% \cdot E_{\rm p}$, where $E_{\rm p}$ is the peak in the CR spectrum.

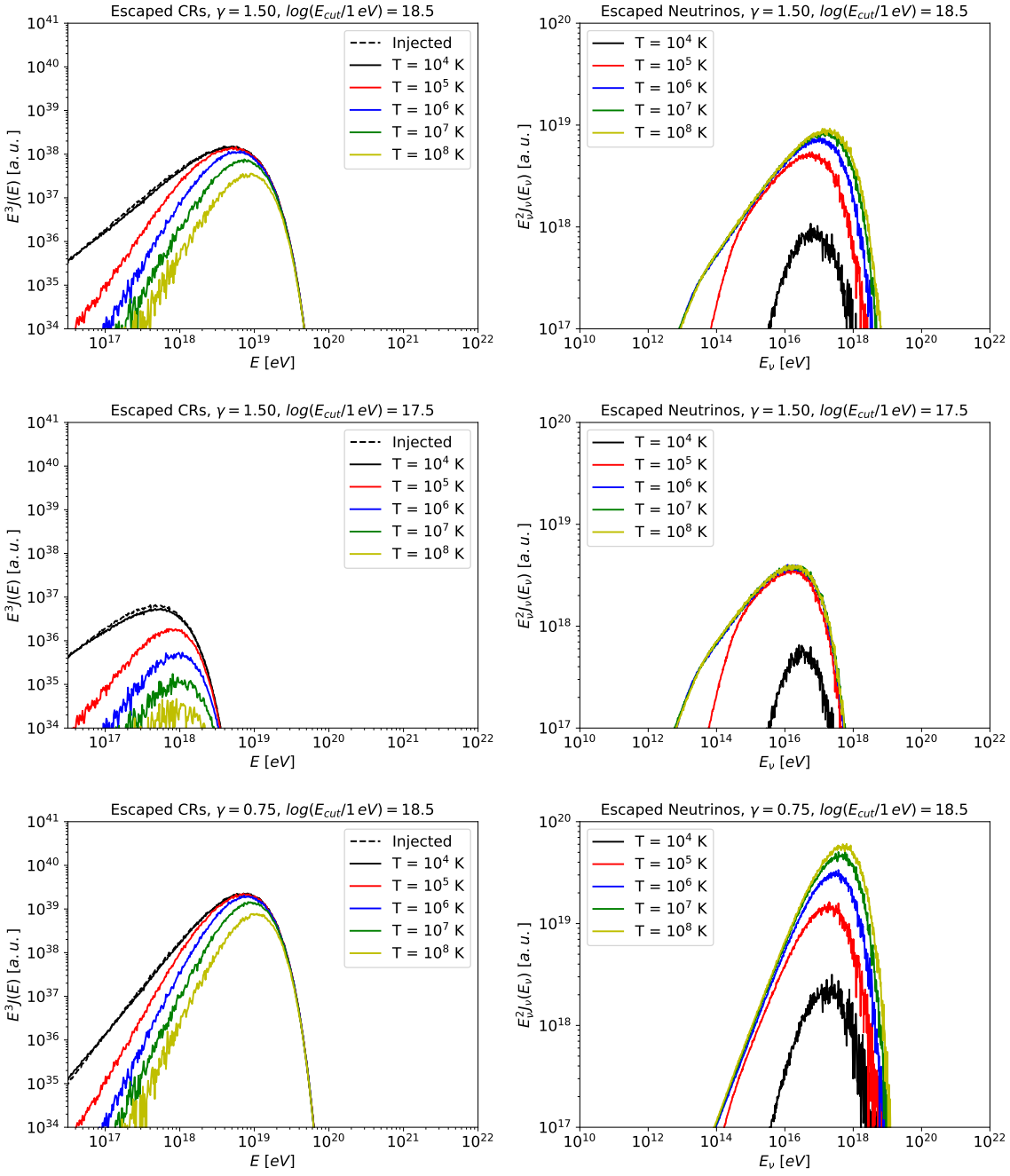

Figure 8.6: Left: energy spectra at the escape from the source for pure proton acceleration, in arbitrary units. Right: neutrino energy spectra at the escape from the source, in arbitrary units. The dashed black line in the cosmic ray spectra corresponds to the injected energy spectrum. The injection parameters are $\gamma = 1.5$ and $E_{\rm cut} = 10^{18.5}$ eV (top panels), $\gamma = 1.5$ and $E_{\rm cut} = 10^{17.5}$ eV (middle panels) and $\gamma = 0.75$ and $E_{\rm cut} = 10^{18.5}$ eV (bottom panels). Different colors refer to different BB temperatures. Figure taken from [388].

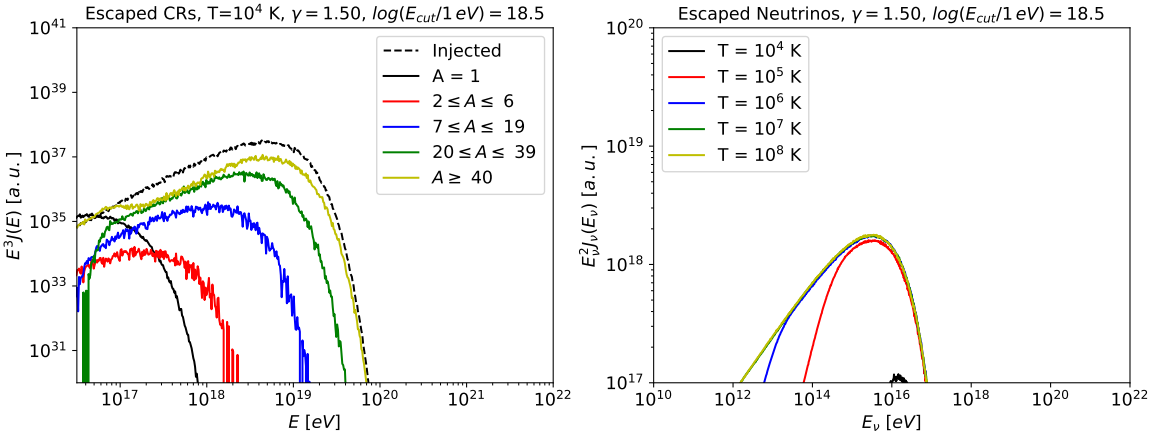

Figure 8.7: Left: energy spectrum at the escape from the source for pure iron acceleration, in arbitrary units. Only the BB temperature $T = 10^4$ K is shown. Different colors correspond to different mass groups at the escape. Note the different range of the y-axis from the proton scenario. Right: neutrino energy spectrum at the escape from the source, in arbitrary units. Different colors refer to the BB temperatures. The dashed black line in the cosmic ray spectra correspond to the injected energy spectrum. The injection parameters are $\gamma = 1.5$ and $E_{\rm cut} = 10^{18.5}$ eV for both panels. Figure taken from [388].

In Fig. 8.7, the escaped spectra for an iron injection scenario are shown for the injection parameters $\gamma = 1.5$ and $E_{\rm cut} = 10^{18.5}$ eV. Only the case with $T = 10^4$ K is shown in the left panel, where different colors correspond to different mass groups. In this case, the escaped CRs are given by a mix of different nuclear species, due to photodisintegration. Correspondingly, the production of high-energy neutrinos is suppressed with respect to the proton scenario, due to the increased threshold for the photopion production. However, the effect of the propagation within the source environment for different temperatures is similar to the case of the proton injection: high temperatures correspond to an enhanced production of neutrinos, and a reduced flux of escaped cosmic rays.

The inverse behavior of the escaped cosmic ray and neutrino fluxes for different temperatures of the interaction region characterizes the efficiency of the source in converting the accelerated baryonic energy into neutrinos. We quantify this effect by computing CR and neutrino emissivities. We define the CR emissivities as

$$\mathcal{E}_{\rm acc} = \sum_A \int dE\, E\, Q^A_{\rm acc}(E) \tag{8.10}$$

and

$$\mathcal{E}_{\rm esc} = \sum_A \int dE\, E\, Q^A_{\rm esc}(E)\,, \tag{8.11}$$

where $Q^A_{\rm acc}(E)$ and $Q^A_{\rm esc}(E)$ are the rates of the nuclear species A at the acceleration and at the escape, respectively, and the integration is performed over the injection energy range. The neutrino emissivity is calculated in the same way starting from the neutrino escape rate $Q^\nu_{\rm esc}(E_\nu)$, but using an energy range shifted by a factor of 5% relative to the energy range of cosmic rays,

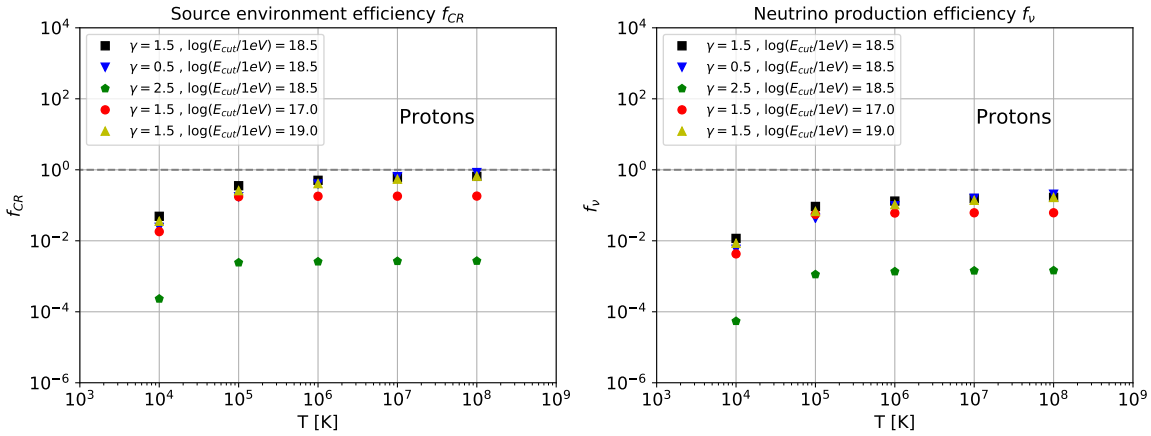

Figure 8.8: Left: source environment efficiency, as defined in Eq. (8.12). Right: neutrino production efficiency, as defined in Eq. (8.13). Different colors correspond to the different injection scenarios: $\gamma = 1.5$ and $\log(E_{\rm cut}/1\,{\rm eV}) = 18.5$ (black), $\gamma = 0.5$ and $\log(E_{\rm cut}/1\,{\rm eV}) = 18.5$ (blue), $\gamma = 2.5$ and $\log(E_{\rm cut}/1\,{\rm eV}) = 18.5$ (green), $\gamma = 1.5$ and $\log(E_{\rm cut}/1\,{\rm eV}) = 17.0$ (red) and $\gamma = 1.5$ and $\log(E_{\rm cut}/1\,{\rm eV}) = 19.0$ (yellow). Both panels refer to a pure proton injection. Figure taken from [388].

and it is denoted by $\mathcal{E}^{\nu}_{\rm esc}$. We can then define the efficiency parameters

$$f_{\rm CR} = \frac{\mathcal{E}_{\rm acc} - \mathcal{E}_{\rm esc}}{\mathcal{E}_{\rm acc}} \tag{8.12}$$

and

$$f_\nu = \frac{\mathcal{E}^{\nu}_{\rm esc}}{\mathcal{E}_{\rm acc}}\,, \tag{8.13}$$

where $f_{\rm CR}$ represents the fraction of energy lost by the accelerated CRs during the propagation within the source (source efficiency), and f_ν the fraction of energy transformed into neutrino energy by in-source interactions (neutrino production efficiency). Given the definitions in Eqs. (8.12) and (8.13), we can see that the maximum interaction efficiency corresponds to$f_{\rm CR}$, $f_\nu \simeq 1$.

In the left panel of Fig. 8.8, the source efficiency $f_{\rm CR}$ is shown for different BB temperatures in the scenarios of a pure proton injection. Different colors correspond to different combinations of acceleration parameters γ and $E_{\rm cut}$. We can see that all the configurations saturate for $T \gtrsim 10^6\,{\rm K}$. This demonstrates that interactions within the source environment are very efficient during the early stages after the merger. However, scenarios with $\gamma \gtrsim 1.5$ are characterized by a maximum fraction of energy lost of $f_{\rm CR} \lesssim 10^{-2}$, due to the large number of low-energy protons escaping the source environment without interacting. In the right panel of Fig. 8.8, the neutrino production efficiency, as defined in Eq. (8.13), is shown for the same combinations of parameters as in the left panel. The neutrino production efficiency is clearly increasing as a function of the increasing temperature. Since protons can only produce neutrinos through photopion production, we observe that the neutrino production saturates at the same temperature of protons. Most of the configurations considered saturate at $f_\nu \simeq 0.1$, corresponding to a $\sim 10\%$ conversion of cosmic ray energy into neutrino flux. The observed saturation of neutrino production is consistent with the known *Waxman-Bahcall bound* for source environments optically thin to photopion

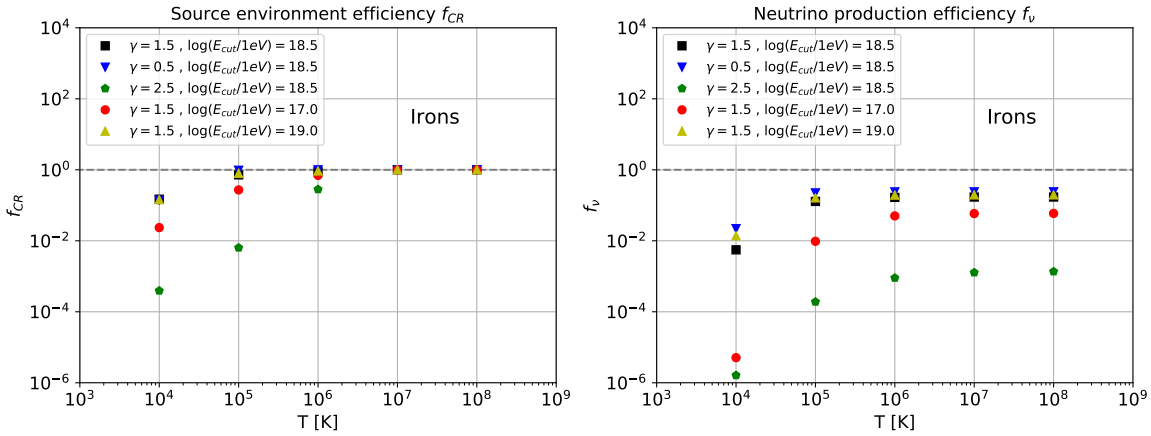

Figure 8.9: Same as Fig. 8.8, but for a pure iron injection. Figure taken from [388].

production [389, 390]. As discussed earlier, scenarios characterized by $\gamma = 2.5$ correspond to $f_\nu \simeq 10^{-3}$, as a result of the fact that escape from the source is favored over interactions.

In Fig. 8.9, we show the same quantities of Fig. 8.8 for a pure iron injection.We can see that all scenarios saturate to $f_{\rm CR} \simeq 1$, for $T > 10^6\,{\rm K}$, as it can be expected from the total interaction length in Fig. 8.3. The neutrino production is almost unchanged for scenarios characterized by low γ values or large $E_{\rm cut}$ values. In contrast, scenarios characterized by a large value of γ or a low value of $E_{\rm cut}$ show a reduced neutrino production when $T \lesssim 10^5\,{\rm K}$. In fact, as shown in Fig. 8.3, the presence of the low-energy minimum in $\lambda_{\rm Fe}$ associated to photodisintegration, corresponds to a low escape rate of iron nuclei, which will continue to interact with local photons without producing neutrinos. We note here that the large interaction efficiency in the case of iron nuclei will have an effect on the normalization of the propagated fluxes, compared to the proton scenario. In fact, in order to reproduce the observed cosmic ray flux, a higher normalization factor will be required with respect to the proton case, resulting in a higher injection rate at the source and an increased neutrino flux on Earth in the case of iron acceleration at the source.

8.4 Extragalactic propagation

The escaped CRs are propagated in the extragalactic space taking into account stochastic interactions with the CMB and the EBL from [226], nuclear decay and adiabatic energy loss. The production and propagation of cosmogenic neutrinos are also simulated. The propagation of high-energy neutrinos produced within the source environment is taken into account by considering the evolution of the neutrino energy on cosmological scales, given by

$$\frac{dE_\nu}{dz} = \frac{E_\nu}{1+z}\,, \tag{8.14}$$

where E_ν is the neutrino energy, z is the redshift and $E_{\nu,0} = E_\nu(z=0)$ is the energy condition at Earth. Therefore, as shown in Appendix B.4, the energy spectrum of the astrophysical neutrinos at Earth can be obtained as

$$J_{\nu,{\rm source}}(E_{\nu,0}) = \frac{c}{4\pi H_0}\int_0^{z_{\rm max}} dz\,\frac{\xi(z)}{\sqrt{\Omega_{\rm m}(1+z)^3+\Omega_\Lambda}} Q^\nu_{\rm esc}(E_\nu(z))\,, \tag{8.15}$$

where $z_{\rm max}$ is the maximum redshift considered for the extragalactic propagation (here $z_{\rm max} = 6$), $H_0 \simeq 70\,{\rm km\,s^{-1}\,Mpc^{-1}}$ is the Hubble constant at present time, $\Omega_{\rm m} \simeq 0.3$ is the matter density, $\Omega_\Lambda \simeq 0.7$ is the dark energy density, and $Q^\nu_{\rm esc}(E_\nu(z))$ is the neutrino production rate of the source (i.e. the number of produced neutrinos per unit energy, time and volume). The function $\xi(z)$ describes the redshift evolution of the source distribution, and it is generically of the form $\xi(z) \propto (1+z)^m$, where m is the source evolution index. We consider the star formation rate evolution (SFR) parameterization from [310],

$$\xi(z) = \begin{cases} (1+z)^{3.4}, & 0 \leq z \leq 1\,; \\ 2^{3.7}(1+z)^{-0.3}, & 1 \leq z \leq 4\,; \\ 2^{3.7}5^{3.2}(1+z)^{-3.5}, & 4 \leq z \leq 6\,, \end{cases} \tag{8.16}$$

together with the case of no source cosmological evolution $m = 0$.

In order to compare our simulations with the measured cosmic ray and neutrino fluxes, we scale the propagated all-particle spectrum. In particular, we require that the propagated all-particle spectrum at $E = E_{\rm cut}$ corresponds to the cosmic ray flux measured by the Pierre Auger Observatory at the same energy[2]. We introduce the scale factor g, such that

$$J_{\rm prop}(E = E_{\rm cut}) = g \cdot J_{\rm exp}(E = E_{\rm cut})\,, \tag{8.17}$$

where $J_{\rm prop}(E) = \sum_A J^A_{\rm prop}(E)$. This means that the scale factor g can be used to soften the assumption on the relative contribution of BNS mergers to the observed cosmic ray flux in the energy range below the ankle. The following values for the scale factor g were considered: $\log g = -5, ..., 0$ with $\Delta \log g = 0.1$. We define a reference scenario characterized by the following parameters: pure proton injection, source temperature of $T = 10^5\,{\rm K}$, and spectral parameters $\gamma = 1.5$ and $E_{\rm cut} = 10^{18.5}\,{\rm eV}$; we also fix the normalization factor $g = 0.4$, as it is roughly what it is obtained from the fit of the nuclear species at Earth at energy $10^{18.5}\,{\rm eV}$ in [155], for the proton component. For this reference scenario, we obtain that $Q^{\rm p}_{0,{\rm acc}} = 8.2 \cdot 10^{39}\,{\rm erg^{-1}\,Mpc^{-3}\,yr^{-1}}$.

We show in Fig. 8.10 the propagated source neutrino spectra for the reference scenario with source evolution $m = 0$ (left) and SFR evolution. In both panels, the single-flavor source neutrino spectrum (blue line) and the cosmogenic neutrino spectrum (black line) are shown. The measured neutrino flux and cosmogenic neutrino limit by IceCube [391] and the cosmogenic neutrino limit by the Pierre Auger Observatory [392] are also shown. We can see that the source neutrino fluxes are compatible with the upper limits from IceCube, but only partially compatible with the observed neutrinos for $E_\nu \gtrsim 10^6\,{\rm GeV}$, in the case $m = 0$. Moreover, the produced cosmogenic neutrino flux is several orders of magnitude below the experimental limits. The SFR evolution scenario is shown in the right panel of Fig. 8.10, where we can see that the production of cosmogenic neutrinos is slightly enhanced, due to the increased interactions with the cosmic fields. However, the production of source neutrinos also increases, making the spectrum of propagated neutrino higher than observations. The propagated CR energy spectra are shown in Appendix D.1.

In Fig. 8.11, the reference scenario is shown for the case of a pure iron composition at the acceleration. In this case, the scaling factor is fixed to $g = 0.1$ and we obtain that $Q^{\rm Fe}_{0,{\rm acc}} =$

[2] The cutoff energy $E_{\rm cut}$ is defined at the acceleration in Eq. (8.9) and it will be modified by interactions within the source environment and during extragalactic propagation. In the normalization condition, in Eq. (8.17), we consider that the normalization of the propagated CR is done at the numerical value of the observed energy $E = E_{\rm cut}$.

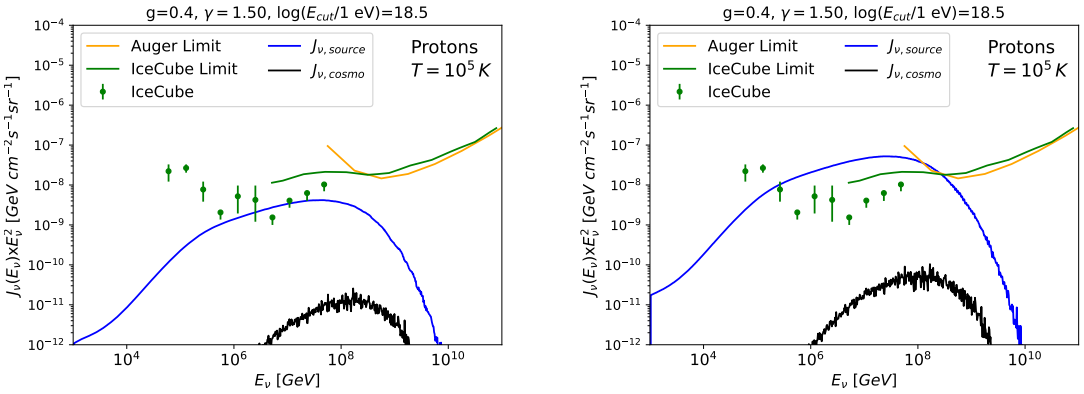

Figure 8.10: Left: single-flavor neutrino energy spectra for a pure proton injection, for a population of BNS mergers, at a fixed time after the merger, with no cosmological evolution: propagated source neutrinos (blue line) and cosmogenic neutrinos (black line). Observed neutrino flux and cosmogenic neutrino limit by IceCube [391] and the cosmogenic neutrino limit by the Pierre Auger Observatory [392] are also shown. Right: same as left panel, but for the SFR source evolution scenario. Figure taken from [388].

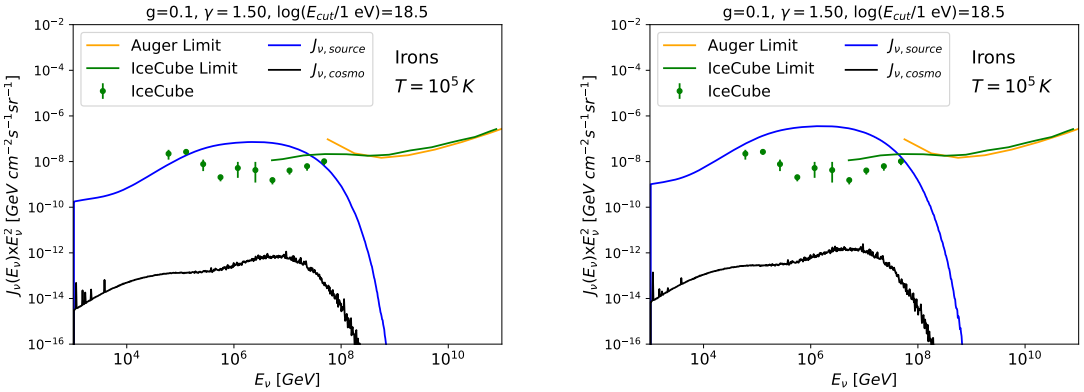

Figure 8.11: Same as Fig. 8.10, but for a pure iron injection. Note the different range of the y-axis with respect to the proton scenarios. Figure taken from [388].

$3.4 \cdot 10^{41}\,\mathrm{erg}^{-1}\,\mathrm{Mpc}^{-3}\,\mathrm{yr}^{-1}$. We can see that the position of the high-energy cutoff is shifted to a lower energy with respect to the proton case, due to the fact that most of the CRs that generate neutrinos are protons produced in the disintegration of iron nuclei. The low-energy region of the spectra is enhanced with respect to the proton scenario, and this can be explained by considering the behavior of the interaction lengths in Figs. 8.2 and 8.3. Moreover, the general effect of a heavier composition is an increase of the number of produced neutrinos, due to the normalization to the observed cosmic ray spectrum. Since photodisintegration within the source environment suppresses the CRs at the escape, compared to the case of pure protons, a larger acceleration rate is required. The result is an increase in the neutrino flux at the escape from the source, and then on Earth. The propagated CR energy spectra can be found in Appendix D.1.

8.4.1 Source parameters

To quantify the compatibility of the obtained spectra of source and cosmogenic neutrinos with the available data and limits, we introduce two *control quantities*. We define the neutrino spectral ratio at $E_\nu = 10^6\,\mathrm{GeV}$ as

$$R_\nu(E_\nu = 10^6\,\mathrm{GeV}) = \frac{J_{\nu,\mathrm{source}}(E_\nu = 10^6\,\mathrm{GeV})}{J_{\mathrm{IceCube}}(E_\nu = 10^6\,\mathrm{GeV})}\,, \tag{8.18}$$

where $J_{\nu,\mathrm{source}}$ is the propagated source-neutrino spectrum and J_{IceCube} is the observed IceCube neutrino spectrum. Additionally, given the total neutrino exposure $\mathcal{E}(E_\nu)$ of the Pierre Auger Observatory [392], we calculate the expected number of neutrinos as

$$N_\nu = \int dE_\nu\, \mathcal{E}(E_\nu)\,[J_{\nu,\mathrm{source}}(E_\nu) + J_{\nu,\mathrm{cosmo}}(E_\nu)]\,. \tag{8.19}$$

and we compare this value to 2.39, being this the *Feldman-Cousins factor* for non-observation of events in the absence of expected background [393]. We compute both the quantities in Eqs. (8.18) and (8.19) for the reference scenario and for both the source evolution scenarios. We then vary one parameter, keeping the others unchanged, to investigate their impact on the control quantities.

The parametric study of the control quantities is shown in Fig. 8.12 for a pure proton composition at the acceleration and evolution parameter $m = 0$. In each row of Fig. 8.12, one parameter among g, γ and E_{cut} is varied, for all the source temperatures T. In the left (right) panels of Fig. 8.12 the neutrino spectral ratios at $E_\nu = 10^6\,\mathrm{GeV}$ (the number of neutrinos N_ν) are shown. Gray lines in the left column indicate the 0.01%, 1.0% and 100.0% contributions to the measured IceCube neutrino flux, while in the right column the Feldman-Cousins factor for the non observation of neutrinos is shown. We can see that the two control quantities clearly depend on the temperature of the BB field, as already discussed above and shown in other studies investigating the neutrino production as a function of the density of photons in the source environment [204, 206, 394, 395]. Since the scale factor g simply scales the cosmic ray flux at Earth, the same scaling is observed in both in the source and cosmogenic neutrinos. The spectral shape of the cosmic ray spectrum at the acceleration affects the spectral ratio at $E_\nu = 10^6\,\mathrm{GeV}$ more than the expected number of neutrinos above $E_\nu = 10^8\,\mathrm{GeV}$. This is mostly due to the fact that a softer spectrum involves a larger number of low-energy protons, that is reflected in a larger number of neutrinos at $E_\nu = 10^6\,\mathrm{GeV}$. Since the Pierre Auger Observatory is sensible to neutrino energies above $10^8\,\mathrm{GeV}$ [392], only the high-energy part of the expected neutrino flux (due to the highest energy region of the CR spectrum) can possibly be measured. Both the spectral ratio at $E_\nu = 10^6\,\mathrm{GeV}$ and the number of neutrinos above $10^8\,\mathrm{GeV}$ increase when E_{cut} decreases. This is due to the fact that for low values of E_{cut} a higher normalization is required.

In Fig. 8.13, the parameter scan is shown for the case of pure iron injection. In this case, the production of neutrinos is even more dependent on the temperature of the BB than in the pure proton scenario. We also find that the number of neutrinos increases rapidly as the spectral index at the acceleration becomes softer. Since a softer spectral index corresponds to a larger number of low-energy iron nuclei in the source environment, compared to the high-energy ones, a much larger normalization is required than in the pure proton scenario due to the presence of photodisintegration. The same effect can be seen when E_{cut} decreases. The cases of SFR source

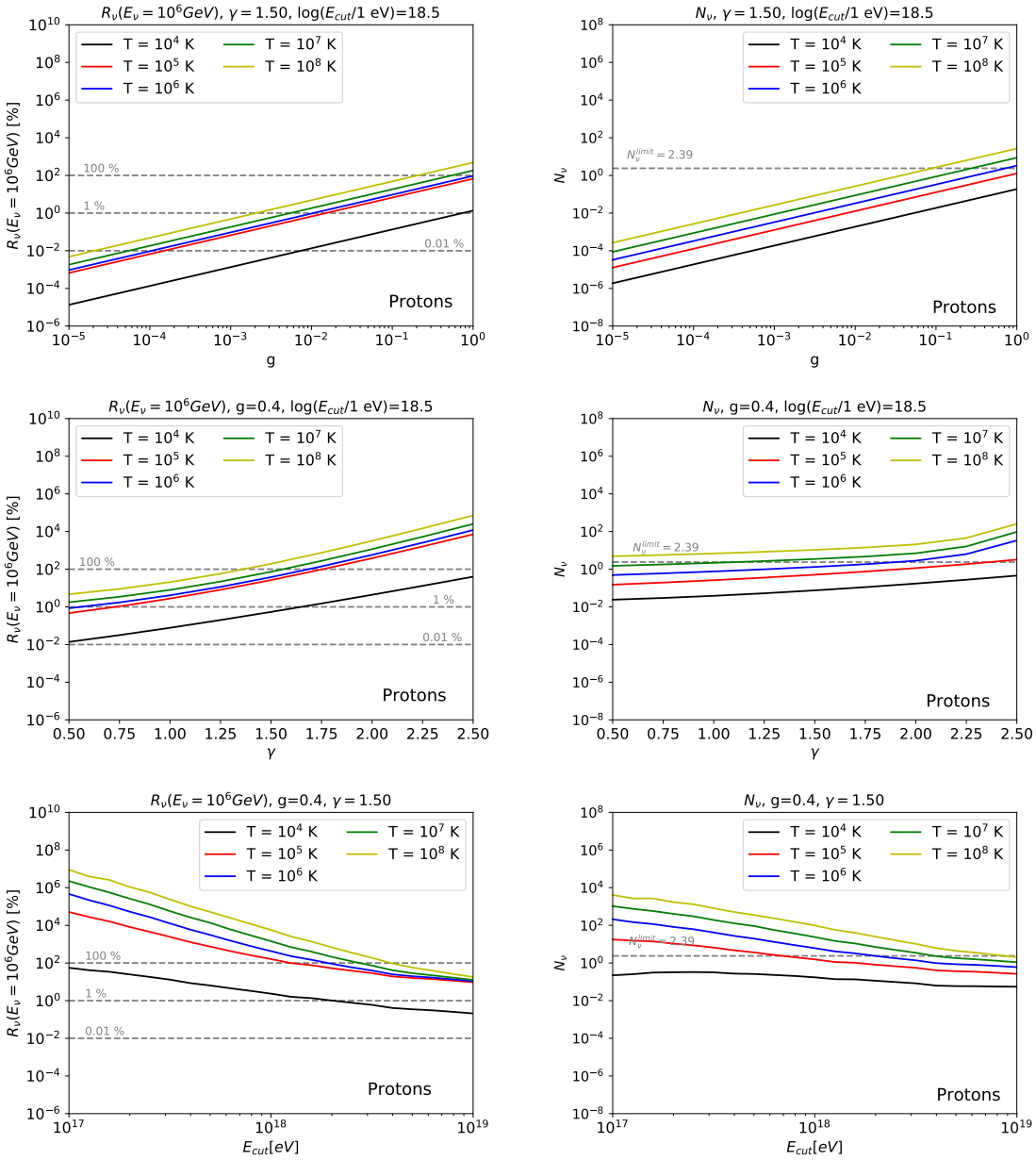

Figure 8.12: Left: neutrino spectral ratio, calculated at $E_\nu = 10^6$ GeV, as defined in Eq. (8.18). Right: number of neutrinos, as defined in Eq. (8.19). Quantities shown as a function of the normalization factor g (top panels), the spectral index γ (middle panels) and the high-energy cutoff $E_{\rm cut}$ (bottom panels). Colors correspond to different temperatures. In the right panels, gray lines indicate some reference ratios. The Feldman-Cousins factor for non-observation of events is indicated with a gray line in the left panels. The injected CR composition in the source environment is pure proton, and the evolution parameter is $m = 0$. Figure taken from [388].

evolution are shown in Appendix D.2 in Fig. D.2.1 for proton injection and Fig. D.2.2 for iron injection. This source evolution assumption slightly increases the neutrino flux with respect to

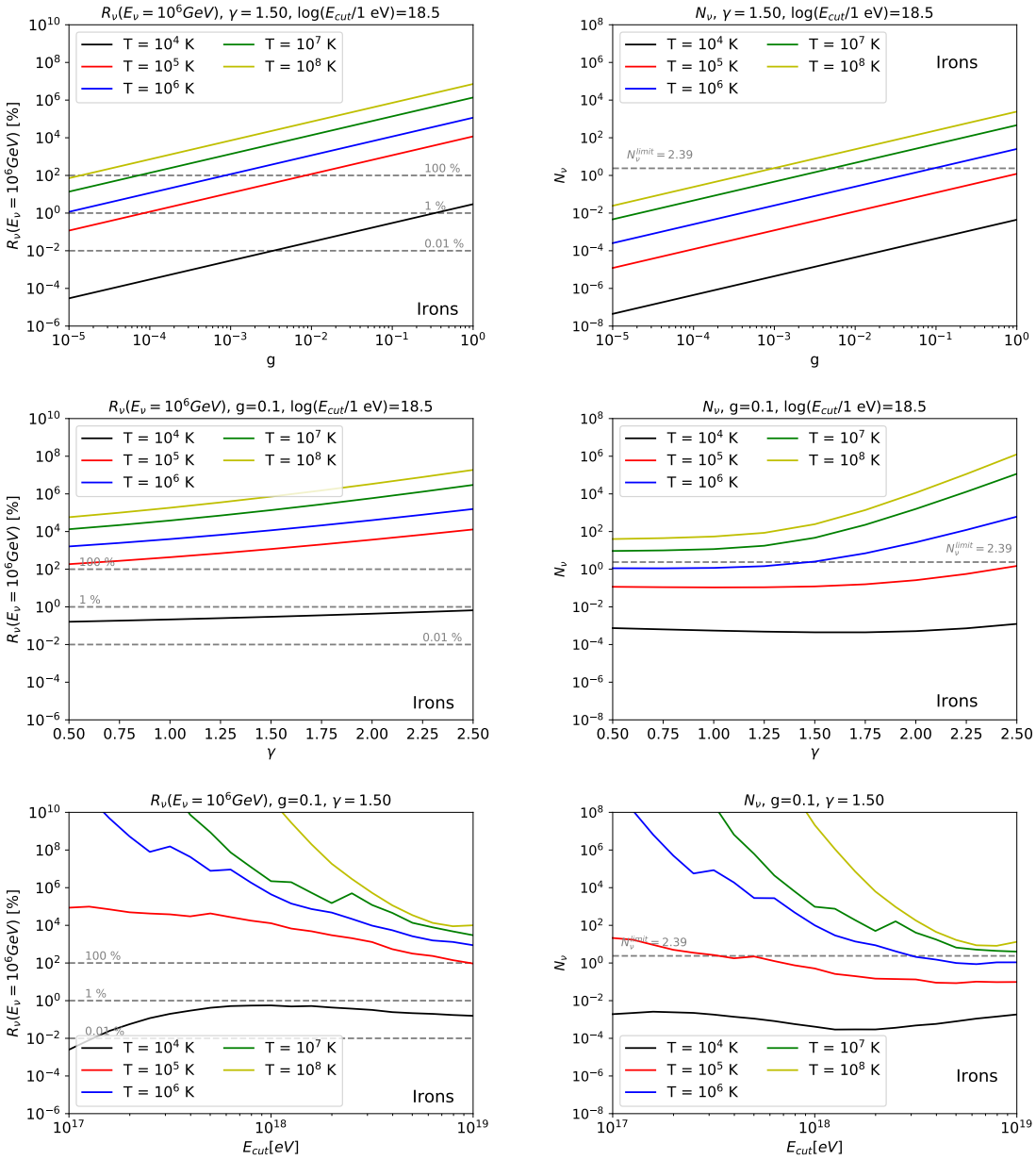

Figure 8.13: Same as Fig. 8.12, but for the case of pure iron injection and evolution parameter $m = 0$. Figure taken from [388].

the $m = 0$ case.

8.4.2 Temporal evolution of the source environment

We have seen that the temporal evolution of SEDs, shown in Fig. 8.1, and of the source radius in Eq. (8.5), are determined by the relation between the time after the merger and the BB temperature in Eq. (8.1). To account for the evolution of the interaction region, and thus the

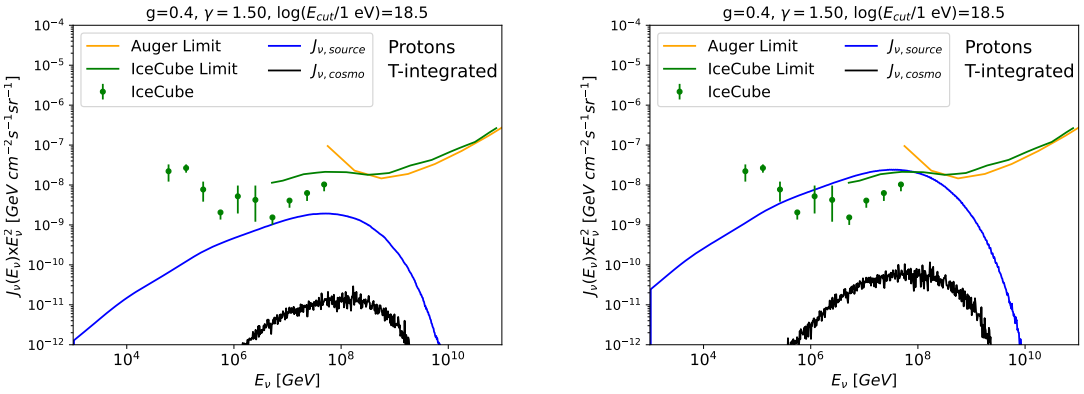

Figure 8.14: Left: single-flavor neutrino energy spectra for a pure proton injection for a population of BNS mergers where the temporal evolution is taken into account and $m = 0$: propagated source neutrinos (blue line) and cosmogenic neutrinos (black line). The observed neutrino flux and cosmogenic neutrino limit by IceCube [391] and the cosmogenic neutrino limit by the Pierre Auger Observatory [392] are also shown. Right: same as left panel, but for the SFR source evolution scenario. Figure taken from [388].

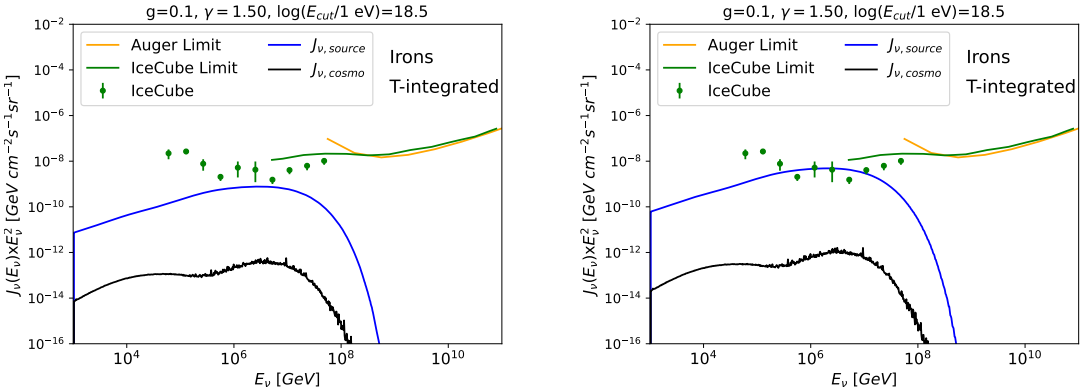

Figure 8.15: Same as Fig. 8.14, but for a pure iron injection. Note the different range of the y-axis with respect to the proton scenarios. Figure taken from [388].

evolution of neutrino production, we integrate the energy spectra of the escaped particles over the time after the merger. We consider the time steps shown in Fig. 8.1: the first time step corresponds to $t = 10^2$ s after the merger ($T = 10^8$ K), and the last time step corresponds to $t = 10^4$ s after the merger ($T = 10^4$ K). We adopt the same normalization procedure described in Sec. 8.4, for the all-particle propagated spectrum integrated over the time evolution of the source. The reference scenarios are again characterized by the spectral parameter $\gamma = 1.5$, $E_{\rm cut} = 10^{18.5}$ eV and $g = 0.4$ in the proton injection case and $g = 0.1$ in the iron case.

In Fig. 8.14, the propagated source neutrino spectra for the reference scenario for a population of BNS mergers with evolution $m = 0$ (left) and SFR (right) are shown. In Fig. 8.15, the pure iron injection scenarios are shown. The general results obtained in Sec. 8.4 also apply here. However, some differences are introduced when the time evolution of the source emission is considered. All the source neutrino spectra in Figs. 8.14 and 8.15 are suppressed with respect

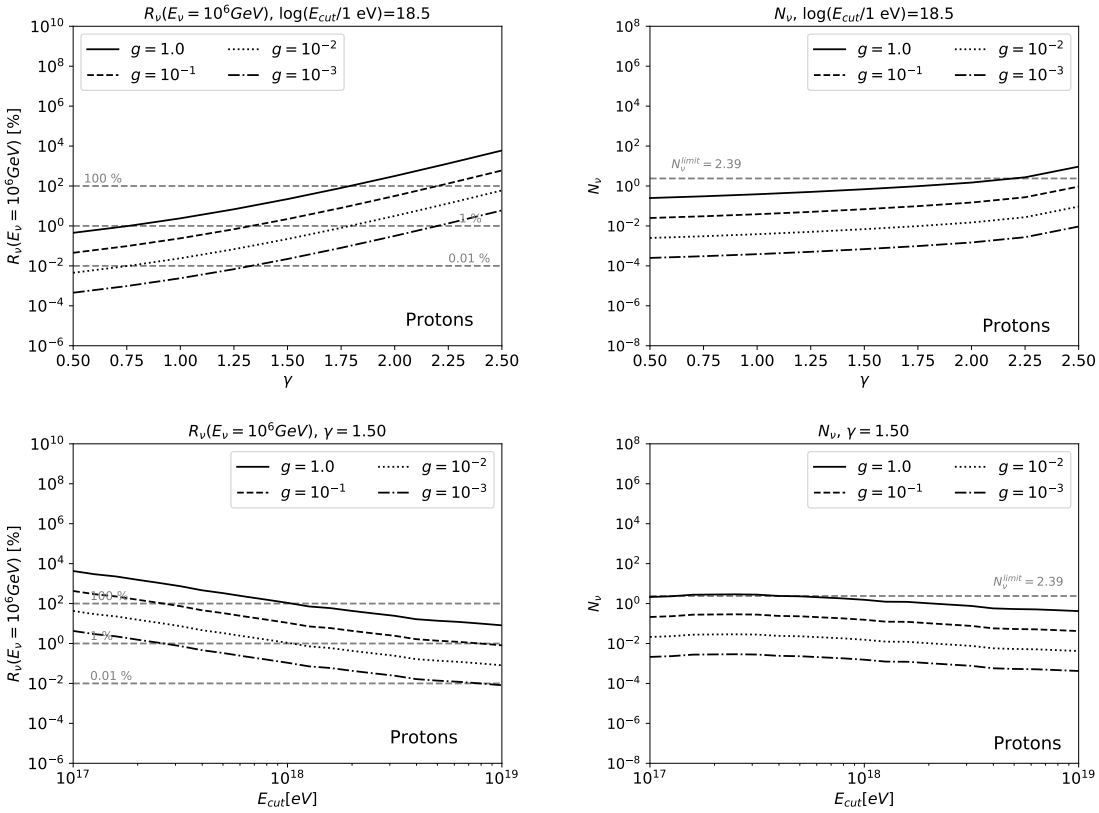

Figure 8.16: Left: neutrino spectral ratio, calculated at $E_\nu = 10^6$ GeV, as defined in Eq. (8.18). Right: number of neutrinos, as defined in Eq. (8.19). These quantities are shown as a function of the spectral index γ (top panels) and the high-energy cutoff $E_{\rm cut}$ (bottom panels), both integrating over the temporal evolution of the source. Several normalization factors g are considered in each panel: $g = 1.0$ (solid lines), $g = 10^{-1}$ (dashed lines), $g = 10^{-2}$ (dotted lines) and $g = 10^{-3}$ (dashed-dotted lines). In the left panels, gray lines indicate some reference ratios. The Feldman-Cousins factor for non-observation of events is indicated with a gray line in the right panels. The injected composition is pure proton, and the evolution parameter is $m = 0$. Figure taken from [388].

to the corresponding spectra in Figs. 8.10 and 8.11. This is due to the normalization of the propagated CRs: in particular, if we consider the latest times after the merger ($T \sim 10^4$ K) most of the injected nuclei escape from the source region without interacting; therefore, a smaller normalization factor is needed compared to the case in which a fixed time after the merger was considered. In addition, different slopes in the low-energy part of source neutrino spectra are obtained as a result of combining different neutrino spectra escaped from the source.

We then evaluate the control quantities in Eqs. (8.18) and (8.19). As done in Sec. 8.4.1, we vary one parameter, keeping the other ones unchanged. In Fig. 8.16, this parametric study is shown for a pure proton composition at the acceleration and source evolution $m = 0$. In each panel of Fig. 8.16 different values of g are shown together. The qualitative behaviors of $R_\nu(E_\nu = 10^6\,\text{GeV})$ and N_ν as functions of γ and $E_{\rm cut}$ are the same discussed for a fixed value of the source temperature. Moreover, $R_\nu(E_\nu = 10^6\,\text{GeV})$ and N_ν are reduced when the scaling factor g decreases. It can be seen that the most stringent constraints are given by

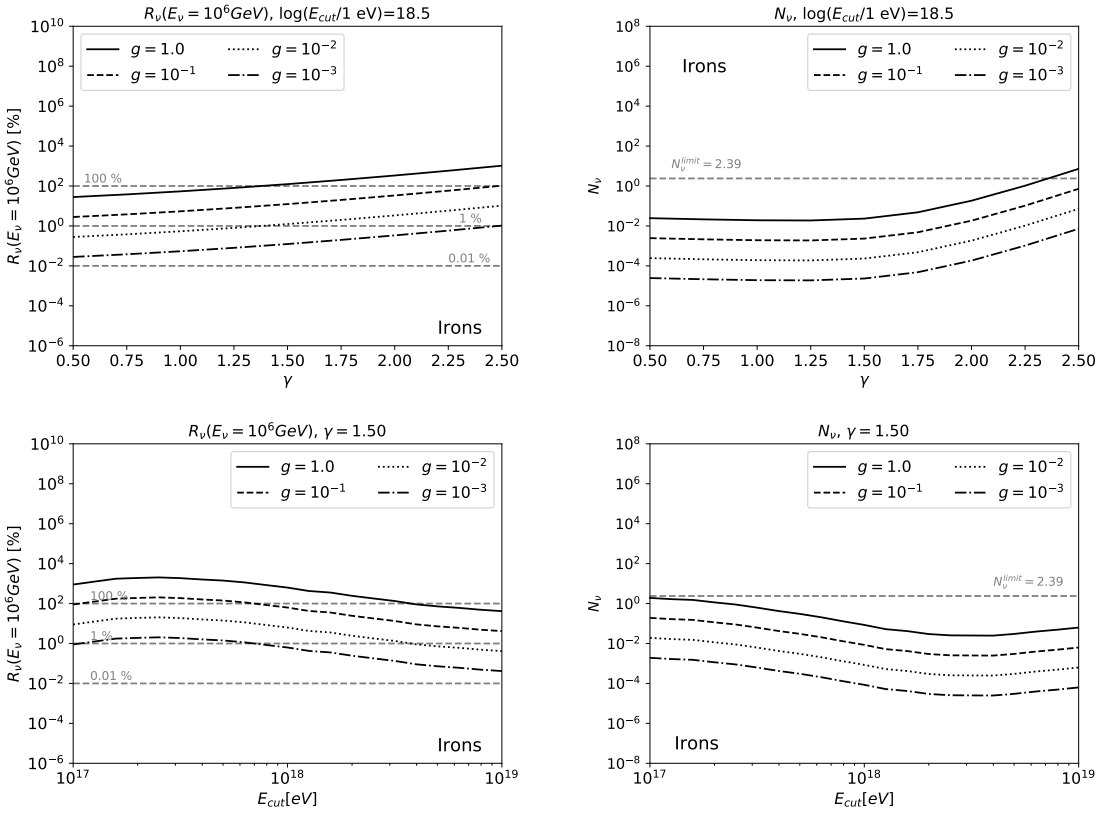

Figure 8.17: Same as Fig. 8.16, but for the case of pure iron injection and evolution parameter $m = 0$. Figure taken from [388].

$R_\nu(E_\nu = 10^6\,\mathrm{GeV})$, while N_ν almost always agrees with the experimental limits and observations, even for the most extreme scenario $g = 1.0$. In Fig. 8.17, the same results are shown for the case of pure iron acceleration. In general, the control quantities in Figs. 8.16 and 8.17 are in better agreement with the neutrino data and limits than in Figs. 8.12 and 8.13. This is because the integration over the source temperature implies that the normalization is mostly defined by the CR flux at low temperature. Therefore, a smaller normalization is required and smaller neutrino fluxes are obtained. The cases of SFR source evolution are shown in Appendix D.2 in Fig. D.2.3.

8.5 Discussion and conclusions

In this chapter, the propagation of CRs in the environment created by a BNS merger has been studied. We have modified the Monte Carlo code `SimProp v2r4` to simulate the in-source propagation and the production of high-energy neutrinos by the interaction of CRs with the local photon fields. The particles escaping from the source environment were then used as an input for the extragalactic propagation, taking into account the interactions with the cosmic photon fields. Finally, the cosmic ray energy spectrum measured by the Pierre Auger Observatory was used to normalize the propagated spectra and obtain the diffuse astrophysical and cosmological neutrino fluxes.

In Sec. 8.2, we have shown that interactions with the non-thermal component of the local photon fields are not efficient enough to produce neutrinos or photodisintegrate the fallback material. For this reason, we have decided to neglect this field in our in-source simulations. On the other hand, BB photons can trigger interactions with both injected protons and iron nuclei. In this case, the opacity is greater than one for $T \gtrsim 10^5\,\mathrm{K}$ ($t \lesssim 10^{3.5}\,\mathrm{s}$) for protons, and for $T \gtrsim 10^4\,\mathrm{K}$ ($t \lesssim 10^4\,\mathrm{s}$) for iron nuclei. However, very low- and very high-energy nuclei can leave the source environment undisturbed, as shown in Figs. 8.2 and 8.3. We have then shown that the efficiency of interactions is higher in the early stages after the merger (i.e. $T \gtrsim 10^6\,\mathrm{K}$) than at later stages. In particular, scenarios of proton injection saturate at 10% conversion of cosmic ray energy into neutrinos. In the case of iron nuclei, we observe that photodisintegration increases the source conversion efficiency in cosmic rays, while the neutrino production is almost unchanged.

We have shown in Secs. 8.4 and 8.4.1 that the observed neutrino flux cannot be associated with cosmogenic neutrinos. The neutrino spectral ratio $R_\nu(E_\nu = 10^6\,\mathrm{GeV})$ and the number of neutrinos N_ν show a dependence on the BB temperature and, in general, very high temperatures correspond to a large neutrino flux at Earth. We have also calculated the propagated neutrino fluxes taking into account the time evolution of the source environment. We have obtained that the high-energy cutoff must be $\gtrsim 10^{18}\,\mathrm{eV}$, if the reference values of the scaling factor g are considered. Moreover, the effect of the variation of the spectral index γ is almost independent of the composition considered and the scaling factor g: for both protons and iron nuclei we find that all the values of gamma are acceptable for $g \lesssim 0.4$. These results depend only weakly on the source evolution model adopted.

The efficiency in producing high-energy neutrinos can be related to the ratio of the total interaction length to the typical size of the interaction region. We have assumed that the typical escape length is given by the radius of the ejected material in Eq. (8.5), where $\beta_{\rm ej} = 0.3$. This corresponds to a source size ranging from $\lambda_{\rm esc} \approx 10^{12}\,\mathrm{cm}$ immediately after the merger, to $\lambda_{\rm esc} \approx 10^{14}\,\mathrm{cm}$ in the last considered stage. Being the typical values of $\beta_{\rm ej} = 0.1$-0.3 [396, 397], different values of $\beta_{\rm ej}$ with respect to what assumed here will only marginally affect the production of neutrinos.

We have considered a population of BNS mergers in the study of the diffuse neutrino flux. Therefore, this flux will depend on the event rate per volume of BNS mergers $\dot{n}$, which also affects the amount of CRs injected in the extragalactic space. We can then constrain the *baryonic loading* η defined as the ratio between the CR luminosity at the acceleration and the fallback luminosity, i.e. $\mathcal{L}_{\rm acc} = \eta \cdot \mathcal{L}_{\rm fb}$. As discussed in Sec. 4.1.3, the CR emissivity at acceleration is related to the number density of mergers as

$$\mathcal{E}_{\rm acc} = E_{\rm acc}\,\dot{n}\,, \tag{8.20}$$

where $E_{\rm acc}$ is the total accelerated CR energy. The energy in cosmic rays is related to the fallback luminosity $\mathcal{L}_{\rm fb}$, being this the luminosity of the outflow powered by accretion. We parameterize the fall-back luminosity as in the *optimistic* scenario of [382] (i.e. the ejected mass by the merger is $10^{-4}\,M_\odot$[3] and $\beta_{\rm ej} = 0.3$) obtaining

$$\mathcal{L}_{\rm fb}(t) = 1.3 \cdot 10^{43} \cdot \left(\frac{t}{10^3\,\mathrm{s}}\right)^{-5/3} \mathrm{erg\,s^{-1}}\,, \tag{8.21}$$

[3]The quantity $M_\odot$ indicates the Solar mass and is equal to $M_\odot \simeq 2 \cdot 10^{30}\,\mathrm{kg}$ [9].

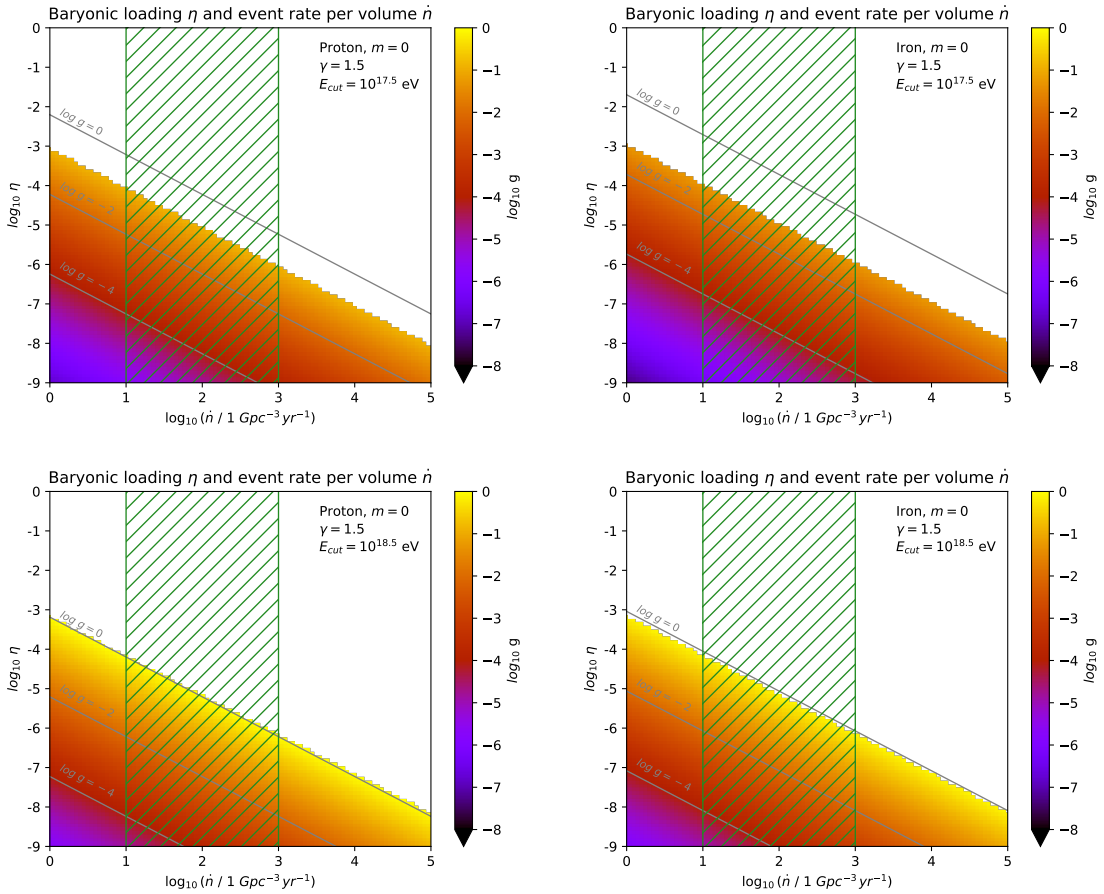

Figure 8.18: Scaling parameter g as a function of the baryonic loading η and the BNS merging event rate per volume $\dot{n}$. The value of $\log_{10} g$ is indicated by the color bar. The gray lines correspond to the reference values of $\log_{10} g$, as shown in the panels. The acceleration parameters of the sources are $\gamma = 1.5$ for the spectral index and $E_{\rm cut} = 10^{17.5}$ eV (top panels) and $E_{\rm cut} = 10^{18.5}$ eV (bottom panels). The left panels correspond to a pure proton injection and the right panels to a pure iron injection. The BNS merger event rate per volume estimated by [26, 398] is shown as a green region. The cosmological source evolution model is $m = 0$. Figure taken from [388].

where t is the time after the merger; the time dependence is taken as in [382], corresponding to the fall-back mass dynamics [396, 399]. Thus, the total accelerated CR energy is given by

$$E_{\rm acc} = \int dt\, \mathcal{L}_{\rm acc}(t) = \eta \int dt\, \mathcal{L}_{\rm fb}(t)\,, \tag{8.22}$$

and then

$$\frac{\mathcal{E}_{\rm acc}}{\dot{n}\,\eta} = \int dt\, \mathcal{L}_{\rm fb}(t)\,. \tag{8.23}$$

As discussed in Sec. 8.4, we scale the propagated cosmic ray spectrum to the observed one with the coefficient g. Therefore, for a given value of g corresponding to a propagated flux that does not overshoot the observed flux, different combinations of the parameters η and $\dot{n}$ are acceptable,

i.e. $g = g(\dot{n} \cdot \eta)$. By construction, the possible values of g are limited by the condition $g \leq 1$ and by the fact that the corresponding neutrino flux must be such that $R_\nu(E_\nu = 10^6\,\mathrm{GeV}) \leq 1$ and $N_\nu \leq 2.39$.

In Fig. 8.18, the possible values of $g(\dot{n} \cdot \eta)$ are shown for different injection scenarios: $\gamma = 1.5$ and $E_{\mathrm{cut}} = 10^{17.5}\,\mathrm{eV}$ (top panels) and $E_{\mathrm{cut}} = 10^{18.5}\,\mathrm{eV}$ (bottom panels). The left panels correspond to a pure proton and the right panels to a pure iron composition. The BNS merger event rate per volume estimated by [26, 398] is shown as a green region. We show the case of source evolution model $m = 0$; the corresponding scenarios for the SFR evolution are shown in Fig. D.2.4. We also indicate some reference values of $\log_{10} g$ with gray lines in each panel: the condition $\log_{10} g = 0$ correspond to the case where the product $\eta\,\dot{n}$ is such that the CR flux saturates the measured flux at the fixed energy. We can immediately notice that, due to the more intense energy loss experienced by nuclei with respect to protons, the required $\eta\,\dot{n}$ is in general larger. For $E_{\mathrm{cut}} = 10^{17.5}\,\mathrm{eV}$, a scaling factor $g \lesssim 10^{-1}$ is required by the constraint on the number of neutrinos produced, since a larger normalization is needed. On the other hand, for $E_{\mathrm{cut}} = 10^{18.5}\,\mathrm{eV}$ the saturation scenario $g = 1.0$ is possible and it corresponds to a baryonic loading $\eta \simeq 10^{-4} - 10^{-6}$ for the values of $\dot{n}$ in the allowed region. In the SFR scenarios, due to the large number of high-redshift sources, for the same values of $\dot{n}$, we obtain a slightly higher baryonic loading.

In conclusion, thanks to the in-source propagation model proposed in this chapter, we have shown that a region of the parameter space of the baryonic loading η and rate of merger events $\dot{n}$ can be excluded, depending on the fraction of the cosmic ray flux below the ankle is associated to BNS mergers. Further measurements by LIGO/Virgo, such as next-generation gravitational wave and neutrino detectors [400–402], might improve the constraining power of such a model, and future possible multimessenger observations might provide further tests of source-propagation models as the one here developed.

9

Modified electromagnetic cascades from distant blazars

This chapter is based on the publication:

- L. E. E. Castro, S. Rossoni, and G. Sigl. (2024). *Influence of plasma instabilities on the propagation of electromagnetic cascades from distant blazars.* arXiv: 2405.15390 [astro-ph.HE]. Submitted for publication to **The Astrophysical Journal**.

The propagation of very-high-energy γ-rays (VHEGRs) is often used as a probe of the extragalactic medium. However, as we discussed in Sec. 4.4, the extragalactic propagation of electromagnetic particles is also affected by interactions with background photon fields. It has been noticed that the observed GeV $\gamma-$ray spectrum of distant steady sources deviates from the theoretical predictions of electromagnetic cascades. This discrepancy is commonly interpreted as the result of the deflection of the cascade-produced charged leptons out of line of sight by the EGMF. However, plasma instabilities could also modify the energy distribution of the secondary leptons and thus affect the evolution of the cascades. In this chapter, we study the influence of plasma instabilities on electromagnetic cascades using the simulation code `CRPropa`.

In Sec. 9.2, the parameterization of the instability energy loss mechanism on the secondary electrons and positrons is presented. We then use the spectral measurements of the blazar 1ES 0229+200 by H.E.S.S., VERITAS, and Fermi-LAT, as explained in Sec. 9.3, to find the best combination of blazar spectral parameters for different instability scenarios. The results on the propagated photon spectra are presented in Sec. 9.4 and discussed in Sec. 9.5.

9.1 Electromagnetic cascades and plasma instabilities

Extragalactic VHEGRs can originate from extremely energetic astrophysical phenomena, such as jet emission from AGNs, or from prompt events, such as GRBs. We have seen in Sec. 4.4 that very-high-energy photons can interact with the photons from cosmic background fields, intializing the chain of processes called electromagnetic cascade. These processes are repeated until the energy of the secondary photons is below the pair production energy threshold. After

this point, the remaining electrons and positrons continue to undergo inverse Compton scattering, populating the photon flux at the GeV energy scale.

The total energy injected by the VHEGR source above the pair production energy threshold, given by Eq. (4.68), is approximately equal to the total energy of the cascade produced. It has been shown in [22] that fully developed cascades are characterized by an universal energy spectrum, independent of the photon spectrum at the source. The propagated spectrum is described by a power-law $J(E) \propto E^{-\gamma}$, with $\gamma = 1.9$ for the cascade multiplication stage, and $\gamma = 1.5$ from inverse Compton cooling at even lower energies. Therefore, astrophysical sources characterized by a photon spectrum harder than $\gamma = 1.9$ are such that the propagated photon flux below a few hundred of GeV will be dominated by cascade photons. On the other hand, sources with a softer spectrum at injection will be characterized by a propagated GeV spectrum dominated by prompt photons.

Observations of VHEGRs provide information not only about their astrophysical sources, but also on the extragalactic medium in which they propagate. Measurements of the photon flux are performed using ground- and space-based detectors. Some ground-based telescopes are the imaging atmospheric Cherenkov telescopes such as H.E.S.S. [403], MAGIC [404], and VERITAS [405]. In the case of space-based detectors, one example is the Fermi Gamma-ray Space Telescope and its Large Area Telescope (Fermi-LAT [406]).

An open problem in the understanding of the extragalactic propagation of VHEGRs is the discrepancy between the predicted and observed photon flux at the GeV energy: the observed photon spectrum shows a suppression in the GeV energy range compared to the expected propagated spectrum. A proposed explanation for this discrepancy is the deflection of the secondary electrons and positrons due to the presence of an EGMF: this field would induce a broadening of the momentum distribution of the electrically charged component of the cascade, beyond the field of view of the detector [407, 408]. Lower limits for the EGMF strength from 10^{-15} G to 10^{-18} G have been obtained in [271, 272, 409]. As discussed in Sec. 4.5, in the case of CRs, the EGMF could also introduce a delay in the arrival time of the secondary photons produced by the deflection of the charged leptons. However, the time delay is more important in the case of transient events, while in the case of continuous sources the magnetic deflection beyond the field of view plays a more important role. Several studies based on simulations of the magnetic deflection of the pairs produced in the electromagnetic cascade have constrained the magnetic field strength $B_{\rm rms}$ and the coherence length $\lambda_{\rm c}$ of the EGMF from observations of the photon spectrum of astrophysical sources [269, 408, 410–416].

Another possible explanation for the observed suppression in the propagated photon spectrum from distant sources can be the effect of *plasma instabilities* on the charged component of the cascades. Plasma instabilities result from the excitation of unstable electrostatic or electromagnetic waves generated by a highly collimated electron-positron beam propagating through a background plasma, such as the intergalactic medium (IGM) [23]. These plasma oscillations are induced by small perturbations in electron density resulting from the electron bunching and subsequent repulsion [417]. Many types of instabilities can arise; however, in the context of astrophysical electromagnetic cascades, electrostatic oblique modes are the most relevant, along with non-linear modulation and damping mechanisms [23–25, 418–421]. The influence of plasma instabilities on the cascades is given by the interaction between the electron-positron pairs and the plasma waves, which affects the energy and momentum distribution of the particles. The effect of plasma instabilities can be divided in two components: the angular broadening of the

cascade [422, 423], and the energy drain from the pairs, due to the heating of the IGM [25].

In several studies involving plasma instabilities in the evolution of extragalactic electromagnetic cascades, it has been found that energy losses due to plasma instabilities can reproduce the cascade suppression [422, 424–428]. However, most of them have concluded that the induced energy loss of the charged component may be too small [422, 427]. It is important to note that, independent of plasma conditions or the instability growth rate, the role of plasma instabilities in the modification of electromagnetic cascades is determined by the fraction of electron (or positron) energy transferred to the IGM on the typical length scale of inverse Compton scattering. For this reason, we will focus on the effect of electron-positron energy losses by parametrizing the magnitude and energy dependence of the fractional energy loss over the typical length scale of inverse Compton scattering.

9.2 Plasma instability energy loss model

The temporal evolution of the momentum distribution function $f(\mathbf{p}, t)$ (i.e. the number of particles per unit of momentum and unit of time) is given by the Fokker-Planck equation

$$\frac{\partial f(\mathbf{p},t)}{\partial t} = -\sum_{i=1}^{3} \frac{\partial}{\partial p_i}\left[V_i(\mathbf{p},t) f(\mathbf{p},t)\right] + \sum_{i,j=1}^{3} \frac{\partial}{\partial p_i}\left[D_{ij}(\mathbf{p},t)\frac{\partial f(\mathbf{p},t)}{\partial p_j}\right], \tag{9.1}$$

where $\mathbf{p}$ is the momentum vector with components $\mathbf{p} = (p_1, p_2, p_3)$, $V_i(\mathbf{p}, t)$ and $D_{ij}(\mathbf{p}, t)$ are the drift vector and diffusion tensor coefficients, respectively, as defined in [429]. The time evolution of the momentum distribution function is given by the interaction of two terms. The first term on the right hand side of (9.1) corresponds to the energy drain, while the second term is related to the angular and longitudinal broadening caused by momentum diffusion. We formulate a simplified model of the electron energy losses[1] induced by plasma instabilities. In particular, we consider only the analysis of the beam energy changes in the kinetic regime of the instabilities [422] and assume that the second term on the right hand side is negligible. This simplification is justified by numerical studies of pair-beam induced plasma instabilities [422, 423, 428], which suggest very small angular broadening of the order of $\sim 10^{-4}$ radians for pairs produced by TeV photons. It has also been shown that the small angular broadening is sufficient to quench the plasma instability, and this would correspond to the saturation of the fractional electron energy loss at the percent level [423]. This means that our approximation will be valid in the scenario where the electrons lose less than $\sim 1\%$ of their energy between subsequent inverse Compton scatterings. We will show that such scenario is able to account for the observed spectral suppression of distant blazars.

In order to perform a parametric study of this scenario, we develop a numerical energy loss module associated with plasma instabilities, which will be include in the numerical framework of `CRPropa` (see Chapter 5). In [426], several models of the instability energy loss time $\tau_{\rm PI}$ are described under the assumption that the plasma instability growth time scale is the same as the energy loss time scale. However, since the only relevant quantity to evaluate the effect of plasma instabilities is the fraction of energy loss over the inverse Compton interaction length $\lambda_{\rm IC}$, we will focus only on this term, without investigating the underlying connection between the instability growth time and the electron energy loss rate. Since inverse Compton is dominated

[1] In this chapter, we will often refer only to electrons, but the same results apply to positrons.

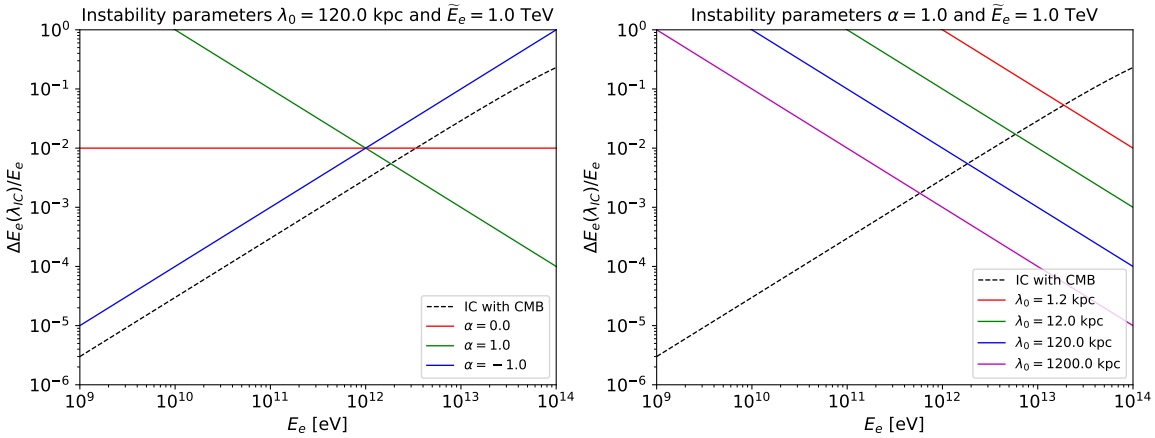

Figure 9.1: Left: plasma instability energy loss fractions given by Eq. (9.2) for $\lambda_0 = 120\,\text{kpc}$ and different values of the instability spectral index α. Right: same as left panel, but for spectral index $\alpha = 1$ and different values of λ_0. The normalization energy is $\widetilde{E}_e = 1\,\text{TeV}$ in both the panels. Energy loss fraction by inverse Compton scattering with CMB photons is shown as a black dashed line. Figure updated from [444].

by interactions with CMB photons, as shown in Fig. 4.5, we only consider the interactions with this field. Then, the corresponding interaction length is almost energy independent for electrons with energy $1\,\text{GeV} \lesssim E_e \lesssim 100\,\text{TeV}$, and it corresponds to $\lambda_{\text{IC}} \simeq 1.2\,\text{kpc}$ [408].

We model the fraction of energy lost due to instabilities as an energy dependent power-law, similar to those discussed in [426]. Then, if $E_e(x)$ is the electron energy at distance x from the injection position, the fraction of energy loss within an inverse Compton interaction length can be parameterized as

$$\left(\frac{E_e - E_e(\lambda_{\text{IC}})}{E_e}\right)_{\text{PI}} = \left(\frac{\Delta E_e(\lambda_{\text{IC}})}{E_e}\right)_{\text{PI}} = \frac{\lambda_{\text{IC}}}{\lambda_0}\left(\frac{E_e}{\widetilde{E}_e}\right)^{-\alpha}, \tag{9.2}$$

where $E_e = E_e(x = 0)$ is the initial electron energy, $E_e(\lambda_{\text{IC}}) = E_e(x = \lambda_{\text{IC}})$ is the electron energy at $x = \lambda_{\text{IC}}$, λ_0 and $\widetilde{E}_e$ are length and energy scales introduced for normalization and α is the power index of the instability energy loss rate (see also Appendix E.2). We consider the expression in Eq. (9.2) in the case where $(\Delta E_e(\lambda_{\text{IC}})/E_e)_{\text{PI}} < 1$. Otherwise, if $(\Delta E_e(\lambda_{\text{IC}})/E_e)_{\text{PI}} \simeq 1$, the electrons would lose most of their energy before undergoing inverse Compton scattering, resulting in the complete suppression of the GeV part of the propagated photon spectrum.

From Eq. (9.2), we can see that the energy loss term in Eq. (9.1), which is then given by $p_e^{-1}\,(dp_e/dt) \simeq E_e^{-1}\,(dE_e/dt) = V(E_e)/E_e = c\lambda_0^{-1}(E_e/\widetilde{E}_e)^{-\alpha}$, is defined by three parameters: the power index α, the normalization electron energy $\widetilde{E}_e$ and the length scale λ_0. However, these three parameters are not independent: the parameter combinations given by λ_0 and α can always be reproduced by the corresponding combinations of $\widetilde{E}_e$ and α. Therefore, we decide to vary only the parameters α and λ_0, fixing the value of the normalization energy to $\widetilde{E}_e = 1\,\text{TeV}$. As shown in [426], the power index of the instability growth time α is such that $-2 \leq \alpha \leq 2$. To investigate the effect of plasma instabilities on the propagated photon spectrum, we consider the values $\alpha = -2, -1.5, ..., 1.5, 2$ with $\Delta\alpha = 0.5$. We also consider different values of λ_0 to study the effect of different typical length scales: we consider $\lambda_0 = 1.2$, 12, 120 and $1,200\,\text{kpc}$.

We emphasize that the plasma instability parameters have been chosen to explore a wide range of scenarios and the normalization length scale values λ_0 have been chosen to be larger than the inverse Compton scattering length. We do not intend to perform plasma instability calculations, but to fit the parametrization in Eq. (9.2) in order to reproduce the propagated spectrum.

In Fig. 9.1, we show the instability energy loss fractions given by Eq. (9.2) as a function of the electron energy, for several plasma instability parameters. The left and right panels correspond to different values of the index α and the length scale λ_0, respectively. The inverse Compton energy loss length in the Thomson regime with CMB photons is given by Eq. (4.74). The integral of Eq. (4.74) over one inverse Compton length $\lambda_{\rm IC} = 1.2\,{\rm kpc}$ is also shown in Fig. 9.1 as a black dashed line. We can see that for $\lambda_0 = 120\,{\rm kpc}$, positive plasma indices ($\alpha > 0$) imply that electrons with energy $E_e \gtrsim 1\,{\rm TeV}$ transfer a small fraction of their energy to the IGM. These electrons will then preferentially lose energy by inverse Compton scattering with CMB photons, producing secondary low-energy photons. On the contrary, for electrons with $E_e \lesssim 1\,{\rm TeV}$ the fraction of energy loss becomes significant.

9.3 Cascade simulations

The development of the electromagnetic cascades initiated by a continuous source of VHEGRs is simulated with the Monte Carlo code `CRPropa 3.2`, described in Sec. 5.2. Given the modular structure of the code, we include the electron energy drain due to plasma instabilities with the implementation of a new energy loss module, as described in Sec. 9.2.

We include in our simulations electron-positron pair production, inverse Compton scattering, as well as double and triplet pair production. As background photon fields we consider the CMB and the EBL from [227]. We consider the observed photon spectrum of the blazar 1ES 0229+200 [269, 410] as reference scenario for our study. As also done in Chapter 7, we simulate an energy spectrum at the injection described by a power-law $J_0(E_0) \propto E_0^{-\gamma}$, where $\gamma = 1.0$ is the spectral index and $1\,{\rm GeV} \leq E_0 \leq 100\,{\rm TeV}$. We will then apply a reweighting procedure to the recorded particles in order to reproduce the observed spectrum. This procedure is described in Sec. 9.3.1. We simulate the propagation of 10^5 primary photons, with a propagation step size of $\Delta x \simeq 10^{14}$ cm ($\Delta t \simeq 10^{-4}\,{\rm yr} \simeq 1\,{\rm hr}$). The distance to the detection point is $L = 580$ Mpc. Since no deflection processes are included in our study, we simulate the propagation of the injected and created particles in one dimension.

9.3.1 Output analysis

To reproduce the realistic blazar emission scenarios, we have to reweigh our simulations to a more general spectral function at the injection. However, the presence of different parametrization of plasma instabilities during extragalactic propagation cannot be reproduced by reweighting the propagated particles. For this reason, we computed the cascade signal function $G(E_0, E; \lambda_0, \alpha)$, where E_0 is the photon energy at injection, and E is the photon energy at the observation, while α and λ_0 are the parameters of the instability scenario consider in the simulation. Therefore, a different cascade signal function is obtained for each combination of α and λ_0. Moreover, since the number of photons increases during the development of the cascade, a photon observed with energy E will correspond to one of the several photons produced by an injected photon with energy E_0.

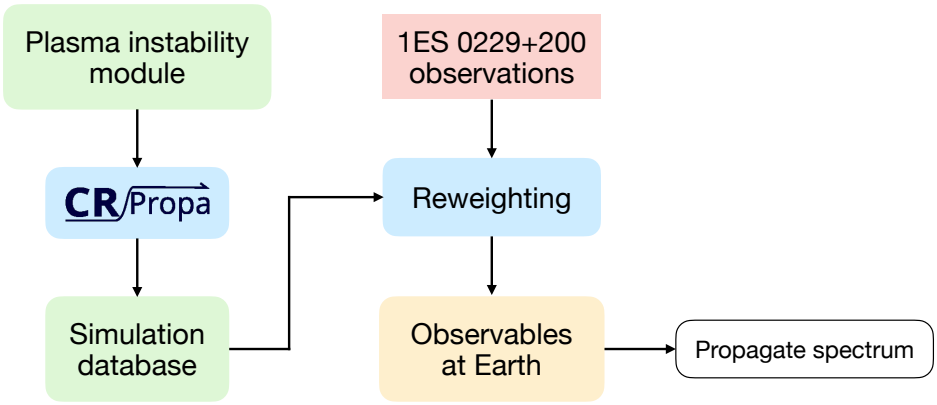

Figure 9.2: Schematic representation of the structure of the study presented in this chapter. The propagation in the extragalactic space, the creation of the simulations database and the analysis of the propagated spectra are shown.

The signal function $G(E_0, E; \lambda_0, \alpha)$ is a two-dimensional function that contains the probability that a photon detected with energy E was produced by a photon with initial energy E_0. The propagated photon spectrum at Earth $J(E; \lambda_0, \alpha)$ can then be obtained from the convolution of the cascade signal function $G(E_0, E; \lambda_0, \alpha)$ and the injected photon spectrum $J_0(E_0)$ as

$$J(E; \lambda_0, \alpha) = \int_{E_0 \geq E} dE_0 \, G(E_0, E; \lambda_0, \alpha) \cdot J_0(E_0) \,, \tag{9.3}$$

as described in [409]. We assume an injected energy spectrum described by a generic power-law function times an exponential high-energy cutoff of the form

$$J_0(E_0) = J_0 \cdot \left(\frac{E_0}{1\,\mathrm{TeV}} \right)^{-\beta} \exp\left(-\frac{E_0}{E_{\mathrm{cut}}} \right) \,, \tag{9.4}$$

where β is the source spectral index, E_{cut} is the high-energy cutoff and J_0 is a normalization constant. We consider $\beta = 0.6, \ldots, 2.0$ with $\Delta\beta = 0.01$, and $E_{\mathrm{cut}} = 1.0, \ldots, 30\,\mathrm{TeV}$ with $\Delta E_{\mathrm{cut}} = 0.1\,\mathrm{TeV}$. The normalization constant J_0 is obtained from the data used in the analysis.

In most of the previous studies, as [426], the spectral parameters of the injected photon spectrum are obtained with only the standard processes of the electromagnetic cascade. In this work, for the first time, we consider electromagnetic processes and plasma instabilities together during the evolution of the electromagnetic cascade. Therefore, the injection spectral parameters are obtained considering the full modified cascade.

We note that there is a degeneracy between the injection and the instability parameters for the reproduction of a given energy spectrum at Earth. For this reason, we first vary the plasma parameters along the ranges discussed in Sec. 9.2. For each combination of instability parameters we found the best-fitting injection parameters β and E_{cut} by comparing the simulated photon spectra with observed data of 1ES 0229+200 from the γ-ray telescopes H.E.S.S. [430], VERITAS [431], and Fermi-LAT[2]. A schematic representation of the analysis procedure used in this chapter

[2]We use the publicly available data within the 12-year source catalogue in https://fermi.gsfc.nasa.gov/cgi-bin/ssc/LAT/LATDataQuery.cgi, also available in the Spectral Energy Distribution Builder of the Space Science Data Center at https://tools.ssdc.asi.it/SED/.

is shown in Fig. 9.2. We quantify the deviation from the observed spectrum by calculating the variable χ^2, defined as

$$\chi^2(\beta, E_{\rm cut}; \lambda_0, \alpha) = \sum_i \left(\frac{J_{\rm data}(E_i) - J_{\rm sim}(E_i; \beta, E_{\rm cut}, \lambda_0, \alpha)}{\sigma_{{\rm data},i}} \right)^2 , \tag{9.5}$$

where $J_{\rm data}(E_i)$ and $J_{\rm sim}(E_i; \beta, E_{\rm cut}, \lambda_0, \alpha)$ are the values of the observed and propagated photon spectra at Earth at the same energy, respectively, and the sum is performed over the observed energy bins. The uncertainty for each value of the observed data is given by $\sigma_{{\rm data},i}$. Thus, the combination of plasma instability and prompt spectral parameters that best reproduces the observed photon spectrum will be given by the scenario that minimises χ^2. We normalise the values of the obtained χ^2 to the number of degrees of freedom $n_{\rm dof}$, which is given by the number of data points in different energy bins used in Eq. (9.5) minus the number of parameters to fit. The combination of the TeV-band data from H.E.S.S. and VERITAS gives $n_{\rm dof} = 8$; while including the GeV-band data by Fermi-LAT gives $n_{\rm dof} = 13$. We also obtain the confidence intervals for the values of β and $E_{\rm cut}$ following the methodology in [432] i.e. requiring that the difference between the test statistic χ^2 and its minimum value $\chi^2_{\rm min}$ to be below the critical value of a χ^2 distribution for a 1σ significance level, which for our combined two parameter fit gives $\chi^2 - \chi^2_{\rm min} \leq 2.30$.

9.4 Results

In this section, we discuss the obtained spectral parameters β and $E_{\rm cut}$ at the injection for the blazar 1ES 0229+200 in different propagation scenarios. The effects of the instability parameters on a given photon spectrum at the injection are discussed in the Appendix E.3. We first consider the propagation scenario where there are no plasma instabilities are present in the IGM. We then present the results corresponding to the effects of different parameterizations of our plasma instability model (i.e. different values of the parameters α and λ_0). In particular, we discuss the combination of prompt spectral parameters and plasma instability model that minimize the $\chi^2(\beta, E_{\rm cut}; \lambda_0, \alpha)$ defined in Eq. (9.5).

9.4.1 Standard electromagnetic cascade

We obtain the propagated photon spectrum without considering the plasma instabilities energy loss term described above. To find the spectral parameters β and $E_{\rm cut}$, we compare the propagated photon spectra with measurements of the spectral energy distribution by H.E.S.S., VERITAS, and Fermi-LAT for the ranges of injection parameters introduced in Section 9.3.1. In the left panel of Fig. 9.3, the $\chi^2(\beta, E_{\rm cut})/n_{\rm dof}$ distribution for different values of β and $E_{\rm cut}$ is shown. We find the minimum value $\chi^2_{\rm min}/n_{\rm dof} = 1.23$, indicated by the orange star in the left panel of Fig. 9.3, for spectral index and cutoff energy values of $\beta = 1.22^{+0.26}_{-0.54}$ and $E_{\rm cut} = 1.6^{+1.4}_{-0.6}$ TeV, respectively. The corresponding propagated photon spectrum is shown in the right panel of Fig. 9.3 (black line) together with the unattenuated prompt photon spectrum (black dashed line). The H.E.S.S., VERITAS, and Fermi-LAT measurements are also shown as blue, green and red points, respectively. We find that a low value for the energy cutoff is preferred to reproduce the GeV energy range of the propagated spectrum. However, for a cutoff energy of $E_{\rm cut} \simeq 2$ TeV, the

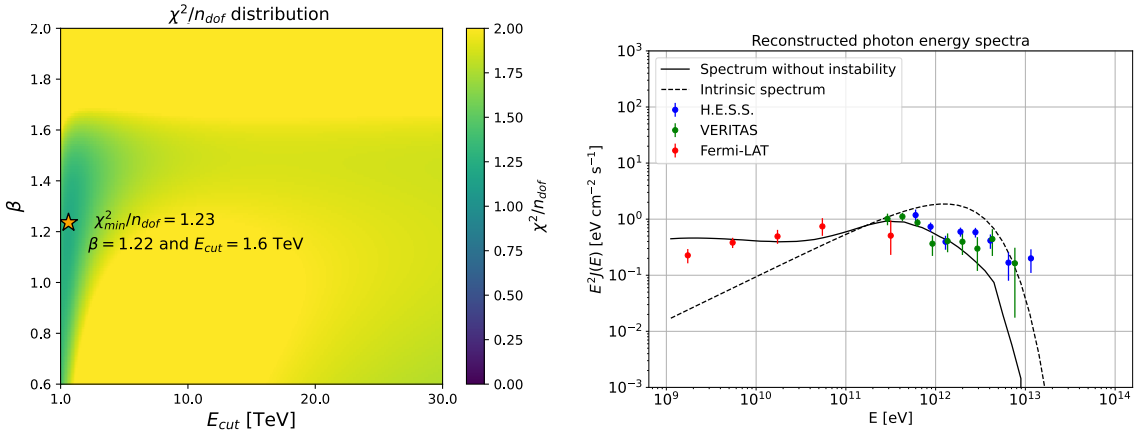

Figure 9.3: Left: $\chi^2(\beta, E_{\rm cut})/n_{\rm dof}$ distribution for the blazar 1ES 0229+200, calculated using H.E.S.S., VERITAS, and Fermi-LAT data ($n_{\rm dof} = 13$), without plasma instabilities. The minimum $\chi^2_{\rm min}/n_{\rm dof} = 1.23$ is indicated by an orange star, and it corresponds to spectral index and cutoff energy values of $\beta = 1.22^{+0.26}_{-0.54}$ and $E_{\rm cut} = 1.6^{+1.4}_{-0.6}$ TeV, respectively. Right: the unattenuated prompt photon spectrum (black dashed line) for the central values $\beta = 1.22$ and $E_{\rm cut} = 1.6$ TeV. The propagated spectrum (black line) and the measurements by H.E.S.S. (blue points), VERITAS (green points), and Fermi-LAT (red points) are shown. Figure updated from [444].

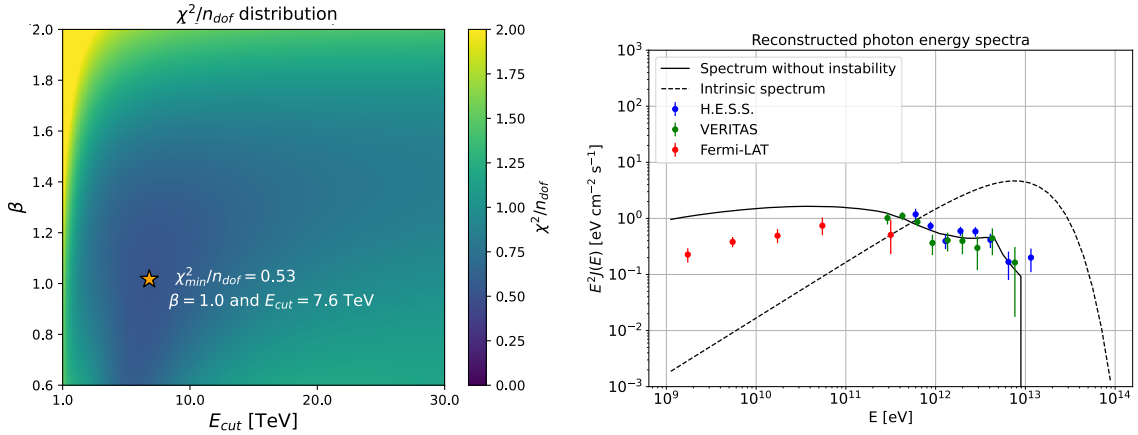

Figure 9.4: Same as Fig. 9.3, but using only the H.E.S.S. and VERITAS data ($n_{\rm dof} = 8$). Figure updated from [444].

propagated spectrum at $E \gtrsim 1$ TeV is too suppressed compared to the H.E.S.S. and VERITAS data.

For comparison, we repeat our analysis considering only the TeV data from H.E.S.S. and VERITAS. The $\chi^2(\beta, E_{\rm cut})/n_{\rm dof}$ distribution and the corresponding photon spectra are shown in Fig. 9.4. In this case, we obtain a minimum value of $\chi^2_{\rm min}/n_{\rm dof} = 0.53$[3] for the spectral

[3]In this scenario, the minimum value of the $\chi^2/n_{\rm dof}$ is smaller than the one obtained when the GeV data are also included in the analysis. However, one must be cautious in comparing the two values, as they were obtained with different data sets in different energy ranges. Although the reproduction of the high-energy part of the spectrum has improved, it can clearly be seen that the low-energy part has worsened.

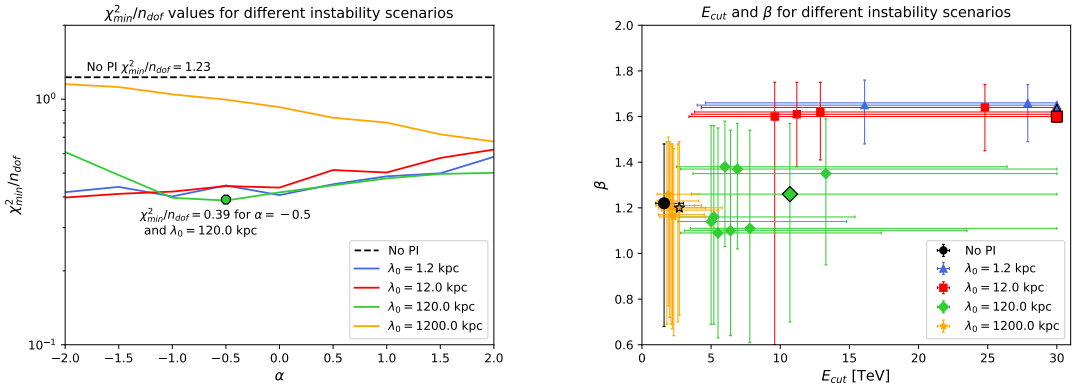

Figure 9.5: Left: $\chi^2_{\rm min}/n_{\rm dof}$ values as a function of α, for $\lambda_0 = 1.2$ kpc (blue), $\lambda_0 = 12$ kpc (red), $\lambda_0 = 120$ kpc (green) and $\lambda_0 = 1200$ kpc (orange). The minimum value of $\chi^2_{\rm min}/n_{\rm dof}$ among the different plasma instability scenarios is indicated by a green circle ($n_{\rm dof} = 13$). The case without plasma instability is indicated by a dashed black line. Right: scatter plot of the mean values and error bars of β and $E_{\rm cut}$ for $\chi^2_{\rm min}/n_{\rm dof}$ for a given choice of α and λ_0. Different colors correspond to different values of λ_0, as in the left panel. A given set of points of the same colour correspond to different values of the instability index α. The *local* minimum values of $\chi^2_{\rm min}/n_{\rm dof}$ for a given value of λ_0 are indicated by larger markers with black border. The case without plasma instability is indicated by a black circle. Figure updated from [444].

parameters $\beta = 1.00^{+0.60}_{-0.40}$ and $E_{\rm cut} = 7.6^{+18.8}_{-4.7}$ TeV. It can be seen that, in order to reproduce the observations in the energy range between 10^{11} eV and 10^{13} eV, a larger value of $E_{\rm cut}$ is needed in comparison to the previous case. However, the low-energy part of the propagated spectrum predicts a much higher flux than the observations. In both scenarios, the low-energy part of the propagated photon spectrum is of the form $J(E) \simeq E^{-2}$. This is due to the universality of the energy spectrum of electromagnetic cascades, which is obtained when the distance from the source is such that the full development of the cascade is possible.

9.4.2 Modified electromagnetic cascade

We have seen in Figs. 9.3 and 9.4 that it is generally difficult to reproduce the observed photon spectrum of blazar 1ES 0229+200 in the GeV and TeV energy ranges using only the standard electromagnetic cascades. Therefore, we include in our simulations the energy loss term associated with plasma instabilities. To study the effect of plasma instabilities on the propagated photon spectrum, we obtain a new set of signal functions $G(E_0, E; \lambda_0, \alpha)$, for each combination of the instability parameters α and λ_0, as defined in Section 9.3.1. As done before, we use H.E.S.S., VERITAS, and Fermi-LAT measurements to find the minimum values $\chi^2_{\rm min}(\beta, E_{\rm cut}; \lambda_0, \alpha)/n_{\rm dof}$ and the corresponding values of β and $E_{\rm cut}$, for each α and λ_0 combination. The left panel of Fig. 9.5 shows the minimum values $\chi^2_{\rm min}/n_{\rm dof}$ for each combination of the instability parameters α and λ_0. In particular, each line corresponds to the $\chi^2_{\rm min}/n_{\rm dof}$ for different values of α, for a given value of λ_0. The scenario without plasma instabilities is also shown for comparison as a black dashed line. The global minimum value is indicated by a green circle. The corresponding mean values of β and $E_{\rm cut}$ are shown in the right panel of Fig. 9.5, where each color corresponds to a certain value of λ_0. We find that the smallest value is given by $\chi^2_{\rm min}/n_{\rm dof} = 0.39$ for the

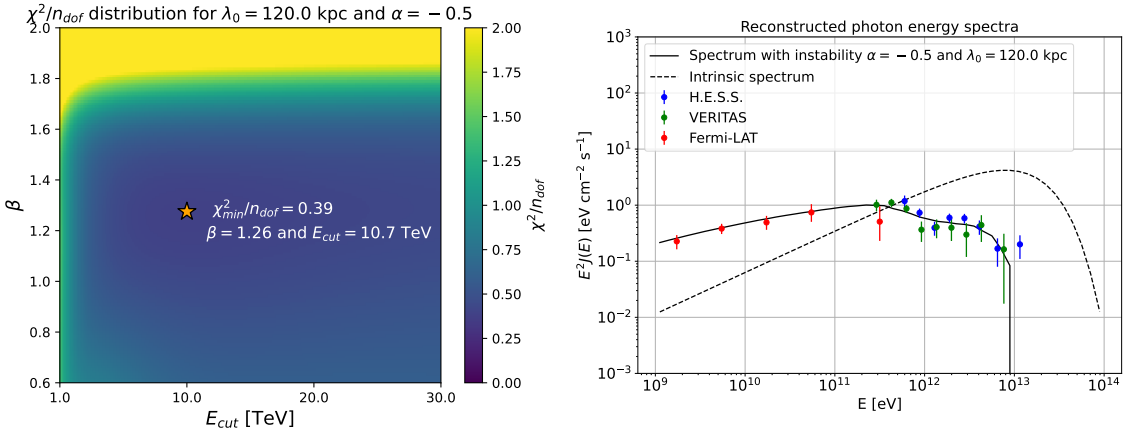

Figure 9.6: Left: $\chi^2(\beta, E_{\rm cut})/n_{\rm dof}$ distribution for the blazar 1ES 0229+200, calculated using H.E.S.S., VERITAS, and Fermi-LAT data ($n_{\rm dof} = 13$). Plasma instability parameters $\lambda_0 = 120\,$kpc and $\alpha = -0.5$. The minimum $\chi^2_{\rm min}/n_{\rm dof} = 0.39$ is marked with an orange star, and it corresponds to spectral index and cutoff energy values of $\beta = 1.26^{+0.31}_{-0.56}$ and $E_{\rm cut} = 10.7^{+19.3}_{-7.1}\,$TeV, respectively. Right: the unattenuated prompt photon spectrum (black dashed line) for the central values $\beta = 1.26$ and $E_{\rm cut} = 10.7\,$TeV. The propagated spectrum (black line) and the measurements by H.E.S.S. (blue points), VERITAS (green points), and Fermi-LAT (red points) are shown. Figure updated from [444].

instability scenario with $\lambda_0 = 120\,$kpc and $\alpha = -0.5$. The corresponding spectral parameters of the prompt spectrum are $\beta = 1.26^{+0.31}_{-0.56}$ and $E_{\rm cut} = 10.7^{+19.3}_{-7.1}\,$TeV.

From Fig. 9.5, it can be seen that λ_0 is the main parameter affecting the development of the electromagnetic cascade. For very large values of λ_0 (orange points in the right panel of Fig. 9.5), the propagation of electrons and positrons is dominated by inverse Compton scattering, and the cascade develops almost as in the case without plasma instabilities when $\alpha \lesssim 0$. On the other hand, for smaller values of λ_0 (red and blue points in the right panel of Fig. 9.5) plasma instabilities are so efficient that the production of secondary photons from inverse Compton scattering of electrons and positrons on background photons is strongly suppressed. In particular, the spectral cutoff is at such a high-energy value that the observed GeV spectrum corresponds to the low energy part of the prompt spectrum. It can be seen that these scenarios can still reproduce the observed spectrum when considering a very large value of $E_{\rm cut}$.

The $\chi^2/n_{\rm dof}$ distribution and the propagated photon spectrum for the case highlighted in the left panel of Fig.9.5 are shown in Fig. 9.6. We can see that a plasma instability energy drain on a typical length scale of $\lambda_0 \simeq 100\,$kpc leads to a very good agreement with the observations of the 1ES 0229+200 photon spectrum in both the GeV and TeV energy bands. This result shows how plasma instability could play an important role in the reconstruction of the photon signal of distant γ-ray sources.

We have discussed in Sec. 9.2 that plasma instabilities reduce the energy of the electrons before they up-scatter background photons. Since the energy of up-scattered photons depends on the energy of the incoming electron, the fraction of energy lost by electrons in plasma instabilities has a direct effect on the suppression of the propagated photon spectrum. We can then calculate the fraction of energy lost by the electrons in our best case scenario $\lambda_0 = 120$ kpc and $\alpha = -0.5$

from Eq. (9.2). We obtain that

$$\left(\frac{\Delta E_e(\lambda_{\rm IC})}{E_e}\right)_{\rm PI} = 10^{-2}\cdot\left(\frac{E_e}{1\,{\rm TeV}}\right)^{1/2}\,, \tag{9.6}$$

which corresponds to a fraction of energy lost within one inverse Compton scattering length equal to $\sim 1-10\%$ for $1-100$ TeV electrons and $< 1\%$ for sub-TeV electrons. Therefore, in order to reproduce the observed photon flux, electrons and positrons must lose $\sim 1\%$ of their energy in plasma instabilities within one inverse Compton scattering length. The final propagated spectrum is given by the *summation* of the electron energy loss over many scattering lengths. On the other hand, the average extragalactic inverse Compton energy loss length for electrons in the Thomson regime is given by Eq. (4.74). For TeV electrons, this corresponds to $\simeq 400\,{\rm kpc}$. The corresponding fractional energy loss due to plasma instabilities within an inverse Compton energy loss length is then $\simeq 85\%$ (or higher if smaller values of λ_0 are considered). Therefore, the energy loss due to plasma instabilities must be comparable to the inverse Compton energy loss in order to reproduce the observed photon spectrum.

9.5 Discussion and conclusions

In this chapter, we have studied the impact of an energy loss term associated to plasma instabilities in the development of electromagnetic cascades from distant blazars. We have performed a parametric study of the instability energy loss term in Eq. (9.2) by simulating the extragalactic propagation of VHEGRs from the blazar 1ES 0229+200. Our results were obtained considering the fully developed cascades: we have computed the propagation matrices that include electromagnetic processes and plasma instabilities. For the first time, the injection spectral parameters were left as free parameters. We minimize the χ^2 in Eq. (9.5) in order to find the best combination of spectral parameters β and $E_{\rm cut}$ and instability parameters α and λ_0 that reproduces the observed photon spectrum.

In Figs. 9.3 and 9.4, the scenarios where the propagated spectrum is obtained without plasma instabilities are shown. We found that, in general, it is difficult to reproduce the observed spectrum in both the GeV and TeV energy ranges using only the standard processes in electromagnetic cascades. In particular, we find the minimum $\chi^2_{\rm min}/n_{\rm dof} = 1.23$, corresponding to the spectral index $\beta = 1.22^{+0.26}_{-0.54}$ and cutoff energy $E_{\rm cut} = 1.6^{+1.4}_{-0.6}\,{\rm TeV}$ required to reproduce the H.E.S.S., VERITAS, and Fermi-LAT observations.

In Fig. 9.5, the results obtained by including plasma instabilities in the extragalactic propagation of VHEGRs are shown. We obtain that for $\lambda_0 \gtrsim 1\,{\rm Mpc}$ the cascade is almost unaffected by plasma instabilities. On the contrary, for $\lambda_0 \lesssim 10\,{\rm kpc}$ the electron energy drain from plasma instabilities is so fast that the production of GeV-secondary photons from inverse Compton scattering of electrons and positrons is strongly suppressed. These scenarios can still reproduce the observations by requiring a very high energy cutoff in the prompt spectrum. Even if our results slightly depend on the value of the instability spectral index α, it is good to remember that the sign and the absolute value of the plasma index α play a crucial role in determining the type of instabilities developed in the IGM. For instance, for large and positive values of the plasma index ($\alpha > 1$), models tend to consider a dominance of the modulation instability for the energy losses, as has been previously studied in [24, 421]. On the contrary, most models that consider

the instabilities to be dominated by oblique instabilities report small or negative indices, such as in [23, 25].

We have shown that the minimum value of $\chi^2/n_{\rm dof}$ can be found for the instability parameters $\lambda_0 \simeq 100\,{\rm kpc}$ and $\alpha \simeq -0.5$. This scenario corresponds to a fraction of electron energy lost over the typical inverse Compton interaction length of $\sim 1-10\%$ for $1-100$ TeV electrons, and $< 1\%$ for sub-TeV electrons. The latter value corresponds to the upper limit of recent theoretical estimates, such as those in [423], which suggest that the maximum fraction of energy lost before the instability is quenched at the percent level or less. We find that in this scenario $\chi^2_{\rm min}/n_{\rm dof} = 0.39$ and the corresponding spectral parameters are $\beta = 1.26^{+0.31}_{-0.56}$ and $E_{\rm cut} = 10.7^{+19.3}_{-7.1}$ TeV. The propagated photon spectrum in this scenario is shown in Fig. 9.6, where the good agreement with the current GeV and TeV data can be seen.

We can therefore conclude that plasma instabilities with energy loss lengths of the order of ~ 100 kpc may play a relevant role in suppressing the energy spectrum of TeV-blazars for energies in the GeV range. Furthermore, the fraction of energy lost by an electron over the average energy loss length (about a factor ~ 100 greater than the interaction length) is expected to be $\simeq 85\%$ and higher for TeV-electrons. This implies that the energy loss mechanism of plasma instabilities has to be comparable to that of inverse Compton scattering for reproducing observations.

Similar studies combining plasma instabilities and magnetic deflections could also help to impose more precise constrains on the EGMF. Blazars with a hard spectral index, such as 1ES 0229+200, are expected to be good candidates for these studies, since their propagated spectra are dominated by cascade photons. Three-dimensional simulations are required to account for the magnetic deflection of the produced leptons and the different momentum distributions of the injected photons at the source. The `CRPropa` framework provides several tools to use synthetic EGMFs and to explore different injection scenarios (e.g. directed emission following a von Mises-Fisher distribution, see [236, 433]). Future works, including the EGMF, may shed light on the possibilities of disentangling these two different phenomena. Therefore, estimates of the instability spectral index are needed for more conclusive studies. In addition, the instability-induced angular spreading should also be included in simulations. This effect will allow the magnetic and instability spreading of the cascade to be compared, as well as their possible interplay. Studies including these terms will be of fundamental importance to examine the suppression in a time-dependent framework, and to compare it with the magnetic suppression due to image broadening and secondary photon time delays.

10

Conclusions

Identifying the sources of the most energetic particles ever observed and understanding their production mechanisms remain challenges in modern astroparticle physics. The information obtained at Earth from the observations of such high-energy particles must be carefully processed to account for the changes due to their extragalactic propagation. This means that the reconstruction of the cosmic journey of these particles is influenced by our limited knowledge of extragalactic space and by the modelling of the processes which they undergo.

In Chapter 4 of this thesis, the effect of the propagation through the extragalactic space of various types of cosmic messengers, such as UHECRs, high-energy neutrinos and VHEGRs, was discussed. The presence of low-energy background photon fields, such as the CMB and the EBL, and the extremely high energies of these particles lead to stochastic photohadronic interactions, which have strong consequences for their properties. In the case of UHECRs, the observed energy spectrum and atomic mass composition are different when they escape their source environments. However, photohadronic interactions also introduce an interaction horizon that limits the maximum possible distance of the sources of the most energetic particles. The correlation of the observed UHECR arrival directions is further complicated by the presence of cosmic magnetic fields, such as the EGMF and the GMF. Large magnetic deflections during the CR propagation may play an important role in obscuring the position of their sources in the sky.

Uncertainties in modelling the propagation of high-energy particles can be studied by performing extensive numerical simulations. In Chapter 5, the two most used and comprehensive numerical frameworks in this field were introduced. These codes are `SimProp v2r4` [292] and `CRPropa 3.2` [236], and they are both Monte Carlo codes that take into account stochastic and continuous energy losses during extragalactic propagation. The main difference in terms of UHECR simulations between the two codes is that `Simprop v2r4` is a fast one-dimensional framework where magnetic deflections are not considered, while `CRPropa 3.2` is a three-dimensional framework where it is possible to consider the presence of galactic and extragalactic magnetic fields. However, simulating the propagation of electrically charged particles in magnetic fields over astrophysical distances can make `CRPropa` simulations very time consuming.

In 2017, the Pierre Auger Observatory has reported the first observation of a dipolar component in the UHECR arrival direction distribution above 8 EeV [16]. The most recent published results, with more than $\sim 50,000$ events above 8 EeV, show a dipole amplitude of $d \simeq 7.5\%$ with

a 6.8σ significance, pointing more than $\sim 100^\circ$ away from the Milky Way galactic center [17] (see also Chapter 3 for more details). These results have also been confirmed by the joint working group with the TA Collaboration [167]. However, even with a full sky coverage, no statistically significant multipole moments with $l \geq 2$ have been observed yet.

In Chapter 7, we have studied the multipole expansion of the UHECR arrival direction distribution above 8 EeV by performing `CRPropa` simulations in constrained numerical replicas of the local Universe. Since the UHECR sources are still unknown, we consider two scenarios: either they follow the LSS of the baryonic distribution in the Universe or they are homogeneously distributed. We have then created synthetic catalogues of source locations for different values of source density, and used these catalogues in our `CRPropa` simulations. To test different propagation scenarios, we have also considered different models for the EGMF, and the effect of the GMF. In particular, with respect to extragalactic propagation, we have considered the scenarios of ballistic propagation, statistically uniform turbulent magnetic field and structured EGMF models from constrained cosmological simulations of the evolution of the cosmic web [338]. In the case of constrained EGMFs, different assumptions on the magnetization of the cosmic voids have been investigated.

In order to reproduce the observed UHECR energy spectrum and mass composition, we have found that a hard spectral index is required at the escape from the sources from $\gamma \simeq -1$ to $\gamma \simeq -3$, depending on the propagation scenario. However, a high-rigidity cutoff of $R_{\rm cut} \simeq 2\,\mathrm{EV}$ and a nitrgen/silicon dominated composition at the source are obtained for all the scenarios considered. We found that the level of magnetization of the cosmic voids from different EGMF models introduces a further suppression of the UHECR horizon. In particular, in the case of primordial or statistically homogeneous fields, where the voids are more strongly magnetized than in the case of astrophysical fields, large deflections up to $\sim 90^\circ$ are possible even for CR sources at $\sim 100\,\mathrm{Mpc}$ from the observer. This implies that, in the case of magnetized voids, the interaction horizon is suppressed from $\sim 500\,\mathrm{Mpc}$ to $\sim 100\,\mathrm{Mpc}$, increasing the contribution of nearby sources to the total UHECR flux.

We have then obtained the angular power spectra $\mathcal{C}_l$ (see Chapter 6) of the simulated arrival direction distributions and we have compared our results with observations. We have found that the main source of fluctuation in the multipoles is the cosmic variance of the source catalogues and that there are no effects due to the different EGMF models considered. Moreover, the GMF introduces a strong suppression of the large multipole components (i.e. $l \gtrsim 5$), which converge to the isotropic prediction. The comparison of the simulated multipoles with the observations of the Pierre Auger Observatory shows that it is possible to reproduce the dipole component within the total variance of the scenarios, while the higher multipoles (e.g. the quadrupole) are larger than observations, regardless of the propagation model considered.

Various extensions and future projects can be considered starting from our study of the UHECR anisotropies from a structured and magnetized Universe. Due to the large number of scenarios considered and the long simulation time, we have only used 10 possible realizations of the source catalogues. A larger number of realizations would improve the understanding of the effect of the cosmic variance on our results. In addition, considering other GMF models would clarify the dependence of the simulated angular power spectrum on the galactic propagation model considered. The Pierre Auger Observatory has shown how the dipole amplitude increases as the minimum UHECR energy considered in the analysis increases [162]. This energy evolution of the multipole components could also be obtained in the case of simulated scenarios.

Moreover, since the interaction horizon depends on the atomic mass of the propagated UHECRs, the multipole expansions of the arrival direction distribution of the particles from different mass groups could be considered to study the mass dependence of the anisotropy signal.

In Chapter 8, we have discussed how the numerical framework used to study the extragalactic propagation of high-energy particles can also be adapted to simulate their propagation within source environments. In particular, the production of weakly interacting secondary particles, such as high-energy neutrinos, allows the study of the interactions taking place within the possible CR sources. The combination of different types of particles, and the combined study of their propagation at different stages of their journey to the Earth, can be used to characterize possible CR source environments in the context of multimessenger astrophysics [369, 370]. In Chapter 8, we have considered the astrophysical environment produced by BNS mergers, as modelled in [382, 387], to study the production of high-energy astrophysical neutrinos from the interaction of accelerated CRs with local photon fields. We consider the extreme scenarios of a pure proton composition and a pure iron composition. We have simulated the in-source propagation with a modified version of the `SimProp` code, from which we have obtained the escaped CR and neutrino spectra. The latter were used as input for the extragalactic propagation to the Earth, simulated with the original `SimProp` code.

The interaction region of a BNS merger remnant is characterized by a thermal black-body photon field and a non-thermal component. We have shown that the non-thermal field is negligible for CR interactions and have not included it in our simulations. On the other hand, the interactions with the BB field are very efficient, especially in the early stages after the merger where the temperature is $T \gtrsim 10^6\,\mathrm{K}$ (i.e. for times $t \lesssim 10^3\,\mathrm{s}$ after the merger). In most of the simulated scenarios, we found that the conversion of CR energy into neutrino energy saturates at $\sim 10\%$. As expected, the CR spectrum at the escape from the interaction region converges to the accelerated spectrum in the late stages after the merger, when the temperature is $T \lesssim 10^4\,\mathrm{K}$.

The CR and neutrino spectra escaped from the sources are then propagated to the Earth and normalized to the observed CR spectrum from the Pierre Auger Observatory. We have considered several scenarios of spectral parameters at the acceleration, redshift evolution of the source density and relative normalization to the observed energy spectrum. We compared or simulated neutrino spectra with the observed diffuse neutrino flux from the IceCube Neutrino Observatory and with the cosmogenic neutrino limits from IceCube [391] and from the Pierre Auger Observatory [392]. We have shown that the observed neutrino flux cannot be attributed to the cosmogenic neutrino flux produced during the extragalactic propagation. Moreover, in order not to overshoot the current data and limits, the CR spectrum should be characterized by a high-energy cutoff $E_{\mathrm{cut}} \gtrsim 1\,\mathrm{EeV}$ at the acceleration. We then characterized the source environment by calculating the baryonic loading η, i.e. the ratio between the CR luminosity at the acceleration and the fallback luminosity, allowed by the current neutrino observations. Given the BNS merger event rate per volume estimated by [26, 398] of $10\,\mathrm{Gpc^{-3}\,yr^{-1}} \lesssim \dot{n} \lesssim 1,000\,\mathrm{Gpc^{-3}\,yr^{-1}}$, we found that, even in extreme scenarios where all the CRs above the ankle observed by the Pierre Auger Observatory are accelerated in BNS mergers, the baryonic loading is limited to $\eta \simeq 10^{-4} - 10^{-6}$. This limit holds for all the scenarios considered.

In our study of the multimessenger signal produced by BNS mergers, we did not study the diffuse γ-ray flux, which could provide further constraints on the characterization of these astrophysical objects. In addition, nuclei heavier than those in the iron group should also be considered in BNS mergers. The propagation of ultra-heavy nuclei in photon fields, as studied

in [434], could also contribute to the production of high-energy neutrinos from these sources. Future extensions of the `SimProp` and `CRPropa` simulation frameworks can be used to include ultra-heavy nuclei in CR physics.

Finally, in Chapter 9, we study the propagation of VHEGRs from distant sources. As discussed in Chapter 4, γ-rays can also interact with background photon fields, producing secondary electrons and positrons. These particles will then interact with the background fields again, producing secondary photons via inverse Compton scattering. The repetition of this chain of processes defines the electromagnetic cascades. Therefore, the propagated photon spectrum of extragalactic sources of VHEGRs, such as distant blazars, will be characterized by a GeV photon component populated by secondary photons. However, the observed suppression of the GeV photon flux with respect to the prediction from standard electromagnetic cascades has been interpreted as the result of the deflection of the electrically charged component of the cascade out of the line of sight by the EGMF [271, 272, 409].

The observed suppression of the propagated photon flux can also be interpreted as resulting from the interaction of high-energy electrons and positrons with the cosmic plasma [23–25, 420, 421, 425, 426]. In particular, highly collimated electron-positron beams passing through the IGM can induce perturbations in the background density, leading to plasma instabilities that can drain energy from the electrons and positrons and suppress the production of secondary GeV photons. To test the impact of plasma instabilities on the development of electromagnetic cascades, we have developed a new energy loss module for the `CRPropa` simulation framework. This module is parameterized by the typical length scale of the instability energy loss λ_0 and by the power index α, which parameterizes the electron energy dependence of the energy loss length. We have then simulated the propagated photon spectrum of the blazar 1ES 0229+200, including the instability module, and we have compared the results with the observed spectrum. For the first time, we have obtained the injection spectral index taking into account the presence of plasma instabilities in our propagation matrices. We found that the best fit value for the instability length scale is $\lambda_0 \simeq 100\,\mathrm{kpc}$, in order to reproduce the propagated photon spectrum from the GeV to the TeV energy scale. This scenario corresponds to a high-energy cutoff in the injected photon spectrum of $E_{\mathrm{cut}} \simeq 10\,\mathrm{TeV}$, with respect to $E_{\mathrm{cut}} \simeq 2\,\mathrm{TeV}$, obtained with the standard electromagnetic cascades. We also found that, in order to reproduce the observed photon spectrum, the fractional energy loss due to plasma instabilities over an inverse Compton energy loss length must be comparable to the inverse Compton energy loss.

It has been shown that plasma instabilities can also induce an angular broadening of the cascade; this effect was not included in our simulations. However, the modular structure of `CRPropa` could be adapted to include this effect. In our study we have neglected the presence of a possible EGMF. Three-dimensional simulations including magnetic deflections and plasma instabilities can lead to more precise constraints on the EGMF. Moreover, the inclusion of all these processes can provide a deeper understanding of the extragalactic development of electromagnetic cascades initiated by distant TeV sources.

References

[1] Victor Francis Hess. "Über Beobachtungen der durchdringenden Strahlung bei sieben Freiballonfahrten". In: *Z. Phys.* 13 (1912), p. 1084 (cit. on pp. 1, 6).

[2] Robert A Millikan and G Harvey Cameron. "The origin of the cosmic rays". In: *Physical review* 32.4 (1928), p. 533 (cit. on pp. 1, 6).

[3] Jacob Clay. "Penetrating radiation". In: *Proceedings of the royal academy of sciences amsterdam*. Vol. 30. 1927, pp. 1115–1127 (cit. on pp. 1, 7).

[4] Walther Bothe and Werner Kolhörster. "Das wesen der höhenstrahlung". In: *Zeitschrift für Physik* 56.11 (1929), pp. 751–777 (cit. on pp. 1, 7).

[5] Bruno Rossi. "On the magnetic deflection of cosmic rays". In: *Physical Review* 36.3 (1930), p. 606 (cit. on pp. 1, 7).

[6] Luis Alvarez and Arthur H Compton. "A positively charged component of cosmic rays". In: *Physical Review* 43.10 (1933), p. 835 (cit. on pp. 1, 7).

[7] Thomas H Johnson. "The azimuthal asymmetry of the cosmic radiation". In: *Physical Review* 43.10 (1933), p. 834 (cit. on pp. 1, 7).

[8] Bruno Rossi. "Directional measurements on the cosmic rays near the geomagnetic equator". In: *Physical Review* 45.3 (1934), p. 212 (cit. on pp. 1, 7).

[9] S. Navas et al. "Review of particle physics". In: *Phys. Rev. D* 110.3 (2024), p. 030001. DOI: 10.1103/PhysRevD.110.030001 (cit. on pp. 1, 17, 18, 27, 41, 43, 44, 47, 49, 130).

[10] Alexander Aab et al. "The Pierre Auger Cosmic Ray Observatory". In: *Nucl. Instrum. Meth. A* 798 (2015), pp. 172–213. DOI: 10.1016/j.nima.2015.06.058. arXiv: 1502.01323 [astro-ph.IM] (cit. on pp. 1, 9, 11, 21).

[11] H. Kawai et al. "Telescope array experiment". In: *Nucl. Phys. B Proc. Suppl.* 175-176 (2008). Ed. by Kwong Sang Cheng et al., pp. 221–226. DOI: 10.1016/j.nuclphysbps.2007.11.002 (cit. on pp. 1, 9).

[12] Arno A. Penzias and Robert Woodrow Wilson. "A Measurement of excess antenna temperature at 4080-Mc/s". In: *Astrophys. J.* 142 (1965), pp. 419–421. DOI: 10.1086/148307 (cit. on pp. 2, 46).

[13] Asantha Cooray. "Extragalactic Background Light: Measurements and Applications". In: (Feb. 2016). arXiv: 1602.03512 [astro-ph.CO] (cit. on pp. 2, 48).

[14] Kenneth Greisen. "End to the cosmic ray spectrum?" In: *Phys. Rev. Lett.* 16 (1966), pp. 748–750. DOI: 10.1103/PhysRevLett.16.748 (cit. on pp. 2, 19, 49).

[15] G. T. Zatsepin and V. A. Kuzmin. "Upper limit of the spectrum of cosmic rays". In: *JETP Lett.* 4 (1966), pp. 78–80 (cit. on pp. 2, 19, 49).

[16] Alexander Aab et al. "Observation of a Large-scale Anisotropy in the Arrival Directions of Cosmic Rays above 8×10^{18} eV". In: *Science* 357.6537 (2017), pp. 1266–1270. DOI: 10.1126/science.aan4338. arXiv: 1709.07321 [astro-ph.HE] (cit. on pp. 2, 30, 31, 87, 145).

[17] A. Abdul Halim et al. "Large-scale Cosmic-ray Anisotropies with 19 yr of Data from the Pierre Auger Observatory". In: *Astrophys. J.* 976.1 (2024), p. 48. DOI: 10.3847/1538-4357/ad843b. arXiv: 2408.05292 [astro-ph.HE] (cit. on pp. 2, 21, 31–33, 35, 87, 89, 95, 97, 104, 106, 146).

[18] Dario Grasso and Hector R. Rubinstein. "Magnetic fields in the early universe". In: *Phys. Rept.* 348 (2001), pp. 163–266. DOI: 10.1016/S0370-1573(00)00110-1. arXiv: astro-ph/0009061 (cit. on pp. 2, 57).

[19] Ruth Durrer and Andrii Neronov. "Cosmological Magnetic Fields: Their Generation, Evolution and Observation". In: *Astron. Astrophys. Rev.* 21 (2013), p. 62. DOI: 10.1007/s00159-013-0062-7. arXiv: 1303.7121 [astro-ph.CO] (cit. on pp. 2, 57).

[20] Rafael Alves Batista and Andrey Saveliev. "The Gamma-ray Window to Intergalactic Magnetism". In: *Universe* 7.7 (2021), p. 223. DOI: 10.3390/universe7070223. arXiv: 2105.12020 [astro-ph.HE] (cit. on pp. 2, 57).

[21] M. G. Aartsen et al. "The IceCube Neutrino Observatory: Instrumentation and Online Systems". In: *JINST* 12.03 (2017). [Erratum: JINST 19, E05001 (2024)], P03012. DOI: 10.1088/1748-0221/12/03/P03012. arXiv: 1612.05093 [astro-ph.IM] (cit. on pp. 2, 110).

[22] V. Berezinsky and O. Kalashev. "High energy electromagnetic cascades in extragalactic space: physics and features". In: *Phys. Rev. D* 94.2 (2016), p. 023007. DOI: 10.1103/PhysRevD.94.023007. arXiv: 1603.03989 [astro-ph.HE] (cit. on pp. 2, 134).

[23] Avery E. Broderick, Philip Chang, and Christoph Pfrommer. "The Cosmological Impact of Luminous TeV Blazars I: Implications of Plasma Instabilities for the Intergalactic Magnetic Field and Extragalactic Gamma-Ray Background". In: *Astrophys. J.* 752 (2012), p. 22. DOI: 10.1088/0004-637X/752/1/22. arXiv: 1106.5494 [astro-ph.CO] (cit. on pp. 2, 134, 144, 148).

[24] R. Schlickeiser, D. Ibscher, and M. Supsar. "PLASMA EFFECTS ON FAST PAIR BEAMS IN COSMIC VOIDS". In: *The Astrophysical Journal* 758.2 (Oct. 2012), p. 102. DOI: 10.1088/0004-637X/758/2/102. URL: https://dx.doi.org/10.1088/0004-637X/758/2/102 (cit. on pp. 2, 134, 143, 148).

[25] Lorenzo Sironi and Dimitrios Giannios. "Relativistic Pair Beams from TeV Blazars: A Source of Reprocessed GeV Emission rather than Intergalactic Heating". In: *Astrophys. J.* 787 (2014), p. 49. DOI: 10.1088/0004-637X/787/1/49. arXiv: 1312.4538 [astro-ph.HE] (cit. on pp. 2, 134, 135, 144, 148).

[26] B. P. Abbott et al. “GW170817: Observation of Gravitational Waves from a Binary Neutron Star Inspiral”. In: *Phys. Rev. Lett.* 119.16 (2017), p. 161101. DOI: 10.1103/PhysRevLett.119.161101. arXiv: 1710.05832 [gr-qc] (cit. on pp. 2, 111, 131, 132, 147).

[27] B. P. Abbott et al. “Multi-messenger Observations of a Binary Neutron Star Merger”. In: *Astrophys. J. Lett.* 848.2 (2017), p. L12. DOI: 10.3847/2041-8213/aa91c9. arXiv: 1710.05833 [astro-ph.HE] (cit. on pp. 2, 111).

[28] B. P. Abbott et al. “Gravitational Waves and Gamma-rays from a Binary Neutron Star Merger: GW170817 and GRB 170817A”. In: *Astrophys. J. Lett.* 848.2 (2017), p. L13. DOI: 10.3847/2041-8213/aa920c. arXiv: 1710.05834 [astro-ph.HE] (cit. on pp. 2, 111).

[29] Alessandro De Angelis and Mario Pimenta. *Introduction to Particle and Astroparticle Physics: Multimessenger Astronomy and its Particle Physics Foundations*. Undergraduate Lecture Notes in Physics. Heidelberg: Springer Nature, 2018. ISBN: 978-3-319-78180-8, 978-3-319-78181-5. DOI: 10.1007/978-3-319-78181-5 (cit. on pp. 5, 6, 36).

[30] Henri Becquerel. “Sur les radiations invisibles émises par les corps phosphorescents.” In: *Comptes rendus* 122 (1896), pp. 501–503. URL: http://gallica.bnf.fr/ark:/12148/bpt6k30780.image.f503 (cit. on p. 5).

[31] Hans Geitel. “Über die Elektrizitätszerstreuung in abgeschlossenen Luftmengen”. In: *Phys. Z* 2 (1900), pp. 116–119 (cit. on p. 6).

[32] E Elster. “Weitere versuche uber die elektrizitatszerstreuung in abgeschlossen luftmengen.” In: *Physik. Z.* 2 (1901), pp. 560–563 (cit. on p. 6).

[33] Charles TR Wilson. “On the leakage of electricity through dust-free air”. In: *Proc. Cambridge Philos. Soc.* Vol. 11. 1900, p. 32 (cit. on p. 6).

[34] Theodor Wulf. “Beobachtungen über die Strahlung hoher Durchdringungsfähigkeit auf dem Eiffelturm”. In: *Physikalische Zeitschrift* 11 (1910), pp. 811–813 (cit. on p. 6).

[35] Domenico Pacini, Michela De Maria, and Alessandro De Angelis. “Penetrating Radiation on the Sea”. In: (Jan. 2011). arXiv: 1101.3015 [physics.hist-ph] (cit. on p. 6).

[36] D. Pacini. “Penetrating Radiation at the Surface of and in Water”. In: *Nuovo Cim.* 8 (1912), pp. 93–100. DOI: 10.1007/BF02957440. arXiv: 1002.1810 [physics.hist-ph] (cit. on p. 6).

[37] Albert Gockel. “Messungen der druchdringenden Strahlung bei Ballonfahren”. In: *Phys. Zeits.* 12 (1911), pp. 595–597 (cit. on p. 6).

[38] S.P. Thompson. *Elementary Lessons in Electricity and Magnetism*. Macmillan, 1915. URL: https://books.google.de/books?id=hLk3AAAAMAAJ (cit. on p. 6).

[39] KOLHORSTER Werner. “Messungen der durchdringenden Strahlung im Freiballon in grosseren Hohen”. In: *Phys. Zeits.* 14 (1913), pp. 1153–1156 (cit. on p. 6).

[40] Werner Kolhörster. “Messungen der durchdringenden Strahlungen bis in Höhen von 9300 m”. In: *Verh. deutsche phys. Gesellschaft* 16 (1914), pp. 719–721 (cit. on p. 6).

[41] Bruno Rossi. “Über die Eigenschaften der durchdringenden Korpuskularstrahlung im Meeresniveau”. In: *Zeitschrift für Physik* 82.3 (1933), pp. 151–178 (cit. on p. 7).

[42] Walther Bothe. “Zur Vereinfachung von Koinzidenzzählungen”. In: *Zeitschrift für Physik* 59.1 (1930), pp. 1–5 (cit. on p. 7).

[43] Bruno Rossi. “Method of registering multiple simultaneous impulses of several Geiger’s counters”. In: *Nature* 125.3156 (1930), pp. 636–636 (cit. on p. 7).

[44] Pierre Auger et al. “Extensive cosmic-ray showers”. In: *Reviews of modern physics* 11.3-4 (1939), p. 288 (cit. on p. 8).

[45] Georg Pfotzer. “Dreifachkoinzidenzen der Ultrastrahlung aus vertikaler Richtung in der Stratosphäre: I. Meßmethode und Ergebnisse”. In: *Zeitschrift für Physik* 102 (1936), pp. 23–40 (cit. on p. 8).

[46] Marcel Schein, William P Jesse, and Ernest O Wollan. “The nature of the primary cosmic radiation and the origin of the mesotron”. In: *Physical Review* 59.7 (1941), p. 615 (cit. on p. 8).

[47] Carl D Anderson. “The positive electron”. In: *Physical review* 43.6 (1933), p. 491 (cit. on p. 8).

[48] Seth H Neddermeyer and Carl D Anderson. “Note on the nature of cosmic-ray particles”. In: *Physical Review* 51.10 (1937), p. 884 (cit. on p. 8).

[49] Cesare Mansueto Giulio Lattes, Giuseppe PS Occhialini, and Cecil Frank Powell. “Observations on the tracks of slow mesons in photographic emulsions”. In: *Nature* 160.4067 (1947), pp. 486–492 (cit. on p. 8).

[50] G. D. Rochester and C. C. Butler. “Evidence for the Existence of New Unstable Elementary Particles”. In: *Nature* 160 (1947), pp. 855–857. DOI: 10.1038/160855a0 (cit. on p. 8).

[51] VD Hopper and S Biswas. “Evidence concerning the existence of the new unstable elementary neutral particle”. In: *Physical Review* 80.6 (1950), p. 1099 (cit. on p. 8).

[52] Pavel Alekseevič Čerenkov. “Visible radiation produced by electrons moving in a medium with velocities exceeding that of light”. In: *Physical Review* 52.4 (1937), p. 378 (cit. on p. 8).

[53] AA Watson. “A Brief History of the Study of High Energy Cosmic Rays using Arrays of Surface Detectors”. In: *EPJ Web of Conferences*. Vol. 283. EDP Sciences. 2023, p. 01002 (cit. on p. 8).

[54] George W Clark, F Scherb, and WB Smith. “Preparation of large plastic scintillators”. In: *Review of Scientific Instruments* 28.6 (1957), pp. 433–437 (cit. on p. 9).

[55] GW Clark et al. “Cosmic-ray air showers at sea level”. In: *Physical Review* 122.2 (1961), p. 637 (cit. on p. 9).

[56] John Linsley. “Primary cosmic rays of energy 10^{17} to 10^{20} eV, the energy spectrum and arrival directions”. In: *International Cosmic Ray Conference*. Vol. 4. 1963, p. 77 (cit. on p. 9).

[57] John Linsley. “Evidence for a primary cosmic-ray particle with energy 10^{20} eV”. In: *Physical Review Letters* 10.4 (1963), p. 146 (cit. on p. 9).

[58] RG Brownlee et al. “Design of an array to record air showers of energy up to 10^{21} eV”. In: *Canadian Journal of Physics* 46.10 (1968), S259–S262 (cit. on p. 9).

[59] RM Tennent. "The Haverah Park extensive air shower array". In: *Proceedings of the Physical Society* 92.3 (1967), p. 622 (cit. on p. 9).

[60] RM Baltrusaitis et al. "The Utah Fly's eye detector". In: *Nuclear Instruments and Methods in Physics Research Section A: Accelerators, Spectrometers, Detectors and Associated Equipment* 240.2 (1985), pp. 410–428 (cit. on p. 9).

[61] D. J. Bird et al. "Detection of a cosmic ray with measured energy well beyond the expected spectral cutoff due to cosmic microwave radiation". In: *Astrophys. J.* 441 (1995), pp. 144–150. DOI: 10.1086/175344. arXiv: astro-ph/9410067 (cit. on p. 9).

[62] R. U. Abbasi et al. "Surface detectors of the TAx4 experiment". In: *Nucl. Instrum. Meth. A* 1019 (2021), p. 165726. DOI: 10.1016/j.nima.2021.165726. arXiv: 2103.01086 [astro-ph.IM] (cit. on p. 9).

[63] Rasha Abbasi et al. "Current status and prospects of surface detector of the TAx4 experiment". In: *PoS* ICRC2021 (2021), p. 203. DOI: 10.22323/1.395.0203 (cit. on p. 9).

[64] K. Martens. "The Telescope Array and its low energy extension". In: *Nucl. Phys. B Proc. Suppl.* 165 (2007). Ed. by R. Caruso et al., pp. 33–36. DOI: 10.1016/j.nuclphysbps.2006.11.006 (cit. on p. 9).

[65] Shoichi Ogio. "Telescope Array Low energy Extension: TALE". In: *JPS Conf. Proc.* 19 (2018). Ed. by K. Kawata et al., p. 011026. DOI: 10.7566/JPSCP.19.011026 (cit. on p. 9).

[66] Shoichi Ogio. "Telescope Array Low energy Extension(TALE) Hybrid". In: *PoS* ICRC2019 (2020), p. 375. DOI: 10.22323/1.358.0375 (cit. on p. 9).

[67] A. Haungs et al. "KCDC - The KASCADE Cosmic-ray Data Centre". In: *J. Phys. Conf. Ser.* 632.1 (2015), p. 012011. DOI: 10.1088/1742-6596/632/1/012011. arXiv: 1504.06696 [astro-ph.IM] (cit. on p. 11).

[68] Ralph Engel, Dieter Heck, and Tanguy Pierog. "Extensive air showers and hadronic interactions at high energy". In: *Ann. Rev. Nucl. Part. Sci.* 61 (2011), pp. 467–489. DOI: 10.1146/annurev.nucl.012809.104544 (cit. on pp. 10, 12–14).

[69] D. Ciampa and R. W. Clay. "THE ZENITH ANGLE DISTRIBUTION OF EXTENSIVE AIR SHOWERS AT SEA LEVEL: A MEASURE OF SHOWER DEVELOPMENT". In: *J. Phys. G* 14 (1988), pp. 787–792. DOI: 10.1088/0305-4616/14/6/019 (cit. on p. 11).

[70] J. Matthews. "A Heitler model of extensive air showers". In: *Astropart. Phys.* 22 (2005), pp. 387–397. DOI: 10.1016/j.astropartphys.2004.09.003 (cit. on pp. 12–14).

[71] W. Heitler. *The quantum theory of radiation*. Vol. 5. International Series of Monographs on Physics. Oxford: Oxford University Press, 1936 (cit. on p. 11).

[72] J. F. Carlson and J. R. Oppenheimer. "On Multiplicative Showers". In: *Phys. Rev.* 51 (1937), pp. 220–231. DOI: 10.1103/PhysRev.51.220 (cit. on p. 11).

[73] Mark Thomson. *Modern particle physics*. New York: Cambridge University Press, Oct. 2013. ISBN: 978-1-107-03426-6, 978-1-139-52536-7. DOI: 10.1017/CBO9781139525367 (cit. on p. 13).

[74] Karl-Heinz Kampert and Michael Unger. "Measurements of the Cosmic Ray Composition with Air Shower Experiments". In: *Astropart. Phys.* 35 (2012), pp. 660–678. DOI: 10.1016/j.astropartphys.2012.02.004. arXiv: 1201.0018 [astro-ph.HE] (cit. on pp. 14, 19).

[75] D. Heck et al. *CORSIKA: A Monte Carlo code to simulate extensive air showers.* Tech. rep. 51.02.03; LK 01; Wissenschaftliche Berichte, FZKA-6019 (Februar 98). 1998. DOI: 10.5445/IR/270043064 (cit. on p. 14).

[76] Till Bergmann et al. "One-dimensional Hybrid Approach to Extensive Air Shower Simulation". In: *Astropart. Phys.* 26 (2007), pp. 420–432. DOI: 10.1016/j.astropartphys.2006.08.005. arXiv: astro-ph/0606564 (cit. on p. 14).

[77] T. Pierog et al. "EPOS LHC: Test of collective hadronization with data measured at the CERN Large Hadron Collider". In: *Phys. Rev. C* 92.3 (2015), p. 034906. DOI: 10.1103/PhysRevC.92.034906. arXiv: 1306.0121 [hep-ph] (cit. on pp. 15, 96, 99).

[78] S. Ostapchenko. "QGSJET-II: Towards reliable description of very high energy hadronic interactions". In: *Nucl. Phys. B Proc. Suppl.* 151 (2006). Ed. by P. K. F. Grieder, B. Pattison, and L. K. Resvanis, pp. 143–146. DOI: 10.1016/j.nuclphysbps.2005.07.026. arXiv: hep-ph/0412332 (cit. on p. 15).

[79] R. S. Fletcher et al. "SIBYLL: An Event generator for simulation of high-energy cosmic ray cascades". In: *Phys. Rev. D* 50 (1994), pp. 5710–5731. DOI: 10.1103/PhysRevD.50.5710 (cit. on p. 15).

[80] Felix Riehn et al. "Hadronic interaction model Sibyll 2.3d and extensive air showers". In: *Phys. Rev. D* 102.6 (2020), p. 063002. DOI: 10.1103/PhysRevD.102.063002. arXiv: 1912.03300 [hep-ph] (cit. on pp. 15, 99).

[81] Thomas K Gaisser and A Michael Hillas. "Reliability of the method of constant intensity cuts for reconstructing the average development of vertical showers". In: *In: International Cosmic Ray Conference, 15th, Plovdiv, Bulgaria, August 13-26, 1977, Conference Papers. Volume 8.(A79-37301 15-93) Sofia, B'lgarska Akademiia na Naukite, 1978, p. 353-357. NSF-supported research.* Vol. 8. 1977, pp. 353–357 (cit. on p. 15).

[82] Manlio De Domenico et al. "Reinterpreting the development of extensive air showers initiated by nuclei and photons". In: *JCAP* 07 (2013), p. 050. DOI: 10.1088/1475-7516/2013/07/050. arXiv: 1305.2331 [hep-ph] (cit. on pp. 15, 16).

[83] Luan B. Arbeletche and Vitor de Souza. "On the parametrization of the distributions of depth of shower maximum of ultra-high energy extensive air showers". In: *Astropart. Phys.* 116 (2020), p. 102389. DOI: 10.1016/j.astropartphys.2019.102389. arXiv: 1903.03174 [astro-ph.HE] (cit. on p. 15).

[84] Koichi Kamata and Jun Nishimura. "The Lateral and the Angular Structure Functions of Electron Showers". In: *Prog. Theor. Phys. Suppl.* 6 (1958), pp. 93–155. DOI: 10.1143/PTPS.6.93 (cit. on p. 15).

[85] K. Greisen. "Cosmic ray showers". In: *Ann. Rev. Nucl. Part. Sci.* 10 (1960), pp. 63–108. DOI: 10.1146/annurev.ns.10.120160.000431 (cit. on p. 15).

[86] Paolo Lipari. "The Concepts of 'Age' and 'Universality' in Cosmic Ray Showers". In: *Phys. Rev. D* 79 (2009), p. 063001. DOI: 10.1103/PhysRevD.79.063001. arXiv: 0809.0190 [astro-ph] (cit. on p. 16).

[87] Günter Sigl. *Astroparticle Physics: Theory and Phenomenology*. Vol. 1. Atlantis Studies in Astroparticle Physics and Cosmology. Springer, 2017. ISBN: 978-94-6239-242-7, 978-94-6239-243-4. DOI: 10.2991/978-94-6239-243-4 (cit. on pp. 16, 19, 43, 50, 54, 55, 57).

[88] Dmitri Ivanov. "Energy Spectrum Measured by the Telescope Array". In: *PoS* ICRC2019 (2020), p. 298. DOI: 10.22323/1.358.0298 (cit. on p. 17).

[89] M. G. Aartsen et al. "Cosmic ray spectrum and composition from PeV to EeV using 3 years of data from IceTop and IceCube". In: *Phys. Rev. D* 100.8 (2019), p. 082002. DOI: 10.1103/PhysRevD.100.082002. arXiv: 1906.04317 [astro-ph.HE] (cit. on p. 17).

[90] Pedro Abreu et al. "Energy spectrum of cosmic rays measured using the Pierre Auger Observatory". In: *PoS* ICRC2021 (2021), p. 324. DOI: 10.22323/1.395.0324 (cit. on pp. 17, 26).

[91] S. P. Knurenko et al. "Cosmic ray spectrum in the energy range 10^{15}-10^{18} eV and the second knee according to the small Cherenkov setup at the Yakutsk EAS array". In: (Oct. 2013). arXiv: 1310.1978 [astro-ph.HE] (cit. on p. 17).

[92] Carlos Juan Arteaga-Velázquez et al. "Measurements of the muon content of EAS in KASCADE-Grande compared with SIBYLL 2.3 predictions". In: *PoS* ICRC2017 (2018), p. 316. DOI: 10.22323/1.301.0316 (cit. on p. 17).

[93] N. M. Budnev et al. "The primary cosmic-ray energy spectrum measured with the Tunka-133 array". In: *Astropart. Phys.* 117 (2020), p. 102406. DOI: 10.1016/j.astropartphys.2019.102406. arXiv: 2104.03599 [astro-ph.HE] (cit. on p. 17).

[94] A. Coleman et al. "Ultra high energy cosmic rays The intersection of the Cosmic and Energy Frontiers". In: *Astropart. Phys.* 149 (2023), p. 102819. DOI: 10.1016/j.astropartphys.2023.102819. arXiv: 2205.05845 [astro-ph.HE] (cit. on pp. 17, 20, 27, 29, 40, 58, 59, 92).

[95] L. J. Gleeson and W. I. Axford. "Solar Modulation of Galactic Cosmic Rays". In: *Astrophys. J.* 154 (1968), p. 1011. DOI: 10.1086/149822 (cit. on p. 17).

[96] GV Kulikov and GB Khristiansen. "On the size spectrum of extensive air showers". In: *Sov. Phys. JETP* 35.8 (1959), pp. 441–444 (cit. on p. 18).

[97] Rafael Alves Batista et al. "Open Questions in Cosmic-Ray Research at Ultrahigh Energies". In: *Front. Astron. Space Sci.* 6 (2019), p. 23. DOI: 10.3389/fspas.2019.00023. arXiv: 1903.06714 [astro-ph.HE] (cit. on pp. 18, 19, 27, 29, 40, 41, 59).

[98] Johannes Blumer, Ralph Engel, and Jorg R. Horandel. "Cosmic Rays from the Knee to the Highest Energies". In: *Prog. Part. Nucl. Phys.* 63 (2009), pp. 293–338. DOI: 10.1016/j.ppnp.2009.05.002. arXiv: 0904.0725 [astro-ph.HE] (cit. on pp. 18, 19).

[99] G. Giacinti, M. Kachelrieß, and D. V. Semikoz. "Escape model for Galactic cosmic rays and an early extragalactic transition". In: *Phys. Rev. D* 91.8 (2015), p. 083009. DOI: 10.1103/PhysRevD.91.083009. arXiv: 1502.01608 [astro-ph.HE] (cit. on p. 18).

[100] B. Peters. "Primary cosmic radiation and extensive air showers". In: *Nuovo Cim.* 22.4 (1961), pp. 800–819. DOI: 10.1007/bf02783106 (cit. on pp. 18, 95).

[101] John Linsley. "Primary cosmic rays of energy 10^{17} to 10^{20} eV: The energy spectrum and arrival directions". In: *8th International Cosmic Ray Conference*. Jan. 1963 (cit. on p. 18).

[102] Veniamin Berezinsky, A. Z. Gazizov, and S. I. Grigorieva. "Dip in UHECR spectrum as signature of proton interaction with CMB". In: *Phys. Lett. B* 612 (2005), pp. 147–153. DOI: 10.1016/j.physletb.2005.02.058. arXiv: astro-ph/0502550 (cit. on pp. 18, 52).

[103] R. Aloisio et al. "A dip in the UHECR spectrum and the transition from galactic to extragalactic cosmic rays". In: *Astropart. Phys.* 27 (2007), pp. 76–91. DOI: 10.1016/j.astropartphys.2006.09.004. arXiv: astro-ph/0608219 (cit. on pp. 18, 52).

[104] Michael Unger, Glennys R. Farrar, and Luis A. Anchordoqui. "Origin of the ankle in the ultrahigh energy cosmic ray spectrum, and of the extragalactic protons below it". In: *Phys. Rev. D* 92.12 (2015), p. 123001. DOI: 10.1103/PhysRevD.92.123001. arXiv: 1505.02153 [astro-ph.HE] (cit. on pp. 18, 53).

[105] T. Pierog and Klaus Werner. "Muon Production in Extended Air Shower Simulations". In: *Phys. Rev. Lett.* 101 (2008), p. 171101. DOI: 10.1103/PhysRevLett.101.171101. arXiv: astro-ph/0611311 (cit. on p. 19).

[106] R. U. Abbasi et al. "First observation of the Greisen-Zatsepin-Kuzmin suppression". In: *Phys. Rev. Lett.* 100 (2008), p. 101101. DOI: 10.1103/PhysRevLett.100.101101. arXiv: astro-ph/0703099 (cit. on p. 18).

[107] J. Abraham et al. "Observation of the suppression of the flux of cosmic rays above 4×10^{19}eV". In: *Phys. Rev. Lett.* 101 (2008), p. 061101. DOI: 10.1103/PhysRevLett.101.061101. arXiv: 0806.4302 [astro-ph] (cit. on p. 18).

[108] T. Abu-Zayyad et al. "The Cosmic Ray Energy Spectrum Observed with the Surface Detector of the Telescope Array Experiment". In: *Astrophys. J. Lett.* 768 (2013), p. L1. DOI: 10.1088/2041-8205/768/1/L1. arXiv: 1205.5067 [astro-ph.HE] (cit. on p. 18).

[109] M. Takeda et al. "Extension of the cosmic ray energy spectrum beyond the predicted Greisen-Zatsepin-Kuz'min cutoff". In: *Phys. Rev. Lett.* 81 (1998), pp. 1163–1166. DOI: 10.1103/PhysRevLett.81.1163. arXiv: astro-ph/9807193 (cit. on p. 18).

[110] J. Abraham et al. "Properties and performance of the prototype instrument for the Pierre Auger Observatory". In: *Nucl. Instrum. Meth. A* 523 (2004), pp. 50–95. DOI: 10.1016/j.nima.2003.12.012 (cit. on p. 21).

[111] Alexander Aab et al. "The Pierre Auger Observatory Upgrade - Preliminary Design Report". In: (Apr. 2016). arXiv: 1604.03637 [astro-ph.IM] (cit. on pp. 21, 25).

[112] *Pierre Auger Observatory*. These contents are released under the CC BY-SA 4.0 International License, unless explicitly stated differently. Last access: 10/02/2025. URL: https://auger.org (cit. on pp. 22, 23).

[113] Karl-Heinz Kampert, Alan A. Watson, and Alan A. Watson. "Extensive Air Showers and Ultra High-Energy Cosmic Rays: A Historical Review". In: *Eur. Phys. J. H* 37 (2012), pp. 359–412. DOI: 10.1140/epjh/e2012-30013-x. arXiv: 1207.4827 [physics.hist-ph] (cit. on p. 23).

[114] J. Abraham et al. "The Fluorescence Detector of the Pierre Auger Observatory". In: *Nucl. Instrum. Meth. A* 620 (2010), pp. 227–251. DOI: 10.1016/j.nima.2010.04.023. arXiv: 0907.4282 [astro-ph.IM] (cit. on pp. 23, 24).

[115] Federico Sánchez. "The AMIGA detector of the Pierre Auger Observatory: overview". In: *32nd International Cosmic Ray Conference*. Vol. 3. Aug. 2011, pp. 149–152. DOI: 10.7529/ICRC2011/V03/0742 (cit. on p. 22).

[116] I. Allekotte et al. "The Surface Detector System of the Pierre Auger Observatory". In: *Nucl. Instrum. Meth. A* 586 (2008), pp. 409–420. DOI: 10.1016/j.nima.2007.12.016. arXiv: 0712.2832 [astro-ph] (cit. on p. 22).

[117] J. Abraham et al. "Trigger and Aperture of the Surface Detector Array of the Pierre Auger Observatory". In: *Nucl. Instrum. Meth. A* 613 (2010), pp. 29–39. DOI: 10.1016/j.nima.2009.11.018. arXiv: 1111.6764 [astro-ph.IM] (cit. on p. 22).

[118] P. Bauleo et al. "Absolute calibration of the Auger fluorescence detectors". In: *29th International Cosmic Ray Conference*. July 2005. arXiv: astro-ph/0507347 (cit. on p. 24).

[119] R. Knapik et al. "The Absolute, Relative and Multi-Wavelength Calibration of the Pierre Auger Observatory Fluorescence Detectors". In: *30th International Cosmic Ray Conference*. Vol. 4. July 2007, pp. 343–346. arXiv: 0708.1924 [astro-ph] (cit. on p. 24).

[120] A. Aab et al. "Data-driven estimation of the invisible energy of cosmic ray showers with the Pierre Auger Observatory". In: *Phys. Rev. D* 100.8 (2019), p. 082003. DOI: 10.1103/PhysRevD.100.082003. arXiv: 1901.08040 [astro-ph.IM] (cit. on p. 24).

[121] M. Unger. "Mass sensitive observables of the Pierre Auger Observatory". In: *EPJ Web Conf.* 53 (2013). Ed. by K. -H. Kampert et al., p. 04009. DOI: 10.1051/epjconf/20135304009 (cit. on p. 24).

[122] T. Hermann-Josef Mathes. "The HEAT telescopes of the Pierre Auger Observatory: Status and first data". In: *32nd International Cosmic Ray Conference*. Vol. 3. Aug. 2011, p. 153. DOI: 10.7529/ICRC2011/V03/0761 (cit. on p. 24).

[123] J. Abraham et al. "A Study of the Effect of Molecular and Aerosol Conditions in the Atmosphere on Air Fluorescence Measurements at the Pierre Auger Observatory". In: *Astropart. Phys.* 33 (2010), pp. 108–129. DOI: 10.1016/j.astropartphys.2009.12.005. arXiv: 1002.0366 [astro-ph.IM] (cit. on p. 25).

[124] S. Y. BenZvi et al. "The Lidar System of the Pierre Auger Observatory". In: *Nucl. Instrum. Meth. A* 574 (2007), pp. 171–184. DOI: 10.1016/j.nima.2007.01.094. arXiv: astro-ph/0609063 (cit. on p. 25).

[125] Alexander Aab et al. "Design and implementation of the AMIGA embedded system for data acquisition". In: *JINST* 16.07 (2021), T07008. DOI: 10.1088/1748-0221/16/07/T07008. arXiv: 2101.11747 [astro-ph.IM] (cit. on p. 25).

[126] Benjamin Fuchs. "The Auger engineering radio array". In: *Nucl. Instrum. Meth. A* 692 (2012). Ed. by Antonio Capone et al., pp. 93–97. DOI: 10.1016/j.nima.2012.01.058 (cit. on p. 25).

[127] Gioacchino Alex Anastasi. "AugerPrime: The Pierre Auger Observatory upgrade". In: *Nucl. Instrum. Meth. A* 1044 (2022), p. 167497. DOI: 10.1016/j.nima.2022.167497 (cit. on p. 25).

[128] Alexander Aab et al. "Observation of inclined EeV air showers with the radio detector of the Pierre Auger Observatory". In: *JCAP* 10 (2018), p. 026. DOI: 10.1088/1475-7516/2018/10/026. arXiv: 1806.05386 [astro-ph.IM] (cit. on p. 25).

[129] Adila Abdul Halim et al. "Status and expected performance of the AugerPrime Radio Detector". In: *PoS* ICRC2023 (2023), p. 344. DOI: 10.22323/1.444.0344 (cit. on p. 25).

[130] Adila Abdul Halim et al. "Update on the Offline Framework for AugerPrime and production of reference simulation libraries using the VO Auger grid resources". In: *PoS* ICRC2023 (2023), p. 248. DOI: 10.22323/1.444.0248 (cit. on p. 25).

[131] Carmina Pérez Bertolli. "The Underground Muon Detector of AugerPrime". In: *PoS* EPS-HEP2023 (2024), p. 535. DOI: 10.22323/1.449.0535 (cit. on p. 25).

[132] Alexander Aab et al. "A Targeted Search for Point Sources of EeV Neutrons". In: *Astrophys. J. Lett.* 789 (2014), p. L34. DOI: 10.1088/2041-8205/789/2/L34. arXiv: 1406.4038 [astro-ph.HE] (cit. on p. 25).

[133] Adila Abdul Halim et al. "Search for evidence of neutron fluxes using Pierre Auger Observatory data". In: *PoS* ICRC2023 (2023), p. 246. DOI: 10.22323/1.444.0246 (cit. on p. 25).

[134] Alexander Aab et al. "Limits on point-like sources of ultra-high-energy neutrinos with the Pierre Auger Observatory". In: *JCAP* 11 (2019), p. 004. DOI: 10.1088/1475-7516/2019/11/004. arXiv: 1906.07419 [astro-ph.HE] (cit. on p. 25).

[135] Nicolas M. Gonzalez. "Searches for primary photons and neutrinos with the Pierre Auger Observatory". In: *58th Rencontres de Moriond on Very High Energy Phenomena in the Universe*. Jan. 2025. arXiv: 2501.02923 [astro-ph.HE] (cit. on p. 25).

[136] Adila Abdul Halim et al. "Search for a diffuse flux of photons with energies above tens of PeV at the Pierre Auger Observatory". In: (Feb. 2025). arXiv: 2502.02381 [astro-ph.HE] (cit. on p. 25).

[137] Roberto Aloisio. "Pierre Auger Observatory and Super Heavy Dark Matter". In: *EPJ Web Conf.* 280 (2023), p. 07001. DOI: 10.1051/epjconf/202328007001. arXiv: 2212.10476 [astro-ph.HE] (cit. on p. 25).

[138] Olivier Deligny. "Limits to gauge coupling in the dark sector of super-heavy dark matter particles from the Pierre Auger Observatory data". In: *SciPost Phys. Proc.* 13 (2023), p. 013. DOI: 10.21468/SciPostPhysProc.13.013 (cit. on p. 25).

[139] Adila Abdul Halim et al. "Constraints on metastable superheavy dark matter coupled to sterile neutrinos with the Pierre Auger Observatory". In: *Phys. Rev. D* 109.8 (2024), p. L081101. DOI: 10.1103/PhysRevD.109.L081101. arXiv: 2311.14541 [hep-ph] (cit. on pp. 25, 36).

[140] Pedro Abreu et al. "Testing effects of Lorentz invariance violation in the propagation of astroparticles with the Pierre Auger Observatory". In: *JCAP* 01.01 (2022), p. 023. DOI: 10.1088/1475-7516/2022/01/023. arXiv: 2112.06773 [astro-ph.HE] (cit. on p. 25).

[141] Caterina Trimarelli. "Searches for Lorentz Invariance Violation at the Pierre Auger Observatory". In: *EPJ Web Conf.* 283 (2023), p. 05003. DOI: 10.1051/epjconf/202328305003 (cit. on p. 25).

[142] Alexander Aab et al. "Ultrahigh-Energy Neutrino Follow-Up of Gravitational Wave Events GW150914 and GW151226 with the Pierre Auger Observatory". In: *Phys. Rev. D* 94.12 (2016), p. 122007. DOI: 10.1103/PhysRevD.94.122007. arXiv: 1608.07378 [astro-ph.HE] (cit. on p. 25).

[143] A. Albert et al. "Search for High-energy Neutrinos from Binary Neutron Star Merger GW170817 with ANTARES, IceCube, and the Pierre Auger Observatory". In: *Astrophys. J. Lett.* 850.2 (2017), p. L35. DOI: 10.3847/2041-8213/aa9aed. arXiv: 1710.05839 [astro-ph.HE] (cit. on p. 25).

[144] E. Santos. "Searches for ultrahigh-energy neutrinos from gravitational wave events with the Pierre Auger Observatory". In: *J. Phys. Conf. Ser.* 1181.1 (2019). Ed. by Anatoly Lagutin, Igor Moskalenko, and Mikhail Panasyuk, p. 012060. DOI: 10.1088/1742-6596/1181/1/012060 (cit. on p. 25).

[145] Alexander Aab et al. "A Search for Ultra-high-energy Neutrinos from TXS 0506+056 Using the Pierre Auger Observatory". In: *Astrophys. J.* 902.2 (2020), p. 105. DOI: 10.3847/1538-4357/abb476. arXiv: 2010.10953 [astro-ph.HE] (cit. on p. 25).

[146] Julien Souchard. "Multi-messengers at ultra-high energies with the Pierre Auger Observatory". In: *4open* 3 (2020), p. 4. DOI: 10.1051/fopen/2020004 (cit. on p. 25).

[147] Vladimír Novotný. "Multi-messenger implications of the Pierre Auger Observatory measurements". In: *J. Phys. Conf. Ser.* 2429.1 (2023), p. 012035. DOI: 10.1088/1742-6596/2429/1/012035 (cit. on p. 25).

[148] Adila Abdul Halim et al. "Search for Ultra-high-energy Photons from Gravitational Wave Sources with the Pierre Auger Observatory". In: *Astrophys. J.* 952.1 (2023), p. 91. DOI: 10.3847/1538-4357/acc862. arXiv: 2307.10839 [astro-ph.HE] (cit. on p. 25).

[149] Alexander Aab et al. "Features of the Energy Spectrum of Cosmic Rays above 2.5×10^{18} eV Using the Pierre Auger Observatory". In: *Phys. Rev. Lett.* 125.12 (2020), p. 121106. DOI: 10.1103/PhysRevLett.125.121106. arXiv: 2008.06488 [astro-ph.HE] (cit. on pp. 26, 27).

[150] Alexander Aab et al. "Measurement of the cosmic-ray energy spectrum above 2.5×10^{18} eV using the Pierre Auger Observatory". In: *Phys. Rev. D* 102.6 (2020), p. 062005. DOI: 10.1103/PhysRevD.102.062005. arXiv: 2008.06486 [astro-ph.HE] (cit. on p. 26).

[151] D. R. Bergman et al. "The energy spectrum of ultra-high energy cosmic rays measured at the Pierre Auger Observatory and the Telescope Array". In: *EPJ Web Conf.* 283 (2023), p. 02003. DOI: 10.1051/epjconf/202328302003 (cit. on p. 27).

[152] O. Deligny. "The energy spectrum of ultra-high energy cosmic rays measured at the Pierre Auger Observatory and at the Telescope Array". In: *PoS* ICRC2019 (2020), p. 234. DOI: 10.22323/1.358.0234. arXiv: 2001.08811 [astro-ph.HE] (cit. on p. 27).

[153] Alexander Aab et al. "Depth of Maximum of Air-Shower Profiles at the Pierre Auger Observatory: Measurements at Energies above $10^{17.8}$ eV". In: *Phys. Rev. D* 90.12 (2014), p. 122005. DOI: 10.1103/PhysRevD.90.122005. arXiv: 1409.4809 [astro-ph.HE] (cit. on p. 28).

[154] Alexey Yushkov. "Mass Composition of Cosmic Rays with Energies above $10^{17.2}$ eV from the Hybrid Data of the Pierre Auger Observatory". In: *PoS* ICRC2019 (2020), p. 482. DOI: 10.22323/1.358.0482 (cit. on pp. 28, 52).

[155] Eric William Mayotte et al. "Measurement of the mass composition of ultra-high-energy cosmic rays at the Pierre Auger Observatory". In: *PoS* ICRC2023 (2023), p. 365. DOI: 10.22323/1.444.0365 (cit. on pp. 28, 92, 96, 99, 122).

[156] C. Bonifazi. "The angular resolution of the Pierre Auger Observatory". In: *Nucl. Phys. B Proc. Suppl.* 190 (2009). Ed. by R. Caruso et al., pp. 20–25. DOI: 10.1016/j.nuclphysbps.2009.03.063. arXiv: 0901.3138 [astro-ph.HE] (cit. on p. 29).

[157] Lord Rayleigh. "XII. On the resultant of a large number of vibrations of the same pitch and of arbitrary phase". In: *The London, Edinburgh, and Dublin Philosophical Magazine and Journal of Science* 10.60 (1880), pp. 73–78 (cit. on pp. 30, 188).

[158] John Linsley. "Fluctuation effects on directional data". In: *Phys. Rev. Lett.* 34 (1975), pp. 1530–1533. DOI: 10.1103/PhysRevLett.34.1530 (cit. on pp. 30, 188).

[159] M. F. Skrutskie et al. "The Two Micron All Sky Survey (2MASS)". In: *Astron. J.* 131 (2006), pp. 1163–1183. DOI: 10.1086/498708 (cit. on p. 31).

[160] Rogerio de Almeida et al. "Large-scale and multipolar anisotropies of cosmic rays detected at the Pierre Auger Observatory with energies above 4 EeV". In: *PoS* ICRC2021 (2021), p. 335. DOI: 10.22323/1.395.0335 (cit. on p. 31).

[161] Esteban Roulet. "Large-scale anisotropies above 0.03 EeV measured by the Pierre Auger Observatory". In: *PoS* ICRC2019 (2021), p. 408. DOI: 10.22323/1.358.0408 (cit. on p. 31).

[162] Pedro Abreu et al. "Arrival Directions of Cosmic Rays above 32 EeV from Phase One of the Pierre Auger Observatory". In: *Astrophys. J.* 935.2 (2022), p. 170. DOI: 10.3847/1538-4357/ac7d4e. arXiv: 2206.13492 [astro-ph.HE] (cit. on pp. 32–34, 88, 146).

[163] Arthur H. Compton and Ivan A. Getting. "An Apparent Effect of Galactic Rotation on the Intensity of Cosmic Rays". In: *Phys. Rev.* 47.11 (1935), p. 817. DOI: 10.1103/PhysRev.47.817 (cit. on p. 33).

[164] M. Kachelriess and Pasquale Dario Serpico. "The Compton-Getting effect on ultra-high energy cosmic rays of cosmological origin". In: *Phys. Lett. B* 640 (2006), pp. 225–229. DOI: 10.1016/j.physletb.2006.08.006. arXiv: astro-ph/0605462 (cit. on p. 33).

[165] D. Harari, S. Mollerach, and E. Roulet. "Effects of the galactic magnetic field upon large scale anisotropies of extragalactic Cosmic Rays". In: *JCAP* 11 (2010), p. 033. DOI: 10.1088/1475-7516/2010/11/033. arXiv: 1009.5891 [astro-ph.HE] (cit. on p. 33).

[166] A. di Matteo et al. "2022 report from the Auger-TA working group on UHECR arrival directions". In: *EPJ Web Conf.* 283 (2023), p. 03002. DOI: 10.1051/epjconf/202328303002. arXiv: 2302.04502 [astro-ph.HE] (cit. on p. 33).

[167] Adila Abdul Halim et al. "Update on the searches for anisotropies in UHECR arrival directions with the Pierre Auger Observatory and the Telescope Array". In: *PoS* ICRC2023 (2023), p. 521. DOI: 10.22323/1.444.0521 (cit. on pp. 33, 88, 106, 146).

[168] T. -P. Li and Y. -Q. Ma. "Analysis methods for results in gamma-ray astronomy". In: *Astrophys. J.* 272 (1983), pp. 317–324. DOI: 10.1086/161295 (cit. on p. 33).

[169] Pedro Abreu et al. "Cosmological implications of photon-flux upper limits at ultrahigh energies in scenarios of Planckian-interacting massive particles for dark matter". In: *Phys. Rev. D* 107.4 (2023), p. 042002. DOI: 10.1103/PhysRevD.107.042002. arXiv: 2208.02353 [astro-ph.HE] (cit. on p. 36).

[170] Nazar R. Ikhsanov and P. L. Biermann. "High-energy emission of fast rotating white dwarfs". In: *Astron. Astrophys.* 445 (2006), p. 305. DOI: 10.1051/0004-6361:20053179. arXiv: astro-ph/0509070 (cit. on p. 36).

[171] Rafael Alves Batista and Joseph Silk. "Ultrahigh-energy cosmic rays from tidally-ignited white dwarfs". In: *Phys. Rev. D* 96.10 (2017), p. 103003. DOI: 10.1103/PhysRevD.96.103003. arXiv: 1702.06978 [astro-ph.HE] (cit. on pp. 36, 42).

[172] Pasquale Blasi, Richard I. Epstein, and Angela V. Olinto. "Ultrahigh-energy cosmic rays from young neutron star winds". In: *Astrophys. J. Lett.* 533 (2000), p. L123. DOI: 10.1086/312626. arXiv: astro-ph/9912240 (cit. on pp. 36, 42).

[173] Kumiko Kotera. "Ultrahigh energy cosmic ray acceleration in newly born magnetars and their associated gravitational wave signatures". In: *Phys. Rev. D* 84 (2011), p. 023002. DOI: 10.1103/PhysRevD.84.023002. arXiv: 1106.3060 [astro-ph.HE] (cit. on pp. 36, 111).

[174] Ke Fang, Kumiko Kotera, and Angela V. Olinto. "Newly-born pulsars as sources of ultrahigh energy cosmic rays". In: *Astrophys. J.* 750 (2012), p. 118. DOI: 10.1088/0004-637X/750/2/118. arXiv: 1201.5197 [astro-ph.HE] (cit. on pp. 36, 42).

[175] Ke Fang, Kumiko Kotera, and Angela V. Olinto. "Ultrahigh Energy Cosmic Ray Nuclei from Extragalactic Pulsars and the effect of their Galactic counterparts". In: *JCAP* 03 (2013), p. 010. DOI: 10.1088/1475-7516/2013/03/010. arXiv: 1302.4482 [astro-ph.HE] (cit. on pp. 36, 42).

[176] T. Stanev. "Propagation of ultra high energy cosmic rays". In: *Comptes Rendus Physique* 5 (2004), pp. 453–461. DOI: 10.1016/j.crhy.2004.03.014 (cit. on pp. 36, 50).

[177] Thomas K. Gaisser, Ralph Engel, and Elisa Resconi. *Cosmic Rays and Particle Physics: 2nd Edition*. Cambridge University Press, June 2016. ISBN: 978-0-521-01646-9 (cit. on pp. 36, 46, 191).

[178] Enrico Fermi. "On the Origin of the Cosmic Radiation". In: *Phys. Rev.* 75 (1949), pp. 1169–1174. DOI: 10.1103/PhysRev.75.1169 (cit. on p. 37).

[179] E. Fermi. "Galactic Magnetic Fields and the Origin of Cosmic Radiation." In: *Astrophys. J.* 119 (1954), pp. 1–6. DOI: 10.1086/145789 (cit. on p. 39).

[180] Abraham Achterberg et al. "Particle acceleration by ultrarelativistic shocks: Theory and simulations". In: *Mon. Not. Roy. Astron. Soc.* 328 (2001), p. 393. DOI: 10.1046/j.1365-8711.2001.04851.x. arXiv: astro-ph/0107530 (cit. on p. 39).

[181] A. M. Hillas. "The Origin of Ultrahigh-Energy Cosmic Rays". In: *Ann. Rev. Astron. Astrophys.* 22 (1984), pp. 425–444. DOI: 10.1146/annurev.aa.22.090184.002233 (cit. on p. 39).

[182] P. O. Lagage and C. J. Cesarsky. "The maximum energy of cosmic rays accelerated by supernova shocks". In: *Astron. Astrophys.* 125 (1983), pp. 249–257 (cit. on p. 40).

[183] Glennys R. Farrar and Andrei Gruzinov. "Giant AGN Flares and Cosmic Ray Bursts". In: *Astrophys. J.* 693 (2009), pp. 329–332. DOI: 10.1088/0004-637X/693/1/329. arXiv: 0802.1074 [astro-ph] (cit. on pp. 40, 42).

[184] Glennys R. Farrar. "Binary Neutron Star Mergers as the Source of the Highest Energy Cosmic Rays". In: *Phys. Rev. Lett.* 134.8 (2025), p. 081003. DOI: 10.1103/PhysRevLett.134.081003. arXiv: 2405.12004 [astro-ph.HE] (cit. on pp. 40, 41, 111).

[185] Robert Antonucci. "Unified models for active galactic nuclei and quasars". In: *Ann. Rev. Astron. Astrophys.* 31 (1993), pp. 473–521. DOI: 10.1146/annurev.aa.31.090193.002353 (cit. on p. 41).

[186] J. Abraham et al. "Correlation of the highest energy cosmic rays with nearby extragalactic objects". In: *Science* 318 (2007), pp. 938–943. DOI: 10.1126/science.1151124. arXiv: 0711.2256 [astro-ph] (cit. on p. 41).

[187] Frank M. Rieger, Valenti Bosch-Ramon, and Peter Duffy. "Fermi acceleration in astrophysical jets". In: *Astrophys. Space Sci.* 309 (2007), pp. 119–125. DOI: 10.1007/s10509-007-9466-z. arXiv: astro-ph/0610141 (cit. on p. 41).

[188] Damiano Caprioli. ""Espresso" Acceleration of Ultra-high-energy Cosmic Rays". In: *Astrophys. J. Lett.* 811.2 (2015), p. L38. DOI: 10.1088/2041-8205/811/2/L38. arXiv: 1505.06739 [astro-ph.HE] (cit. on p. 41).

[189] Elisa Resconi et al. "Connecting blazars with ultrahigh-energy cosmic rays and astrophysical neutrinos". In: *Mon. Not. Roy. Astron. Soc.* 468.1 (2017), pp. 597–606. DOI: 10.1093/mnras/stx498. arXiv: 1611.06022 [astro-ph.HE] (cit. on p. 41).

[190] Björn Eichmann et al. "Ultra-High-Energy Cosmic Rays from Radio Galaxies". In: *JCAP* 02 (2018), p. 036. DOI: 10.1088/1475-7516/2018/02/036. arXiv: 1701.06792 [astro-ph.HE] (cit. on p. 41).

[191] Rostom Mbarek and Damiano Caprioli. "Espresso and Stochastic Acceleration of Ultra-high-energy Cosmic Rays in Relativistic Jets". In: *Astrophys. J.* 921.1 (2021), p. 85. DOI: 10.3847/1538-4357/ac1da8. arXiv: 2105.05262 [astro-ph.HE] (cit. on p. 41).

[192] M. G. Aartsen et al. "Multimessenger observations of a flaring blazar coincident with high-energy neutrino IceCube-170922A". In: *Science* 361.6398 (2018), eaat1378. DOI: 10.1126/science.aat1378. arXiv: 1807.08816 [astro-ph.HE] (cit. on pp. 41, 110).

[193] Yu Gao and Philip M. Solomon. "The Star formation rate and dense molecular gas in galaxies". In: *Astrophys. J.* 606 (2004), pp. 271–290. DOI: 10.1086/382999. arXiv: astro-ph/0310339 (cit. on p. 41).

[194] G. H. Rieke et al. "Determining Star Formation Rates for Infrared Galaxies". In: *Astrophys. J.* 692 (2009), pp. 556–573. DOI: 10.1088/0004-637X/692/1/556. arXiv: 0810.4150 [astro-ph] (cit. on p. 41).

[195] Antonio Condorelli et al. "Starburst Galaxies as possible sources of UHECRs and neutrinos". In: *PoS* ICRC2021 (2021), p. 959. DOI: 10.22323/1.395.0959 (cit. on p. 41).

[196] Antonio Condorelli et al. "Testing hadronic and photohadronic interactions as responsible for ultrahigh energy cosmic rays and neutrino fluxes from starburst galaxies". In: *Phys. Rev. D* 107.8 (2023), p. 083009. DOI: 10.1103/PhysRevD.107.083009. arXiv: 2209.08593 [astro-ph.HE] (cit. on pp. 41, 92).

[197] L. A. Anchordoqui, G. E. Romero, and J. A. Combi. "Heavy nuclei at the end of the cosmic ray spectrum?" In: *Phys. Rev. D* 60 (1999), p. 103001. DOI: 10.1103/PhysRevD.60.103001. arXiv: astro-ph/9903145 (cit. on p. 41).

[198] Luis Alfredo Anchordoqui. "Acceleration of ultrahigh-energy cosmic rays in starburst superwinds". In: *Phys. Rev. D* 97.6 (2018), p. 063010. DOI: 10.1103/PhysRevD.97.063010. arXiv: 1801.07170 [astro-ph.HE] (cit. on p. 41).

[199] Enrico Peretti et al. "Particle acceleration and multimessenger emission from starburst-driven galactic winds". In: *Mon. Not. Roy. Astron. Soc.* 511.1 (2022), pp. 1336–1348. DOI: 10.1093/mnras/stac084. arXiv: 2104.10978 [astro-ph.HE] (cit. on p. 41).

[200] Eli Waxman. "Cosmological gamma-ray bursts and the highest energy cosmic rays". In: *Phys. Rev. Lett.* 75 (1995), pp. 386–389. DOI: 10.1103/PhysRevLett.75.386. arXiv: astro-ph/9505082 (cit. on p. 41).

[201] Mario Vietri. "On the acceleration of ultrahigh-energy cosmic rays in gamma-ray bursts". In: *Astrophys. J.* 453 (1995), pp. 883–889. DOI: 10.1086/176448. arXiv: astro-ph/9506081 (cit. on p. 41).

[202] Kohta Murase et al. "High-energy cosmic-ray nuclei from high- and low-luminosity gamma-ray bursts and implications for multi-messenger astronomy". In: *Phys. Rev. D* 78 (2008), p. 023005. DOI: 10.1103/PhysRevD.78.023005. arXiv: 0801.2861 [astro-ph] (cit. on p. 41).

[203] B. Theodore Zhang et al. "Low-luminosity gamma-ray bursts as the sources of ultrahigh-energy cosmic ray nuclei". In: *Phys. Rev. D* 97.8 (2018), p. 083010. DOI: 10.1103/PhysRevD.97.083010. arXiv: 1712.09984 [astro-ph.HE] (cit. on p. 41).

[204] Daniel Biehl et al. "Cosmic-Ray and Neutrino Emission from Gamma-Ray Bursts with a Nuclear Cascade". In: *Astron. Astrophys.* 611 (2018), A101. DOI: 10.1051/0004-6361/201731337. arXiv: 1705.08909 [astro-ph.HE] (cit. on pp. 41, 124).

[205] Noemie Globus et al. "UHECR acceleration at GRB internal shocks". In: *Mon. Not. Roy. Astron. Soc.* 451.1 (2015), pp. 751–790. DOI: 10.1093/mnras/stv893. arXiv: 1409.1271 [astro-ph.HE] (cit. on p. 41).

[206] Denise Boncioli, Daniel Biehl, and Walter Winter. "On the common origin of cosmic rays across the ankle and diffuse neutrinos at the highest energies from low-luminosity Gamma-Ray Bursts". In: *Astrophys. J.* 872.1 (2019), p. 110. DOI: 10.3847/1538-4357/aafda7. arXiv: 1808.07481 [astro-ph.HE] (cit. on pp. 41, 124).

[207] Kumiko Kotera and Angela V. Olinto. "The Astrophysics of Ultrahigh Energy Cosmic Rays". In: *Ann. Rev. Astron. Astrophys.* 49 (2011), pp. 119–153. DOI: 10.1146/annurev-astro-081710-102620. arXiv: 1101.4256 [astro-ph.HE] (cit. on p. 42).

[208] Kohta Murase, Susumu Inoue, and Shigehiro Nagataki. "Cosmic Rays Above the Second Knee from Clusters of Galaxies and Associated High-Energy Neutrino Emission". In: *Astrophys. J. Lett.* 689 (2008), p. L105. DOI: 10.1086/595882. arXiv: 0805.0104 [astro-ph] (cit. on p. 42).

[209] K. Kotera et al. "Propagation of ultrahigh energy nuclei in clusters of galaxies: resulting composition and secondary emissions". In: *Astrophys. J.* 707 (2009), pp. 370–386. DOI: 10.1088/0004-637X/707/1/370. arXiv: 0907.2433 [astro-ph.HE] (cit. on p. 42).

[210] Martin J. Rees. "Tidal disruption of stars by black holes of 10 to the 6th-10 to the 8th solar masses in nearby galaxies". In: *Nature* 333 (1988), pp. 523–528. DOI: 10.1038/333523a0 (cit. on p. 42).

[211] Glennys R. Farrar and Tsvi Piran. "Tidal disruption jets as the source of Ultra-High Energy Cosmic Rays". In: (Nov. 2014). arXiv: 1411.0704 [astro-ph.HE] (cit. on p. 42).

[212] Claire Guépin et al. "Ultra-High Energy Cosmic Rays and Neutrinos from Tidal Disruptions by Massive Black Holes". In: *Astron. Astrophys.* 616 (2018). [Erratum: Astron.Astrophys. 636, C3 (2020)], A179. DOI: 10.1051/0004-6361/201732392. arXiv: 1711.11274 [astro-ph.HE] (cit. on p. 42).

[213] Daniel Biehl et al. "Tidally disrupted stars as a possible origin of both cosmic rays and neutrinos at the highest energies". In: *Sci. Rep.* 8.1 (2018), p. 10828. DOI: 10.1038/s41598-018-29022-4. arXiv: 1711.03555 [astro-ph.HE] (cit. on p. 42).

[214] Robert Stein et al. "A tidal disruption event coincident with a high-energy neutrino". In: *Nature Astron.* 5.5 (2021), pp. 510–518. DOI: 10.1038/s41550-020-01295-8. arXiv: 2005.05340 [astro-ph.HE] (cit. on pp. 42, 111).

[215] Simeon Reusch et al. "Candidate Tidal Disruption Event AT2019fdr Coincident with a High-Energy Neutrino". In: *Phys. Rev. Lett.* 128.22 (2022), p. 221101. DOI: 10.1103/PhysRevLett.128.221101. arXiv: 2111.09390 [astro-ph.HE] (cit. on pp. 42, 111).

[216] Kumiko Kotera, Elena Amato, and Pasquale Blasi. "The fate of ultrahigh energy nuclei in the immediate environment of young fast-rotating pulsars". In: *JCAP* 08 (2015), p. 026. DOI: 10.1088/1475-7516/2015/08/026. arXiv: 1503.07907 [astro-ph.HE] (cit. on pp. 42, 111).

[217] Alexander Friedman. "Über die krümmung des raumes". In: *Zeitschrift für Physik* 10.1 (1922), pp. 377–386 (cit. on pp. 42, 43).

[218] Georges Lemaitre. "A Homogeneous Universe of Constant Mass and Increasing Radius accounting for the Radial Velocity of Extra-galactic Nebulæ". In: *Mon. Not. Roy. Astron. Soc.* 91.5 (1931), pp. 483–490. DOI: 10.1093/mnras/91.5.483 (cit. on p. 42).

[219] H. P. Robertson. "Kinematics and World-Structure". In: *Astrophys. J.* 82 (1935), pp. 284–301. DOI: 10.1086/143681 (cit. on p. 42).

[220] A. G. Walker. "On Milne's Theory of World-Structure". In: *Proc. Lond. Math. Soc. s* 2-42.1 (1937), pp. 90–127. DOI: 10.1112/plms/s2-42.1.90 (cit. on p. 42).

[221] Edwin Hubble. "A relation between distance and radial velocity among extra-galactic nebulae". In: *Proc. Nat. Acad. Sci.* 15 (1929), pp. 168–173. DOI: 10.1073/pnas.15.3.168 (cit. on p. 43).

[222] Christian Doppler. *Ueber das farbridge Lict der Doppelsterne und einiger anderer Gestirne des Himmels: versuch einer das Bradley'sche aberrations-theorem als integrirrenden Theil in sich schliessenden allgemeineren Theorie*. K. Böhm Gesellschaft der Wissenschaften, 1903 (cit. on p. 43).

[223] Alexander Friedmann. "Über die Möglichkeit einer Welt mit konstanter negativer Krümmung des Raumes". In: *Zeitschrift für Physik* 21.1 (1924), pp. 326–332 (cit. on p. 43).

[224] R. H. Dicke et al. "Cosmic Black-Body Radiation". In: *Astrophys. J.* 142 (1965), pp. 414–419. DOI: 10.1086/148306 (cit. on p. 46).

[225] Tanja M. Kneiske et al. "Implications of cosmological gamma-ray absorption. 2. Modification of gamma-ray spectra". In: *Astron. Astrophys.* 413 (2004), pp. 807–815. DOI: 10.1051/0004-6361:20031542. arXiv: astro-ph/0309141 (cit. on pp. 47, 48, 65, 67).

[226] Floyd W. Stecker, M. A. Malkan, and S. T. Scully. "Intergalactic photon spectra from the far ir to the uv lyman limit for $0 < Z < 6$ and the optical depth of the universe to high energy gamma-rays". In: *Astrophys. J.* 648 (2006), pp. 774–783. DOI: 10.1086/506188. arXiv: astro-ph/0510449 (cit. on pp. 47, 48, 65, 67, 121).

[227] Alberto Franceschini, Giulia Rodighiero, and Mattia Vaccari. "The extragalactic optical-infrared background radiations, their time evolution and the cosmic photon-photon opacity". In: *Astron. Astrophys.* 487 (2008), p. 837. DOI: 10.1051/0004-6361:200809691. arXiv: 0805.1841 [astro-ph] (cit. on pp. 47, 48, 54, 67, 137).

[228] Justin D. Finke, Soebur Razzaque, and Charles D. Dermer. "Modeling the Extragalactic Background Light from Stars and Dust". In: *Astrophys. J.* 712 (2010), pp. 238–249. DOI: 10.1088/0004-637X/712/1/238. arXiv: 0905.1115 [astro-ph.HE] (cit. on pp. 47, 48, 67).

[229] A. Dominguez et al. "Extragalactic Background Light Inferred from AEGIS Galaxy SED-type Fractions". In: *Mon. Not. Roy. Astron. Soc.* 410 (2011), p. 2556. DOI: 10.1111/j.1365-2966.2010.17631.x. arXiv: 1007.1459 [astro-ph.CO] (cit. on pp. 47, 48, 51, 52, 65, 67).

[230] R. C. Gilmore et al. "Semi-analytic modeling of the EBL and consequences for extragalactic gamma-ray spectra". In: *Mon. Not. Roy. Astron. Soc.* 422 (2012), p. 3189. DOI: 10.1111/j.1365-2966.2012.20841.x. arXiv: 1104.0671 [astro-ph.CO] (cit. on pp. 47, 48, 65, 67, 94).

[231] Floyd W. Stecker, Sean T. Scully, and Matthew A. Malkan. "An Empirical Determination of the Intergalactic Background Light from UV to FIR Wavelengths Using FIR Deep Galaxy Surveys and the Gamma-ray Opacity of the Universe". In: *Astrophys. J.* 827.1 (2016). [Erratum: Astrophys.J. 863, 112 (2018)], p. 6. DOI: 10.3847/0004-637X/827/1/6. arXiv: 1605.01382 [astro-ph.HE] (cit. on pp. 47, 48, 67).

[232] Alberto Saldana-Lopez et al. "An observational determination of the evolving extragalactic background light from the multiwavelength HST/CANDELS survey in the Fermi and CTA era". In: *Mon. Not. Roy. Astron. Soc.* 507.4 (2021), pp. 5144–5160. DOI: 10.1093/mnras/stab2393. arXiv: 2012.03035 [astro-ph.CO] (cit. on pp. 47, 48, 67).

[233] R. J. Protheroe and P. L. Biermann. "A New estimate of the extragalactic radio background and implications for ultrahigh-energy gamma-ray propagation". In: *Astropart. Phys.* 6 (1996). [Erratum: Astropart.Phys. 7, 181 (1997)], pp. 45–54. DOI: 10.1016/S0927-6505(96)00041-2. arXiv: astro-ph/9605119 (cit. on pp. 47, 48, 67).

[234] D. J. Fixsen et al. "ARCADE 2 Measurement of the Extra-Galactic Sky Temperature at 3-90 GHz". In: *Astrophys. J.* 734 (2011), p. 5. DOI: 10.1088/0004-637X/734/1/5. arXiv: 0901.0555 [astro-ph.CO] (cit. on pp. 47, 48, 67).

[235] I. C. Niţu et al. "An updated estimate of the cosmic radio background and implications for ultra-high-energy photon propagation". In: *Astropart. Phys.* 126 (2021), p. 102532. DOI: 10.1016/j.astropartphys.2020.102532. arXiv: 2004.13596 [astro-ph.HE] (cit. on pp. 47, 48, 67).

[236] Rafael Alves Batista et al. "CRPropa 3.2 — an advanced framework for high-energy particle propagation in extragalactic and galactic spaces". In: *JCAP* 09 (2022), p. 035. DOI: 10.1088/1475-7516/2022/09/035. arXiv: 2208.00107 [astro-ph.HE] (cit. on pp. 47, 51, 54, 63, 65, 66, 94, 144, 145, 194).

[237] Leonel Morejon et al. "Propagation of Ultra High-Energy Cosmic Rays in light of the latest EBL constraints". In: *PoS* ICRC2023 (2023), p. 283. DOI: 10.22323/1.444.0283 (cit. on p. 48).

[238] H. Bethe and W. Heitler. "On the Stopping of fast particles and on the creation of positive electrons". In: *Proc. Roy. Soc. Lond. A* 146 (1934), pp. 83–112. DOI: 10.1098/rspa.1934.0140 (cit. on p. 48).

[239] G. R. Blumenthal. "Energy loss of high-energy cosmic rays in pair-producing collisions with ambient photons". In: *Phys. Rev. D* 1 (1970), pp. 1596–1602. DOI: 10.1103/PhysRevD.1.1596 (cit. on pp. 48, 49, 57).

[240] R. Aloisio, V. Berezinsky, and S. Grigorieva. "Analytic calculations of the spectra of ultra high energy cosmic ray nuclei. II. The general case of background radiation". In: *Astropart. Phys.* 41 (2013), pp. 94–107. DOI: 10.1016/j.astropartphys.2012.06.003. arXiv: 1006.2484 [astro-ph.CO] (cit. on pp. 49, 52, 194).

[241] V. Berezinsky, A. Z. Gazizov, and S. I. Grigorieva. "On astrophysical solution to ultrahigh-energy cosmic rays". In: *Phys. Rev. D* 74 (2006), p. 043005. DOI: 10.1103/PhysRevD.74.043005. arXiv: hep-ph/0204357 (cit. on pp. 49, 52, 193).

[242] Markus Ahlers. "Neutrino Sources from a Multi-Messenger Perspective". In: *EPJ Web Conf.* 209 (2019). Ed. by M. De Vincenzi, A. Capone, and A. Morselli, p. 01013. DOI: 10.1051/epjconf/201920901013. arXiv: 1811.07633 [astro-ph.HE] (cit. on p. 49).

[243] A. Mucke et al. "SOPHIA: Monte Carlo simulations of photohadronic processes in astrophysics". In: *Comput. Phys. Commun.* 124 (2000), pp. 290–314. DOI: 10.1016/S0010-4655(99)00446-4. arXiv: astro-ph/9903478 (cit. on pp. 50, 65).

[244] J. L. Puget, F. W. Stecker, and J. H. Bredekamp. "Photonuclear Interactions of Ultrahigh-Energy Cosmic Rays and their Astrophysical Consequences". In: *Astrophys. J.* 205 (1976), pp. 638–654. DOI: 10.1086/154321 (cit. on pp. 50, 65, 116).

[245] Denise Boncioli, Anatoli Fedynitch, and Walter Winter. "Nuclear Physics Meets the Sources of the Ultra-High Energy Cosmic Rays". In: *Sci. Rep.* 7.1 (2017), p. 4882. DOI: 10.1038/s41598-017-05120-7. arXiv: 1607.07989 [astro-ph.HE] (cit. on p. 50).

[246] M. Goldhaber and E. Teller. "On nuclear dipole vibrations". In: *Phys. Rev.* 74 (1948), pp. 1046–1049. DOI: 10.1103/PhysRev.74.1046 (cit. on p. 50).

[247] J. S. Levinger. "The High-energy nuclear photoeffect". In: *Phys. Rev.* 84 (1951), pp. 43–51. DOI: 10.1103/PhysRev.84.43 (cit. on p. 50).

[248] V. S. Berezinsky and S. I. Grigor'eva. "A Bump in the ultrahigh-energy cosmic ray spectrum". In: *Astron. Astrophys.* 199 (1988), pp. 1–12 (cit. on pp. 52, 193).

[249] Jonas Heinze et al. "Cosmogenic Neutrinos Challenge the Cosmic Ray Proton Dip Model". In: *Astrophys. J.* 825.2 (2016), p. 122. DOI: 10.3847/0004-637X/825/2/122. arXiv: 1512.05988 [astro-ph.HE] (cit. on p. 52).

[250] R. Aloisio, V. Berezinsky, and S. Grigorieva. "Analytic calculations of the spectra of ultra-high energy cosmic ray nuclei. I. The case of CMB radiation". In: *Astropart. Phys.* 41 (2013), pp. 73–93. DOI: 10.1016/j.astropartphys.2012.07.010. arXiv: 0802.4452 [astro-ph] (cit. on pp. 52, 194).

[251] R. Aloisio, V. Berezinsky, and P. Blasi. "Ultra high energy cosmic rays: implications of Auger data for source spectra and chemical composition". In: *JCAP* 10 (2014), p. 020. DOI: 10.1088/1475-7516/2014/10/020. arXiv: 1312.7459 [astro-ph.HE] (cit. on p. 53).

[252] Noemie Globus, Denis Allard, and Etienne Parizot. "A complete model of the cosmic ray spectrum and composition across the Galactic to extragalactic transition". In: *Phys. Rev. D* 92.2 (2015), p. 021302. DOI: 10.1103/PhysRevD.92.021302. arXiv: 1505.01377 [astro-ph.HE] (cit. on p. 53).

[253] Roberto Aloisio and Veniamin Berezinsky. "Towards solving the mass-composition problem in ultra high energy cosmic rays". In: *J. Exp. Theor. Phys.* 128.1 (2019), pp. 52–63. DOI: 10.1134/S1063776118120014. arXiv: 1703.08671 [astro-ph.HE] (cit. on p. 53).

[254] A. Abdul Halim et al. "Constraining the sources of ultra-high-energy cosmic rays across and above the ankle with the spectrum and composition data measured at the Pierre Auger Observatory". In: *JCAP* 05 (2023), p. 024. DOI: 10.1088/1475-7516/2023/05/024. arXiv: 2211.02857 [astro-ph.HE] (cit. on pp. 53, 95, 98).

[255] G. Breit and John A. Wheeler. "Collision of two light quanta". In: *Phys. Rev.* 46.12 (1934), pp. 1087–1091. DOI: 10.1103/PhysRev.46.1087 (cit. on p. 53).

[256] Sangjin Lee. "On the propagation of extragalactic high-energy cosmic and gamma-rays". In: *Phys. Rev. D* 58 (1998), p. 043004. DOI: 10.1103/PhysRevD.58.043004. arXiv: astro-ph/9604098 (cit. on pp. 53–55, 57).

[257] O. Klein and Y. Nishina. "Über die Streuung von Strahlung durch freie Elektronen nach der neuen relativistischen Quantendynamik von Dirac". In: *Z. Phys.* 52.11 (1929), pp. 853–868. DOI: 10.1007/BF01366453 (cit. on p. 54).

[258] Arthur H. Compton. "A Quantum Theory of the Scattering of X-rays by Light Elements". In: *Phys. Rev.* 21 (1923), pp. 483–502. DOI: 10.1103/PhysRev.21.483 (cit. on p. 54).

[259] G. R. Blumenthal and R. J. Gould. "Bremsstrahlung, synchrotron radiation, and compton scattering of high-energy electrons traversing dilute gases". In: *Rev. Mod. Phys.* 42 (1970), pp. 237–270. DOI: 10.1103/RevModPhys.42.237 (cit. on pp. 55, 57).

[260] John David Jackson. *Classical Electrodynamics*. 3rd. New York: Wiley, 1999. ISBN: 978-0-471-30932-1 (cit. on p. 55).

[261] R. Aloisio and Veniamin Berezinsky. "Diffusive propagation of UHECR and the propagation theorem". In: *Astrophys. J.* 612 (2004), pp. 900–913. DOI: 10.1086/421869. arXiv: astro-ph/0403095 (cit. on p. 56).

[262] Martin Lemoine. "Extra-galactic magnetic fields and the second knee in the cosmic-ray spectrum". In: *Phys. Rev. D* 71 (2005), p. 083007. DOI: 10.1103/PhysRevD.71.083007. arXiv: astro-ph/0411173 (cit. on p. 56).

[263] Silvia Mollerach and Esteban Roulet. "Magnetic diffusion effects on the ultra-high energy cosmic ray spectrum and composition". In: *JCAP* 10 (2013), p. 013. DOI: 10.1088/1475-7516/2013/10/013. arXiv: 1305.6519 [astro-ph.HE] (cit. on p. 56).

[264] Silvia Mollerach and Esteban Roulet. "Ultrahigh energy cosmic rays from a nearby extragalactic source in the diffusive regime". In: *Phys. Rev. D* 99.10 (2019), p. 103010. DOI: 10.1103/PhysRevD.99.103010. arXiv: 1903.05722 [astro-ph.HE] (cit. on p. 56).

[265] Juan Manuel González, Silvia Mollerach, and Esteban Roulet. "Magnetic diffusion and interaction effects on ultrahigh energy cosmic rays: Protons and nuclei". In: *Phys. Rev. D* 104.6 (2021), p. 063005. DOI: 10.1103/PhysRevD.104.063005. arXiv: 2105.08138 [astro-ph.HE] (cit. on pp. 56, 57).

[266] Eli Waxman and Jordi Miralda-Escude. "Images of bursting sources of high-energy cosmic rays. 1. Effects of magnetic fields". In: *Astrophys. J. Lett.* 472 (1996), pp. L89–L92. DOI: 10.1086/310367. arXiv: astro-ph/9607059 (cit. on p. 56).

[267] Eli Waxman and Paolo Coppi. "Delayed Gev - TeV photons from gamma-ray bursts producing high-energy cosmic rays". In: *Astrophys. J. Lett.* 464 (1996), pp. L75–L78. DOI: 10.1086/310090. arXiv: astro-ph/9603144 (cit. on p. 57).

[268] R. J. Protheroe and P. A. Johnson. "Propagation of ultrahigh-energy protons over cosmological distances and implications for topological defect models". In: *Astropart. Phys.* 4 (1996), p. 253. DOI: 10.1016/0927-6505(95)00039-9. arXiv: astro-ph/9506119 (cit. on p. 57).

[269] A. Neronov and I. Vovk. "Evidence for strong extragalactic magnetic fields from Fermi observations of TeV blazars". In: *Science* 328 (2010), pp. 73–75. DOI: 10.1126/science.1184192. arXiv: 1006.3504 [astro-ph.HE] (cit. on pp. 58, 134, 137).

[270] Rafael Alves Batista and Andrey Saveliev. "Multimessenger Constraints on Intergalactic Magnetic Fields from the Flare of TXS 0506+056". In: *Astrophys. J. Lett.* 902.1 (2020), p. L11. DOI: 10.3847/2041-8213/abb816. arXiv: 2009.12161 [astro-ph.HE] (cit. on p. 58).

[271] Ie. Vovk et al. "Constraints on the intergalactic magnetic field from Fermi/LAT observations of the 'pair echo' of GRB 221009A". In: *Astron. Astrophys.* 683 (2024), A25. DOI: 10.1051/0004-6361/202347310. arXiv: 2306.07672 [astro-ph.HE] (cit. on pp. 58, 134, 148).

[272] F. Aharonian et al. "Constraints on the Intergalactic Magnetic Field Using Fermi-LAT and H.E.S.S. Blazar Observations". In: *Astrophys. J. Lett.* 950.2 (2023), p. L16. DOI: 10.3847/2041-8213/acd777. arXiv: 2306.05132 [astro-ph.HE] (cit. on pp. 58, 134, 148).

[273] P. A. R. Ade et al. "Planck 2015 results. XIX. Constraints on primordial magnetic fields". In: *Astron. Astrophys.* 594 (2016), A19. DOI: 10.1051/0004-6361/201525821. arXiv: 1502.01594 [astro-ph.CO] (cit. on p. 58).

[274] Karsten Jedamzik and Andrey Saveliev. "Stringent Limit on Primordial Magnetic Fields from the Cosmic Microwave Background Radiation". In: *Phys. Rev. Lett.* 123.2 (2019), p. 021301. DOI: 10.1103/PhysRevLett.123.021301. arXiv: 1804.06115 [astro-ph.CO] (cit. on p. 58).

[275] A. Bonafede et al. "The Coma cluster magnetic field from Faraday rotation measures". In: *Astron. Astrophys.* 513 (2010), A30. DOI: 10.1051/0004-6361/200913696. arXiv: 1002.0594 [astro-ph.CO] (cit. on p. 58).

[276] Jacques P. Vallee. "Magnetic fields in the galactic Universe, as observed in supershells, galaxies, intergalactic and cosmic realms". In: *New Astron. Rev.* 55 (2011), pp. 91–154. DOI: 10.1016/j.newar.2011.01.002 (cit. on p. 58).

[277] Luigina Feretti et al. "Clusters of galaxies: observational properties of the diffuse radio emission". In: *Astron. Astrophys. Rev.* 20 (2012), p. 54. DOI: 10.1007/s00159-012-0054-z. arXiv: 1205.1919 [astro-ph.CO] (cit. on p. 58).

[278] Franco Vazza et al. "Magnetogenesis and the Cosmic Web: A Joint Challenge for Radio Observations and Numerical Simulations". In: *Galaxies* 9.4 (2021), p. 109. DOI: 10.3390/galaxies9040109. arXiv: 2111.09129 [astro-ph.CO] (cit. on p. 58).

[279] Nicola Locatelli et al. "New constraints on the magnetic field in cosmic web filaments". In: *Astron. Astrophys.* 652 (2021), A80. DOI: 10.1051/0004-6361/202140526. arXiv: 2101.06051 [astro-ph.CO] (cit. on p. 58).

[280] Tessa Vernstrom et al. "Discovery of magnetic fields along stacked cosmic filaments as revealed by radio and X-ray emission". In: *Mon. Not. Roy. Astron. Soc.* 505.3 (2021), pp. 4178–4196. DOI: 10.1093/mnras/stab1301. arXiv: 2101.09331 [astro-ph.CO] (cit. on p. 58).

[281] Tess R. Jaffe. "Practical Modeling of Large-Scale Galactic Magnetic Fields: Status and Prospects". In: *Galaxies* 7.2 (2019), p. 52. DOI: 10.3390/galaxies7020052. arXiv: 1904.12689 [astro-ph.GA] (cit. on p. 59).

[282] George E. Hale. "On the probable existence of a magnetic field in sun-spots". In: *Terrestrial Magnetism and Atmospheric Electricity* 13.4 (1908), pp. 159–160. DOI: https://doi.org/10.1029/TE013i004p00159. eprint: https://agupubs.onlinelibrary.wiley.com/doi/pdf/10.1029/TE013i004p00159. URL: https://agupubs.onlinelibrary.wiley.com/doi/abs/10.1029/TE013i004p00159 (cit. on p. 59).

[283] G. L. Verschuur. "Positive Determination of an Interstellar Magnetic Field by Measurement of the Zeeman Splitting of the 21-cm Hydrogen Line". In: *Phys. Rev. Lett.* 21 (11 1968), pp. 775–778. DOI: 10.1103/PhysRevLett.21.775. URL: https://link.aps.org/doi/10.1103/PhysRevLett.21.775 (cit. on p. 59).

[284] P. Zeeman and. "XXXII. On the influence of magnetism on the nature of the light emitted by a substance". In: *The London, Edinburgh, and Dublin Philosophical Magazine and Journal of Science* 43.262 (1897), pp. 226–239. DOI: 10.1080/14786449708620985. eprint: https://doi.org/10.1080/14786449708620985. URL: https://doi.org/10.1080/14786449708620985 (cit. on p. 59).

[285] Alexander Korochkin, Dmitri Semikoz, and Peter Tinyakov. "UHECR deflections in the Galactic magnetic field". In: (Jan. 2025). arXiv: 2501.16158 [astro-ph.HE] (cit. on pp. 60, 89).

[286] Ronnie Jansson and Glennys R. Farrar. "A New Model of the Galactic Magnetic Field". In: *Astrophys. J.* 757 (2012), p. 14. DOI: 10.1088/0004-637X/757/1/14. arXiv: 1204.3662 [astro-ph.GA] (cit. on pp. 60, 67, 89).

[287] Ronnie Jansson and Glennys R. Farrar. "The Galactic Magnetic Field". In: *Astrophys. J. Lett.* 761 (2012), p. L11. DOI: 10.1088/2041-8205/761/1/L11. arXiv: 1210.7820 [astro-ph.GA] (cit. on pp. 60, 67, 89).

[288] M. S. Pshirkov et al. "Deriving global structure of the Galactic Magnetic Field from Faraday Rotation Measures of extragalactic sources". In: *Astrophys. J.* 738 (2011), p. 192. DOI: 10.1088/0004-637X/738/2/192. arXiv: 1103.0814 [astro-ph.GA] (cit. on p. 61).

[289] T. R. Jaffe et al. "Comparing Polarised Synchrotron and Thermal Dust Emission in the Galactic Plane". In: *Mon. Not. Roy. Astron. Soc.* 431 (2013), p. 683. DOI: 10.1093/mnras/stt200. arXiv: 1302.0143 [astro-ph.GA] (cit. on p. 61).

[290] Michael Unger and Glennys R. Farrar. "The Coherent Magnetic Field of the Milky Way". In: *Astrophys. J.* 970.1 (2024), p. 95. DOI: 10.3847/1538-4357/ad4a54. arXiv: 2311.12120 [astro-ph.GA] (cit. on p. 61).

[291] Alexander Korochkin, Dmitri Semikoz, and Peter Tinyakov. "The coherent magnetic field of the Milky Way halo, Local Bubble and Fan Region". In: (July 2024). arXiv: 2407.02148 [astro-ph.GA] (cit. on p. 61).

[292] Roberto Aloisio et al. "SimProp v2r4: Monte Carlo simulation code for UHECR propagation". In: *JCAP* 11 (2017), p. 009. DOI: 10.1088/1475-7516/2017/11/009. arXiv: 1705.03729 [astro-ph.HE] (cit. on pp. 63, 64, 145).

[293] R. Aloisio et al. "SimProp: a Simulation Code for Ultra High Energy Cosmic Ray Propagation". In: *JCAP* 10 (2012), p. 007. DOI: 10.1088/1475-7516/2012/10/007. arXiv: 1204.2970 [astro-ph.HE] (cit. on pp. 63, 64).

[294] R. Aloisio et al. "SimProp v2r2: a Monte Carlo simulation to compute cosmogenic neutrino fluxes". In: (May 2015). arXiv: 1505.01347 [astro-ph.HE] (cit. on p. 63).

[295] Roberto Aloisio et al. "SimProp v2r3: Monte Carlo simulation code of UHECR propagation". In: (Feb. 2016). arXiv: 1602.01239 [astro-ph.HE] (cit. on p. 63).

[296] I. Antcheva et al. "ROOT: A C++ framework for petabyte data storage, statistical analysis and visualization". In: *Comput. Phys. Commun.* 180 (2009), pp. 2499–2512. DOI: 10.1016/j.cpc.2009.08.005. arXiv: 1508.07749 [physics.data-an] (cit. on p. 63).

[297] F. W. Stecker and M. H. Salamon. "Photodisintegration of ultrahigh-energy cosmic rays: A New determination". In: *Astrophys. J.* 512 (1999), pp. 521–526. DOI: 10.1086/306816. arXiv: astro-ph/9808110 (cit. on pp. 65, 116).

[298] Arjan J Koning, Stephane Hilaire, and Marieke C Duijvestijn. "TALYS-1.0". In: *International Conference on Nuclear Data for Science and Technology*. EDP Sciences. 2007, pp. 211–214 (cit. on p. 65).

[299] Eric Armengaud et al. "Crpropa: a numerical tool for the propagation of uhe cosmic rays, gamma-rays and neutrinos". In: *Astropart. Phys.* 28 (2007), pp. 463–471. DOI: 10.1016/j.astropartphys.2007.09.004. arXiv: astro-ph/0603675 (cit. on p. 65).

[300] Karl-Heinz Kampert et al. "CRPropa 2.0 – a Public Framework for Propagating High Energy Nuclei, Secondary Gamma Rays and Neutrinos". In: *Astropart. Phys.* 42 (2013), pp. 41–51. DOI: 10.1016/j.astropartphys.2012.12.001. arXiv: 1206.3132 [astro-ph.IM] (cit. on pp. 65, 68).

[301] Rafael Alves Batista et al. "CRPropa 3 - a Public Astrophysical Simulation Framework for Propagating Extraterrestrial Ultra-High Energy Particles". In: *JCAP* 05 (2016), p. 038. DOI: 10.1088/1475-7516/2016/05/038. arXiv: 1603.07142 [astro-ph.IM] (cit. on pp. 65, 68).

[302] Lukas Merten et al. "CRPropa 3.1—a low energy extension based on stochastic differential equations". In: *JCAP* 06 (2017), p. 046. DOI: 10.1088/1475-7516/2017/06/046. arXiv: 1704.07484 [astro-ph.IM] (cit. on pp. 65, 66).

[303] Philippe Terral and Katia M. Ferrière. "Constraints from Faraday rotation on the magnetic field structure in the Galactic halo". In: *arXiv: Astrophysics of Galaxies* (2016). URL: https://api.semanticscholar.org/CorpusID:119337320 (cit. on p. 67).

[304] Hans-Peter Bretz et al. "PARSEC: A Parametrized Simulation Engine for Ultra-High Energy Cosmic Ray Protons". In: *Astropart. Phys.* 54 (2014), pp. 110–117. DOI: 10.1016/j.astropartphys.2013.12.002. arXiv: 1302.3761 [astro-ph.HE] (cit. on p. 67).

[305] A Koning, S Hilaire, and S Goriely. "User manual of TALYS-1.8". In: *Nuclear Research and Consultancy Group, Petten, The Netherlands* (2015) (cit. on p. 68).

[306] A. M. Hillas. "Shower simulation: Lessons from MOCCA". In: *Nucl. Phys. B Proc. Suppl.* 52 (1997). Ed. by H. Rebel, G. Schatz, and J. Knapp, pp. 29–42. DOI: 10.1016/S0920-5632(96)00847-X (cit. on p. 68).

[307] M. Kachelriess, S. Ostapchenko, and R. Tomas. "ELMAG: A Monte Carlo simulation of electromagnetic cascades on the extragalactic background light and in magnetic fields". In: *Comput. Phys. Commun.* 183 (2012), pp. 1036–1043. DOI: 10.1016/j.cpc.2011.12.025. arXiv: 1106.5508 [astro-ph.HE] (cit. on p. 68).

[308] M. Blytt, M. Kachelriess, and S. Ostapchenko. "ELMAG 3.01: A three-dimensional Monte Carlo simulation of electromagnetic cascades on the extragalactic background light and in magnetic fields". In: (Sept. 2019). DOI: 10.1016/j.cpc.2020.107163. arXiv: 1909.09210 [astro-ph.HE] (cit. on p. 68).

[309] R. Alves Batista et al. "Effects of uncertainties in simulations of extragalactic UHECR propagation, using CRPropa and SimProp". In: *JCAP* 10 (2015), p. 063. DOI: 10.1088/1475-7516/2015/10/063. arXiv: 1508.01824 [astro-ph.HE] (cit. on p. 68).

[310] Rafael Alves Batista et al. "Secondary neutrino and gamma-ray fluxes from SimProp and CRPropa". In: *JCAP* 05 (2019), p. 006. DOI: 10.1088/1475-7516/2019/05/006. arXiv: 1901.01244 [astro-ph.HE] (cit. on pp. 68, 69, 122).

[311] P. Sommers. "Cosmic ray anisotropy analysis with a full-sky observatory". In: *Astropart. Phys.* 14 (2001), pp. 271–286. DOI: 10.1016/S0927-6505(00)00130-4. arXiv: astro-ph/0004016 (cit. on pp. 72, 73, 78).

[312] J. Aublin and Etienne Parizot. "Generalized 3D-reconstruction method of a dipole anisotropy in cosmic-ray distributions". In: *Astron. Astrophys.* 441 (2005), p. 407. DOI: 10.1051/0004-6361:20052833. arXiv: astro-ph/0504575 (cit. on pp. 72, 73, 78).

[313] Olivier Deligny et al. "Sensibility of the Pierre Auger Observatory to large scale anisotropies". In: *JCAP* 10 (2004), p. 008. DOI: 10.1088/1475-7516/2004/10/008. arXiv: astro-ph/0404253 (cit. on p. 77).

[314] Pierre Billoir and Olivier Deligny. "Estimates of multipolar coefficients to search for cosmic ray anisotropies with non-uniform or partial sky coverage". In: *JCAP* 02 (2008), p. 009. DOI: 10.1088/1475-7516/2008/02/009. arXiv: 0710.2290 [astro-ph] (cit. on pp. 77, 78).

[315] Luis A. Anchordoqui et al. "Full-Sky Search for Ultra High Energy Cosmic Ray Anisotropies". In: *Phys. Rev. D* 68 (2003), p. 083004. DOI: 10.1103/PhysRevD.68.083004. arXiv: astro-ph/0305158 (cit. on pp. 78, 97).

[316] Simone Rossoni and Günter Sigl. "Anisotropy signal of ultrahigh-energy cosmic rays from a structured magnetized universe". In: *Phys. Rev. D* 112.2 (2025), p. 023015. DOI: 10.1103/4zt7-s48v. arXiv: 2502.19324 [astro-ph.HE] (cit. on pp. 84, 90, 91, 93, 94, 98–101, 103–106, 199, 201–206).

[317] Andrea Zonca et al. "healpy: equal area pixelization and spherical harmonics transforms for data on the sphere in Python". In: *Journal of Open Source Software* 4.35 (2019), p. 1298. DOI: 10.21105/joss.01298 (cit. on pp. 84, 97).

[318] K. M. Górski et al. "HEALPix - A Framework for high resolution discretization, and fast analysis of data distributed on the sphere". In: *Astrophys. J.* 622 (2005), pp. 759–771. DOI: 10.1086/427976. arXiv: astro-ph/0409513 (cit. on pp. 84, 97).

[319] A. Aab et al. "Large-scale cosmic-ray anisotropies above 4 EeV measured by the Pierre Auger Observatory". In: *Astrophys. J.* 868.1 (2018), p. 4. DOI: 10.3847/1538-4357/aae689. arXiv: 1808.03579 [astro-ph.HE] (cit. on p. 87).

[320] Geraldina Golup. "An update on the arrival direction studies made with data from the Pierre Auger Observatory". In: *Proceedings of 38th International Cosmic Ray Conference — PoS(ICRC2023)*. Vol. 444. 2023, p. 252. DOI: 10.22323/1.444.0252 (cit. on pp. 87, 106).

[321] R. U. Abbasi et al. "Search for Large-scale Anisotropy on Arrival Directions of Ultra-high-energy Cosmic Rays Observed with the Telescope Array Experiment". In: *Astrophys. J. Lett.* 898.2 (2020), p. L28. DOI: 10.3847/2041-8213/aba0bc. arXiv: 2007.00023 [astro-ph.HE] (cit. on p. 88).

[322] Alexander Aab et al. "An Indication of anisotropy in arrival directions of ultra-high-energy cosmic rays through comparison to the flux pattern of extragalactic gamma-ray sources". In: *Astrophys. J. Lett.* 853.2 (2018), p. L29. DOI: 10.3847/2041-8213/aaa66d. arXiv: 1801.06160 [astro-ph.HE] (cit. on p. 88).

[323] R. U. Abbasi et al. "Indications of Intermediate-Scale Anisotropy of Cosmic Rays with Energy Greater Than 57 EeV in the Northern Sky Measured with the Surface Detector of the Telescope Array Experiment". In: *Astrophys. J. Lett.* 790 (2014), p. L21. DOI: 10.1088/2041-8205/790/2/L21. arXiv: 1404.5890 [astro-ph.HE] (cit. on p. 88).

[324] Jihyun Kim et al. "Hotspot Update, and a new Excess of Events on the Sky Seen by the Telescope Array Experiment". In: *Proceedings of 37th International Cosmic Ray Conference — PoS(ICRC2021)*. Vol. 395. 2021, p. 328. DOI: 10.22323/1.395.0328 (cit. on p. 88).

[325] R. U. Abbasi et al. "Indications of a Cosmic Ray Source in the Perseus-Pisces Supercluster". In: (Oct. 2021). arXiv: 2110.14827 [astro-ph.HE] (cit. on p. 88).

[326] Jihyun Kim. "Highlights from the Telescope Array Experiment". In: *Proceedings of 38th International Cosmic Ray Conference — PoS(ICRC2023)*. Vol. 444. 2023, p. 008. DOI: 10.22323/1.444.0008 (cit. on p. 88).

[327] Jihyun Kim et al. "Anisotropies in the arrival direction distribution of ultra-high energy cosmic rays measured by the Telescope Array surface detector". In: *Proceedings of 38th International Cosmic Ray Conference — PoS(ICRC2023)*. Vol. 444. 2023, p. 244. DOI: 10.22323/1.444.0244 (cit. on p. 88).

[328] A. M. Taylor, J. H. Matthews, and A. R. Bell. "UHECR echoes from the Council of Giants". In: *Mon. Not. Roy. Astron. Soc.* 524.1 (2023), pp. 631–642. DOI: 10.1093/mnras/stad1716. arXiv: 2302.06489 [astro-ph.HE] (cit. on p. 88).

[329] Hao-Ning He et al. "Evidence for the Sombrero Galaxy as an Accelerator of the Highest-Energy Cosmic Rays". In: (Dec. 2024). arXiv: 2412.11966 [astro-ph.HE] (cit. on p. 88).

[330] Guenter Sigl, Francesco Miniati, and Torsten A. Ensslin. "Ultrahigh-energy cosmic rays in a structured and magnetized universe". In: *Phys. Rev. D* 68 (2003), p. 043002. DOI: 10.1103/PhysRevD.68.043002. arXiv: astro-ph/0302388 (cit. on p. 88).

[331] Gunter Sigl, Francesco Miniati, and Torsten A. Ensslin. "Ultrahigh energy cosmic ray probes of large scale structure and magnetic fields". In: *Phys. Rev. D* 70 (2004), p. 043007. DOI: 10.1103/PhysRevD.70.043007. arXiv: astro-ph/0401084 (cit. on p. 88).

[332] Eric Armengaud, Guenter Sigl, and Francesco Miniati. "Ultrahigh energy nuclei propagation in a structured, magnetized Universe". In: *Phys. Rev. D* 72 (2005), p. 043009. DOI: 10.1103/PhysRevD.72.043009. arXiv: astro-ph/0412525 (cit. on p. 88).

[333] Andrej Dundović and Günter Sigl. "Anisotropies of Ultra-high Energy Cosmic Rays Dominated by a Single Source in the Presence of Deflections". In: *JCAP* 01 (2019), p. 018. DOI: 10.1088/1475-7516/2019/01/018. arXiv: 1710.05517 [astro-ph.HE] (cit. on p. 88).

[334] K. Dolag et al. "Mapping deflections of extragalactic ultra high energy cosmic rays in magnetohydrodynamic simulations of the local universe". In: *Nucl. Phys. B Proc. Suppl.* 136 (2004). Ed. by C. Aramo, A. Insolia, and C. Tuve, pp. 234–243. DOI: 10.1016/j.nuclphysbps.2004.10.030 (cit. on p. 88).

[335] Klaus Dolag et al. "Constrained simulations of the magnetic field in the local Universe and the propagation of UHECRs". In: *JCAP* 01 (2005), p. 009. DOI: 10.1088/1475-7516/2005/01/009. arXiv: astro-ph/0410419 (cit. on p. 88).

[336] Santabrata Das et al. "Propagation of UHE Protons through Magnetized Cosmic Web". In: *Astrophys. J.* 682 (2008), p. 29. DOI: 10.1086/588278. arXiv: 0801.0371 [astro-ph] (cit. on p. 88).

[337] Stefan Hackstein et al. "Propagation of ultrahigh energy cosmic rays in extragalactic magnetic fields: a view from cosmological simulations". In: *Mon. Not. Roy. Astron. Soc.* 462.4 (2016), pp. 3660–3671. DOI: 10.1093/mnras/stw1903. arXiv: 1607.08872 [astro-ph.CO] (cit. on pp. 88, 97, 200).

[338] Stefan Hackstein et al. "Simulations of ultra-high Energy Cosmic Rays in the local Universe and the origin of Cosmic Magnetic Fields". In: *Mon. Not. Roy. Astron. Soc.* 475.2 (2018), pp. 2519–2529. DOI: 10.1093/mnras/stx3354. arXiv: 1710.01353 [astro-ph.CO] (cit. on pp. 88, 90–92, 95, 146).

[339] Rafael Alves Batista et al. "Implications of strong intergalactic magnetic fields for ultrahigh-energy cosmic-ray astronomy". In: *Phys. Rev. D* 96.2 (2017), p. 023010. DOI: 10.1103/PhysRevD.96.023010. arXiv: 1704.05869 [astro-ph.HE] (cit. on p. 88).

[340] Sang-jin Lee, Angela Olinto, and Guenter Sigl. "Extragalactic magnetic field and the highest energy cosmic rays". In: *Astrophys. J. Lett.* 455 (1995), p. L21. DOI: 10.1086/309812. arXiv: astro-ph/9508088 (cit. on p. 88).

[341] J. D. Bray and A. M. M. Scaife. "An upper limit on the strength of the extragalactic magnetic field from ultra-high-energy cosmic-ray anisotropy". In: *Astrophys. J.* 861.1 (2018), p. 3. DOI: 10.3847/1538-4357/aac777. arXiv: 1805.07995 [astro-ph.CO] (cit. on p. 88).

[342] Glennys R. Farrar and Michael S. Sutherland. "Deflections of UHECRs in the Galactic magnetic field". In: *JCAP* 05 (2019), p. 004. DOI: 10.1088/1475-7516/2019/05/004. arXiv: 1711.02730 [astro-ph.HE] (cit. on p. 89).

[343] Rita C. dos Anjos et al. "Ultrahigh-Energy Cosmic Ray Composition from the Distribution of Arrival Directions". In: *Phys. Rev. D* 98.12 (2018), p. 123018. DOI: 10.1103/PhysRevD.98.123018. arXiv: 1810.04251 [astro-ph.HE] (cit. on p. 89).

[344] Silvia Mollerach, Esteban Roulet, and Oscar Taborda. "Large-scale anisotropies of extragalactic cosmic rays below the ankle". In: *JCAP* 12 (2022), p. 021. DOI: 10.1088/1475-7516/2022/12/021. arXiv: 2207.11540 [astro-ph.HE] (cit. on p. 89).

[345] Alena Bakalová, Jakub Vícha, and Petr Trávniíček. "Modification of the dipole in arrival directions of ultra-high-energy cosmic rays due to the Galactic magnetic field". In: *JCAP* 12 (2023), p. 016. DOI: 10.1088/1475-7516/2023/12/016. arXiv: 2303.08766 [astro-ph.HE] (cit. on p. 89).

[346] Vasundhara Shaw, Arjen Van Vliet, and Andrew M. Taylor. "Influence of the Galactic Halo on the UHECR Multipoles". In: (Jan. 2025). arXiv: 2501.16881 [astro-ph.HE] (cit. on p. 89).

[347] Armando di Matteo and Peter Tinyakov. "How isotropic can the UHECR flux be?" In: *Mon. Not. Roy. Astron. Soc.* 476.1 (2018), pp. 715–723. DOI: 10.1093/mnras/sty277/4835522. arXiv: 1706.02534 [astro-ph.HE] (cit. on p. 89).

[348] David Wittkowski and Karl-Heinz Kampert. "On the anisotropy in the arrival directions of ultra-high-energy cosmic rays". In: *Astrophys. J. Lett.* 854.1 (2018), p. L3. DOI: 10.3847/2041-8213/aaa2f9. arXiv: 1710.05617 [astro-ph.HE] (cit. on p. 89).

[349] Noémie Globus et al. "Cosmic-Ray Anisotropy from Large Scale Structure and the effect of magnetic horizons". In: *Mon. Not. Roy. Astron. Soc.* 484.3 (2019), pp. 4167–4173. DOI: 10.1093/mnras/stz164. arXiv: 1808.02048 [astro-ph.HE] (cit. on p. 89).

[350] Chen Ding, Noemie Globus, and Glennys R. Farrar. "The Imprint of Large Scale Structure on the Ultra-High-Energy Cosmic Ray Sky". In: *Astrophys. J. Lett.* 913.1 (2021), p. L13. DOI: 10.3847/2041-8213/abf11e. arXiv: 2101.04564 [astro-ph.HE] (cit. on p. 89).

[351] D. Allard et al. "What can be learnt from UHECR anisotropies observations - I. Large-scale anisotropies and composition features". In: *Astron. Astrophys.* 664 (2022), A120. DOI: 10.1051/0004-6361/202142491. arXiv: 2110.10761 [astro-ph.HE] (cit. on p. 89).

[352] Teresa Bister and Glennys R. Farrar. "Constraints on UHECR Sources and Extragalactic Magnetic Fields from Directional Anisotropies". In: *Astrophys. J.* 966.1 (2024), p. 71. DOI: 10.3847/1538-4357/ad2f3f. arXiv: 2312.02645 [astro-ph.HE] (cit. on pp. 89, 92, 98).

[353] Denis Allard et al. "What can be learnt from UHECR anisotropies observations - II. Intermediate-scale anisotropies". In: *Astron. Astrophys.* 686 (2024), A292. DOI: 10.1051/0004-6361/202347034. arXiv: 2305.17811 [astro-ph.HE] (cit. on p. 89).

[354] Arjen van Vliet et al. "Extragalactic magnetic field constraints from ultrahigh-energy cosmic rays from local galaxies". In: *Mon. Not. Roy. Astron. Soc.* 510.1 (2021), pp. 1289–1297. DOI: 10.1093/mnras/stab3495. arXiv: 2104.05732 [astro-ph.HE] (cit. on pp. 89, 92).

[355] Teresa Bister, Glennys R. Farrar, and Michael Unger. "The Large-scale Anisotropy and Flux (de)magnification of Ultrahigh-energy Cosmic Rays in the Galactic Magnetic Field". In: *Astrophys. J. Lett.* 975.1 (2024), p. L21. DOI: 10.3847/2041-8213/ad856f. arXiv: 2408.00614 [astro-ph.HE] (cit. on pp. 89, 92).

[356] Sullivan Marafico et al. "Closing the Net on Transient Sources of Ultrahigh-energy Cosmic Rays". In: *Astrophys. J.* 972.1 (2024), p. 4. DOI: 10.3847/1538-4357/ad5a11. arXiv: 2405.17179 [astro-ph.HE] (cit. on p. 89).

[357] Rostom Mbarek and Damiano Caprioli. "Propagation Delays of Ultra-High-Energy Cosmic Ray from Active Galactic Nuclei". In: (Feb. 2025). arXiv: 2502.01022 [astro-ph.HE] (cit. on p. 89).

[358] Greg L. Bryan et al. "Enzo: An Adaptive Mesh Refinement Code for Astrophysics". In: *Astrophys. J. Suppl.* 211 (2014), p. 19. DOI: 10.1088/0067-0049/211/2/19. arXiv: 1307.2265 [astro-ph.IM] (cit. on p. 90).

[359] Olena Tkachenko. "Studies of the mass composition of cosmic rays and proton-proton interaction cross-sections at ultra-high energies with the Pierre Auger Observatory". In: *Proceedings of 38th International Cosmic Ray Conference — PoS(ICRC2023)*. Vol. 444. 2023, p. 438. DOI: 10.22323/1.444.0438 (cit. on pp. 92, 96, 99).

[360] A. N. Kolmogorov. "The Local Structure of Turbulence in Incompressible Viscous Fluid for Very Large Reynolds Numbers". In: *Proceedings: Mathematical and Physical Sciences* 434.1890 (1991), pp. 9–13. ISSN: 09628444. URL: http://www.jstor.org/stable/51980 (visited on 04/14/2025) (cit. on p. 92).

[361] Christopher J. Conselice et al. "THE EVOLUTION OF GALAXY NUMBER DENSITY ATz< 8 AND ITS IMPLICATIONS". In: *Astrophys. J.* 830.2 (2016), p. 83. DOI: 10.3847/0004-637x/830/2/83 (cit. on p. 92).

[362] C. Gruppioni et al. "The Herschel PEP/HerMES Luminosity Function. I: Probing the Evolution of PACS selected Galaxies to z˜4". In: *Mon. Not. Roy. Astron. Soc.* 432 (2013), p. 23. DOI: 10.1093/mnras/stt308. arXiv: 1302.5209 [astro-ph.CO] (cit. on p. 92).

[363] David Wittkowski. "Reconstructed properties of the sources of UHECR and their dependence on the extragalactic magnetic field". In: *Proceedings of 35th International Cosmic Ray Conference — PoS(ICRC2017)*. Vol. 301. 2017, p. 563. DOI: 10.22323/1.301.0563 (cit. on p. 95).

[364] A. Abdul Halim et al. "Constraining models for the origin of ultra-high-energy cosmic rays with a novel combined analysis of arrival directions, spectrum, and composition data measured at the Pierre Auger Observatory". In: *JCAP* 01 (2024), p. 022. DOI: 10.1088/1475-7516/2024/01/022. arXiv: 2305.16693 [astro-ph.HE] (cit. on pp. 95, 98).

[365] A. Abdul Halim et al. "Impact of the magnetic horizon on the interpretation of the Pierre Auger Observatory spectrum and composition data". In: *JCAP* 07 (2024), p. 094. DOI: 10.1088/1475-7516/2024/07/094. arXiv: 2404.03533 [astro-ph.HE] (cit. on pp. 95, 98).

[366] Domenik Ehlert, Foteini Oikonomou, and Michael Unger. "Curious case of the maximum rigidity distribution of cosmic-ray accelerators". In: *Phys. Rev. D* 107.10 (2023), p. 103045. DOI: 10.1103/PhysRevD.107.103045. arXiv: 2207.10691 [astro-ph.HE] (cit. on p. 96).

[367] P. Abreu et al. "The energy spectrum of cosmic rays beyond the turn-down around 10^{17} eV as measured with the surface detector of the Pierre Auger Observatory". In: *Eur. Phys. J. C* 81.11 (2021), p. 966. DOI: 10.1140/epjc/s10052-021-09700-w. arXiv: 2109.13400 [astro-ph.HE] (cit. on pp. 96, 99).

[368] Sheldon S. Campbell. "Angular Power Spectra with Finite Counts". In: *Mon. Not. Roy. Astron. Soc.* 448.3 (2015), pp. 2854–2878. DOI: 10.1093/mnras/stv135. arXiv: 1411.4031 [astro-ph.CO] (cit. on p. 97).

[369] Markus Ackermann et al. "Astrophysics Uniquely Enabled by Observations of High-Energy Cosmic Neutrinos". In: *Bull. Am. Astron. Soc.* 51 (2019), p. 185. arXiv: 1903.04334 [astro-ph.HE] (cit. on pp. 110, 147).

[370] Markus Ackermann et al. "Fundamental Physics with High-Energy Cosmic Neutrinos". In: *Bull. Am. Astron. Soc.* 51 (2019), p. 215. arXiv: 1903.04333 [astro-ph.HE] (cit. on pp. 110, 147).

[371] M. G. Aartsen et al. "Evidence for High-Energy Extraterrestrial Neutrinos at the IceCube Detector". In: *Science* 342 (2013), p. 1242856. DOI: 10.1126/science.1242856. arXiv: 1311.5238 [astro-ph.HE] (cit. on p. 110).

[372] R. Abbasi et al. "Improved Characterization of the Astrophysical Muon–neutrino Flux with 9.5 Years of IceCube Data". In: *Astrophys. J.* 928.1 (2022), p. 50. DOI: 10.3847/1538-4357/ac4d29. arXiv: 2111.10299 [astro-ph.HE] (cit. on p. 110).

[373] M. G. Aartsen et al. "Characteristics of the diffuse astrophysical electron and tau neutrino flux with six years of IceCube high energy cascade data". In: *Phys. Rev. Lett.* 125.12 (2020), p. 121104. DOI: 10.1103/PhysRevLett.125.121104. arXiv: 2001.09520 [astro-ph.HE] (cit. on p. 110).

[374] M. G. Aartsen et al. "The contribution of Fermi-2LAC blazars to the diffuse TeV-PeV neutrino flux". In: *Astrophys. J.* 835.1 (2017), p. 45. DOI: 10.3847/1538-4357/835/1/45. arXiv: 1611.03874 [astro-ph.HE] (cit. on p. 110).

[375] R. Abbasi et al. "Evidence for neutrino emission from the nearby active galaxy NGC 1068". In: *Science* 378.6619 (2022), pp. 538–543. DOI: 10.1126/science.abg3395. arXiv: 2211.09972 [astro-ph.HE] (cit. on p. 110).

[376] Sjoert van Velzen et al. "Establishing accretion flares from supermassive black holes as a source of high-energy neutrinos". In: *Mon. Not. Roy. Astron. Soc.* 529.3 (2024), pp. 2559–2576. DOI: 10.1093/mnras/stae610. arXiv: 2111.09391 [astro-ph.HE] (cit. on p. 111).

[377] P. Padovani et al. "The neutrino background from non-jetted active galactic nuclei". In: *Astron. Astrophys.* 684 (2024), p. L21. DOI: 10.1051/0004-6361/202450025. arXiv: 2404.05690 [astro-ph.HE] (cit. on p. 111).

[378] Shan Gao et al. "Modelling the coincident observation of a high-energy neutrino and a bright blazar flare". In: *Nature Astron.* 3.1 (2019), pp. 88–92. DOI: 10.1038/s41550-018-0610-1. arXiv: 1807.04275 [astro-ph.HE] (cit. on p. 111).

[379] Björn Eichmann et al. "Solving the Multimessenger Puzzle of the AGN-starburst Composite Galaxy NGC 1068". In: *Astrophys. J.* 939.1 (2022), p. 43. DOI: 10.3847/1538-4357/ac9588. arXiv: 2207.00102 [astro-ph.HE] (cit. on p. 111).

[380] Walter Winter and Cecilia Lunardini. "Interpretation of the Observed Neutrino Emission from Three Tidal Disruption Events". In: *Astrophys. J.* 948.1 (2023), p. 42. DOI: 10.3847/1538-4357/acbe9e. arXiv: 2205.11538 [astro-ph.HE] (cit. on p. 111).

[381] M. G. Aartsen et al. "IceCube Search for Neutrinos Coincident with Compact Binary Mergers from LIGO-Virgo's First Gravitational-wave Transient Catalog". In: *Astrophys. J. Lett.* 898.1 (2020), p. L10. DOI: 10.3847/2041-8213/ab9d24. arXiv: 2004.02910 [astro-ph.HE] (cit. on p. 111).

[382] Valentin Decoene et al. "High-energy neutrinos from fallback accretion of binary neutron star merger remnants". In: *JCAP* 04 (2020), p. 045. DOI: 10.1088/1475-7516/2020/04/045. arXiv: 1910.06578 [astro-ph.HE] (cit. on pp. 111–113, 115, 116, 130, 131, 147).

[383] Shigeo S. Kimura et al. "High-Energy Neutrino Emission from Short Gamma-Ray Bursts: Prospects for Coincident Detection with Gravitational Waves". In: *Astrophys. J. Lett.* 848.1 (2017), p. L4. DOI: 10.3847/2041-8213/aa8d14. arXiv: 1708.07075 [astro-ph.HE] (cit. on p. 111).

[384] Shigeo S. Kimura, Kohta Murase, and Peter Mészáros. "Super-Knee Cosmic Rays from Galactic Neutron Star Merger Remnants". In: *Astrophys. J.* 866.1 (2018), p. 51. DOI: 10.3847/1538-4357/aadc0a. arXiv: 1807.03290 [astro-ph.HE] (cit. on p. 111).

[385] Shigeo S. Kimura et al. "Transejecta high-energy neutrino emission from binary neutron star mergers". In: *Phys. Rev. D* 98.4 (2018), p. 043020. DOI: 10.1103/PhysRevD.98.043020. arXiv: 1805.11613 [astro-ph.HE] (cit. on p. 111).

[386] Xavier Rodrigues et al. "Binary neutron star merger remnants as sources of cosmic rays below the "Ankle"". In: *Astropart. Phys.* 106 (2019), pp. 10–17. DOI: 10.1016/j.astropartphys.2018.10.007. arXiv: 1806.01624 [astro-ph.HE] (cit. on pp. 111, 113, 116).

[387] R. Margutti et al. "The Binary Neutron Star Event LIGO/Virgo GW170817 160 Days after Merger: Synchrotron Emission across the Electromagnetic Spectrum". In: *Astrophys. J. Lett.* 856.1 (2018), p. L18. DOI: 10.3847/2041-8213/aab2ad. arXiv: 1801.03531 [astro-ph.HE] (cit. on pp. 111, 112, 147).

[388] Simone Rossoni, Denise Boncioli, and Günter Sigl. "Investigating binary-neutron-star mergers as production sites of high-energy neutrinos". In: *JCAP* 01 (2025), p. 009. DOI: 10.1088/1475-7516/2025/01/009. arXiv: 2407.19957 [astro-ph.HE] (cit. on pp. 112, 114, 115, 118–121, 123, 125–129, 131, 208–213).

[389] Eli Waxman and John N. Bahcall. "High-energy neutrinos from astrophysical sources: An Upper bound". In: *Phys. Rev. D* 59 (1999), p. 023002. DOI: 10.1103/PhysRevD.59.023002. arXiv: hep-ph/9807282 (cit. on p. 121).

[390] John N. Bahcall and Eli Waxman. "High-energy astrophysical neutrinos: The Upper bound is robust". In: *Phys. Rev. D* 64 (2001), p. 023002. DOI: 10.1103/PhysRevD.64.023002. arXiv: hep-ph/9902383 (cit. on p. 121).

[391] M. G. Aartsen et al. "The IceCube Neutrino Observatory - Contributions to ICRC 2017 Part II: Properties of the Atmospheric and Astrophysical Neutrino Flux". In: (Oct. 2017). arXiv: 1710.01191 [astro-ph.HE] (cit. on pp. 122, 123, 127, 147).

[392] A. Aab et al. "Probing the origin of ultra-high-energy cosmic rays with neutrinos in the EeV energy range using the Pierre Auger Observatory". In: *JCAP* 10 (2019), p. 022. DOI: 10.1088/1475-7516/2019/10/022. arXiv: 1906.07422 [astro-ph.HE] (cit. on pp. 122–124, 127, 147).

[393] Gary J. Feldman and Robert D. Cousins. "A Unified approach to the classical statistical analysis of small signals". In: *Phys. Rev. D* 57 (1998), pp. 3873–3889. DOI: 10.1103/PhysRevD.57.3873. arXiv: physics/9711021 (cit. on p. 124).

[394] Marco Stein Muzio, Michael Unger, and Glennys R. Farrar. "Progress towards characterizing ultrahigh energy cosmic ray sources". In: *Phys. Rev. D* 100.10 (2019), p. 103008. DOI: 10.1103/PhysRevD.100.103008. arXiv: 1906.06233 [astro-ph.HE] (cit. on p. 124).

[395] Marco Stein Muzio, Glennys R. Farrar, and Michael Unger. "Probing the environments surrounding ultrahigh energy cosmic ray accelerators and their implications for astrophysical neutrinos". In: *Phys. Rev. D* 105.2 (2022), p. 023022. DOI: 10.1103/PhysRevD.105.023022. arXiv: 2108.05512 [astro-ph.HE] (cit. on p. 124).

[396] Brian D. Metzger. "Kilonovae". In: *Living Rev. Rel.* 23.1 (2020), p. 1. DOI: 10.1007/s41114-019-0024-0. arXiv: 1910.01617 [astro-ph.HE] (cit. on pp. 130, 131).

[397] Masaru Shibata and Kenta Hotokezaka. "Merger and Mass Ejection of Neutron-Star Binaries". In: *Ann. Rev. Nucl. Part. Sci.* 69 (2019), pp. 41–64. DOI: 10.1146/annurev-nucl-101918-023625. arXiv: 1908.02350 [astro-ph.HE] (cit. on p. 130).

[398] R. Abbott et al. "GWTC-3: Compact Binary Coalescences Observed by LIGO and Virgo during the Second Part of the Third Observing Run". In: *Phys. Rev. X* 13.4 (2023), p. 041039. DOI: 10.1103/PhysRevX.13.041039. arXiv: 2111.03606 [gr-qc] (cit. on pp. 131, 132, 147).

[399] Stephan Rosswog. "Fallback accretion in the aftermath of a compact binary merger". In: *Mon. Not. Roy. Astron. Soc.* 376 (2007), pp. L48–L51. DOI: 10.1111/j.1745-3933.2007.00284.x. arXiv: astro-ph/0611440 (cit. on p. 131).

[400] Mainak Mukhopadhyay, Shigeo S. Kimura, and Kohta Murase. "Gravitational wave triggered searches for high-energy neutrinos from binary neutron star mergers: Prospects for next generation detectors". In: *Phys. Rev. D* 109.4 (2024), p. 043053. DOI: 10.1103/PhysRevD.109.043053. arXiv: 2310.16875 [astro-ph.HE] (cit. on p. 132).

[401] Mainak Mukhopadhyay et al. "Ultrahigh-energy neutrino searches using next-generation gravitational wave detectors at radio neutrino detectors: GRAND, IceCube-Gen2 Radio, and RNO-G". In: *Phys. Rev. D* 110.6 (2024), p. 063004. DOI: 10.1103/PhysRevD.110.063004. arXiv: 2406.19440 [astro-ph.HE] (cit. on p. 132).

[402] Mainak Mukhopadhyay, Shigeo S. Kimura, and Brian D. Metzger. "High-energy neutrino signatures from pulsar remnants of binary neutron-star mergers: coincident detection prospects with gravitational waves". In: (July 2024). arXiv: 2407.04767 [astro-ph.HE] (cit. on p. 132).

[403] W. Hofmann. "The High Energy Stereoscopic System (HESS) project". In: *AIP Conf. Proc.* 515.1 (2000). Ed. by B. L. Dingus, M. H. Salamon, and D. B. Kieda, p. 500. DOI: 10.1063/1.1291416 (cit. on p. 134).

[404] Javier Rico. "Review of fundamental physics results with the MAGIC telescopes". In: *AIP Conf. Proc.* 1792.1 (2017), p. 060001. DOI: 10.1063/1.4968984 (cit. on p. 134).

[405] T. C. Weekes et al. "VERITAS: The Very energetic radiation imaging telescope array system". In: *Astropart. Phys.* 17 (2002), pp. 221–243. DOI: 10.1016/S0927-6505(01)00152-9. arXiv: astro-ph/0108478 (cit. on p. 134).

[406] W. B. Atwood et al. "The Large Area Telescope on the Fermi Gamma-ray Space Telescope Mission". In: *Astrophys. J.* 697 (2009), pp. 1071–1102. DOI: 10.1088/0004-637X/697/2/1071. arXiv: 0902.1089 [astro-ph.IM] (cit. on p. 134).

[407] A. Neronov and Dmitry V. Semikoz. "A method of measurement of extragalactic magnetic fields by TeV gamma ray telescopes". In: *JETP Lett.* 85 (2007), pp. 473–477. DOI: 10.1134/S0021364007100013. arXiv: astro-ph/0604607 (cit. on p. 134).

[408] A. Neronov and D. V. Semikoz. "Sensitivity of gamma-ray telescopes for detection of magnetic fields in intergalactic medium". In: *Phys. Rev. D* 80 (2009), p. 123012. DOI: 10.1103/PhysRevD.80.123012. arXiv: 0910.1920 [astro-ph.CO] (cit. on pp. 134, 136).

[409] V. A. Acciari et al. "A lower bound on intergalactic magnetic fields from time variability of 1ES 0229+200 from MAGIC and Fermi/LAT observations". In: *Astron. Astrophys.* 670 (2023), A145. DOI: 10.1051/0004-6361/202244126. arXiv: 2210.03321 [astro-ph.HE] (cit. on pp. 134, 138, 148).

[410] A. M. Taylor, I. Vovk, and A. Neronov. "Extragalactic magnetic fields constraints from simultaneous GeV-TeV observations of blazars". In: *Astron. Astrophys.* 529 (2011), A144. DOI: 10.1051/0004-6361/201116441. arXiv: 1101.0932 [astro-ph.HE] (cit. on pp. 134, 137).

[411] Alexander Korochkin et al. "Sensitivity reach of gamma-ray measurements for strong cosmological magnetic fields". In: *Astrophys. J.* 906.2 (2021), p. 116. DOI: 10.3847/1538-4357/abc697. arXiv: 2007.14331 [astro-ph.CO] (cit. on p. 134).

[412] Paolo Da Vela et al. "Intergalactic magnetic field studies by means of γ-ray emission from GRB 190114C". In: *Phys. Rev. D* 107.6 (2023), p. 063030. DOI: 10.1103/PhysRevD.107.063030. arXiv: 2303.03137 [astro-ph.HE] (cit. on p. 134).

[413] Timur A Dzhatdoev, Egor I Podlesnyi, and Grigory I Rubtsov. "First constraints on the strength of the extragalactic magnetic field from gamma-ray observations of GRB 221009A". In: *Mon. Not. Roy. Astron. Soc. Lett.* 527.1 (2023), pp. L95–L102. DOI: 10.1093/mnrasl/slad142. arXiv: https://doi.org/10.1093/mnrasl/slad142 [astro-ph.HE] (cit. on p. 134).

[414] Yi-Yun Huang et al. "Constraints on the Intergalactic Magnetic Field Strength from Gamma-Ray Observations of GRB 221009A". In: *Astrophys. J. Lett.* 955.1 (2023), p. L10. DOI: 10.3847/2041-8213/acf66a. arXiv: http://dx.doi.org/10.3847/2041-8213/acf66a [astro-ph.HE] (cit. on p. 134).

[415] Zi-Qing Xia et al. "A delayed 400 GeV photon from GRB 221009A and implication on the intergalactic magnetic field". In: *Nat. Commun.* 15.1 (2024), p. 4280. DOI: 10.1038/s41467-024-48668-5. arXiv: https://doi.org/10.1038/s41467-024-48668-5 [astro-ph.HE] (cit. on p. 134).

[416] E I Podlesnyi, T A Dzhatdoev, and V I Galkin. "Constraints on the extragalactic magnetic field strength from blazar spectra based on 145 months of Fermi-LAT observations". In: *Mon. Not. Roy. Astron. Soc.* 516.4 (2024), pp. 5379–5388. DOI: 10.1093/mnras/stac2509. arXiv: http://dx.doi.org/10.1093/mnras/stac2509 [astro-ph.HE] (cit. on p. 134).

[417] Lewi Tonks and Irving Langmuir. "Oscillations in Ionized Gases". In: *Phys. Rev.* 33 (2 Feb. 1929), pp. 195–210. DOI: 10.1103/PhysRev.33.195. URL: https://link.aps.org/doi/10.1103/PhysRev.33.195 (cit. on p. 134).

[418] A. Bret. "Weibel, Two-Stream, Filamentation, Oblique, Bell, Buneman... which one grows faster ?" In: *Astrophys. J.* 699.2 (2009), p. 990. DOI: 10.1088/0004-637x/699/2/990. arXiv: 0903.2658 [astro-ph.HE] (cit. on p. 134).

[419] M. Lemoine and G. Pelletier. "On electromagnetic instabilities at ultra-relativistic shock waves". In: *Mon. Not. Roy. Astron. Soc.* 402.1 (2009), p. 321. DOI: 10.1111/j.1365-2966.2009.15869.x. arXiv: 0904.2657 [astro-ph.HE] (cit. on p. 134).

[420] F. Miniati and A. Elyiv. "Relaxation of Blazar Induced Pair Beams in Cosmic Voids". In: *Astrophys. J.* 770.1 (2013), p. 54. DOI: 10.1088/0004-637x/770/1/54. arXiv: 1208.1761 [astro-ph.HE] (cit. on pp. 134, 148).

[421] S. Vafin et al. "The electrostatic instability for realistic pair distributions in blazar/EBL cascades". In: *Astrophys. J.* 857.1 (2018), p. 43. DOI: 10.3847/1538-4357/aab552. arXiv: 1803.02990 [astro-ph.HE] (cit. on pp. 134, 143, 148).

[422] Roy Perry and Yuri Lyubarsky. "The role of resonant plasma instabilities in the evolution of blazar induced pair beams". In: *Mon. Not. Roy. Astron. Soc.* 503.2 (2021), pp. 2215–2228. DOI: 10.1093/mnras/stab324. arXiv: 2102.03190 [astro-ph.HE] (cit. on p. 135).

[423] Mahmoud Alawashra and Martin Pohl. "Nonlinear Feedback of the Electrostatic Instability on the Blazar-induced Pair Beam and GeV Cascade". In: *Astrophys. J.* 964.1 (2024), p. 82. DOI: 10.3847/1538-4357/ad24ea. arXiv: 2402.03127 [astro-ph.HE] (cit. on pp. 135, 144).

[424] R. Schlickeiser, S. Krakau, and M. Supsar. "Plasma effects on fast pair beams II. Reactive versus kinetic instability of parallel electrostatic wave". In: *Astrophys. J.* 777.1 (2013), p. 49. DOI: 10.1088/0004-637x/777/1/49. arXiv: 1308.4594 [astro-ph.HE] (cit. on p. 135).

[425] Andrey Saveliev, Carmelo Evoli, and Guenter Sigl. "The Role of Plasma Instabilities in the Propagation of Gamma-Rays from Distant Blazars". In: (Nov. 2013). arXiv: 1311.6752 [astro-ph.HE] (cit. on pp. 135, 148).

[426] Rafael Alves Batista, Andrey Saveliev, and Elisabete M. de Gouveia Dal Pino. "The Impact of Plasma Instabilities on the Spectra of TeV Blazars". In: *Mon. Not. Roy. Astron. Soc.* 489.3 (2019), pp. 3836–3849. DOI: 10.1093/mnras/stz2389. arXiv: 1904.13345 [astro-ph.HE] (cit. on pp. 135, 136, 138, 148).

[427] Mahmoud Alawashra and Martin Pohl. "Suppression of the TeV Pair-beam–Plasma Instability by a Tangled Weak Intergalactic Magnetic Field". In: *Astrophys. J.* 929.1 (2022), p. 67. DOI: 10.3847/1538-4357/ac5a4b. arXiv: 2203.01022 [astro-ph.HE] (cit. on p. 135).

[428] Mahmoud Alawashra, Ievgen Vovk, and Martin Pohl. "Marginal Role of the Electrostatic Instability in the GeV-scale Cascade Flux from 1ES 0229+200". In: *Astrophys. J.* 978.1 (2025), p. 95. DOI: 10.3847/1538-4357/ad98f9. arXiv: 2412.01406 [astro-ph.HE] (cit. on p. 135).

[429] D.R. Nicholson. *Introduction to Plasma Physics*. New York: John Wiley & Sons, 1983 (cit. on p. 135).

[430] F. Aharonian et al. "New constraints on the Mid-IR EBL from the HESS discovery of VHE gamma rays from 1ES 0229+200". In: *Astron. Astrophys.* 475 (2007), pp. L9–L13. DOI: 10.1051/0004-6361:20078462. arXiv: 0709.4584 [astro-ph] (cit. on p. 138).

[431] E. Aliu et al. "A three-year multi-wavelength study of the very-high-energy γ-ray blazar 1ES 0229+200". In: *Astrophys. J.* 782.1 (2014), p. 13. DOI: 10.1088/0004-637X/782/1/13. arXiv: 1312.6592 [astro-ph.HE] (cit. on p. 138).

[432] Yoram Avni. "Energy spectra of X-ray clusters of galaxies". In: *The Astrophysical Journal* 210 (1976), pp. 642–646. URL: https://api.semanticscholar.org/CorpusID:122675786 (cit. on p. 139).

[433] Jens Jasche, Arjen van Vliet, and Jörg P. Rachen. "Targeting Earth: CRPropa learns to aim". In: *PoS* ICRC2019 (2020), p. 447. DOI: 10.22323/1.358.0447. arXiv: 1911.05048 [astro-ph.HE] (cit. on p. 144).

[434] B. Theodore Zhang et al. "Ultraheavy Ultrahigh-Energy Cosmic Rays". In: (May 2024). arXiv: 2405.17409 [astro-ph.HE] (cit. on p. 148).

[435] W.E. Byerly. *An Elementary Treatise on Fourier's Series and Spherical, Cylindrical, and Ellipsoidal Harmonics: With Applications to Problems in Mathematical Physics*. Ginn, 1893. URL: https://books.google.de/books?id=DWQSAAAAIAAJ (cit. on p. 183).

[436] Emily C. Cunningham et al. "Quantifying the Stellar Halo's Response to the LMC's Infall with Spherical Harmonics". In: *Astrophys. J.* 898.1 (2020), p. 4. DOI: 10.3847/1538-4357/ab9b88. arXiv: 2006.08621 [astro-ph.GA] (cit. on p. 185).

[437] Ronald Aylmer Fisher. "Dispersion on a sphere". In: *Proceedings of the Royal Society of London. Series A. Mathematical and Physical Sciences* 217.1130 (1953), pp. 295–305 (cit. on p. 186).

[438] Nicholas I Fisher, Toby Lewis, and Brian JJ Embleton. *Statistical analysis of spherical data*. Cambridge university press, 1993 (cit. on p. 186).

[439] Julian Straub. *Bayesian inference with the von-Mises-Fisher distribution in 3d*. Last access 26/02/2025. URL: https://jstraub.github.io/download/straub2017vonMisesFisherInference.pdf (cit. on pp. 186, 187).

[440] Leonida Rosino. *Lezioni di astronomia*. Padova: CEDAM, 1979 (cit. on p. 187).

[441] Denise Boncioli, Simone Rossoni, and Caterina Trimarelli. "Ultra-high-energy cosmic rays: propagation and detection". In: *PoS* CORFU2021 (2022), p. 320. DOI: 10.22323/1.406.0320 (cit. on p. 191).

[442] R. J. Protheroe. "Acceleration and interaction of ultrahigh-energy cosmic rays". In: (Dec. 1998). Ed. by M. A. DuVernois, pp. 259–297. arXiv: astro-ph/9812055 (cit. on p. 192).

[443] *The Pierre Auger Observatory: Contributions to the 36th International Cosmic Ray Conference (ICRC 2019): Madison, Wisconsin, USA, July 24- August 1, 2019*. Sept. 2019. arXiv: 1909.09073 [astro-ph.HE] (cit. on pp. 207, 208).

[444] Luis Enrique Espinosa Castro, Simone Rossoni, and Günter Sigl. "Influence of plasma instabilities on the propagation of electromagnetic cascades from distant blazars". In: (May 2024). arXiv: 2405.15390 [astro-ph.HE] (cit. on pp. 136, 140–142, 219).

A

Sky distributions

This appendix presents some general concepts for the study of spherical quantities.

A.1 Spherical harmonics

The study of CR arrival directions and anisotropies are fundamental when stydying their sources. A natural choice to study the arrival directions distribution is the use of spherical coordinates. The most widely used mathematical tool for this type of study is the complete basis given by the spherical harmonics. In this appendix, we will review the definition and the most useful properties of this set of functions.

Given a position vector in $\mathbb{R}^3$ in Cartesian coordinates $\mathbf{r} = (x, y, z)$, the spherical coordinates r, θ and ϕ are given by

$$r = \sqrt{x^2 + y^2 + z^2} \quad , \quad \theta = \arccos\left(\frac{z}{r}\right) \quad \text{and} \quad \phi = \text{sgn}(y) \arccos\left(\frac{x}{\sqrt{x^2 + y^2}}\right) , \tag{A.1.1}$$

and we can see that $r \geq 0$, $0 \leq \theta \leq \pi$ and $0 \leq \phi \leq 2\pi$. A representation of the spherical coordinates is shown in Fig. A.1.1. Given the function $f : \mathbb{R}^2 \to \mathbb{C}$, the spherical harmonics are then obtained by solving the Laplace's equation in spherical coordinates [435]

$$\nabla^2 f = \frac{1}{r^2}\frac{\partial}{\partial r}\left(r^2 \frac{\partial f}{\partial r}\right) + \frac{1}{r^2 \sin\theta}\frac{\partial}{\partial \theta}\left(\sin\theta \frac{\partial f}{\partial \theta}\right) + \frac{1}{r^2 \sin^2\theta}\frac{\partial^2 f}{\partial \phi^2} = 0 , \tag{A.1.2}$$

where ∇^2 is the Laplace operator in spherical coordinates. The solution of Eq. (A.1.2) defines the spherical harmonic functions as

$$Y_{lm}(\theta, \phi) = (-1)^m \sqrt{\frac{2l+1}{4\pi}\frac{(l-m)!}{(l+m)!}} P_{lm}(\cos\theta) e^{im\phi} , \tag{A.1.3}$$

where $P_{lm}(\cos\theta)$ are the associated Legendre polynomials without the Condon-Shortley phase factor. The spherical harmonics are identified by the two integers l and m: for the value $l = 0, 1, 2, ...$ we have that $-l \leq m \leq l$. So for each value of l there are $2l + 1$ spherical harmonics.

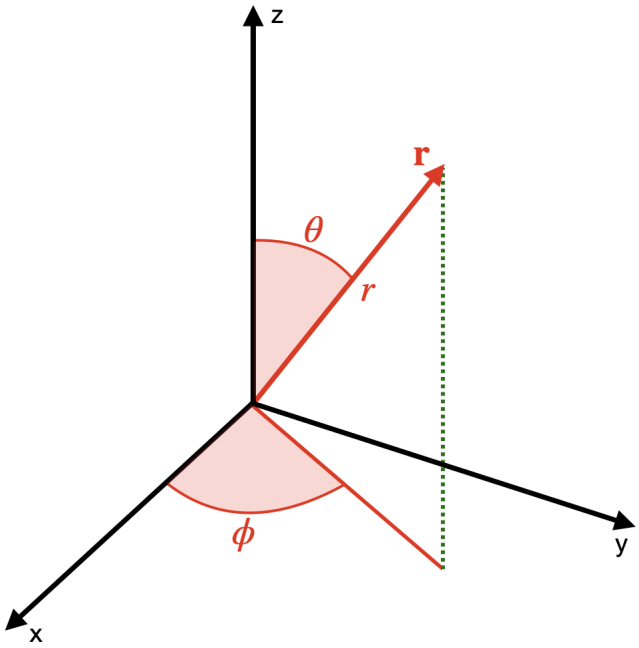

Figure A.1.1: Spherical coordinate convention.

The spherical harmonics are characterized by the following properties

$$Y_{l,-m}(\theta,\phi) = (-1)^m Y^*_{lm}(\theta,\phi)\,, \tag{A.1.4}$$

$$\sum_{m=-l}^{l} Y_{lm}(\theta,\phi)Y^*_{lm}(\theta,\phi) = \frac{2l+1}{4\pi}\,, \tag{A.1.5}$$

$$\sum_{l=0}^{+\infty}\sum_{m=-l}^{l} Y_{lm}(\theta,\phi)Y^*_{lm}(\theta',\phi') = \delta\left(\phi-\phi'\right)\delta\left(\cos\theta-\cos\theta'\right)\,, \tag{A.1.6}$$

$$\int_0^{2\pi} d\phi \int_{-1}^{1} d\cos\theta\, Y_{lm}(\theta,\phi)Y^*_{l'm'}(\theta,\phi) = \delta_{ll'}\delta_{mm'}\,, \tag{A.1.7}$$

where z^* is the complex conjugation operation, $\delta_{xx'}$ is the Kronecker delta symbol and $\delta(x-x')$ is the Dirac delta function. The latter property was obtained under a specific normalization convention for the spherical harmonics. In general, the orthonormality condition is

$$\int_0^{2\pi} d\phi \int_{-1}^{1} d\cos\theta\, Y_{lm}(\theta,\phi)Y^*_{l'm'}(\theta,\phi) = \mathcal{A}\,\delta_{ll'}\delta_{mm'}\,, \tag{A.1.8}$$

where $\mathcal{A}$ is a normalization factor. In this work we consider the complex representation of the

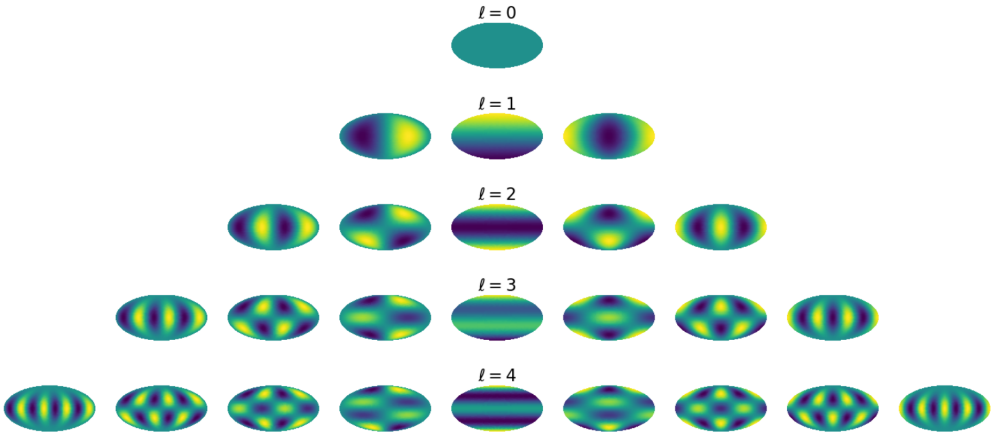

Figure A.1.2: Real spherical harmonics in Mollweide projection for l from 0 to 4 and all the corresponding values of m. The z-axis is oriented upwards with $\theta = 0$ at the north pole and $\theta = \pi$ at the south pole. The angle ϕ goes from π to $-\pi$, from the left to the right of the figure. The value of of m is 0 in the central plots, negative in the left plots and positive in the right plots. Figure taken from [436].

spherical harmonics such that $\mathcal{A} = 1$. The expressions for the first harmonics are given by

$$Y_{00}(\theta,\phi) = \frac{1}{\sqrt{4\pi}}\,, \tag{A.1.9}$$

$$Y_{1-1}(\theta,\phi) = \frac{1}{2}\sqrt{\frac{3}{2\pi}}\sin\theta\, e^{-i\phi}\,, \tag{A.1.10}$$

$$Y_{10}(\theta,\phi) = \frac{1}{2}\sqrt{\frac{3}{\pi}}\cos\theta\,, \tag{A.1.11}$$

$$Y_{11}(\theta,\phi) = -\frac{1}{2}\sqrt{\frac{3}{2\pi}}\sin\theta\, e^{i\phi}\,, \tag{A.1.12}$$

$$Y_{2-2}(\theta,\phi) = \frac{1}{4}\sqrt{\frac{15}{2\pi}}\sin^2\theta\, e^{-2i\phi}\,, \tag{A.1.13}$$

$$Y_{2-1}(\theta,\phi) = \frac{1}{2}\sqrt{\frac{15}{2\pi}}\sin\theta\cos\theta\, e^{-i\phi}\,, \tag{A.1.14}$$

$$Y_{20}(\theta,\phi) = \frac{1}{4}\sqrt{\frac{5}{\pi}}\left(3\cos^2\theta - 1\right)\,, \tag{A.1.15}$$

$$Y_{21}(\theta,\phi) = -\frac{1}{2}\sqrt{\frac{15}{2\pi}}\sin\theta\cos\theta\, e^{i\phi}\,, \tag{A.1.16}$$

$$Y_{22}(\theta,\phi) = \frac{1}{4}\sqrt{\frac{15}{2\pi}}\sin^2\theta\, e^{2i\phi}\,, \tag{A.1.17}$$

The first spherical harmonics are shown in Fig A.1.2. Given the definition of $Y_{00}(\theta,\phi)$, we can also derive another property that will be useful in this type of analysis. In particular, the integral

of a given spherical harmonic $Y_{lm}(\theta, \phi)$ can be written as

$$\int_0^{2\pi} d\phi \int_{-1}^{1} d\cos\theta \, Y_{lm}(\theta, \phi) = \sqrt{4\pi} \int_0^{2\pi} d\phi \int_{-1}^{1} d\cos\theta \, Y_{lm}(\theta, \phi) Y_{00}^*(\theta, \phi) = \sqrt{4\pi} \, \delta_{l0}\delta_{m0} \, . \tag{A.1.18}$$

If we consider a generic function of the two spherical angles $f(\theta, \phi)$, we can expand it into spherical harmonics as

$$f(\theta, \phi) = \sum_{l=0}^{+\infty} \sum_{m=-l}^{l} a_{lm} Y_{lm}(\theta, \phi) \, , \tag{A.1.19}$$

where the spherical coefficients a_{lm} are given by the projection

$$a_{lm} = \int_0^{2\pi} d\phi \int_{-1}^{1} d\cos\theta \, f(\theta, \phi) Y_{lm}^*(\theta, \phi) \, . \tag{A.1.20}$$

As we have seen, for each value of l there are $2l + 1$ spherical coefficients. Using the property for $Y_{l,-m}(\theta, \phi)$, we can immediately see that for a real value function $f(\theta, \phi)$ the following property holds

$$a_{l-m} = (-1)^m a_{lm}^* \, . \tag{A.1.21}$$

The angular power spectrum of $f(\theta, \phi)$ is then defined as the average values of the spherical coefficients

$$\mathcal{C}_l = \frac{1}{2l+1} \sum_{m=-l}^{l} |a_{lm}|^2 \, , \tag{A.1.22}$$

from which it immediately follows that

$$\int_0^{2\pi} d\phi \int_{-1}^{1} d\cos\theta \, |f(\theta, \phi)|^2 = \sum_{l=0}^{+\infty} (2l + 1)\mathcal{C}_l \, . \tag{A.1.23}$$

A.2 The von Mises-Fisher distribution

The *von Mises-Fisher* distribution function is a probability function usually used to describe directional data on a sphere [437, 438]. It can be also interpreted as a generalization of a normal distribution on a sphere. In particular, given the d-dimensional unit vector $\hat{\mathbf{n}}$ on the sphere $\mathbb{S}^{d-1}$, the von Mises-Fisher distribution function is given by

$$\Pi_{\text{vMF}}(\hat{\mathbf{n}}; \hat{\mu}, \kappa) = C_d(\kappa) \exp\left(\kappa \, \hat{\mathbf{n}} \cdot \hat{\boldsymbol{\mu}}\right) \, , \tag{A.2.1}$$

where $\hat{\boldsymbol{\mu}}$ is the mean direction on the sphere $\mathbb{S}^{d-1}$, $\kappa > 0$ is the concentration parameter, $\hat{\boldsymbol{n}} \cdot \hat{\boldsymbol{\mu}}$ is the scalar vector of the two unit vectors and $C_d(\kappa)$ is a normalization constant [439].

If we consider the two-dimensional sphere $\mathbb{S}^2$, we can assume that the vector $\hat{\boldsymbol{\mu}}$ is directed along the z-axis. The normalization constant is then given by

$$C_2(\kappa) = \int_0^{2\pi} d\phi \int_{-1}^{1} d\cos\theta \, \exp\left(\kappa \cos\theta\right) = \frac{4\pi \sinh\kappa}{\kappa} \, , \tag{A.2.2}$$

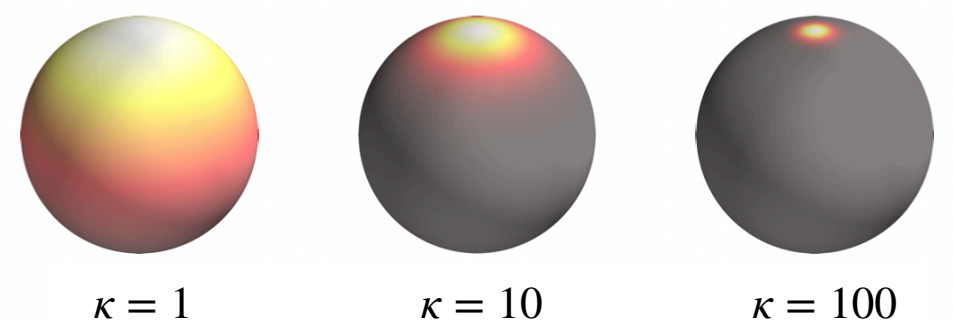

Figure A.2.1: Representation of the von Mises-Fisher distribution in Eq. (A.2.3) with the mean direction $\hat{\boldsymbol{\mu}}$ at the pole and for different values of the concentration parameter κ. Figure taken from [439].

and then the von Mises-Fisher distribution in three dimensions is

$$\Pi_{\text{vMF}}(\hat{\mathbf{n}}; \hat{\boldsymbol{\mu}}, \kappa) = \frac{\kappa \, \exp\left(\kappa \, \hat{\mathbf{n}} \cdot \hat{\boldsymbol{\mu}}\right)}{4\pi \sinh \kappa} \,. \tag{A.2.3}$$

We can see that for κ small the distribution $\Pi_{\text{vMF}}(\hat{\mathbf{n}}; \hat{\boldsymbol{\mu}}, \kappa)$ converges to the uniform distribution on the sphere $\Pi_{\text{vMF}}(\hat{\mathbf{n}}; \hat{\boldsymbol{\mu}}, \kappa) \to (4\pi)^{-1}$. For κ very large, the von Mises-Fisher distribution approaches a Dirac delta function on the sphere in the direction of $\hat{\boldsymbol{\mu}}$. A representation of the distribution in Eq. (A.2.3) is shown in Fig. A.2.1.

A.3 Coordinate systems

We have seen that the study of directional quantities, such as the arrival directions of CRs, requires the use of spherical coordinates in the sky. This means that a specific coordinate system must be defined. This section briefly describes the most commonly used coordinate systems in astrophysics (see [440] for a more detailed discussion).

The first coordinate system is the *local system*: in this system, the main direction is given by the vertical direction, which coincides with the gravitational acceleration. The intersection of this vertical with the celestial sphere (i.e. the imaginary sphere with an infinite radius and with the Earth at its center) defines the *zenit* point, while the opposite point is called *nadir*. This vertical represents the z axis of the local system. The first coordinate is then the *zenith angle* θ, defined as in Fig. A.1.1. Sometimes, the altitude $a = 90° - \theta$ is also used. The second coordinate is the *azimuth angle* φ, which is defined as zero in the North direction and then opens clockwise[1]. We can already see that this coordinate system has a limitation: it depends on the location of the observer and on the time of the observation.

The *equatorial system* is defined to remove the ambiguity present in the local system. The fundamental plane in the equatorial system is the *clestial equatorial plane*, defined as the projection of the Earth's equatorial plane onto the celestial sphere. Since the equatorial plane is inclined with respect to the plane of the ecliptic (i.e. the imaginary plane containing the orbit of the Earth around the Sun), the Sun intersects the equatorial plane twice a year. The point of intersection as the Sun passes from the celestial southern hemisphere to the celestial northern

[1]The Pierre Auger Observatory uses a slightly different convention for the local coordinate system: the altitude a is called *elevation* Ω, and the azimuth angle φ opens counterclockwise..

hemisphere is called the vernal equinox (or γ-point). The *declination* δ is then defined to be zero at the vernal equinox and it varies between 90° at the North Pole and −90° at the South Pole. The *right ascension* α is also zero at the vernal equinox and it runs counterclockwise. We can see that a set of equatorial coordinates (α, δ) defines a unique point in the sky.

Both the local system and the equatorial system are still dependent on the fact that they express coordinates relative to the Earth's motion. A coordinate system independent of the Earth's position is the *Galactic system*. The center of the Galactic system is the Sun, and the fundamental plane is in the Galactic plane. The *Galactic latitude* b is defined as the angular distance of an object from the Galactic plane, and it has values between −90° and 90°. The *Galactic longitude* l is the angular distance measured on the Galactic plane, it has values from −180° to 180° and it is positive in the counterclockwise direction. In the Galactic system, the Galactic center has the coordinates $b = 0°$ and $l = 0°$.

The last coordinate system considered in this work is the *Supergalactic system*, which is based on the Supergalactic plane where the supercluster of galaxies containing the Milky Way is located. The *Supergalactic latitude* SGB and the *Supergalactic longitude* SGL. The origin point SGL = 0 and SGB = 0 lies in the constellation Cassiopeia in Galactic coordinates $\sim (l = 137°, b = 0°)$, while the North Pole SGB = 90° is in the constellation Hercules $\sim (l = 47°, b = 6°)$. Unlike the Galactic longitude, the Supergalactic longitude takes values from 0° to 360° counterclockwise.

A.4 Rayleigh analysis

The Rayleigh analysis is a technique used to study directional anisotropies in cosmic ray data [157, 158]. Given the Fourier expansion of the angular coordinate φ of N events

$$\frac{dN}{d\varphi} = N\left[1 + \sum_{k=0}^{+\infty} a_k \cos(k\varphi) + \sum_{k=0}^{+\infty} b_k \sin(k\varphi)\right], \tag{A.4.1}$$

the coefficients a_k and b_k are given by

$$a_k = \frac{2}{\mathcal{N}} \sum_{i=1}^{N} \omega_i \cos(k\varphi_i) \quad \text{and} \quad b_k = \frac{2}{\mathcal{N}} \sum_{i=1}^{N} \omega_i \sin(k\varphi_i), \tag{A.4.2}$$

where $\mathcal{N} = \sum_{i=1}^{N} \omega_i$ and ω_i are weights to account for the experiment exposure. The amplitude r_k and the phase φ_k are given by

$$r_k = \sqrt{a_k^2 + b_k^2} \quad \text{and} \quad \varphi_k = \frac{1}{k} \arctan\left(\frac{b_k}{a_k}\right). \tag{A.4.3}$$

We can test the significance of the amplitude r_k by assuming that the coordinates φ_i follow a homogeneous distribution. Therefore, for a large number of events, the coefficients a_k and b_k will follow a normal distribution centered on zero and with variance $\sigma = \sqrt{2/\mathcal{N}}$. The combined probability distribution of a_k and b_k is then given by

$$\mathcal{P}(a_k, b_k) = \mathcal{P}(a_k) \cdot \mathcal{P}(b_k) = \frac{1}{2\pi\sigma^2} \exp\left(-\frac{a_k^2 + b_k^2}{2\sigma^2}\right). \tag{A.4.4}$$

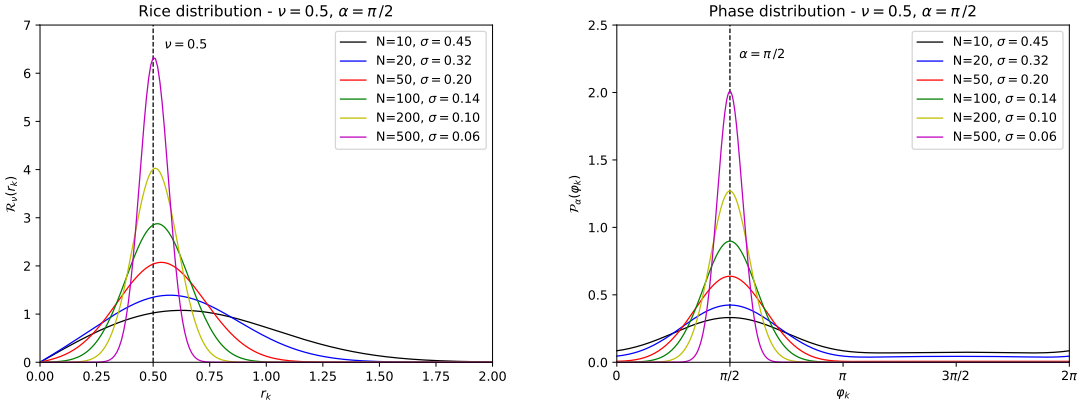

Figure A.4.1: Left: Rice distribution in Eq. (A.4.9) for $\nu = 0.5$ and $\alpha = \pi/2$. Different colors correspond to different values of N. Right: same as left panel, but for the phase distribution in Eq. (A.4.11).

We can then obtain the probability distribution of r_k and φ_k taking into account the change of variables in Eq. (A.4.3).

$$\mathcal{P}(r_k, \phi_k) = \frac{r_k}{2\pi\sigma^2} \exp\left(-\frac{r_k^2}{2\sigma^2}\right) . \tag{A.4.5}$$

The marginalized distribution of Eq. (A.4.5) is the *Rayleigh distribution*, given by

$$\mathcal{R}(r_k) = \int_0^{2\pi} \mathcal{P}(r_k, \phi_k)\, d\varphi_k = \frac{r_k}{\sigma^2} \exp\left(-\frac{r_k^2}{2\sigma^2}\right) , \tag{A.4.6}$$

which has expectation value $\sigma\sqrt{\pi/2} = \sqrt{\pi/\mathcal{N}}$. The probability of getting an amplitude value greater than a given r'_k is then given by

$$P(r_k \geq r'_k) = \int_{r'_k}^{+\infty} \mathcal{R}(r_k)\, dr_k = \exp\left(-\frac{r_k^2}{2\sigma^2}\right) = \exp\left(-\frac{\mathcal{N} r_k^2}{4}\right) . \tag{A.4.7}$$

The same analysis can be repeated assuming that the population of arrival directions considered is characterized by a dipolar distribution in the direction α with intensity ν. In this case, the coefficients a_k and b_k will follow a normal distribution centered on $\nu\cos\alpha$ and $\nu\sin\alpha$, respectively. Following the same derivation as in the above case, the combined probability distribution of r_k and φ_k is now given by

$$\mathcal{P}(r_k, \varphi_k) = \frac{r_k}{2\pi\sigma^2} \exp\left[-\frac{r_k^2 + \nu^2 - r_k\nu\cos(\varphi_k - \alpha)}{2\sigma^2}\right] . \tag{A.4.8}$$

We can now test the significance of the amplitude r_k and of the phase ϕ_k by marginalizing Eq. (A.4.8). For r_k we obtain the *Rice distribution*

$$\mathcal{R}_\nu(r_k) = \frac{r_k}{\sigma^2} \exp\left(-\frac{r_k^2 + \nu^2}{2\sigma^2}\right) I_0\left(\frac{r_k\nu}{\sigma^2}\right) , \tag{A.4.9}$$

where $I_0(x)$ is the modified Bessel function of the first kind with order zero given by

$$I_0(x) = \frac{1}{2\pi} \int_0^{2\pi} e^{-x\cos\theta}\, d\theta\,. \tag{A.4.10}$$

We can see that the Rice distribution is a generalization of the Rayleigh distribution, where $\nu = 0$. Similarly, the maginalized distribution for the phase φ_k is given by

$$\begin{aligned}\mathcal{P}_\alpha(\varphi_k) &= \int_0^{+\infty} \mathcal{P}(r_k, \varphi_k)\, dr_k \\ &= \frac{1}{2\pi} \exp\left(-\frac{\nu^2}{2\sigma^2}\right) \left[1 + \frac{\nu}{\sigma}\sqrt{\frac{\pi}{2}} \cos\left(\varphi_k - \alpha\right) \exp\left(\frac{\nu^2}{2\sigma^2}\cos(\varphi_k - \alpha)\right)\right. \\ &\qquad \left. \cdot \left(1 + \operatorname{erf}\left(\frac{\nu}{\sqrt{2}\sigma}\cos(\varphi_k - \alpha)\right)\right)\right]\,,\end{aligned} \tag{A.4.11}$$

where $\operatorname{erf}(x)$ is the Gaussian error function. In Fig. A.4.1 the distributions in Eqs. (A.4.9) and (A.4.11) are shown for $\nu = 0.5$ and $\alpha = \pi/2$ and several values of N[2]. It can be seen that the expectation value of $\mathcal{R}_\nu$ is always slightly larger than ν, while the expectation value of $\mathcal{P}_\alpha$ is α. Both the distributions become narrower as ν^2/σ^2 increases (i.e. as N increases).

[2] In Fig. (A.4.1) we have assumed that $\omega_i = 1$ for all evetns. Therefore $\mathcal{N} = N$.

B

Cosmic ray interactions

In this appendix some important quantities realated to photohadronic interactions are presented and discussed.

B.1 Interaction rate

In this appendix, the derivation of the interaction rate in Eq. (4.45) is demonstrated. In particular, the following procedure is based on the derivation presented in [177, 441]. Let us define the particle flux Φ as the number of particles crossing a plane of area dA orthogonal to the direction of the particle beam in the time dt, i.e.

$$\Phi = \frac{d^2N}{dA\,dt}\,. \tag{B.1.1}$$

Given the interaction process $a+b \to X$, where a is the projectile particle, b is the target particle and X is the final state of the process, the number of interactions per unit time in the case of a single target particle is given by

$$\frac{dN_{\rm int}}{dt} = \Phi_a \sigma\,, \tag{B.1.2}$$

where σ is the cross section of the process. If we now consider a distribution of target particles, the number of target particles encountered by the beam particles during the time dt is given by

$$dN_b = n_b \beta_a\, dA\, dt = n_b\, dl\, dA = n_b\, dV\,, \tag{B.1.3}$$

where n_b is the number density of the particles b and β_a is the velocity of the particles a. Therefore, Eq. (B.1.2) becomes

$$\frac{d^2N_{\rm int}}{dV\,dt} = \Phi_a n_b \sigma\,. \tag{B.1.4}$$

The interaction rates derived in Eqs. (B.1.2) and (B.1.4) have been obtained under the assumption that both the particles a and b are monochromatic in energy. However, it is possible to generalized the results to the case of different energy distributions. In particular, if the energy

distributions of particles a and b are given by $n_a(E_a)$ and $n_b(E_b)$ respectively, the interaction rate is given by

$$\frac{d^3N_{\rm int}}{dE_X\,dV\,dt} = \int \frac{d\sigma}{dE_X}\beta_{\rm rel}(1-\boldsymbol{\beta}_a\cdot\boldsymbol{\beta}_b)n_a(E_a)n_b(E_b)\,dE_a\,dE_b\,, \tag{B.1.5}$$

where $d\sigma/dE_X$ is the differential cross section, $\boldsymbol{\beta}_a$ and $\boldsymbol{\beta}_b$ are the velocity vectors of particles a and b in the laboratory frame, and $\beta_{\rm rel}$ is the relative velocity between two particles. If we consider that the target particles to be photons, we obtain that $\boldsymbol{\beta}_a\cdot\boldsymbol{\beta}_b = \beta_a\cos\theta$ and $\beta_{\rm rel}=1$, where θ is the angle between the two particle momenta in the laboratory frame. If we also consider only one projectile particle b with fixed energy, Eq. (B.1.5) becomes

$$\frac{d^2N_{\rm int}}{dE_X\,dt} = \int \frac{d\sigma}{dE_X}(1-\beta_a\cos\theta)n(\varepsilon)\,d\varepsilon\,, \tag{B.1.6}$$

where ε is the photon energy. We can now integrate over dE_X as we are interested in the total interaction rate. Assuming that the target photon field is isotropic, we obtain that

$$\frac{dN_{\rm int}}{dt} = \frac{1}{4\pi}\int \sigma(\varepsilon)(1-\beta_a\cos\theta)n(\varepsilon)\,d\varepsilon\,d\Omega\,, \tag{B.1.7}$$

where Ω is the solid angle. We can now write the photon energy in the rest frame of the particle a as $\varepsilon' = \varepsilon\,\Gamma_a(1-\beta_a\cos\theta)$, from which we see that

$$d\varepsilon' = -\varepsilon\Gamma_a\beta_a d\cos\theta\,, \tag{B.1.8}$$

and then

$$\frac{dN_{\rm int}}{dt} = \frac{1}{2\Gamma_a^2}\int_{\varepsilon'_{\rm th}}^{+\infty}\sigma(\varepsilon')\varepsilon'\int_{\varepsilon'/2\Gamma_a}^{+\infty}\frac{n(\varepsilon)}{\varepsilon^2}\,d\varepsilon\,d\varepsilon'\,, \tag{B.1.9}$$

where $\varepsilon'_{\rm th}$ is the photon energy threshold of the considered process in the reference frame of the particle a, and we have integrated over the azimuthal angle.

B.2 Initial state kinematics

Given the interaction process between a CR with energy $E_{\rm CR}$ and mass $m_{\rm CR}$ and a photon with energy ε, the center of mass energy s is given by

$$s(E_{\rm CR},\varepsilon,\theta) = m_{\rm CR}^2 + 2E_{\rm CR}\varepsilon(1-\beta_{\rm CR}\cos\theta)\,, \tag{B.2.1}$$

where $\beta_{\rm CR}$ is the CR velocity and θ is the angle between the cosmic ray and photon momentum vectors. The maximum value of s corresponds to a head-on collision, where

$$s_{\rm max}(E_{\rm CR},\varepsilon) = m_{\rm CR}^2 + 4E_{\rm CR}\varepsilon\,. \tag{B.2.2}$$

We can then write the interaction rate in Eq. (B.1.9) as in [442]

$$\begin{aligned}\tau_{\rm int}^{-1}(E_{\rm CR}) &= \frac{1}{8E_{\rm CR}^2\beta_{\rm CR}}\int_{\varepsilon_{\rm th}}^{\infty}\frac{n(\varepsilon)}{\varepsilon^2}\int_{s_{\rm th}}^{s_{\rm max}(E_{\rm CR},\varepsilon)}\sigma(s)(s-m_{\rm CR}^2)\,ds\,d\varepsilon \\ &= \frac{1}{8E_{\rm CR}^2\beta_{\rm CR}}\int_{\varepsilon_{\rm th}}^{\infty}\frac{n(\varepsilon)}{\varepsilon^2}\phi(s_{\rm max}(E_{\rm CR},\varepsilon))\,d\varepsilon\,,\end{aligned} \tag{B.2.3}$$

where

$$\phi(s_{\max}(E_{\rm CR},\varepsilon)) = \int_{s_{\rm th}}^{s_{\max}(E_{\rm CR},\varepsilon)} \sigma(s)(s-m_{\rm CR}^2)\,ds\,. \tag{B.2.4}$$

From Eq. (B.2.3) we can see that the probability distribution of the interaction between a cosmic ray with energy $E_{\rm CR}$ and a photon with energy ε from the field $n(\varepsilon)$ is given by

$$\mathcal{P}(\varepsilon) \propto \frac{n(\varepsilon)}{\varepsilon^2}\phi(s_{\max}(E_{\rm CR},\varepsilon))\,, \tag{B.2.5}$$

for $\varepsilon \geq \varepsilon_{\rm th}$. Similarly, the center of mass energy is distributed as

$$\mathcal{Q}(s) \propto \sigma(s)(s-m_{\rm CR}^2)\,, \tag{B.2.6}$$

for $s_{\rm th} \leq s \leq s_{\max}(E_{\rm CR},\varepsilon)$. The kinematics of the initial state is closed by calculating the angle θ as

$$\cos\theta = \frac{1}{\beta_{\rm CR}}\left(1+\frac{m_{\rm CR}^2-s}{2E_{\rm CR}\varepsilon}\right)\,. \tag{B.2.7}$$

B.3 Connecting energy intervals

The presence of energy loss during the propagation of UHECRs implies the fact that the observed energy E at redshift $z=0$ is different from the energy $E_s(z)$ at a generic redshift value z. In [241, 248], the connection between these two energy intervals was shown for protons, which lose energy due to the adiabatic term Eq. (4.32) and interactions with CMB photons (see Eq. (4.51)).

In this case, the energy loss equation is given by

$$-\frac{1}{E_s}\frac{dE_s}{dt} = \beta(E_s,z(t)) + H(z(t))\,, \tag{B.3.1}$$

where the right hand side contains the photohadronic interaction term $\beta(E_s,z(t))$ and the adiabatic term from Eq. (4.32). It is more convenient to use Eq. (4.31) to write the energy loss equation in terms of the redshift variable. We obtain that

$$\frac{1}{E_s}\frac{dE_s}{dz} = \frac{\beta(E_s,z)}{(1+z)H(z)} + \frac{1}{1+z}\,. \tag{B.3.2}$$

Given the initial condition $E_s(z=0)=E$, Eq. (B.3.2) becomes

$$E_s(z) = E + \int_0^z \frac{E_s(z')\beta(E_s(z'),z')}{(1+z')H(z')}\,dz' + \int_0^z \frac{E_s(z')}{1+z'}\,dz'\,. \tag{B.3.3}$$

We can now use the Eqs. (4.49) and (4.54) to show that

$$\beta(E_s(z),z) = (1+z)^3\beta_0((1+z)E_s(z)) = \frac{(1+z)^2}{E_s(z)}b_0((1+z)E_s(z))\,, \tag{B.3.4}$$

and then

$$E_s(z) = E + \int_0^z \frac{1+z'}{H(z')}b_0((1+z')E_s(z'))\,dz' + \int_0^z \frac{E_s(z')}{1+z'}\,dz'\,. \tag{B.3.5}$$

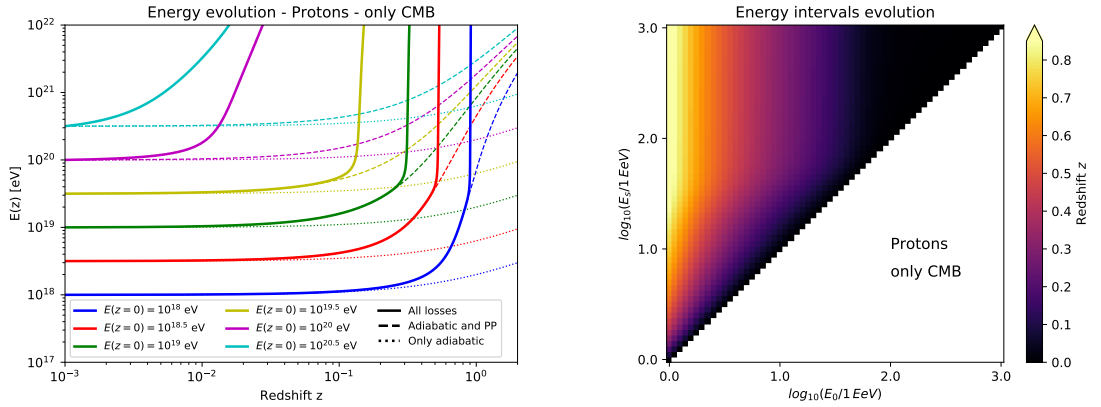

Figure B.3.1: Left: solution of Eq. (B.3.2) for protons interacting with CMB photons in an expanding Universe. Different energies at redshift $z = 0$ are shown in different colors. The dotted lines correspond to the scenarios with adiabatic losses only, the dashed lines to the scenarios with adiabatic and pair production losses and the continuous lines to the scenarios with adiabatic, pair production and pion production losses. Right: energy and redshift at the source of a given observed proton of energy E_0 interacting with CMB photons in an expanding Universe. Figures created with `CRPropa` [236].

We define the variable $y(z)$ as

$$y(z) = \frac{dE_s(z)}{dE}\,, \tag{B.3.6}$$

from which we can see that

$$y(z) = 1 + \int_0^z \frac{(1+z')^2}{H(z')} \frac{db_0((1+z')E_s(z'))}{d((1+z')E_s(z'))} y(z')\,dz' + \int_0^z \frac{y(z')}{1+z'}\,dz'\,. \tag{B.3.7}$$

The result in Eq. (B.3.7) corresponds to the solution of the following differential equation

$$\frac{1}{y}\frac{dy}{dz} = \frac{(1+z)^2}{H(z)} \frac{db_0((1+z)E_s(z)}{d((1+z)E_s(z))} + \frac{1}{1+z}\,, \tag{B.3.8}$$

the solution of which can be written as

$$y(z) = \frac{dE_s(z)}{dE} = (1+z)\exp\left[\int_0^z \frac{(1+z')^2}{H(z')} \frac{db_0((1+z')E_s(z')}{d((1+z')E_s(z'))}\,dz'\right]\,. \tag{B.3.9}$$

The result in Eq. (B.3.9) gives the connection between energy intervals at zero redshift and at larger redshift values.

Solutions of Eq. (B.3.2) for protons of different energies at $z = 0$ losing energy adiabatically and via pair production and pion production on the CMB background are shown in the left panel of Fig. B.3.1. The contribution of different energy loss mechanisms is shown with different line styles. We can clearly see that photopion production strongly limits the flux of high-energy protons to the sources at low redshift. The redshift dependence of E_s as a function of the energy at redshift $z = 0$ is also shown in the right panel of Fig. B.3.1.

Corresponding solutions in the case of nuclei heavier than protons can be found in [240, 250]. In this case, the energy loss equation can be written taking into account the fact that

$$\frac{1}{E_s}\frac{dE_s}{dt} = \frac{1}{\Gamma_s}\frac{d\Gamma_s}{dt} + \frac{1}{A_s}\frac{dA_s}{dt}\,, \tag{B.3.10}$$

where $E = Am_p\Gamma$ and m_p is the proton mass. In this way it is possible to separate the processes that change the nucleus Lorentz factor from those that change the mass number. The evolution functions $\Gamma_s(z)$ and $A_s(z)$ are then given by the coupled system of equations

$$\frac{1}{\Gamma_s}\frac{d\Gamma_s}{dz} = \frac{\beta(\Gamma_s, A_s, z)}{(1+z)H(z)} + \frac{1}{1+z}\,, \tag{B.3.11}$$

$$\frac{1}{A_s}\frac{dA_s}{dz} = \frac{\chi(\Gamma_s, A_s, z)}{(1+z)H(z)}\,, \tag{B.3.12}$$

where the β function characterizes the interactions that change only the Lorentz factor and the χ function characterizes the interactions that change only the atomic mass number.

B.4 Neutrino propagation

The extragalactic propagation of neutrinos produced by astrophysical sources is only affected by the expansion of the Universe. Therefore, the neutrino energy loss rate is given by

$$-\frac{1}{E_\nu}\frac{dE_\nu}{dt} = H(z(t))\,, \tag{B.4.1}$$

where $H(z(t))$ is given by Eq. (4.30). We can use the relation between cosmic time t and redshift z in Eq. (4.31) to obtain

$$\frac{dE_\nu}{dz} = \frac{E_\nu}{1+z}\,, \tag{B.4.2}$$

which has the solution $E_\nu(z) = E_{\nu,0}(1+z)$, where $E_{\nu,0}$ is the neutrino energy at redshift $z = 0$.

Given the neutrino injection rate (i.e. the number of neutrinos emitted per unit of energy, unit of time and unit of volume) of an astrophysical source $Q_\nu(E_\nu, t)$, the observed neutrino spectral energy density (i.e. the number of neutrinos per unit of energy and unit of time) $n_\nu(E_{\nu,0})$ is given by

$$n_\nu(E_{\nu,0}) = \int_t^{t_0} d\tau\, Q_\nu(E_\nu(\tau), \tau)\,\frac{dE_\nu(\tau)}{dE_{\nu,0}}\,, \tag{B.4.3}$$

where $t_0 > t$. Since the observation time t_0 corresponds to the redshift $z = 0$ and the minimum emission time t corresponds to the maximum redshift $z_{\max}$, we can write Eq. (B.4.3) as

$$n_\nu(E_{\nu,0}) = \int_0^{z_{\max}} dz\,\frac{Q_\nu(E_\nu(z), z)}{(1+z)H(z)}\,\frac{dE_\nu(z)}{dE_{\nu,0}}\,. \tag{B.4.4}$$

Since $dE_\nu(z)/dE_{\nu,0} = 1+z$, we have that

$$n_\nu(E_{\nu,0}) = \frac{1}{H_0}\int_0^{z_{\max}} dz\,\frac{Q_\nu(E_\nu(z), z)}{\sqrt{(1+z)^3\Omega_m + \Omega_\Lambda}}\,. \tag{B.4.5}$$

We can now write the neutrino injection rate as

$$Q_\nu(E_\nu(z), z) = \xi(z) Q_\nu(E_\nu(z))\,, \tag{B.4.6}$$

where the function $\xi(z)$ describes the redshift evolution of the source distribution. The astrophysical neutrino flux is then given by

$$\begin{aligned} J_\nu(E_{\nu,0}) &= \frac{c}{4\pi} n_\nu(E_{\nu,0}) \\ &= \frac{c}{4\pi H_0} \int_0^{z_{\max}} dz \, \frac{\xi(z)}{\sqrt{\Omega_{\mathrm{m}}(1+z)^3 + \Omega_\Lambda}} Q_\nu(E_\nu(z)) \,, \end{aligned} \tag{B.4.7}$$

where $J_\nu(E_{\nu,0})$ is the observed number of neutrinos per unit of energy, per unit of area, per unit of time and per unit of solid angle.

C

Technical details for UHECR anisotropy simulations

This appendix is based on the publication:

- S. Rossoni and G. Sigl. (2025). *Anisotropy signal of UHECRs from a structured magnetized Universe*. **Phys. Rev. D**, 112, 023015. arXiv:2502.19324 [astro-ph.HE]. https://doi.org/10.1103/4zt7-s48v.

This appendix provides some technical details for the UHECR anisotropy simulations described in Chapter 7.

C.1 Weighting procedure

In this section, we will derive the weight factor to assign to a given observed particle at end of a simulation to reproduce a different injection scenario than the simulated one. Let us start considering the case of simulations where the injection rate in the energy interval between $E_{\rm min}$ and $E_{\rm max}$ is given by

$$Q_{\rm sim}(E) = \sum_A Q^A_{\rm sim}(E) \propto \sum_A b_A \left(\frac{E}{E_0}\right)^{-\alpha} , \tag{C.1.1}$$

where $Q^A_{\rm sim}(E)$ is the injection rate of a single species, the coefficients b_A characterize the simulated abundances, such that $\sum_A b_A = 1$, E_0 is a reference energy and α is the simulated spectral index. The probability of injecting a cosmic ray with mass A and energy E can be obtained as

$$p^A_{\rm sim}(E) = \frac{b_A}{N_{\rm sim}} \left(\frac{E}{E_0}\right)^{-\alpha} , \tag{C.1.2}$$

where the normalization factor $N_{\rm sim}$ is

$$N_{\rm sim} = \sum_A b_A \int_{E_{\rm min}}^{E_{\rm max}} dE \left(\frac{E}{E_0}\right)^{-\alpha} = E_0^\alpha \mathcal{I}_{\rm sim} , \tag{C.1.3}$$

and the integral $\mathcal{I}_{\rm sim}$ is defined as

$$\mathcal{I}_{\rm sim} = \int_{E_{\rm min}}^{E_{\rm max}} dE\, E^{-\alpha}\,. \tag{C.1.4}$$

The new injection rate that we want our simulations to reproduce is usually given by

$$Q_{\rm rep}(E) = \sum_A Q^A_{\rm rep}(E) \propto \sum_A a_A \left(\frac{E}{E_0}\right)^{-\gamma} f_{\rm cut}\left(\frac{E}{Z_A R_{\rm cut}}\right)\,, \tag{C.1.5}$$

where, as before, the coefficients a_A represent the new abundances, such that $\sum_A a_A = 1$, γ is the new spectral index and the cutoff function $f_{\rm cut}$ now depends on the charge Z_A of the injected particle and on a given rigidity cutoff value $R_{\rm cut}$. Therefore, the corresponding cutoff energy of the species A is given by $E_{{\rm cut},A} = Z_A R_{\rm cut}$. Once more, we can write the injection probability as

$$p^A_{\rm rep}(E) = \frac{a_A}{N_{\rm rep}} \left(\frac{E}{E_0}\right)^{-\gamma} f_{\rm cut}\left(\frac{E}{Z_A R_{\rm cut}}\right)\,, \tag{C.1.6}$$

with the normalization factor

$$N_{\rm rep} = \sum_A a_A \int_{E_{\rm min}}^{E_{\rm max}} dE \left(\frac{E}{E_0}\right)^{-\gamma} f_{\rm cut}\left(\frac{E}{Z_A R_{\rm cut}}\right) = E_0^\gamma R_{\rm cut}^{1-\gamma} \sum_A a_A Z_A^{1-\gamma} \mathcal{I}^A_{\rm rep}\,, \tag{C.1.7}$$

where we have defined the integrals

$$\mathcal{I}^A_{\rm rep} = \int_{x_{{\rm min},A}}^{x_{{\rm max},A}} dx_A\, x_A^{-\gamma} f_{\rm cut}(x_A)\,, \tag{C.1.8}$$

over the variable $x_A = E/(Z_A R_{\rm cut})$. Therefore, the integration extremes are given by $x_{{\rm min},A} = E_{\rm min}/(Z_A R_{\rm cut})$ and $x_{{\rm max},A} = E_{\rm max}/(Z_A R_{\rm cut})$.

The weight to be assigned to an observed event at the end of the simulation, where E_i and A_i are the energy and the mass number at the injection, is then given by the ratio of the probabilities in Eqs. (C.1.6) and (C.1.2)

$$\omega_{A_i}(E_i) = \frac{p^{A_i}_{\rm rep}(E_i)}{p^{A_i}_{\rm sim}(E_i)} = \frac{\mathcal{I}_{\rm sim}}{\sum_{A'} a_{A'} E^{1-\gamma}_{{\rm cut},A'} \mathcal{I}^{A'}_{\rm rep}} \frac{a_{A_i}}{b_{A_i}} E_i^{-\gamma+\alpha} f_{\rm cut}\left(\frac{E_i}{Z_{A_i} R_{\rm cut}}\right)\,. \tag{C.1.9}$$

It is important to note that in the previous calculations have assumed that all the sources inject particles with the same rate. In general, we can define the relative injection rate factor of a source as $\tilde{\omega}(s_i)$, where s_i denotes the source in the catalogue. The final weight factor of the particle i emitted by the source s_i with injection energy E_i and mass A_i can then be written as

$$\omega_i = \tilde{\omega}(s_i) \cdot \omega_{A_i}(E_i)\,. \tag{C.1.10}$$

C.2 Arrival direction correction

The simulated UHECRs are usually recorded by a spherical observer. In this thesis we chose an observer with radius $R_{\rm O} = 1\,{\rm Mpc}$, which is much larger than the radius of the Milky Way

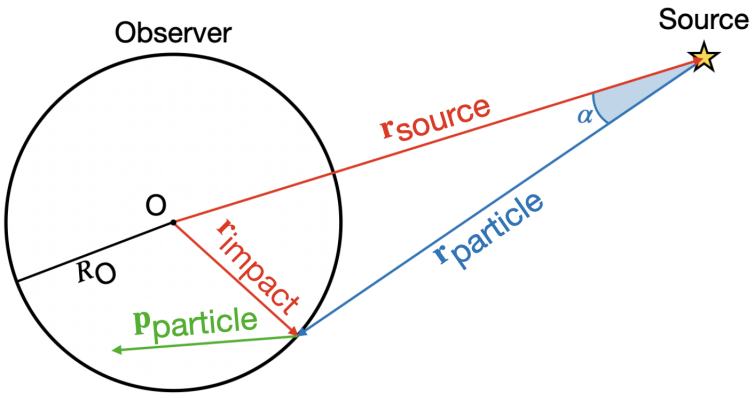

Figure C.2.1: Schematic representation for the correction of UHECR arrival directions on an observer with finite size. Vectors shown: position of the cosmic ray source relative to the center of the observer $\mathbf{r}_{\text{source}}$ (red), position of the cosmic ray impact point on the surface of the observer relative to the center of the observer $\mathbf{r}_{\text{impact}}$ (red), position of the cosmic ray impact point on the surface of the observer relative to the source $\mathbf{r}_{\text{particle}} = \mathbf{r}_{\text{impact}} - \mathbf{r}_{\text{source}}$ (blue) and recorded momentum vector at the end of the simulation $\mathbf{p}_{\text{particle}}$ (green). The rotation angle α is also shown in blue. Figure taken from [316].

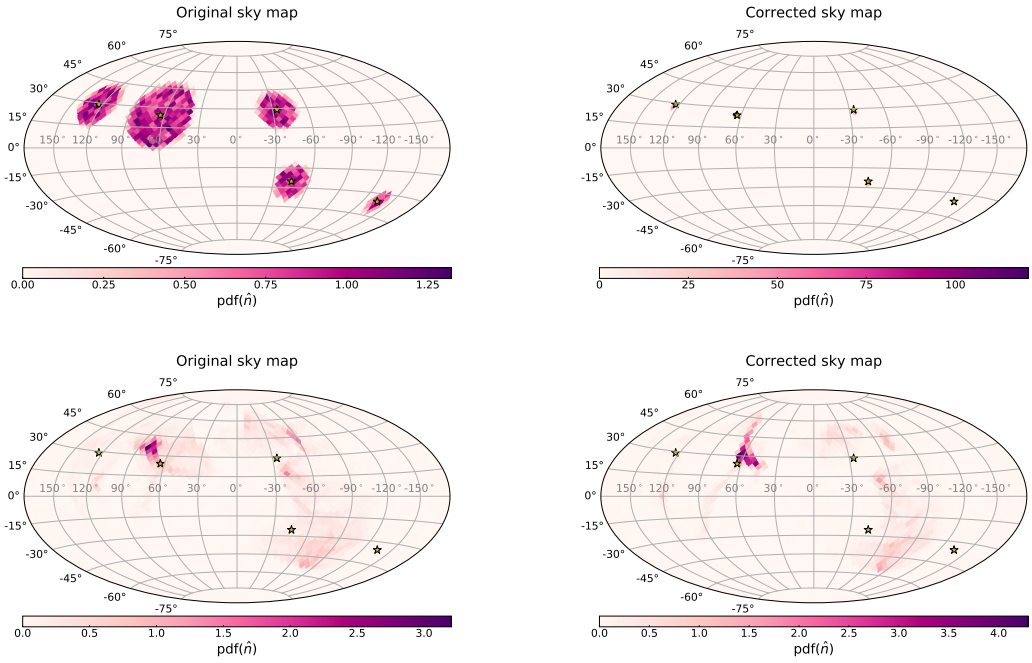

Figure C.2.2: Top: arrival direction probability distribution on the observer's surface before (left) and after (right) correcting for the finite size of the observer, in the case of ballistic propagation. Bottom: same as top panels, but in the case of propagation in a magnetic filed given by a Kolmogorov-like power-law spectrum with root-mean-square field strength $B_{\text{rms}} = 1\,\text{nG}$ and coherence length $\lambda_{\text{c}} = 1\,\text{Mpc}$. In all the cases, five cosmic ray sources (yellow stars) are considered.

($R_{\rm MW} \simeq 20\,{\rm kpc}$). Unfortunately, the use of a large observer is almost mandatory to collect enough statistics, and it introduces numerical effects on the simulated arrival direction distributions. Here we consider a geometric procedure to correct for the finite size of the observer (for a discussion of the role of a finite observer size in three-dimensional simulations, see also [337]).

Given the position of the cosmic ray source relative to the center of the observer $\mathbf{r}_{\rm source}$ and the position of the cosmic ray impact point on the surface of the observer $\mathbf{r}_{\rm impact}$, we define the normalized rotation vector $\hat{\mathbf{n}} \propto \mathbf{r}_{\rm source} \times \mathbf{r}_{\rm particle}$, where $\mathbf{r}_{\rm particle} = \mathbf{r}_{\rm impact} - \mathbf{r}_{\rm source}$. We can also define the rotation angle

$$\sin\alpha = \frac{|\mathbf{r}_{\rm source} \times \mathbf{r}_{\rm particle}|}{|\mathbf{r}_{\rm source}||\mathbf{r}_{\rm particle}|} \,. \tag{C.2.1}$$

Therefore, given the normalized rotation axis $\hat{\mathbf{n}}$ and the angle α, the rotation matrix $R(\hat{\mathbf{n}}, \alpha)$ is given by

$$R(\hat{\mathbf{n}}, \alpha) = \begin{pmatrix} n_x^2(1-\cos\alpha) + \cos\alpha & n_x n_y(1-\cos\alpha) - n_z \sin\alpha & n_x n_z(1-\cos\alpha) + n_y \sin\alpha \\ n_x n_y(1-\cos\alpha) + n_z \sin\alpha & n_y^2(1-\cos\alpha) + \cos\alpha & n_y n_z(1-\cos\alpha) - n_x \sin\alpha \\ n_x n_z(1-\cos\alpha) - n_y \sin\alpha & n_y n_z(1-\cos\alpha) + n_x \sin\alpha & n_z^2(1-\cos\alpha) + \cos\alpha \end{pmatrix} . \tag{C.2.2}$$

We use the rotation matrix $R(\hat{\mathbf{n}}, \alpha)$ to compute the corrected momentum vector as $\mathbf{p}_{\rm corrected} = R(\hat{\mathbf{n}}, \alpha) \cdot \mathbf{p}_{\rm particle}$, where $\mathbf{p}_{\rm particle}$ is the momentum vector at the end of the simulation. A schematic representation of the correction procedure described above is shown in Fig. C.2.1.

In Fig. C.2.2, an example of the arrival direction correction procedure described above is shown in the case of a spherical observer with radius 1 Mpc. The case of five cosmic ray sources (yellow stars) at which emit isotropically protons with energy 1 EeV is simulated with `CRPropa`. The source are at coordinates

$$\mathbf{r}_1 = (1.0\,{\rm Mpc},\, 2.0\,{\rm Mpc},\, 1.0\,{\rm Mpc}) \quad \Rightarrow \quad d_1 \simeq 2.5\,{\rm Mpc}\,, \tag{C.2.3}$$
$$\mathbf{r}_2 = (-2.0\,{\rm Mpc},\, 3.0\,{\rm Mpc},\, 2.0\,{\rm Mpc}) \quad \Rightarrow \quad d_2 \simeq 4.1\,{\rm Mpc}\,, \tag{C.2.4}$$
$$\mathbf{r}_3 = (3.0\,{\rm Mpc},\, -2.0\,{\rm Mpc},\, 2.0\,{\rm Mpc}) \quad \Rightarrow \quad d_3 \simeq 4.1\,{\rm Mpc}\,, \tag{C.2.5}$$
$$\mathbf{r}_4 = (3.0\,{\rm Mpc},\, -3.0\,{\rm Mpc},\, 2.0\,{\rm Mpc}) \quad \Rightarrow \quad d_4 \simeq 4.7\,{\rm Mpc}\,, \tag{C.2.6}$$
$$\mathbf{r}_5 = (-5.0\,{\rm Mpc},\, -5.0\,{\rm Mpc},\, -5.0\,{\rm Mpc}) \quad \Rightarrow \quad d_5 \simeq 8.7\,{\rm Mpc}\,, \tag{C.2.7}$$

with respect to the observer in the origin. The original arrival direction distributions are shown in the left panels of Fig. C.2.2, while the corrected distributions are shown in the right panels. The case of ballisitic propagation is shown in the top panels: we can see that the finite size of the observer corresponds to much larger source images than the real ones. The same correction procedue is shown in the bottom panels of Fig. C.2.2, where the propagation in a magnetic field given by a statistically homogeneous Kolmogorov-like power-law spectrum with root-mean-square field strength $B_{\rm rms} = 1\,{\rm nG}$ and coherence length $\lambda_{\rm c} = 1\,{\rm Mpc}$ is considered.

C.3 Homogeneous source scenario

In this appendix, the results obtained for the *homogeneous* source catalogues are presented, following the same analysis procedure discussed in Sec. 7.4. The minimization results of Eq. (7.9) for the *homogeneous* scenarios are shown in Table C.1 for both the source number densities considered. We find the same general results as for the *mass density* scenarios: a hard spectral

$n_s = 10^{-4}\,\mathrm{Mpc}^{-3}$

	ballistic	*astrophysicalR*	*primordial2R*	*statistical*
γ	-3.06	-0.66	-2.13	-2.25
$\log(R_{\mathrm{cut}}/1\,\mathrm{EV})$	0.09	0.28	0.13	0.17
I_p	$4.2 \cdot 10^{-2}$	$4.2 \cdot 10^{-2}$	$8.2 \cdot 10^{-2}$	$1.6 \cdot 10^{-1}$
I_{He}	0.0	$2.0 \cdot 10^{-1}$	$1.4 \cdot 10^{-1}$	$1.8 \cdot 10^{-2}$
I_N	$7.1 \cdot 10^{-1}$	$4.6 \cdot 10^{-1}$	$4.2 \cdot 10^{-1}$	$5.5 \cdot 10^{-1}$
I_{Si}	$2.1 \cdot 10^{-1}$	$1.5 \cdot 10^{-1}$	$3.6 \cdot 10^{-1}$	$2.4 \cdot 10^{-1}$
I_{Fe}	$4.2 \cdot 10^{-2}$	$1.5 \cdot 10^{-1}$	$3.0 \cdot 10^{-3}$	$3.9 \cdot 10^{-2}$

$n_s = 10^{-2}\,\mathrm{Mpc}^{-3}$

	ballistic	*astrophysicalR*	*primordial2R*	*statistical*
γ	-1.49	-0.93	-1.52	-2.01
$\log(R_{\mathrm{cut}}/1\,\mathrm{EV})$	0.28	0.45	0.25	0.24
I_p	$1.4 \cdot 10^{-1}$	0.0	$6.6 \cdot 10^{-2}$	$7.3 \cdot 10^{-3}$
I_{He}	0.0	0.0	$1.1 \cdot 10^{-1}$	0.0
I_N	$5.4 \cdot 10^{-1}$	$6.3 \cdot 10^{-1}$	$5.3 \cdot 10^{-1}$	$8.0 \cdot 10^{-1}$
I_{Si}	$3.2 \cdot 10^{-1}$	$3.7 \cdot 10^{-1}$	$2.2 \cdot 10^{-1}$	$1.3 \cdot 10^{-1}$
I_{Fe}	$6.5 \cdot 10^{-3}$	0.0	$7.4 \cdot 10^{-2}$	$5.7 \cdot 10^{-2}$

Table C.1: Minimization results of Eq. (7.9) for the *homogeneous* source scenarios. Different columns correspond to different EGMF models. The source number density of a given model is indicated at the top of the table. Table taken from [316].

index up to $\gamma \simeq -3$ and a rigidity cutoff of $\log(R_{\mathrm{cut}}/1\,\mathrm{EV}) \simeq 0.2$ on average. The mass composition is again dominated by nitrogen and silicon mass groups. The propagated energy spectra and mass compositions are shown in Fig. C.3.1: also in this case, we do not observe any signature due to the EGMF model considered.

In Fig. C.3.3, the distributions of the angular deflection of the propagated UHECRs are shown. We obtain the same extragalactic deflection pattern than in the *mass density* scenarios. Similar results are obtained for the flux ratios, shown in Fig. C.3.2. As expected, we observe a smaller cosmic variance in the case of the *homogeneous* catalogues.

Compared to the case of a strucuted source distributions, the arrival direction distributions shown in Figs. C.3.4 and C.3.5 are more isotropic both at the edge of the Galaxy and at Earth. This can also be seen in the multipole distribution in Fig. C.3.6, where no significant large dipole or quadrupole values are observed. We found that the angular power spectrum obtained in the low density scenario, without any EGMF, is larger than in the magnetized cases. This is due to the ballistic propagation of the UHECRs emitted by a small number of local sources. The effect of the GMF on the angular power spectra is shown in Fig. C.3.7, where we observe the same suppression as in the *mass density* scenarios. We still obtain an anisotropic signal due to the

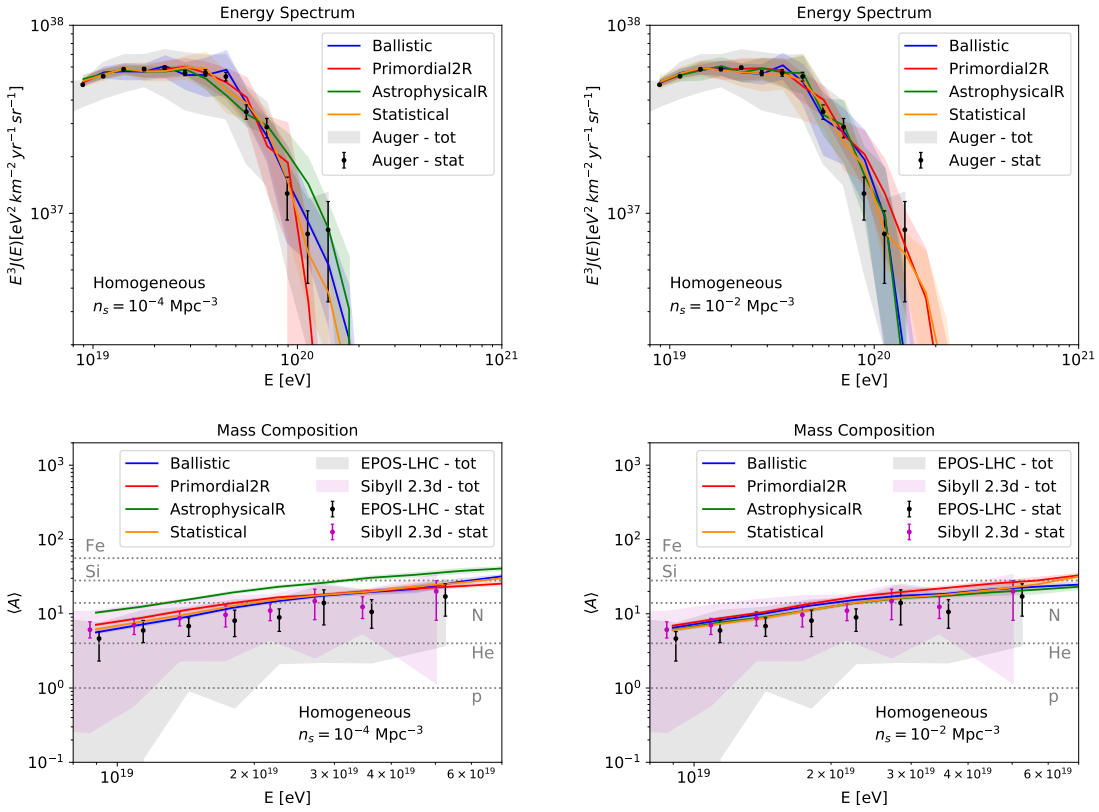

Figure C.3.1: Same as Fig. 7.6, but for the *homogeneous* scenarios. Figure taken from [316].

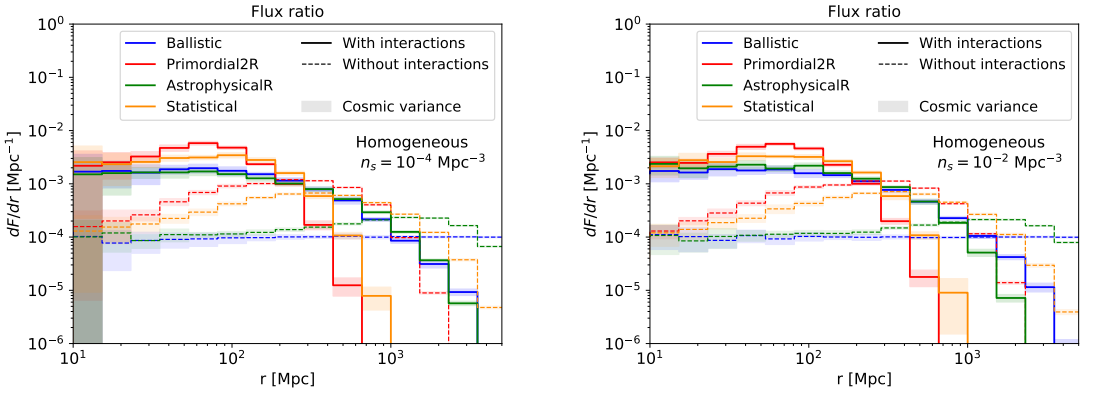

Figure C.3.2: Same as Fig. 7.8, but for the *homogeneous* scenarios. Figure taken from [316].

cosmic variance of the source catalogues and, in general, lower source densities still correspond to stronger anisotropic signals.

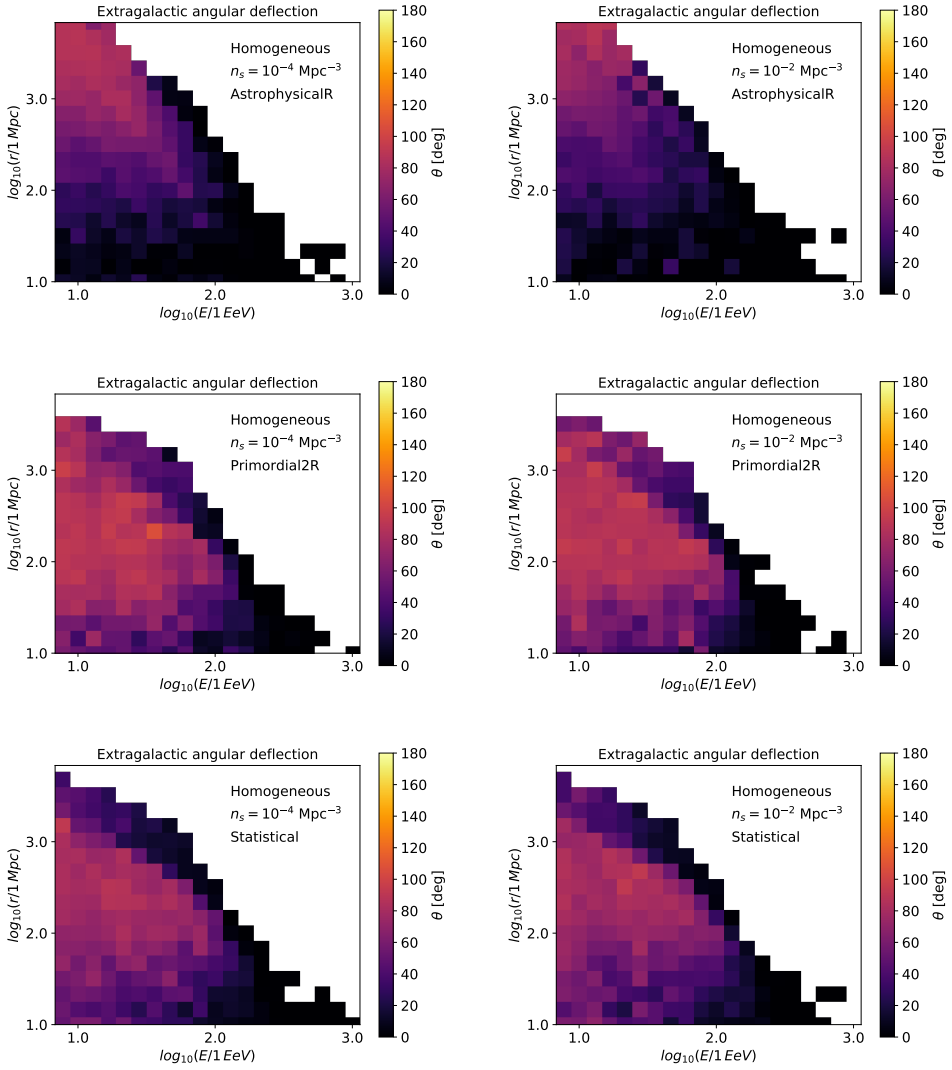

Figure C.3.3: Same as Fig. 7.7, but for the *homogeneous* scenarios. Figure taken from [316].

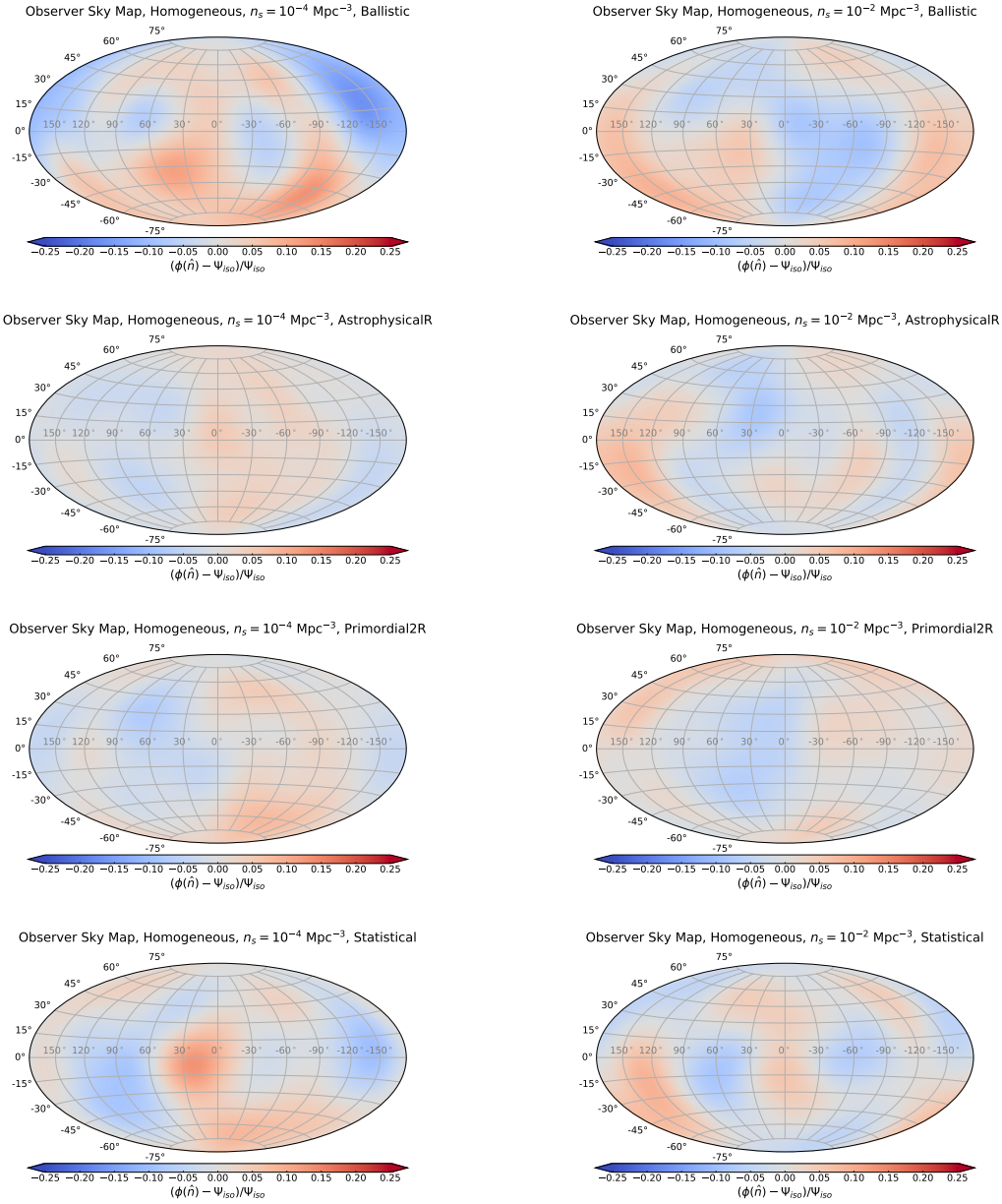

Figure C.3.4: Same as Fig. 7.9, but for the *homogeneous* scenarios. Figure taken from [316].

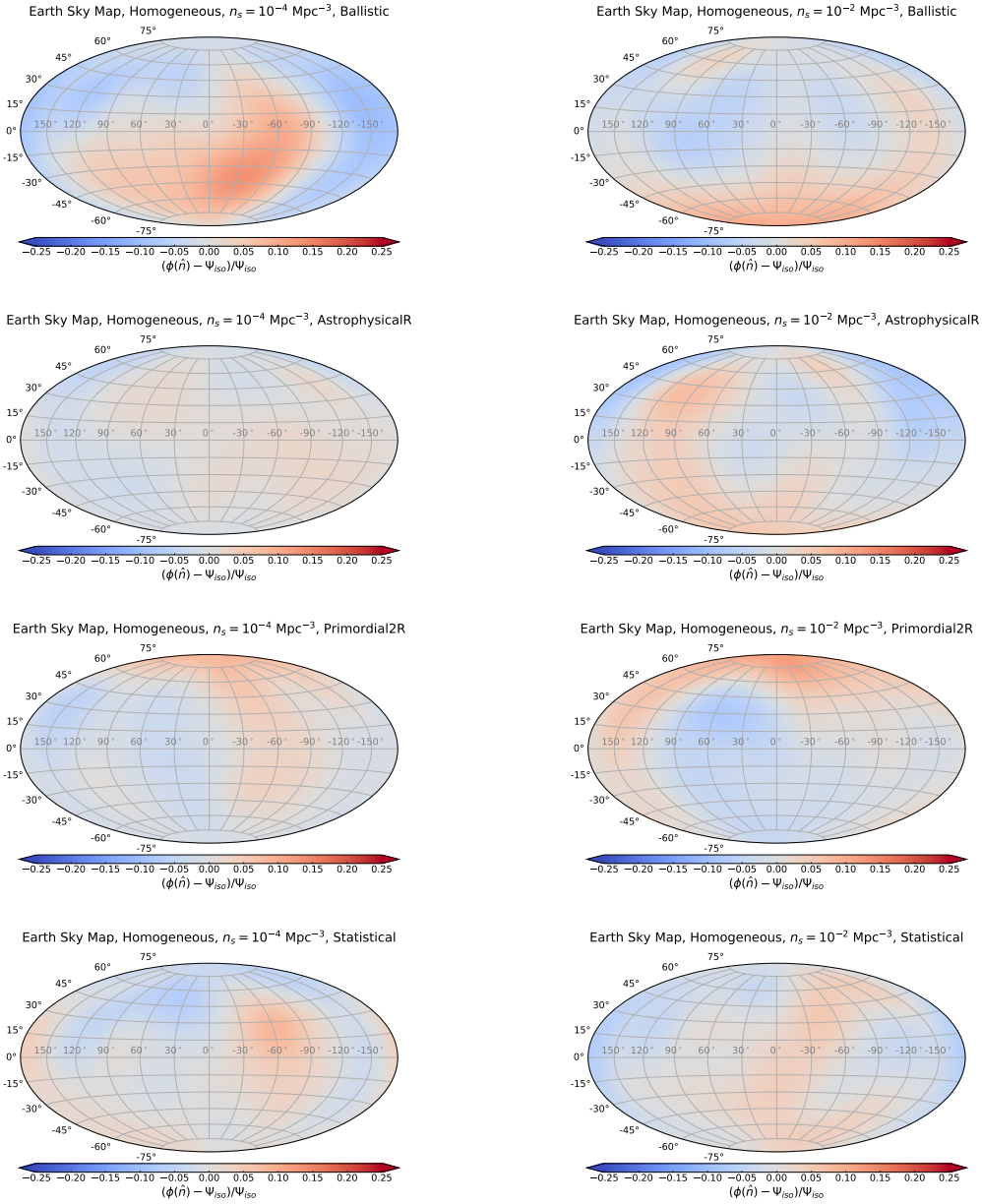

Figure C.3.5: Same as Fig. 7.11, but for the *homogeneous* scenarios. Figure taken from [316].

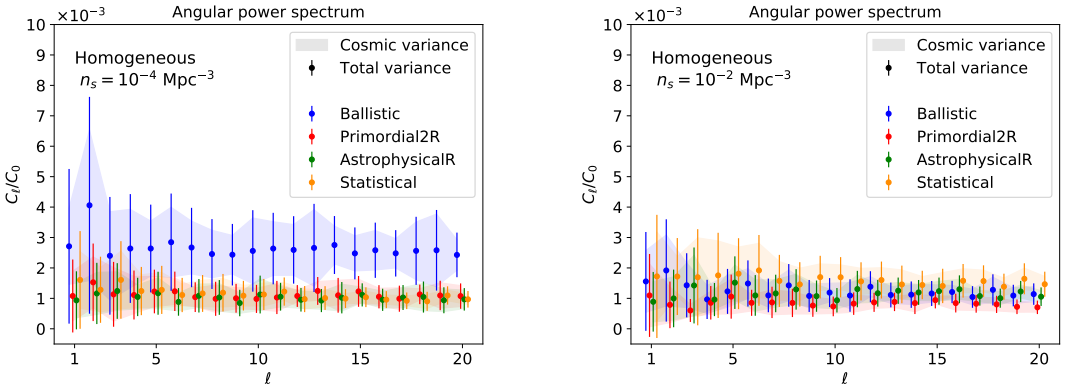

Figure C.3.6: Same as Fig. 7.10, but for the *homogeneous* scenarios. Figure taken from [316].

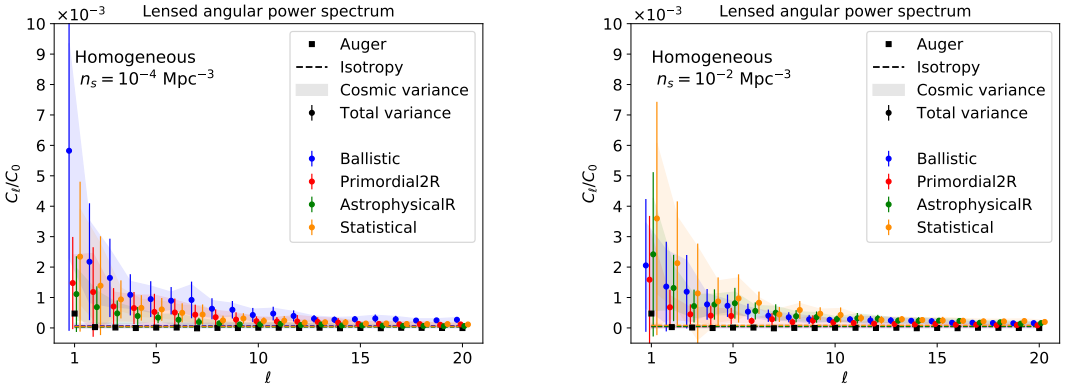

Figure C.3.7: Same as Fig. 7.12, but for the *homogeneous* scenarios. Figure taken from [316].

D

Further scenarios for astrophysical neutrinos

This appendix is based on the publication:

- S. Rossoni, D. Boncioli, and G. Sigl. (2025). *Investigating binary-neutron-star mergers as production sites of high-energy neutrinos.* **JCAP**, 01, 009. arXiv:2407.19957 [astro-ph.HE]. https://doi.org/10.1088/1475-7516/2025/01/009.

This appendix presents further scenarios from Chapter 8.

D.1 Cosmic ray energy spectra

In this appendix, the CR spectra corresponding to the predicted neutrino fluxes shown in Figs. 8.10 and 8.11 are shown. In general, the accelerated and escaped spectra are given in different units than the observed spectrum. In this appendix, we refer to the accelerated and escaped spectra as predicted in the absence of interactions within the source or during propagation, respectively. The pure proton scenario is shown in Fig. D.1.1, and the pure iron scenario is shown in Fig. D.1.2. In the case of protons, the accelerated (red), the escaped (blue) and the propagated (black) spectra are shown together with observed data. For iron nuclei, the accelerated spectrum (black dotted) is shown with the total propagated spectrum (black) and the different mass components (colored lines). Observed cosmic ray flux by the Pierre Auger Observatory [443] is also shown (black dots).

In Figs. D.1.3 and D.1.4 the CR energy spectra corresponding to the predicted neutrino fluxes shown in Figs. 8.14 and 8.15 are shown.

D.2 Parameter study with the SFR

The same analysis presented in Sec. 8.4.1 is reported in this appendix for the scenarios in which the source evolution is that of the SFR , given in Eq. (8.16).

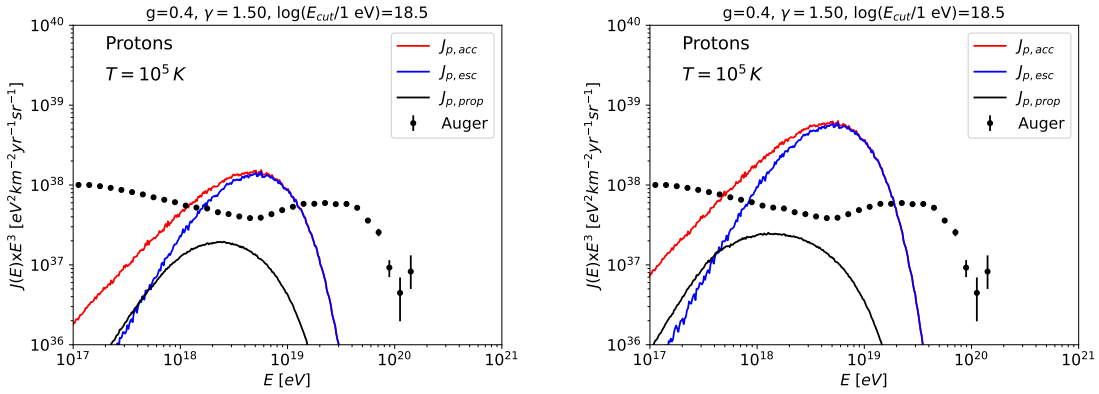

Figure D.1.1: Left: energy spectra for a pure proton injection with $m = 0$: injected in the source (red line), escaped from the source (blue line) and propagated at Earth (black line). Observed cosmic ray flux by the Pierre Auger Observatory [443] is also shown (black dots). Right: same as left panel, but for the SFR source evolution in Eq. (8.16). Figure taken from [388].

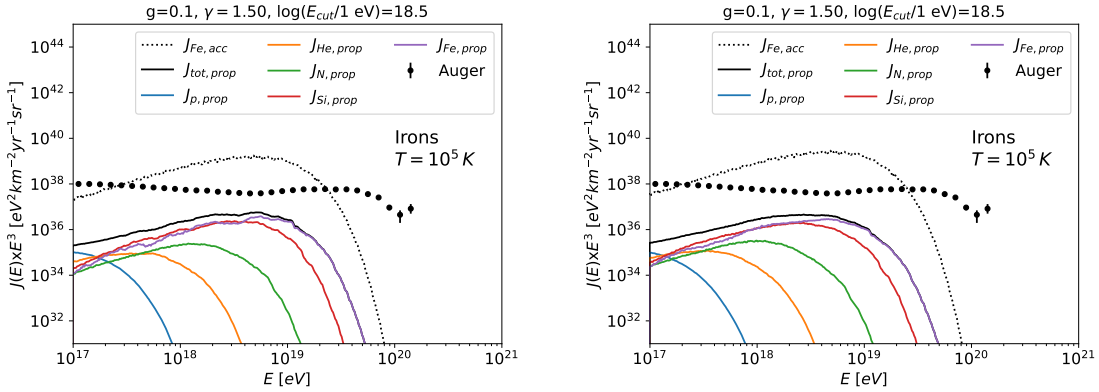

Figure D.1.2: Same as Fig. D.1.1, but for pure iron injection. Injected iron nuclei are shown with black dotted line. Propagated mass groups (colored lines) and the total flux (black line) are shown. Note the different range of the y-axis with respect to the proton scenarios. Figure taken from [388].

The results for proton and iron acceleration are shown in Figs. D.2.1 and D.2.2, respectively. No relevant differences are observed with respect to the case $m = 0$. In Fig. D.2.3, we show the same analysis of Figs. 8.16 and 8.17 for the SFR source evolution model. In Fig. D.2.4, the same constraints of Fig. 8.18 are shown.

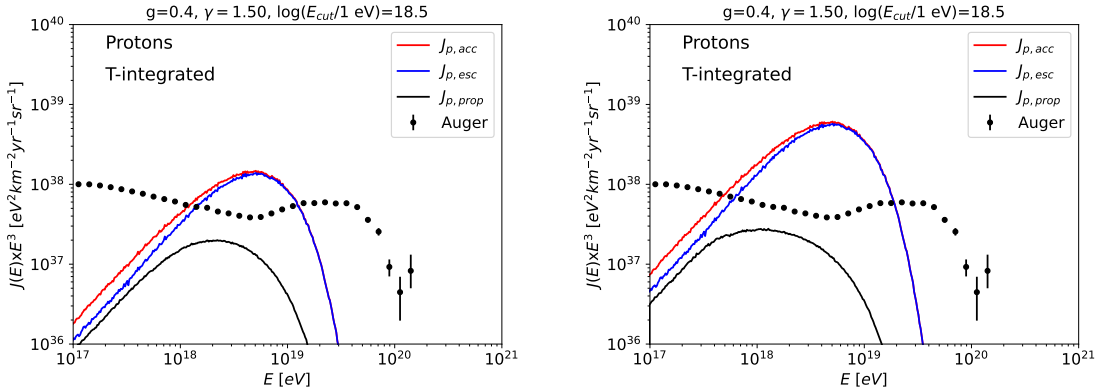

Figure D.1.3: Same as Fig. D.1.1, but integrating on the temporal evolution of the source. Figure taken from [388].

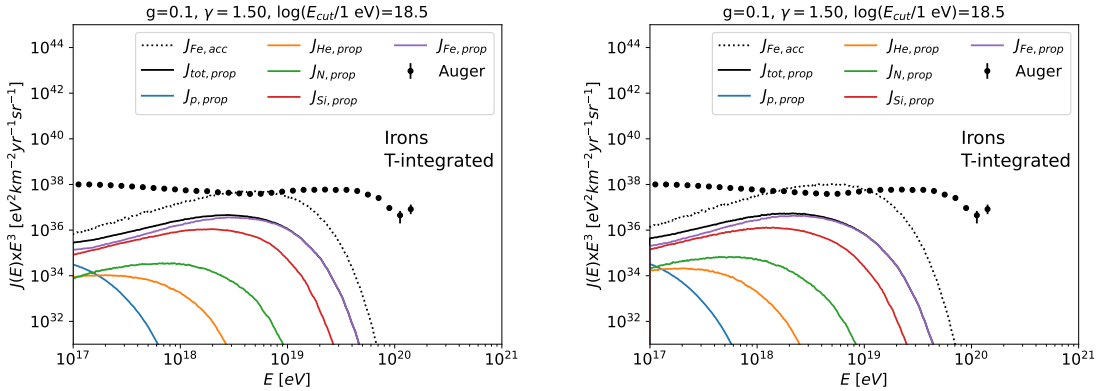

Figure D.1.4: Same as Fig. D.1.3, but for a pure iron injection. Note the different range of the y-axis with respect to the proton scenarios. Figure taken from [388].

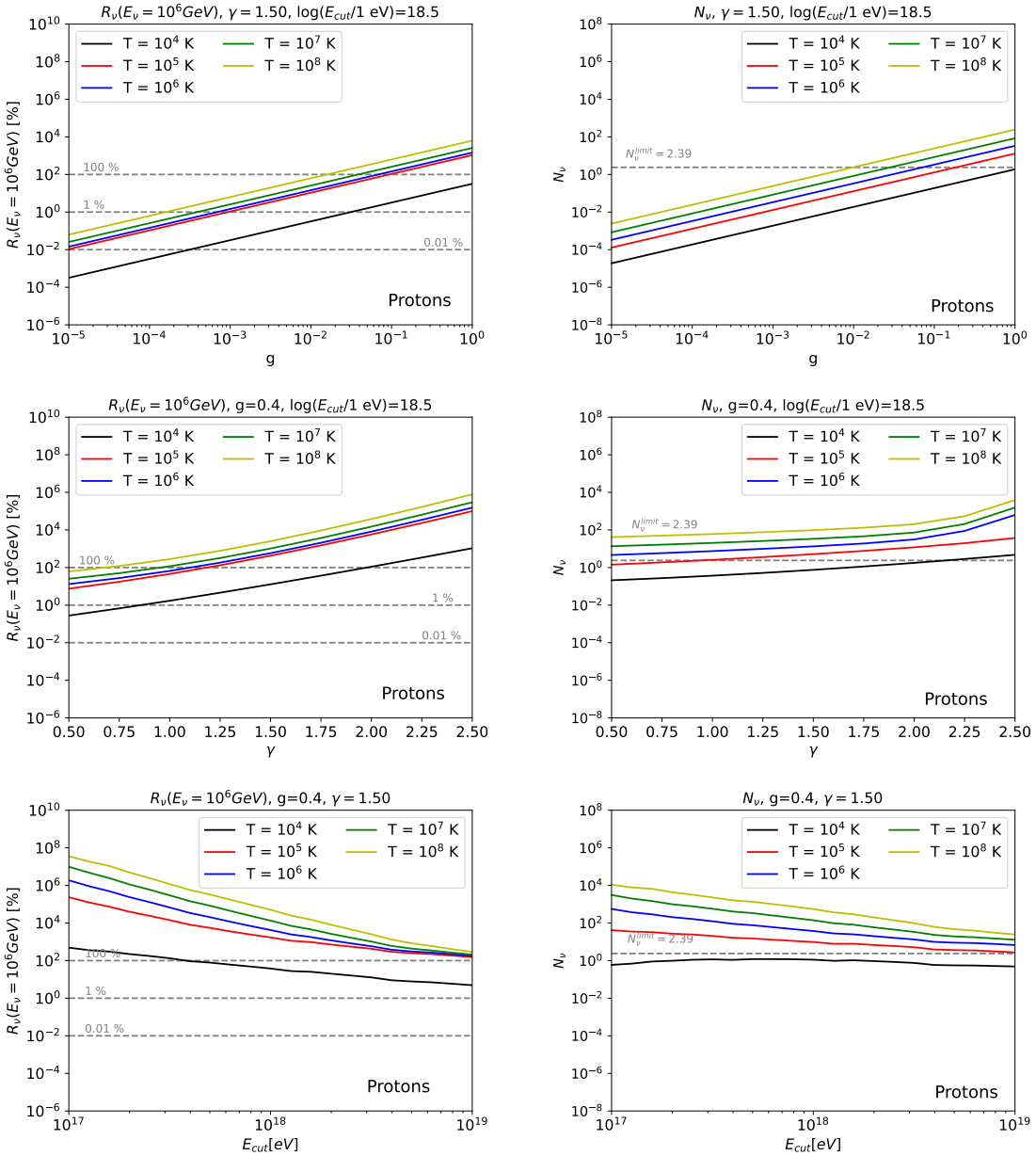

Figure D.2.1: Same as Fig. 8.12, but for the SFR source evolution in Eq. (8.16). Figure taken from [388].

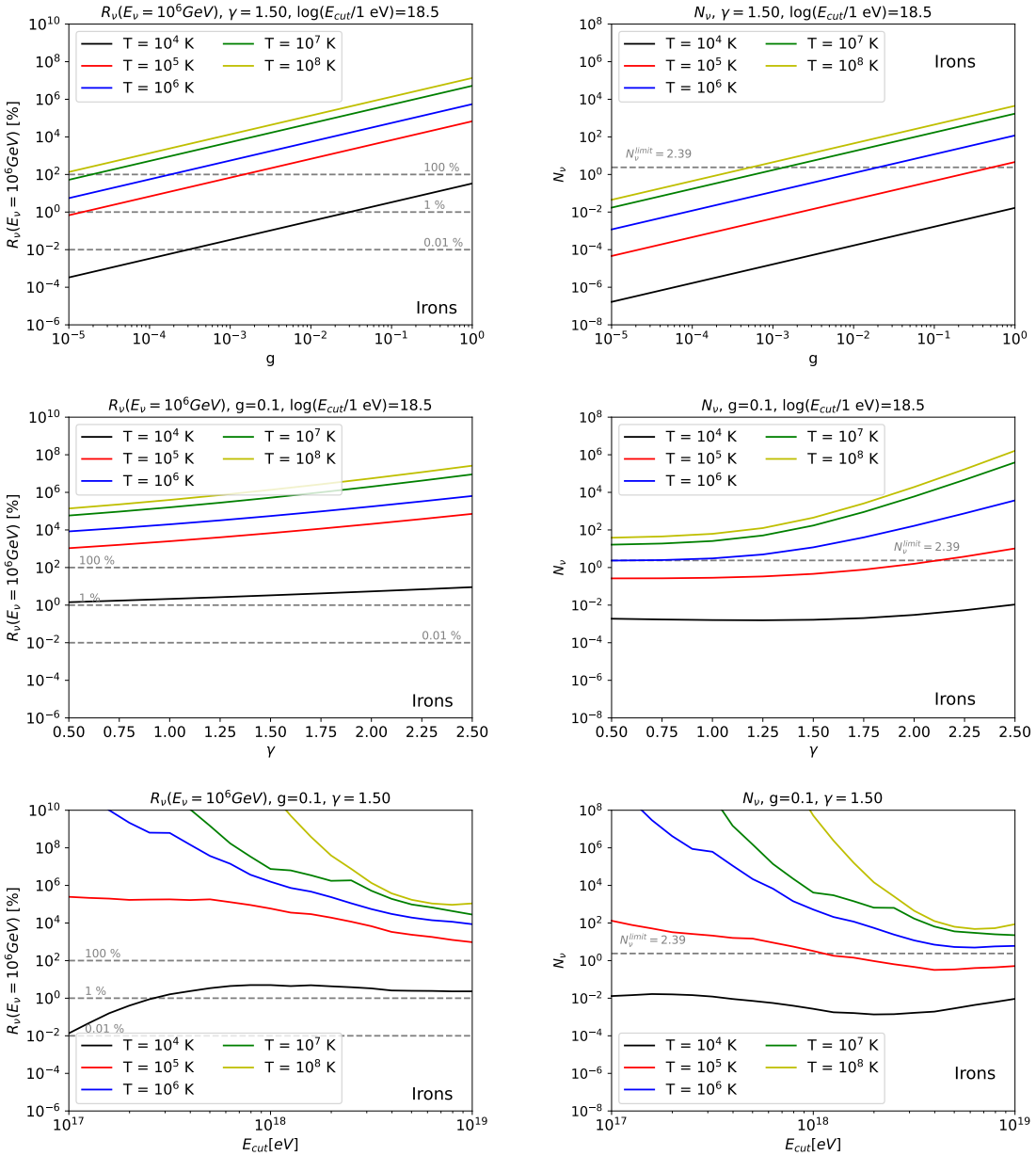

Figure D.2.2: Same as Fig. 8.13, but for the SFR source evolution in Eq. (8.16). Figure taken from [388].

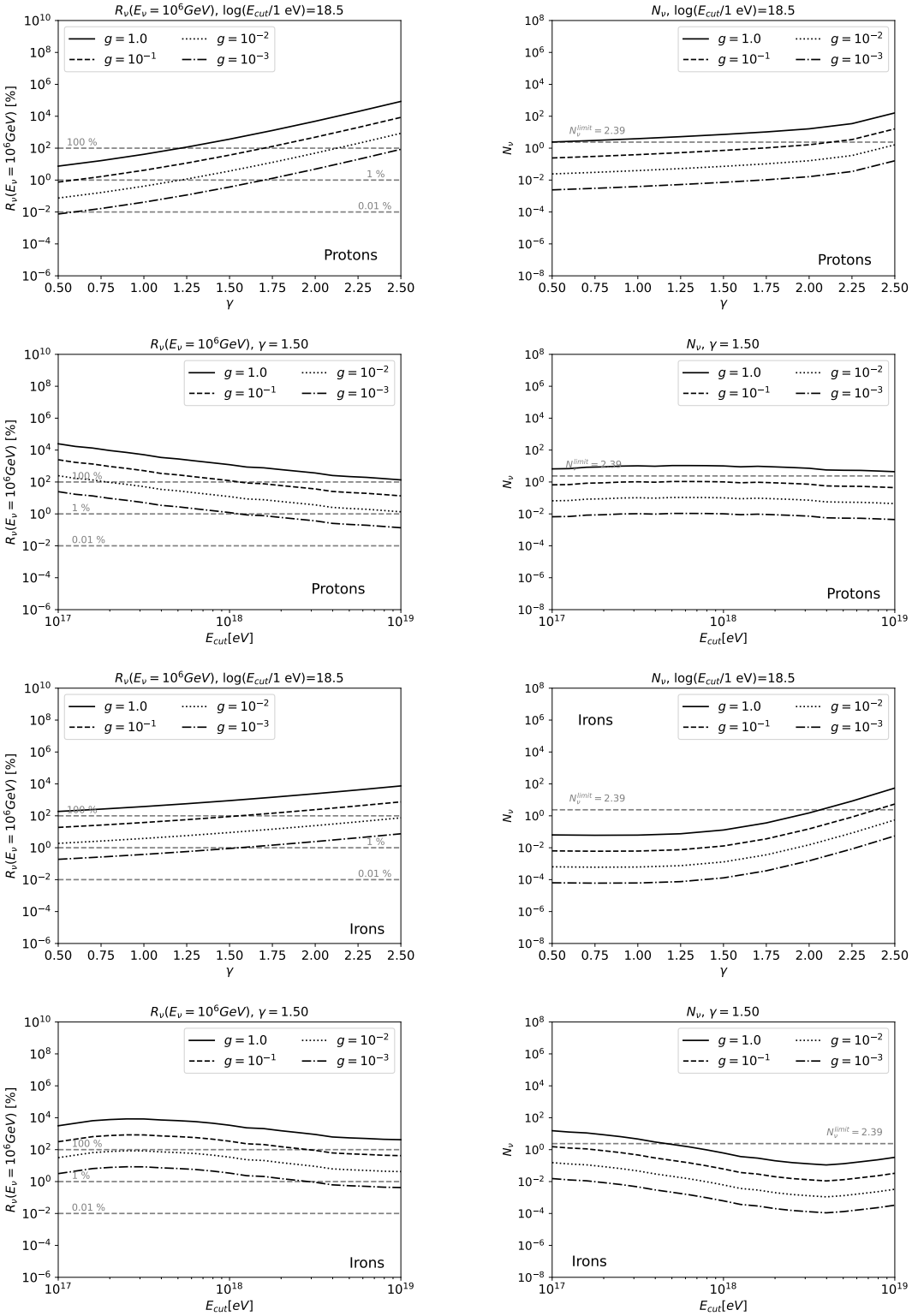

Figure D.2.3: Top four panels: same as Fig. 8.16, but for the SFR source evolution in Eq. (8.16). Bottom four panels: same as Fig. 8.17, but for the SFR source evolution in Eq. (8.16). Figure taken from [388].

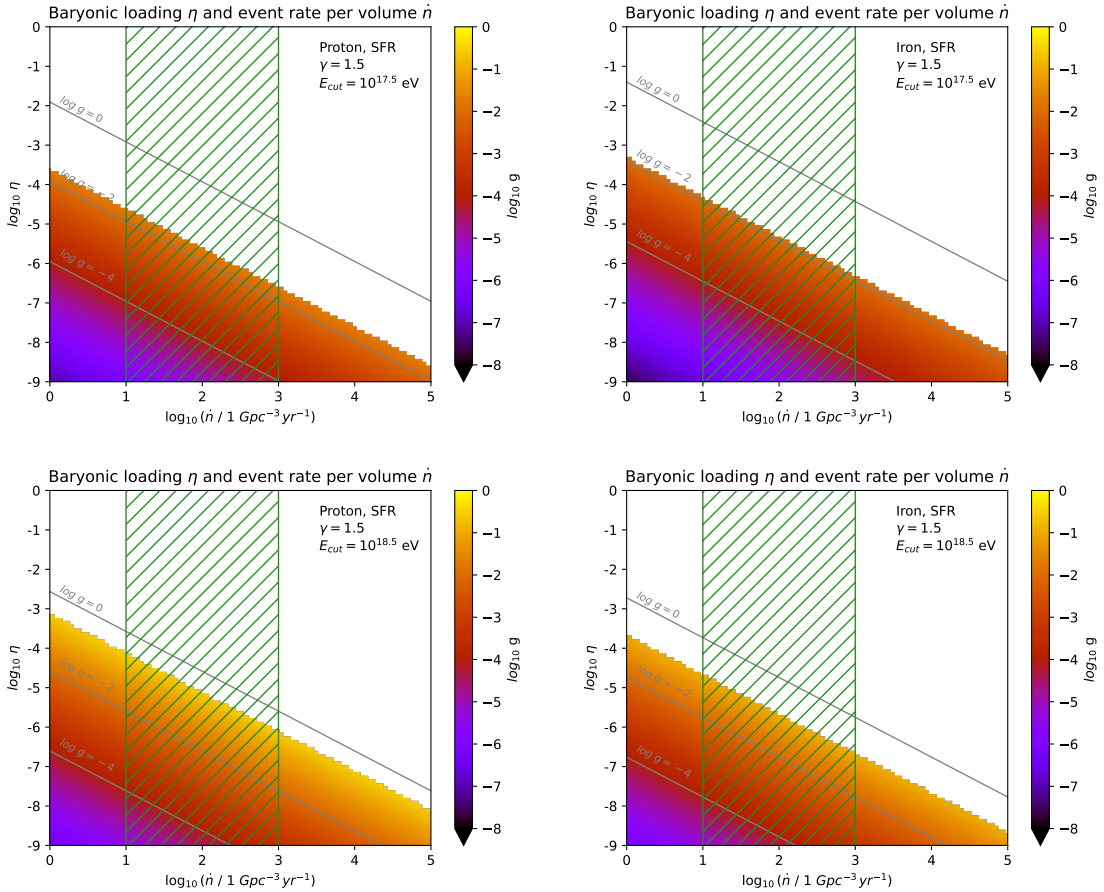

Figure D.2.4: Same as Fig. 8.18, but for the SFR source evolution in Eq. (8.16). Figure taken from [388].

E

CRPropa module for plasma instabilities in electromagnetic cascades

This appendix is based on the publication:

- L. E. E. Castro, S. Rossoni, and G. Sigl. (2024). *Influence of plasma instabilities on the propagation of electromagnetic cascades from distant blazars.* arXiv: 2405.15390 [astro-ph.HE]. Submitted for publication to **The Astrophysical Journal**.

This appendix provides details on the `CRPropa` module for plasma instabilities discussed in Chapter 9.

E.1 Plasma instability module

The modular structure of `CRPropa 3` offers the possibility to easily add new features to the code framework. This section presents the modifications and new files required for our study of the effects of plasma instabilities on electromagnetic cascades.

The source file for the calculation of the energy loss of electrons and positrons is called `PlasmaInstability.cpp`, and it is shown in the Listing E.1. The corresponding header file, called `PlasmaInstability.h`, is shown in the Listing E.2. Following the `CRPropa 3` code structure at `https://github.com/CRPropa/CRPropa3`, the source file must be included in the **src**/**module** directory, while the header file must be included in the **include**/**crpropa**/**module** directory. The other changes and additions to the code are

- in `CMakeLists.txt` add the line `src/module/PlasmaInstability.cpp`,
- in **include**/**CRPropa.h** add the line `#include ''crpropa/module/PlasmaInstability.h''`,
- in **python**/**2_headers.i** add the line `%include ''crpropa/module/PlasmaInstability.h''`.

The module can then be used by including it in the `Python` interface of `CRPropa` the commad line `add(PlasmaInstability(index, energy_scale, length_scale))`. The input variables ofn the module are defined in Sec. E.2.

```
#include "crpropa/module/PlasmaInstability.h"

PlasmaInstability::PlasmaInstability(double a, double Energyscale,
    double Lengthscale) : crpropa::Module() {
    setPlasmaIndex(a);
    setPlasmaEnergyScale(Energyscale);
    setPlasmaLengthScale(Lengthscale);
    setDescription("PlasmaInstability");
}

void PlasmaInstability::setPlasmaIndex(double alpha) {
    index = alpha;
}

void PlasmaInstability::setPlasmaEnergyScale(double Escale) {
    tildeE = Escale;
}

void PlasmaInstability::setPlasmaLengthScale(double lambdascale) {
    lambda = lambdascale;
}

double PlasmaInstability::getPlasmaIndex() const {
    return index;
}

double PlasmaInstability::getPlasmaEnergyScale() const {
    return tildeE;
}

double PlasmaInstability::getPlasmaLengthScale() const {
    return lambda;
}

void PlasmaInstability::process(crpropa::Candidate *candidate) const {
    int id = candidate->current.getId();

    // only works for electrons and positrons
    if (fabs(id) != 11)
    return;

    double dx = candidate->getCurrentStep();
    double z = candidate->getRedshift();
    double E = candidate->current.getEnergy();
    double dEdx = coolingPower(E, z);

    if (dEdx < 0)
    dEdx = 0;
    double Enew = E - dEdx * dx;
    candidate->current.setEnergy(Enew);
```

```
50      candidate->limitNextStep(0.1 * E / dEdx);
51  }
52
53  double PlasmaInstability::coolingPower(double E, double z) const {
54      double dEdx = 0;
55      E /= (1 + z);
56      return (tildeE / lambda) * pow( E  / tildeE, 1-index);
57  }
58
59  std::string PlasmaInstability::getDescription() const {
60      std::stringstream s;
61      s << "PlasmaInstability";
62
63      return s.str();
64  }
```

Listing E.1: Source file `PlasmaInstability.cpp`.

```
1       #ifndef CRPROPA_PLASMAINSTABILITY_H
2       #define CRPROPA_PLASMAINSTABILITY_H
3
4       #include <crpropa/Cosmology.h>
5       #include <crpropa/Module.h>
6       #include <crpropa/ParticleID.h>
7       #include <crpropa/ParticleMass.h>
8       #include <crpropa/Random.h>
9       #include <crpropa/Units.h>
10
11      class PlasmaInstability : public crpropa::Module {
12          protected:
13          double index;
14          double tildeE;
15          double lambda;
16
17          public:
18          PlasmaInstability(double index, double tildeE, double lambda);
19          void setPlasmaIndex(double indexplasma);
20          void setPlasmaEnergyScale(double tildeEplasma);
21          void setPlasmaLengthScale(double lambdaplasma);
22          double getPlasmaIndex() const;
23          double getPlasmaEnergyScale() const;
24          double getPlasmaLengthScale() const;
25          double coolingPower(double energy, double redshift) const;
26          std::string getDescription() const;
27          void process(crpropa::Candidate *candidate) const;
28      };
29
30      #endif
```

Listing E.2: Header file `PlasmaInstability.h`.

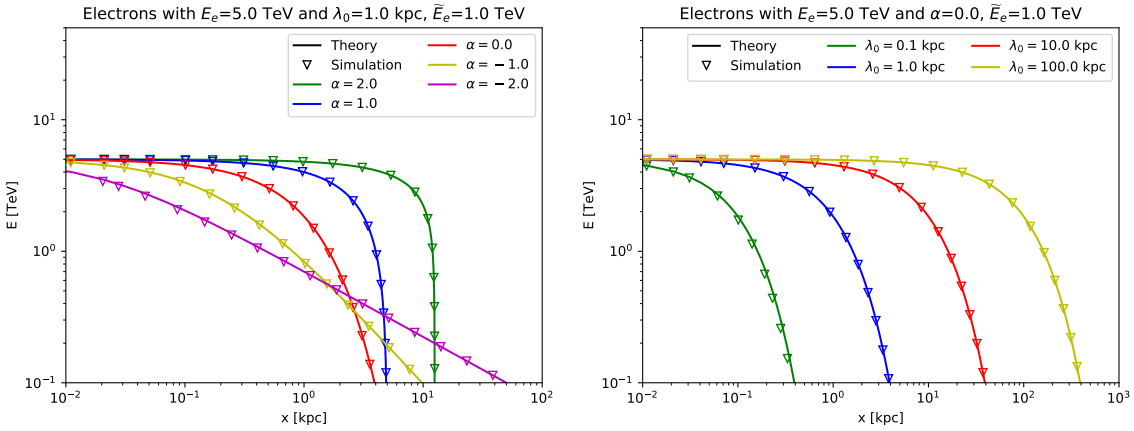

Figure E.2.1: Left: evolution of the energy of a single electron under the effect of plasma instabilities. The initial electron energy is $E_{e,0} = 5\,\mathrm{TeV}$. Different values of α and $\lambda_0 = 1\,\mathrm{kpc}$ and $\widetilde{E}_e = 1\,\mathrm{TeV}$ are considered. Right: same as left panel, but for $\alpha = 0$ and different values of λ_0 are shown. In both panels, the solid lines correspond to the analytic solution and the triangles to the `CRPropa` simulations.

E.2 Testing the plasma instability module

In Section 9.2, the fraction of energy loss by electrons within an inverse Compton scattering length λ_{IC} due to plasma instabilities is given by Eq. (9.2). We have implemented this energy loss mechanism in the `CRPropa 3` framework by considering an energy loss length of the form

$$\left(-\frac{1}{E_e}\frac{dE_e}{dx}\right)^{-1}_{\mathrm{PI}} = \lambda_0 \left(\frac{E_e}{\widetilde{E}_e}\right)^{\alpha}, \tag{E.2.1}$$

where the definition of α, λ_0 and $\widetilde{E}_e$ are given in Sec. 9.2. We can obtain the evolution of the electron energy $E_e(x)$ as a function of the distance x from the injection position by integrating Eq. (E.2.1). Therefore, given the initial condition $E_e(x = x_0) = E_{e,0}$, we find that for $\alpha = 0$ the solution is

$$E_e(x) = E_{e,0} \exp\left[-\frac{x - x_0}{\lambda_0}\right], \tag{E.2.2}$$

while for $\alpha \neq 0$ the solution is

$$E_e(x) = E_{e,0}\left[1 - \alpha\frac{x - x_0}{\lambda_0}\left(\frac{E_{e,0}}{\widetilde{E}_e}\right)^{-\alpha}\right]^{1/\alpha}. \tag{E.2.3}$$

To test the implementation in `CRPropa` of our energy loss module, we compare simulations of a single electron with the analytical results described above. We consider the propagation of an electron with initial energy $E_{e,0} = 5\,\mathrm{TeV}$ from the position $x_0 = 0\,\mathrm{kpc}$, taking into account only the plasma instability energy loss term. In the left panel of Fig. E.2.1 we show the evolution of the electron energy during the propagation for different values of α and fixing $\lambda_0 = 1\,\mathrm{kpc}$ and $\widetilde{E}_e = 1\,\mathrm{TeV}$. The solid lines represent the integration of the equation of motion and the triangles represent the result obtained with the `CRPropa` simulations. It can be seen that our

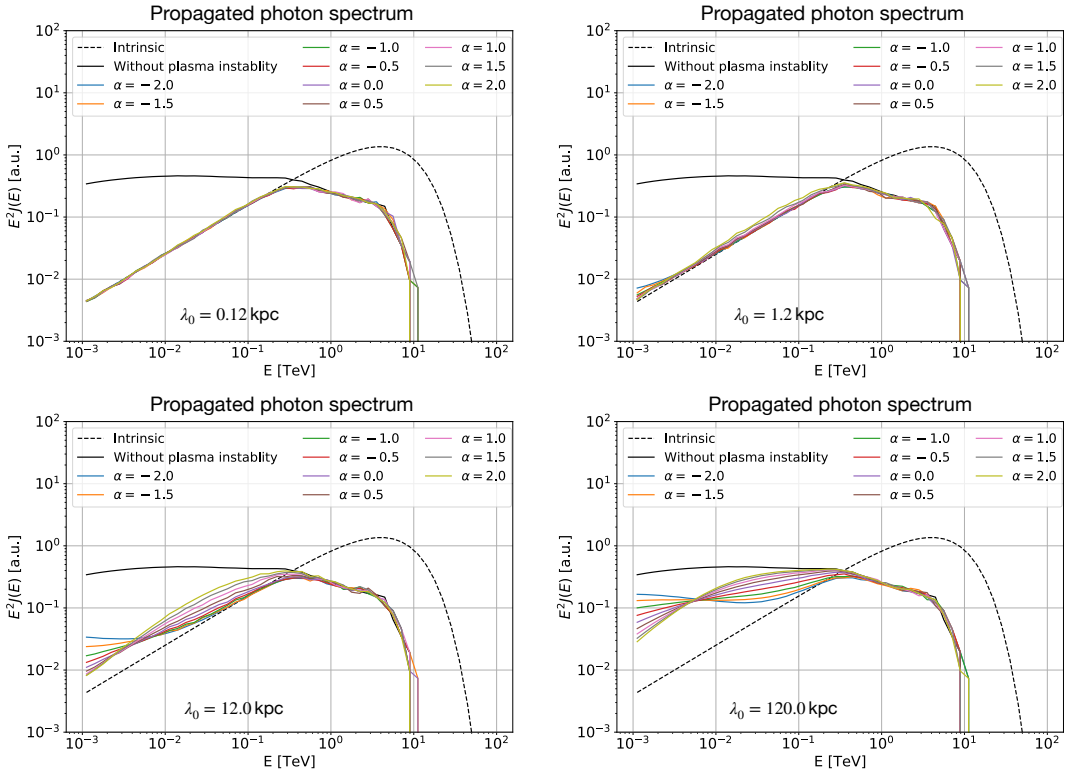

Figure E.3.1: Propagated photon spectra for an injected energy spectrum (dashed black line) with spectral index $\beta = 1.2$ and high-energy cutoff $E_{\rm cut} = 5\,\text{TeV}$. The parameterizations of the plasma instability energy loss term are $\widetilde{E} = 1\,\text{TeV}$ and $\lambda_0 = 0.12$ kpc (top left), $\lambda_0 = 1.2$ kpc (top right), $\lambda_0 = 12$ kpc (bottom left) and $\lambda_0 = 120$ kpc (bottom right). The coloured lines represent different values of the plasma index α. The solid black line represents the propagated spectrum without plasma instabilities. Figure adapted from [444].

implementation correctly reproduces the expected results. We repeat the same test for different values of λ_0 and for $\alpha = 0$. These results are show in the right panel of Fig. E.2.1. Again, the agreement between simulations and analytical results is confirmed.

The fraction of energy loss by electrons within an inverse Compton length due to plasma instabilities in Eq. (9.2) can be obtained from Eqs. (E.2.2) and (E.2.3) by considering $x - x_0 = \lambda_{\rm IC}$ and $\lambda_0 \gtrsim \lambda_{\rm IC}$. We obtain that

$$E_e(\lambda_{\rm IC}) \simeq E_{e,0}\left[1 - \frac{\lambda_{\rm IC}}{\lambda_0}\left(\frac{E_{e,0}}{\widetilde{E}_e}\right)^{-\alpha}\right], \tag{E.2.4}$$

from which the expression for $\Delta E_e(\lambda_{\rm IC})/E_{e,0}$ in Eq. (9.2) can be obtained.

E.3 Dependence of the spectrum on instability parameters

In this appendix, we evaluate the effect of different plasma instability parameters on the propagated photon spectrum. We consider an injected photon spectrum of the form in Eq. (9.4) with spectral parameters $\beta = 1.2$ and $E_{\rm cut} = 5\,\text{TeV}$. We consider the values $\alpha = -2.0, -1.5, ..., 1.5, 2.0$

with $\Delta\alpha = 0.5$ and $\lambda_0 = 0.12$, 1.2, 12 and 120 kpc. We fix the distance of the source to the observer to 580 Mpc, as done in Chapter 9.

The propagated photon spectra are shown in Fig. E.3.1 for all combinations of instability parameters tested. The injected spectrum and the spectrum in the case without instabilities (i.e. considering the standard electromagnetic cascades) are also shown as dashed and solid black lines, respectively. In the top panels of Fig. E.3.1 we can see that all the values of the plasma instability index produce similar results: a strong suppression of the secondary photons in the GeV energy range is observed. This is due to the fact that instabilities dominate over inverse Compton, since their typical length scale is such that $\lambda_0 \lesssim \lambda_{IC}$. Therefore, the propagated spectrum tends to approach the prompt spectrum. We also note that it is not possible to obtain propagated photon spectra below the prompt spectrum, as this part of the spectrum is populated by photons that do not produce electron-positron pairs and therefore plasma instabilites can not play a role.

In the bottom panels of Fig. E.3.1, where $\lambda_0 > \lambda_{IC}$, the propagated spectra start to deviate from the prompt emission. The propagated spectra still show a suppression for $E \lesssim 100$ GeV with respect to the case without instabilities. For $\alpha \geq 0$, the suppression of the spectrum continues down to the GeV energy scale. This is due to the fact that for electron-positron pairs plasma instabilities are still more efficient than the inverse Compton scattering. For $\alpha < 0$, a relative increase in the photon spectrum is observed at $E \lesssim 10$ GeV. In this case, the energy of the electron-positrons pairs decrease to the point where inverse Compton scattering becomes again the dominant process.

Acknowledgements

I have made many new friends and acquaintances during these years of doctoral studies in Hamburg, and I really hope to be able to say thank you to all those who have contributed to my life and growth during this experience.

I would like to start by thanking Professor Günter Sigl for giving me the opportunity to pursue my PhD at the University of Hamburg. I would also like to thank him for the freedom and independence he granted me in carrying out the studies presented in this thesis, and for the many stimulating discussions on the results obtained.

Special thanks go to Professor Denise Boncioli, for all the help - both scientific and personal - that she never hesitated to offer me. Although she has not officially been my supervisor in these years, she has continued to be a source of inspiration and guidance in my personal development.

This journey would not have been possible without the help and support of the many people at the University of Hamburg. Firstly, I would like to thank Elizabeth Duarte for her invaluable assistance with all administrative and bureaucratic matters. I would also like to thank Martin Stieben for his assistance with the numerical resources provided by the PHYSnet Compute Cloud. Finally, although not directly related to my research, I would like to thank Dr. Maria Vittoria Garzelli for all the times the door to her office was open, even if it was only for a simple chat.

I thank all the people who have passed through our research group over the years: Dr. Julien Manshanden, Dr. Marvin Beck, Dr. Oindrila Ghosh, Dennis Maseizik, Suman Dey, Dr. Károly Seller and Dr. Danelise de Oliveira Franco. Thank you for all the time spent together and for sharing this experience with me. Special thanks go to Dr. Danelise de Oliveira Franco for not hesitating for a second when I asked her to read and comment on this thesis. I truly appreciated all your help and I hope one day to return the favor.

During my PhD I had the pleasure of being part of various scientific groups and collaborations. I would like to thank all the members of the Pierre Auger Collaboration, of which I was fortunate to be a part, and in particular the Phenomenology Task. My work would not have been possible without the groups of developers behind the simulation codes that I have used extensively over the years: CRPropa and SimProp. Thank you all for your help with problems and technical details, and for the maintenance and updating work you do.

I owe everything I have achieved in life to the support of my family. I would like to thank my mother, Antonietta, and my father, Marco, for encouraging me and helping me to embark on this adventure abroad. I know that you have paid the price of distance, and I will always be grateful. I would also like to thank my grandparents, Pietro and Silvana, for their love and support, one from here, and the other from up there.

I would also like to thank my closest friends: Alessio Garofalo, Emanuele Trulli and Alessia Boaretto from our hometown, and Cristian Ferrante, Leo D'Amato and Dr. Licia Romagnoli,

wherever life has taken us since our time in L'Aquila. Thank you for always doing your best to make me feel closer to home. I also want to thank my dear friend Samanta Porrini, for always being ready to listen whenever I needed it.

Life in Hamburg would not have been so memorable without the many friends I had the honour of meeting here. Firstly, I would like to thank Dr. Ilaria Quaglia, who I shared my first year in Hamburg with. I would also like to thank Marta D'Angelo for being a reliable friend and for always helping me navigate the bureaucracy of a foreign country. Thanks also go to my friends at the university Guest House: Valentino Neduhal, Dr. Sándor Mahó, Zsolt Mihályi, Dr. Bharat Parthasarathy and Dr. Mahesh Ramadoss. I will always carry with me the memories of our evenings and trips together. Finally, I would like to thank Gabriele Milella and Carla Stange, friends I might never have met if not for Hamburg, and I am grateful that life brought us together.

I decided to end these acknowledgments by addressing my partner, María Jesús Rapanague. We met almost by chance - you were the girl from the apartment across the hall - but from that moment on, we have never been apart. I am grateful to you for many things, but above all for being, at every moment, a friend, an adventure companion, and a constant presence by my side. Thank you for the love you show me every day, and for the way you always push me to move forward and overcome my limits. I never imagined I would meet someone like you when I set off on this adventure, but I am deeply thankful it happened. Thank you for choosing to share these years with me.

Ringraziamenti

Sono state tante le nuove amicizie e conoscenze nate in questi anni di dottorato ad Amburgo, e spero davvero di riuscire a dedicare un ringraziamento a tutti coloro che hanno contribuito alla mia vita e alla mia crescita durante questa esperienza.

Voglio iniziare ringraziando il Professor Günter Sigl per avermi dato la possibilità di svolgere il mio dottorato presso l'Università di Amburgo. Vorrei anche ringraziarlo per la libertà e l'indipendenza che mi ha concesso nello svolgere gli studi presentati in questa tesi, e per le numerose e stimolanti discussioni sui risultati ottenuti.

Un ringraziamento speciale va alla Professoressa Denise Boncioli, per tutto l'aiuto - sia in ambito scientifico che personale - che non ha mai esitato a offrirmi. Anche se negli ultimi anni non è stata ufficialmente la mia relatrice, ha continuato a essere una figura di riferimento e di ispirazione per la mia crescita personale.

Questo percorso non sarebbe stato possibile senza le molte persone da cui ho ricevuto aiuto e supporto all'Università di Amburgo. Prima di tutto, voglio ringraziare Elizabeth Duarte per il grande aiuto con tutte le questioni amministrative e burocratiche. Ringrazio Martin Stieben per l'aiuto e la disponibilità con le risorse numeriche fornite dal PHYSnet Compute Cloud. Anche se non direttamente collegata alla mia attività di ricerca, desidero ringraziare la Dottoressa Maria Vittoria Garzelli per tutte le volte in cui la porta del suo ufficio è stata aperta, anche solo per una semplice chiacchierata.

Ringrazio tutte le persone che sono passate per il nostro gruppo di ricerca in questi anni: il Dottor Julien Manshanden, il Dottor Marvin Beck, la Dottoressa Oindrila Ghosh, Dennis Maseizik, Suman Dey, il Dottor Károly Seller e la Dottoressa Danelise de Oliveira Franco. Vi ringrazio per tutto il tempo trascorso insieme e per aver condiviso con me questa esperienza. Un ringraziamento speciale va alla Dottoressa Danelise de Oliveira Franco per non aver esitato nemmeno un secondo quando le ho chiesto di leggere e commentare questa tesi. Ho davvero apprezzato tutto il tuo aiuto e spero un giorno di poter ricambiare.

Durante il dottorato ho avuto il piacere di far parte di vari gruppi e collaborazioni scientifiche. Ringrazio tutti i membri della Collaborazione Pierre Auger, di cui ho avuto la fortuna di far parte, e in particolare il Task di Fenomenologia. Il mio lavoro non sarebbe stato possibile senza i gruppi di sviluppatori dietro ai codici di simulazione che ho ampiamente utilizzato in questi anni: CRPropa e SimProp. Grazie a tutti per l'aiuto con problemi e dettagli tecnici, e per il lavoro di mantenimento e aggiornamento che svolgete.

Nulla nella mia vita sarebbe stato possibile senza il supporto della mia famiglia. Ringrazio mia madre Antonietta e mio padre Marco per l'incoraggiamento e l'aiuto nel lanciarmi in questa avventura all'estero. So che avete pagato il prezzo della distanza, e ve ne sarò sempre grato. Ringrazio mio nonno Pietro e mia nonna Silvana, che mi amano e mi supportano, chi da qui e

chi da lassù.

Un ringraziamento va ai miei più cari gruppi di amici: Alessio Garofalo, Emanuele Trulli e Alessia Boaretto dalla nostra città natale, e Cristian Ferrante, Leo D'Amato e la Dottoressa Licia Romagnoli da ovunque la vita ci abbia portati dopo gli anni a L'Aquila. Grazie per aver sempre fatto del vostro meglio per farmi sentire meno lontano da casa. Ringrazio anche la mia cara amica Samanta Porrini, per essere sempre stata pronta ad ascoltarmi quando ne ho avuto bisogno.

La vita ad Amburgo non sarebbe stata così memorabile senza il contributo dei molti amici che ho avuto l'onore di incontrare qui. Ringrazio la Dottoressa Ilaria Quaglia, con la quale ho condiviso il mio primo anno ad Amburgo. Un grazie va a Marta D'Angelo, per essere un'amica sulla quale si può davvero contare e per avermi sempre aiutato a non perdermi nella burocrazia di un paese straniero. Ringrazio di cuore gli amici della Guest House dell'università: Valentino Neduhal, il Dottor Sándor Mahó, Zsolt Mihályi, il Dottor Bharat Parthasarathy, il Dottor Mahesh Ramadoss. Porterò sempre con me i ricordi delle nostre serate e dei nostri viaggi insieme. Ringrazio Gabriele Milella e Carla Stange, amici che probabilmente non avrei incontrato se non fosse stato per Amburgo, ma sono grato che la vita ci abbia portati sulla stessa strada.

Ho deciso di concludere questi ringraziamenti rivolgendomi alla mia compagna, María Jesús Rapanague. Ci siamo conosciuti quasi per caso – eri la ragazza dell'appartamento di fronte – ma da quel momento non ci siamo più lasciati. Ti sono grato per molte cose, ma soprattutto per essere stata, in ogni momento, un'amica, una compagna di avventure e una presenza costante al mio fianco. Grazie per l'amore che mi dimostri ogni giorno, e per il modo in cui riesci sempre a spronarmi ad andare avanti e superare i miei limiti. Non avrei mai immaginato di trovare una persona come te quando sono partito per questa avventura, ma sono grato che sia accaduto. Grazie per aver scelto di condividere questi anni con me.